

# Convolutional neural networks for the CHIPS neutrino detector R&D project

Josh Chalcraft Tingey  
University College London

Submitted to University College London in fulfilment  
of the requirements for the award of the  
degree of **Doctor of Philosophy**



## Declaration

I, Josh Chalcraft Tingey confirm that the work presented in this thesis is my own. Where information has been derived from other sources, I confirm that this has been indicated in the thesis.

Josh Chalcraft Tingey



## Abstract

The CHerenkov detectors In mine PitS (CHIPS) neutrino detector R&D project aims to develop novel strategies and technologies for very large yet ‘cheap as chips’ water Cherenkov neutrino detectors. Via deployment in a body of water, use of commercially available components, and instrumentation coverage optimisation for the study of only accelerator beam neutrinos, CHIPS will enable megaton scale detectors to become a reality at the cost of \$200k-\$300k per kt of sensitive mass. During the summer of 2019 a 5 kt prototype CHIPS detector, CHIPS-5, was deployed into the Wentworth 2W disused mine pit in northern Minnesota, 7 mrad off the NuMI beam axis. A novel data acquisition system was introduced using cheap single-board computers and open-source software.

This work presents a novel approach to water Cherenkov neutrino detector event reconstruction and classification. Three forms of a Convolutional Neural Network, a type of deep learning algorithm, have been trained to reject cosmic muon events, classify beam events, and estimate neutrino energies, all using only a slightly modified version of the raw detector event as input. When evaluated on the expected distribution of CHIPS-5 events, this new approach is shown to be robust and explainable as well as providing a significant performance increase over the standard likelihood-based reconstruction and simple neural network classification. Promisingly, the performance presented here is comparable to the more complex (and expensive) neutrino oscillation experiments within the field.



## Impact Statement

The impact of this work inside the domain of academia is straightforward and explained in great detail throughout the thesis. A novel application of modern machine learning techniques is made to the reconstruction and classification of neutrino events within a water Cherenkov detector studying neutrino oscillations. Although other experiments within the field have conducted similar preliminary work, this is the first known comprehensive application of such methods. Hopefully, this work will promote the use of these techniques for water Cherenkov neutrino detectors more broadly.

Outside of academia, the impact of this work is less clear. Still, it is probably most pronounced in the field of machine learning, which promises to bring substantial societal advancements. Sometimes the application of machine learning to real-world problems is seen as somewhat secondary to achieving marginally incremental improvements on standardised challenges. This work hopefully works as part of a broader effort to not only make the application of machine learning methods more important but also to broaden the scope of tasks considered. Currently, the field is dominated by the commercial needs of a small number of large technology companies, such as Google and Facebook, any work that applies machine learning to a novel task can only help to broaden the scope of machine learning and make it more applicable to a wider range of real-world tasks.



## Acknowledgements

Firstly I would like to thank my supervisor Jenny for the independence she has given me throughout my PhD and for leading the whole CHIPS collaboration through two intense summers of construction activity.

I would also like to thank everyone within the broader CHIPS collaboration. Foremost Stefano for all of his incredible support and advice throughout all the stages of my PhD, as well as the UCL gang of Tom, Sim, Petr, and John for always being around and making the gulag bearable.

I would also like to thank everyone else within the UCL HEP group, particularly my office mates within D14.

Most importantly, I must thank Becca and my family for all of their endless support.



# Contents

<b>1</b>	<b>Introduction</b>	<b>15</b>
<b>2</b>	<b>Neutrino physics</b>	<b>17</b>
2.1	A history . . . . .	17
2.1.1	Discovery of the neutrinos . . . . .	17
2.1.2	Discovery of neutrino oscillations . . . . .	20
2.2	The Standard Model and neutrinos . . . . .	21
2.3	Neutrino oscillations . . . . .	23
2.3.1	Neutrino mixing . . . . .	23
2.3.2	Oscillations in a vacuum . . . . .	24
2.3.3	Oscillations in matter . . . . .	26
2.4	Neutrino interactions . . . . .	26
2.5	Current status and the future . . . . .	30
2.5.1	Current status . . . . .	30
2.5.2	Open questions . . . . .	33
2.5.3	The future . . . . .	36
<b>3</b>	<b>The CHIPS R&amp;D project</b>	<b>37</b>
3.1	The CHIPS concept . . . . .	38
3.1.1	The neutrino beam . . . . .	40
3.1.2	Water Cherenkov detectors . . . . .	43
3.2	CHIPS-5 . . . . .	47
3.2.1	Location . . . . .	47
3.2.2	Structure . . . . .	49
3.2.3	Instrumentation . . . . .	50
3.2.4	Filtration . . . . .	55
3.2.5	Construction and deployment . . . . .	56
3.2.6	Current status . . . . .	58

3.3	Detector simulation and event generation . . . . .	60
3.3.1	Detector simulation . . . . .	60
3.3.2	Beam event generation . . . . .	63
3.3.3	Cosmic event generation . . . . .	63
<b>4</b>	<b>Data acquisition for CHIPS</b>	<b>67</b>
4.1	White Rabbit timing . . . . .	68
4.2	Hardware . . . . .	70
4.2.1	Nikhef hardware . . . . .	70
4.2.2	Madison hardware . . . . .	74
4.2.3	Combined systems . . . . .	76
4.3	Software and the flow of data . . . . .	79
4.3.1	Control . . . . .	80
4.3.2	Hit handling . . . . .	82
4.3.3	Monitoring . . . . .	84
<b>5</b>	<b>Convolutional neural networks for CHIPS</b>	<b>87</b>
5.1	Previous applications of deep learning for neutrino experiments . . . . .	88
5.2	Standard event reconstruction and classification . . . . .	89
5.2.1	Likelihood-based reconstruction . . . . .	89
5.2.2	Event classification . . . . .	93
5.3	The theory of neural networks . . . . .	94
5.3.1	Neural network basics . . . . .	94
5.3.2	Training neural networks . . . . .	96
5.3.3	Convolutional neural networks . . . . .	100
5.3.4	Regularisation . . . . .	104
5.4	A baseline implementation for CHIPS . . . . .	107
5.4.1	Baseline inputs . . . . .	108
5.4.2	Baseline architecture . . . . .	112
5.4.3	Baseline outputs . . . . .	114
5.4.4	Baseline training . . . . .	115
5.5	Specific implementations for CHIPS . . . . .	116
5.5.1	Cosmic rejection . . . . .	117
5.5.2	Beam classification . . . . .	119
5.5.3	Energy estimation . . . . .	121

<b>6 Network evaluation</b>	<b>125</b>
6.1 Performance . . . . .	126
6.1.1 Evaluation sample and preselection . . . . .	126
6.1.2 Cosmic rejection and containment . . . . .	128
6.1.3 Beam classification . . . . .	132
6.1.4 Energy and vertex estimation . . . . .	143
6.1.5 Combined performance . . . . .	149
6.2 Explainability . . . . .	149
6.2.1 Feature map visualisation . . . . .	153
6.2.2 t-SNE visualisation . . . . .	153
6.3 Robustness . . . . .	157
6.3.1 Time smearing . . . . .	158
6.3.2 Charge smearing and shifting . . . . .	160
6.3.3 Random noise . . . . .	163
6.4 Alternative implementations . . . . .	165
6.4.1 Alternative inputs . . . . .	165
6.4.2 Alternative training samples . . . . .	168
6.4.3 Alternative architectures . . . . .	170
<b>7 Summary and conclusion</b>	<b>173</b>
<b>Bibliography</b>	<b>177</b>
<b>List of figures</b>	<b>191</b>
<b>List of tables</b>	<b>197</b>



# Chapter 1

## Introduction

It is abundantly evident that machine learning and the broader field of artificial intelligence will play an ever-increasing role in the world around us over the coming years. Virtually every industry and human on the planet are promised to be touched by their proliferation. Whether this change will have an entirely positive or somewhat detrimental effect on society as a whole is still up for debate, however, within the field of physics, especially experimental particle physics, machine learning applications can only be seen in a positive light.

Already, a widespread revolution is underway across the field. From the way particle interactions are simulated to the way recorded events are analysed, machine learning techniques, usually deep learning algorithms, are yielding dramatic performance improvements. This is particularly true of the study of the vastly abundant yet incredibly difficult to detect neutrino. Principally driven by the fact that the raw output from neutrino detectors is well suited to the algorithms at the forefront of computer vision research, many neutrino experiments now routinely use deep learning methods for event analysis.

However, to date, a thorough end-to-end implementation of such techniques is not yet in use for the reconstruction and classification of neutrino events within long-baseline water Cherenkov detectors studying accelerator beam neutrinos. Without redress, this lack of progress could have significant implications for the future of neutrino physics, especially when such experiments are deemed a highly promising (and potentially cheap) channel for answering some of the critical unsolved problems of the field.

This thesis presents a broad range of work conducted for one such experiment, the CHerenkov detectors In mine PitS (CHIPS) neutrino detector R&D project. CHIPS aims to develop very large yet ‘cheap as chips’ water Cherenkov detectors that can be deployed

into deep bodies of water on the Earth’s surface, allowing megaton scale detectors to become a reality. The author’s principal contribution comes from the novel application of Convolutional Neural Networks, a type of deep learning algorithm, to the reconstruction, classification, and energy estimation of neutrino events within the CHIPS-5 prototype detector module.

It is hoped that the work presented in this thesis will achieve three principal goals. Firstly, motivate the need for the CHIPS project and detail how it accomplishes its aims. Secondly, show that Convolutional Neural Networks can be used to fully reconstruct and classify neutrino events within water Cherenkov detectors in an explainable and robust manner whilst also providing significant performance improvements. Finally, inform the development of similar Convolutional Neural Network implementations for other water Cherenkov neutrino detectors.

To begin, Chapter 2 introduces the history of neutrino physics, as well as the theoretical background and current status of the field as motivation for the CHIPS project. A full description of the CHIPS detector concept follows in Chapter 3, with a principal focus on the CHIPS-5 prototype detector module deployed into the NuMI neutrino beam during the autumn of 2019. A particularly detailed overview of the CHIPS-5 data acquisition and monitoring systems is then given in Chapter 4, for which the author played a major role.

Chapter 5 begins by introducing the standard reconstruction and classification methods to be replaced alongside a review of the relevant neural network theory and current deep learning applications within the field of neutrino physics. The chapter concludes by detailing the three Convolutional Neural Networks that have been developed for CHIPS-5, including that for cosmic muon rejection, beam event classification, and neutrino energy estimation. This work is solely that of the author’s.

The thesis closes in Chapter 6 with a comprehensive evaluation of the new Convolutional Neural Network approach. Firstly, the final combined performance is determined and compared with similar experiments. Secondly, the inner workings of the trained networks are explored. Thirdly, the robustness of the network outputs to distributional changes in the input is studied. Finally, alternative implementations are discussed to highlight the key factors driving performance.

# Chapter 2

## Neutrino physics

Vast numbers of neutrinos pass through everything that surrounds us each second, each one incredibly unlikely to interact even once. Nearly a century since they were first proposed, these mysterious particles have now conclusively been proven to undergo oscillations between their flavour states. This profound discovery has opened the door to physics beyond that initially conceived within the Standard Model, which may reveal new, fundamental insights into the universe. This chapter aims to outline the historical context, theoretical background, and open questions surrounding the neutrino to motivate the CHIPS R&D project.

### 2.1 A history

#### 2.1.1 Discovery of the neutrinos

In the early 20th century, beta decays were assumed to follow the simple two-body process,  $A \rightarrow B + e$ , where  $A$  spontaneously emits a single electron. To conserve both energy and angular momentum, the ejected electron was believed to have discrete kinetic energy defined by the difference in binding energies between  $A$  and  $B$ . However, in 1914, J. Chadwick instead measured a continuous electron energy spectrum [1], placing this assumption in doubt.

W. Pauli proposed a ‘desperate solution’ to this paradox in 1930 [2]. If a light, neutrally charged, spin 1/2 particle was also produced in the interaction, the continuous energy distribution could be explained. Initially, this peculiar new particle was named the *neutron*. However, to avoid confusion with the heavy baryon of the same name

discovered in 1932, E. Fermi renamed it the *neutrino* when he formalised his theory of beta decay in 1934 [3].

The same year, H. Bethe and R. Peierls [4] used Fermi's work to estimate the cross-section for the inverse beta decay process

$$\bar{\nu} + p^+ \rightarrow n + e^+. \quad (2.1)$$

They calculated an upper limit of  $\sigma < 10^{-44}\text{cm}^2$  for neutrinos of energy 2.3 MeV, an incredibly small value. When summarising, they declared that 'it seems highly improbable that, even for cosmic ray energies,  $\sigma$  becomes large enough to allow the process to be observed'. Although this estimation did not prove accurate, and extensive neutrino observations have since been made, it hinted at the great difficulties experimentalists would face measuring the neutrino in the years to come.

After an initial tentative identification in 1953, F. Reines and C. Cowan made the first confirmed observation of the neutrino in 1956 [5]. Electron antineutrinos produced within the Savannah River Plant nuclear reactor were detected via the inverse beta decay process outlined in equation (2.1). In an underground room of the reactor building, a 'club-sandwich' detector was constructed containing three 1500 litre liquid scintillator tanks interspersed with two 200 litre cadmium doped water target tanks. A total of 330 photomultiplier tubes then measured the characteristic signal for the interaction, a positron annihilation followed shortly afterwards by a gamma-ray burst from the neutron capture.

A second distinct neutrino, the muon neutrino, was discovered in 1962 at the Brookhaven based Alternating Gradient Synchrotron (AGS) [6]. Protons from the AGS beam incident upon a fixed target produced charged pions which then decayed into a beam of muons and neutrinos. After passing through steel and lead absorbers to remove the muons, neutrino interactions were detected in a series of downstream spark chambers.

If only a single neutrino existed, both interactions

$$\nu + p^+ \rightarrow \mu^+ + n, \quad (2.2)$$

$$\nu + p^+ \rightarrow e^+ + n, \quad (2.3)$$

were expected to occur at the same rate. However, only muons, identified by a single long track in the spark chambers were detected, confirming the existence of the muon neutrino.

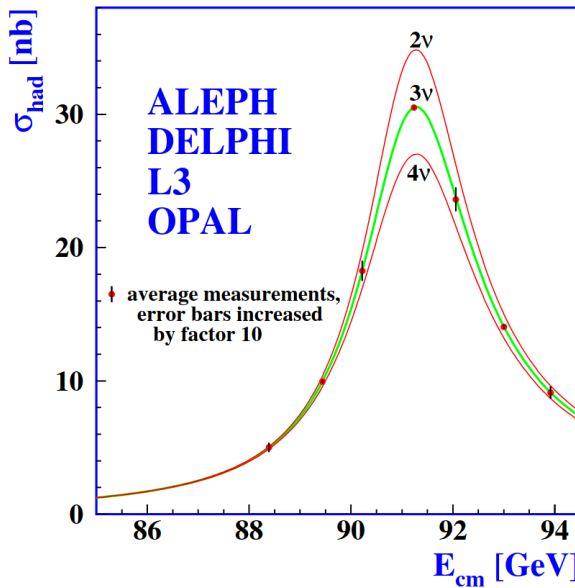


**Figure 2.1:** Combined hadron production cross-section measurements around the  $Z^0$  resonance from the LEP experiments. The curves show the predicted cross-section for two, three, and four active neutrinos. Note how the data fits the three active neutrino hypothesis incredibly well. Figure taken from reference [9].

Not only was this experiment the first to construct and use an artificial neutrino beam, but it also won the 1988 Nobel Prize in Physics.

The  $Z^0$  and  $W^\pm$  bosons were discovered at the CERN based Super Proton Synchrotron in 1983 [7, 8]. Crucially, as  $Z^0$  bosons were expected to decay to neutrinos, measurements made to the decay width could strongly constrain the number of neutrino flavours. The ALEPH, DELPHI, L3, and OPAL experiments at the LEP  $e^+e^-$  collider in the 1990s made such precise measurements (see Figure 2.1), indicating that the number of light active neutrino flavours was  $2.984 \pm 0.008$  [9].

This indication from LEP combined with the discovery of the charged tau lepton in 1975 [10] made the existence of a third tau neutrino extremely likely. The Fermilab based DONUT experiment finally discovered this particle in 2001 using 800 GeV protons from the Tevatron [11], completing the trio of neutrinos we know today. However, additional *sterile* neutrino flavours which do not couple to the weak force are still a possibility, with various hints to their existence having been observed [12].

### 2.1.2 Discovery of neutrino oscillations

At the Homestake mine in the 1960s, a 400 000 litre tank, placed 1.5 km underground, was filled with the dry cleaning fluid perchloroethylene ( $C_4Cl_8$ ). Its goal was to measure the electron neutrino flux incident upon the Earth from the Sun via the interaction



This process (equation (2.4)) allowed the neutrino flux to convert the chlorine contained within the tank into the noble gas argon. Every few weeks the tank was purged with gaseous helium and the amount of argon generated, and indirectly the solar neutrino flux, measured.

After analysis, the number of electron neutrino interactions per  $^{37}Cl$  per second, was found to be no greater than 3 [13]. When compared to the predictions made by the Standard Solar Model ranging between 4.4 and 22 [14], a deficit was observed. Dubbed the *solar neutrino problem*, this was initially believed to be due to an unexplained experimental flaw. However, other experiments, such as the water Cherenkov Kamiokande II [15] and the SAGE and GALLEX gallium based capture tanks also observed this discrepancy [16, 17].

A second deficit, the *atmospheric neutrino anomaly*, was also indirectly observed for neutrinos generated in the Earth's upper atmosphere by cosmic rays. Such neutrinos formed a pivotal background to both the Kamiokande and IMD experiments, which were primarily designed to measure proton decay. When evaluating their backgrounds, a deficit in the number of muon neutrinos compared to electron neutrinos was observed [18, 19]. The successor to the Kamiokande experiment, Super-Kamiokande also measured a similar deficit [20].

The phenomenon of neutrino oscillations was put forward as a solution to this problem. If neutrinos could change flavour as they propagated, the measured deficits could be explained. The SNO experiment finally confirmed such oscillations in 2001 [21].

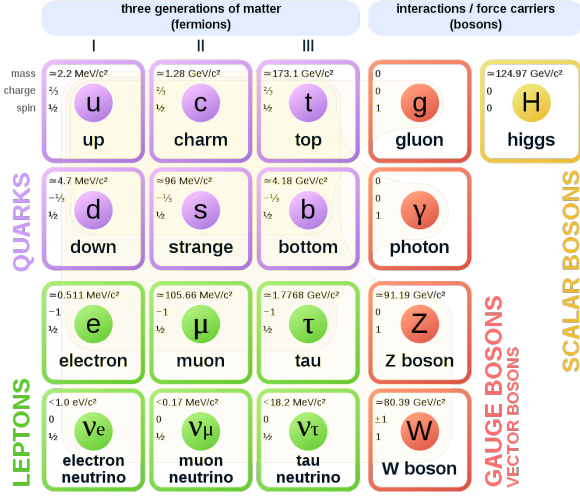


**Figure 2.2:** The particles of the Standard Model. Figure taken from reference [22].

SNO consisted of a 1 kt tank of deuterium (heavy water), equipped with 9500 photomultiplier tubes. Light from three separate neutrino interaction channels:

$$\nu_i + e \rightarrow \nu_i + e, \quad (2.5)$$

$$\nu_i + d \rightarrow p + n + \nu_i, \quad (2.6)$$

$$\nu_e + d \rightarrow p + p + e, \quad (2.7)$$

was measured, where  $d$  is the deuterium nucleus. The first and second channels were sensitive to all three neutrino flavours, but crucially only electron neutrinos could interact via the third channel. By comparing the relative rates between the channels, SNO was able to prove to  $5.3 \sigma$  that electron neutrinos had oscillated to other flavours.

## 2.2 The Standard Model and neutrinos

The Standard Model of particle physics describes the seventeen known fundamental subatomic particles and their interactions. Combining both quantum chromodynamics (describing the strong force) and electroweak theory (describing the electromagnetic and weak forces), the Standard Model is a gauge theory obeying the local gauge symmetries of  $U(1) \times SU(2) \times SU(3)$ . The particles, along with their various properties, are outlined in Figure 2.2. Additionally, all have an associated anti-particle with the same quantum numbers except the electric charge, which is opposite.

The six quarks and six leptons, all spin 1/2 particles, are named fermions. Further divided into three generations (or flavours), they make up all the matter content of the universe. The quarks never exist in a free state and bind together into mesons or baryons, such as pions and protons, respectively. Three charged massive particles, the electron, the muon, and the tau and their three corresponding (initially assumed to be massless) neutrinos, make up the leptons.

The spin 1 gauge bosons carry the electromagnetic, strong, and weak forces. The photon carries the electromagnetic force (affecting all charged particles), the gluons carry the strong force (binding the quarks together), and the massive  $Z^0$  and  $W^\pm$  carry the weak force. The final particle, the Higgs, is a massive scalar boson. Via the process of spontaneous symmetry breaking, the Higgs provides the mechanism to give the particles their mass.

Within the Standard Model, neutrinos only interact via the weak force, exclusively coupling to the  $Z^0$  and  $W^\pm$  bosons. As the weak interaction maximally violates parity, in that it only couples to left-handed chiral particles, the original Standard Model only contains left-handed neutrinos and their corresponding right-handed anti-neutrinos.

Although neutrinos were initially thought to be massless, and no direct detection of their mass has been made, it is now believed that neutrinos are massive (albeit very light) particles. This belief is due to the substantial amount of evidence in support of neutrino oscillations, such as the result from SNO amongst others detailed in Section 2.5. These oscillations require three distinct neutrino mass states, implying at least two are non-zero.

The Standard Model does not strictly rule out massive neutrinos, which are permitted as either *Dirac* or *Majorana* particles. If neutrinos are Dirac in nature, they acquire their mass via a Yukawa coupling, just like the other fermions. This coupling mixes both left-handed and right-handed fields, requiring the existence of right-handed neutrinos (left-handed antineutrinos) that do not interact via the weak force. Conversely, if neutrinos are Majorana in nature, a mass term can be introduced containing just the left-handed neutrino states. This term requires that the neutrino is its own anti-particle, which as neutrinos do not carry a charge, is possible [12].

Strongly model-dependent cosmological observations of the cosmic microwave background currently provide the best limit on the combined sum of the neutrino masses at  $\sum m_\nu < 0.12$  eV [23]. Furthermore, the KATRIN experiment has been able to make

model-independent direct measurements of the upper mass limit by looking at the energy spectrum of electrons emitted from beta decay, giving a result of  $m_\nu < 1.1$  eV [24].

## 2.3 Neutrino oscillations

B. Pontecorvo, Z. Maki, M. Nakagawa, and S. Sakata developed the theory of neutrino oscillations in the 1960s [25–27]. Fundamentally, it is a manifestation of the phenomenon of quantum interference. If neutrinos are massive, their mass eigenstates are not necessarily the same as their weakly interacting flavour eigenstates. Instead, the flavour states are a superposition of the three mass states, each propagating as distinct waves evolving differently with time. As a direct consequence, if a neutrino is created with a specific flavour  $\alpha$ , its flavour composition will change with time, such that it may later be detected as having a flavour  $\beta$ . The probability of this change is found to be periodic (hence oscillations) and dependent on the neutrino energy, the propagation distance, and a rotational mixing matrix.

### 2.3.1 Neutrino mixing

The mixing between the flavour eigenstates  $|\nu_\alpha\rangle$ , where  $\alpha = e, \mu, \tau$ , and the mass eigenstates  $|\nu_k\rangle$ , where  $k = 1, 2, 3$ , is described by the *Pontecorvo-Maki-Nakagawa-Sakata* (PMNS) matrix  $U$ , such that

$$|\nu_\alpha\rangle = \sum_k^3 U_{\alpha k}^* |\nu_k\rangle, \quad (2.8)$$

and vice-versa

$$|\nu_k\rangle = \sum_\alpha^3 U_{\alpha k} |\nu_\alpha\rangle. \quad (2.9)$$

The PMNS matrix is a unitary, complex,  $3 \times 3$  matrix, similar to the Cabibbo-Kobayashi-Maskawa (CKM) matrix for quark mixing, and has the form

$$\begin{pmatrix} |\nu_e\rangle \\ |\nu_\mu\rangle \\ |\nu_\tau\rangle \end{pmatrix} = \begin{pmatrix} U_{e1} & U_{e2} & U_{e3} \\ U_{\mu 1} & U_{\mu 2} & U_{\mu 3} \\ U_{\tau 1} & U_{\tau 2} & U_{\tau 3} \end{pmatrix} \begin{pmatrix} |\nu_1\rangle \\ |\nu_2\rangle \\ |\nu_3\rangle \end{pmatrix}. \quad (2.10)$$

Three mixing angles and six complex phases can generally describe a  $3 \times 3$  matrix such as this. However, the majority of these phases can be removed without affecting any physical process. This leaves three mixing angles  $\theta_{12}$ ,  $\theta_{23}$ ,  $\theta_{13}$  and a single phase  $\delta$  which if non-zero produces CP violation and so is commonly denoted  $\delta_{CP}$ .

With  $s_{ij} = \sin \theta_{ij}$  and  $c_{ij} = \cos \theta_{ij}$ , the standard parametrisation of  $U$  assuming neutrinos are Dirac particles is given by

$$U = \begin{pmatrix} 1 & 0 & 0 \\ 0 & c_{23} & s_{23} \\ 0 & -s_{23} & c_{23} \end{pmatrix} \begin{pmatrix} c_{13} & 0 & s_{13}e^{-i\delta_{CP}} \\ 0 & 1 & 0 \\ -s_{13}e^{-i\delta_{CP}} & 0 & c_{13} \end{pmatrix} \begin{pmatrix} c_{12} & s_{12} & 0 \\ -s_{12} & c_{12} & 0 \\ 0 & 0 & 1 \end{pmatrix} \quad (2.11)$$

$$= \begin{pmatrix} c_{12}c_{13} & s_{12}c_{13} & s_{13}e^{-i\delta_{CP}} \\ -s_{12}c_{23} - c_{12}s_{23}s_{13}e^{i\delta_{CP}} & c_{12}c_{23} - s_{12}s_{23}s_{13}e^{i\delta_{CP}} & s_{23}c_{13} \\ s_{12}s_{23} - c_{12}c_{23}s_{13}e^{i\delta_{CP}} & -c_{12}s_{23} - s_{12}c_{23}s_{13}e^{i\delta_{CP}} & c_{23}c_{13} \end{pmatrix}. \quad (2.12)$$

If neutrinos are instead Majorana in nature two additional phases  $\alpha_{21}$  and  $\alpha_{31}$  are required, such that the mixing matrix needs to be multiplied by

$$\text{diag}(1, e^{\frac{i\alpha_{21}}{2}}, e^{\frac{i\alpha_{31}}{2}}). \quad (2.13)$$

### 2.3.2 Oscillations in a vacuum

As the neutrino mass states are eigenstates of the hamiltonian with energy eigenvalues  $E_k$ :

$$H |\nu_k\rangle = E_k |\nu_k\rangle, \quad (2.14)$$

their time evolution is described by the Schrödinger equation. Therefore, the neutrino flavour state evolves with time  $t$ , such that

$$|\nu_\alpha(t)\rangle = \sum_k^3 U_{\alpha k}^* e^{-iE_k t} |\nu_k\rangle. \quad (2.15)$$

After a time  $t$ , the probability of finding  $|\nu_\alpha\rangle$  in the state  $|\nu_\beta\rangle$  is then given by

$$P(\nu_\alpha \rightarrow \nu_\beta, t) = |\langle \nu_\beta | \nu_\alpha(t) \rangle|^2 = \left| \sum_k^3 U_{\alpha k}^* U_{\beta k} e^{-iE_k t} \right|^2 \quad (2.16)$$

$$= \sum_k^3 \sum_j^3 U_{\alpha k}^* U_{\beta k} U_{\alpha j} U_{\beta j}^* e^{i(E_k - E_j)t}. \quad (2.17)$$

As neutrinos are ultrarelativistic ( $p \simeq E$ ) the approximation can be made that

$$E_k = \sqrt{\vec{p}_k^2 + m_k^2} \simeq E + \frac{m_k^2}{2E}, \quad (2.18)$$

where  $\vec{p}_k$  and  $m_k$  are the neutrino momentum and energy, and  $E$  is the neutrino energy without the mass. This allows the substitution

$$E_k - E_j \sim \frac{\Delta m_{kj}^2}{2E}, \quad (2.19)$$

where  $\Delta m_{kj}^2$  is the squared mass difference (*mass splitting*) between the  $k$  and  $j$  mass states. Additionally, the relativistic limit allows the simplification  $t = L$ , where  $L$  is the distance from neutrino creation to detection. Combined, the oscillation probability can be written as

$$\begin{aligned} P(\nu_\alpha \rightarrow \nu_\beta, t) &= \delta_{\alpha\beta} - 4 \sum_{k>j} \text{Re}(U_{\alpha k}^* U_{\beta k} U_{\alpha j} U_{\beta j}^*) \sin^2 \left( \frac{\Delta m_{kj}^2 L}{4E} \right) \\ &\quad \pm 2 \sum_{k>j} \text{Im}(U_{\alpha k}^* U_{\beta k} U_{\alpha j} U_{\beta j}^*) \sin \left( \frac{\Delta m_{kj}^2 L}{4E} \right), \end{aligned} \quad (2.20)$$

where the last term has a positive sign for neutrinos and a negative sign for anti-neutrinos.

From inspecting equation (2.20), the superposition of mass eigenstates is seen to drive the oscillation of the flavour state, with the amplitude arising from the elements of the PMNS matrix. Furthermore, as a fixed experimental location and neutrino source define

a constant  $L/E$ , the period of oscillation is determined by the squared mass difference between the flavour states  $\Delta m_{kj}^2$ .

### 2.3.3 Oscillations in matter

As neutrinos propagate through matter, they undergo coherent forward scattering with nucleons. These interactions do not change the neutrino state or momentum, but they do impart an interaction potential onto the neutrinos. Two types of interaction can take place, either through the exchange of a  $Z^0$  in a *neutral-current* (NC) interaction, or a  $W^\pm$  in a *charged-current* (CC) process. The two interaction potentials are given by:

$$V_{NC} = \pm \frac{1}{\sqrt{2}} G_F n_n, \quad (2.21)$$

$$V_{CC} = \pm \sqrt{2} G_F n_e, \quad (2.22)$$

were  $n_n$  and  $n_e$  are the number density of neutrons and electrons in the propagation medium respectively and  $G_F$  is Fermi's constant. The sign of the potential is positive for neutrinos and negative for anti-neutrinos.

Crucially, as matter is full of electrons but empty of muons or taus, only electron neutrinos will interact via the CC channel as shown in Figure 2.3. Consequently, only electron neutrinos are affected by the  $V_{CC}$  potential, while all flavours are affected by the  $V_{NC}$  potential. When quantitatively applied as an additional potential to the vacuum hamiltonian, a resonance oscillation term is introduced which significantly modifies the vacuum oscillation probabilities. This phenomenon is known as the Mikheev, Smirnov, and Wolfenstein (MSW) effect [28, 29].

It is important to note two things. Firstly, the  $\pm$  in the  $V_{CC}$  potential introduces a difference between neutrinos and anti-neutrinos. Secondly, the modified oscillation probability is found to be non-symmetric with respect to the sign of the  $\Delta m_{kj}^2$  parameters.

## 2.4 Neutrino interactions

As outlined in Section 2.3.3, there are two types of weak neutrino interactions with nucleons: charged-current (CC) and neutral-current (NC), occurring via the exchange of a  $Z^0$  or  $W^\pm$  respectively. During a CC interaction, the neutrino is transformed into a

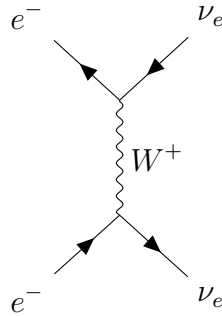


**Figure 2.3:** Feynman diagram of a charged-current coherent scattering interaction between an electron neutrino and an electron.

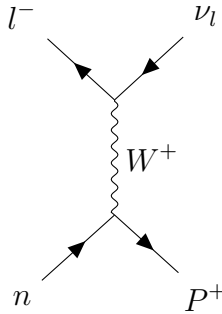


**Figure 2.4:** Feynman diagram of a charged-current quasi-elastic interaction between a neutrino and a neutron. By identifying the flavour of the final state charged lepton the flavour of the original neutrino can be determined.

charged lepton of the same flavour, conserving charge, flavour, and lepton number as shown in Figure 2.4. Contrastingly, during a NC interaction, there is no charge or flavour exchange, and the neutrino continues into the final state as shown in Figure 2.5.

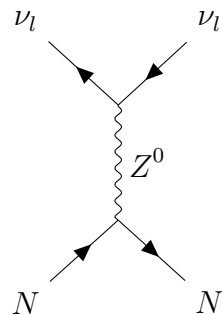


**Figure 2.5:** Feynman diagram of a neutral-current interaction between a neutrino and a nucleon. The flavour of the neutrino can not be identified as there is no charged lepton in the final state.

CC interactions provide the signal events for the majority of neutrino experiments as the original neutrino flavour can be determined via identification of the charged lepton. Conversely, NC interactions are commonly background events as there is no way to identify the original neutrino given the absence of a charged lepton in the final state.

For CHIPS the relevant neutrino interaction energy regime is commonly referred to as the *transition region*, covering a range of energies between 1 and 10 GeV. Both CC and NC interactions within this regime fall into one of five main categories:

- **Quasi-Elastic scattering (QEL)** is the dominant channel for energies below 1 GeV and involves the neutrino scattering off the entire nucleon. In the CC neutrino case, this converts the target neutron to a proton (reversed for antineutrinos). The same process can also occur in a NC interaction, where it is referred to as *elastic* scattering.
- **Meson Exchange Current (MEC)** provides an additional contribution to the energy range dominated by QEL interactions, involving two nucleons and producing two protons in the final state. Sometimes referred to as the  $2p2h$  interaction, it has become essential for explaining the discrepancy between theory and observations within many modern neutrino experiments, and is now included by default in the popular event generators [30].
- **Resonant pion production (Res)** is the dominant channel between 1 and 2 GeV and involves the neutrino exciting the nucleon into a resonant state. The resonance then decays the vast majority of the time to produce a single pion and nucleon. Resonant production is responsible for the majority of NC  $\pi^0$  events within water Cherenkov detectors such as CHIPS. This channel, as discussed further in Section 3.1.2 forms an incredibly tricky component of the background as it can mimic the event topology of a single electron.
- **Coherent pion production (Coh)** is a much rarer interaction mechanism where the neutrino scatters coherently from the entire nucleus. This process transfers negligible energy to the target and produces a significantly forward scattered single pion with no nuclear recoil in the final state.
- **Deep Inelastic Scattering (DIS)** is dominant for neutrino energies above 3 GeV with the additional energy allowing for the neutrino to resolve the individual quark content of the nucleon. The subsequent scattering from an individual quark produces

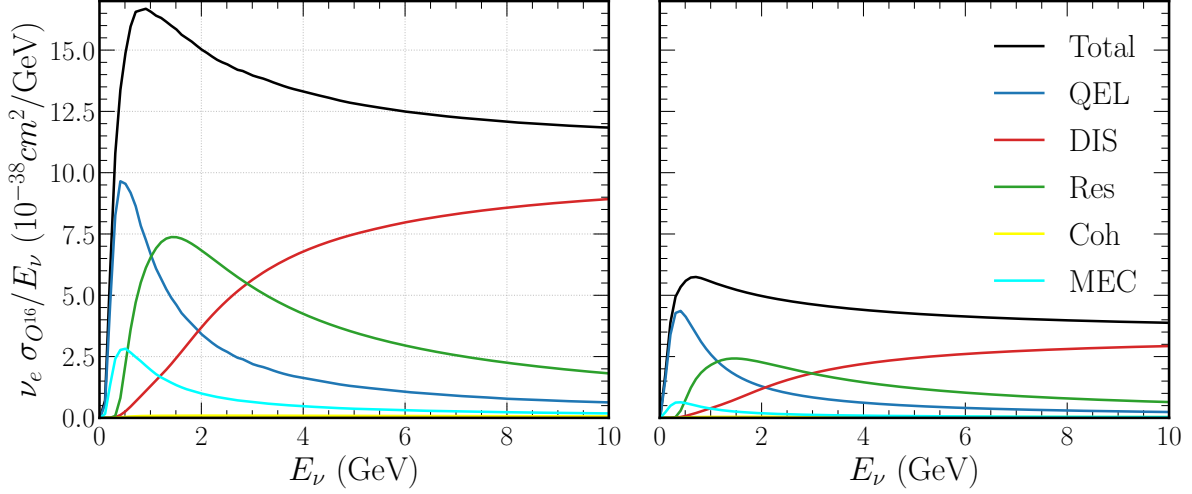


**Figure 2.6:** GENIE cross-sections on oxygen divided by neutrino energy for CC  $\nu_e$  (left) and NC  $\nu_e$  (right). Shown are the total and contributing process cross-sections. Note how the total cross-section approaches a linear dependence on energy and the NC cross-sections are smaller than their CC counterparts. See reference [32] for generation details.

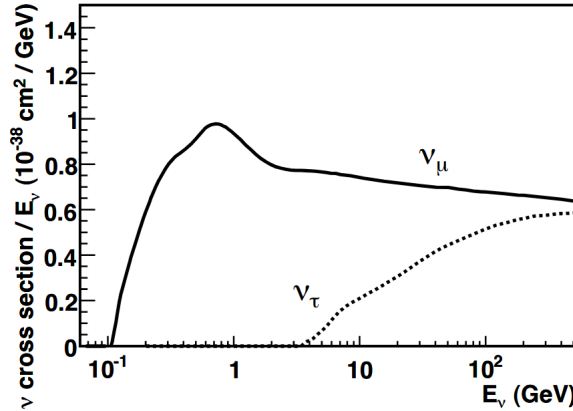


**Figure 2.7:** The total CC interaction cross-section per nucleon divided by the neutrino energy for  $\nu_\mu$  and  $\nu_\tau$ . Figure taken from reference [33].

a hadronic shower in the final state containing multiple pions which are often a challenge to reconstruct.

The standard  $\nu_e$  cross-sections (very similar to those for  $\nu_\mu$ ) included with the GENIE event generator [31, 32] are shown in Figure 2.6 for both CC and NC interactions. For  $\nu_\tau$  interactions the CC cross-sections differ considerably due to the large tau lepton mass, as shown in Figure 2.7, only becoming non-negligible for energies above  $\sim 5$  GeV.

## 2.5 Current status and the future

The three-component representation of the PMNS matrix presented in equation (2.11) splits our understanding of neutrino oscillations into three sectors. Historically, the sectors corresponded to experiments observing different sources of neutrinos, from either the Sun, atmosphere, or nuclear reactors. Hence the standard names given to each: the *solar sector*, *atmospheric sector*, and *reactor sector*. However, it is perhaps more rigorous to think of each sector as corresponding to the parameters they encompass:  $\Delta m_{21}^2$  and  $\theta_{12}$  for solar,  $\Delta m_{32}^2$  and  $\theta_{23}$  for atmospheric, and  $\theta_{13}$  for reactor.

During the last couple of decades, the focus of neutrino experiments across all sectors has shifted from the discovery of neutrino fundamentals to the precise measurement of oscillation parameters. This change has led to a corresponding shift into using increasingly abundant neutrino sources (such as accelerator neutrino beams) and larger and larger detectors. Here we outline the current status, open questions, and future for neutrino physics.

### 2.5.1 Current status

Global fits to neutrino oscillation data best summarise the current state of neutrino physics. These aggregate the latest experimental results to constrain the neutrino oscillation parameters. The best-fit results from one such fit, NuFIT [34, 35], are shown in Figure 2.8. A detailed overview of other global fits is given in The Particle Data Group's 2020 Review of Particle Physics (see reference [12]). In summary, all mixing angles  $\theta_{12}$ ,  $\theta_{23}$ , and  $\theta_{13}$  are found to be non-zero and  $\Delta m_{21}^2$  is found to be much smaller than  $\Delta m_{32}^2$ .

#### Solar parameters: $\theta_{12}$ and $\Delta m_{21}^2$

Current best fit results for the solar sector parameters yield  $\theta_{12} \sim 34^\circ$  with  $\sim 1.5^\circ$  of uncertainty, and  $\Delta m_{21}^2 \sim 7.4 \times 10^{-5} \text{ eV}^2$  with  $\sim 0.4 \times 10^{-5} \text{ eV}^2$  of uncertainty.

These results primarily come from a range of historical and currently running experiments studying neutrinos generated by the Sun: the radiochemical chlorine-based Homestake [36]; the gallium-based GALLEX [37] and SAGE [38]; the deuterium Cherenkov SNO [39]; the water Cherenkov Super-Kamiokande [40–43]; and the liquid scintillator

NuFIT 5.0 (2020)					
		Normal Ordering (best fit)		Inverted Ordering ( $\Delta\chi^2 = 2.7$ )	
		bfp $\pm 1\sigma$	$3\sigma$ range	bfp $\pm 1\sigma$	$3\sigma$ range
without SK atmospheric data	$\sin^2 \theta_{12}$	$0.304^{+0.013}_{-0.012}$	$0.269 \rightarrow 0.343$	$0.304^{+0.013}_{-0.012}$	$0.269 \rightarrow 0.343$
	$\theta_{12}/^\circ$	$33.44^{+0.78}_{-0.75}$	$31.27 \rightarrow 35.86$	$33.45^{+0.78}_{-0.75}$	$31.27 \rightarrow 35.87$
	$\sin^2 \theta_{23}$	$0.570^{+0.018}_{-0.024}$	$0.407 \rightarrow 0.618$	$0.575^{+0.017}_{-0.021}$	$0.411 \rightarrow 0.621$
	$\theta_{23}/^\circ$	$49.0^{+1.1}_{-1.4}$	$39.6 \rightarrow 51.8$	$49.3^{+1.0}_{-1.2}$	$39.9 \rightarrow 52.0$
	$\sin^2 \theta_{13}$	$0.02221^{+0.00068}_{-0.00062}$	$0.02034 \rightarrow 0.02430$	$0.02240^{+0.00062}_{-0.00062}$	$0.02053 \rightarrow 0.02436$
	$\theta_{13}/^\circ$	$8.57^{+0.13}_{-0.12}$	$8.20 \rightarrow 8.97$	$8.61^{+0.12}_{-0.12}$	$8.24 \rightarrow 8.98$
	$\delta_{CP}/^\circ$	$195^{+51}_{-25}$	$107 \rightarrow 403$	$286^{+27}_{-32}$	$192 \rightarrow 360$
	$\frac{\Delta m_{21}^2}{10^{-5} \text{ eV}^2}$	$7.42^{+0.21}_{-0.20}$	$6.82 \rightarrow 8.04$	$7.42^{+0.21}_{-0.20}$	$6.82 \rightarrow 8.04$
	$\frac{\Delta m_{3\ell}^2}{10^{-3} \text{ eV}^2}$	$+2.514^{+0.028}_{-0.027}$	$+2.431 \rightarrow +2.598$	$-2.497^{+0.028}_{-0.028}$	$-2.583 \rightarrow -2.412$
with SK atmospheric data		Normal Ordering (best fit)		Inverted Ordering ( $\Delta\chi^2 = 7.1$ )	
		bfp $\pm 1\sigma$	$3\sigma$ range	bfp $\pm 1\sigma$	$3\sigma$ range
	$\sin^2 \theta_{12}$	$0.304^{+0.012}_{-0.012}$	$0.269 \rightarrow 0.343$	$0.304^{+0.013}_{-0.012}$	$0.269 \rightarrow 0.343$
	$\theta_{12}/^\circ$	$33.44^{+0.77}_{-0.74}$	$31.27 \rightarrow 35.86$	$33.45^{+0.78}_{-0.75}$	$31.27 \rightarrow 35.87$
	$\sin^2 \theta_{23}$	$0.573^{+0.016}_{-0.020}$	$0.415 \rightarrow 0.616$	$0.575^{+0.016}_{-0.019}$	$0.419 \rightarrow 0.617$
	$\theta_{23}/^\circ$	$49.2^{+0.9}_{-1.2}$	$40.1 \rightarrow 51.7$	$49.3^{+0.9}_{-1.1}$	$40.3 \rightarrow 51.8$
	$\sin^2 \theta_{13}$	$0.02219^{+0.00062}_{-0.00063}$	$0.02032 \rightarrow 0.02410$	$0.02238^{+0.00063}_{-0.00062}$	$0.02052 \rightarrow 0.02428$
	$\theta_{13}/^\circ$	$8.57^{+0.12}_{-0.12}$	$8.20 \rightarrow 8.93$	$8.60^{+0.12}_{-0.12}$	$8.24 \rightarrow 8.96$
	$\delta_{CP}/^\circ$	$197^{+27}_{-24}$	$120 \rightarrow 369$	$282^{+26}_{-30}$	$193 \rightarrow 352$
	$\frac{\Delta m_{21}^2}{10^{-5} \text{ eV}^2}$	$7.42^{+0.21}_{-0.20}$	$6.82 \rightarrow 8.04$	$7.42^{+0.21}_{-0.20}$	$6.82 \rightarrow 8.04$
	$\frac{\Delta m_{3\ell}^2}{10^{-3} \text{ eV}^2}$	$+2.517^{+0.026}_{-0.028}$	$+2.435 \rightarrow +2.598$	$-2.498^{+0.028}_{-0.028}$	$-2.581 \rightarrow -2.414$

**Figure 2.8:** Three-flavour results from the NuFIT v5.0 global fit as of July 2020, showing both  $1\sigma$  uncertainties and  $\pm 3\sigma$  ranges. The first column shows results for an assumed normal hierarchy while the second for an inverted hierarchy. The lower section includes atmospheric neutrino data from the Super-Kamiokande experiment, while the upper section does not. Figure taken from reference [35].

detector Borexino [44–46]. Most of which were mentioned previously in Section 2.1.2, originally involved in studying the solar neutrino problem.

Additionally, by locating a 1 kt liquid scintillator detector between several nuclear reactors, the KamLAND experiment has probed the solar sector in a terrestrial setting using reactor antineutrinos [47]. Unlike solar neutrinos, which are heavily influenced by the high electron density of the Sun and the subsequent MSW effect, the antineutrinos detected by KamLAND were not influenced, removing any measurement ambiguity.

### Atmospheric parameters: $\theta_{23}$ and $\Delta m_{32}^2$

Current best fit results for the atmospheric sector parameters yield  $\theta_{23} \sim 48^\circ$  with  $\sim 2^\circ$  of uncertainty, and  $\Delta m_{32}^2 \sim 2.45 \times 10^{-3}\text{eV}^2$  (assuming normal hierarchy as discussed in Section 2.5.2) with  $\sim 0.03 \times 10^{-3}\text{eV}^2$  of uncertainty. These results come from one of two primary sources.

Firstly, experiments studying atmospheric neutrinos generated in the upper atmosphere by cosmic rays, such as IceCube [48, 49] and the previously mentioned Super-Kamiokande [50]. IceCube is a neutrino observatory based at the Amundsen-Scott South Pole Station in Antarctica, consisting of strings of PMTs embedded deep within the ice. Whilst, Super-Kamiokande is a large 50 kt water Cherenkov detector, equipped with 11000 PMTs, and located 1 km underground in Gifu Prefecture, Japan.

Furthermore, experiments measuring  $P(\nu_\mu \rightarrow \nu_\mu)$  using accelerator beam generated muon neutrinos over a long-baseline of many hundreds of kilometres are sensitive to the atmospheric parameters. Such experiments include: MINOS [51, 52] (now complete) and NOvA [53, 54] using a beam generated at Fermilab with detectors in northern Minnesota, and T2k [55] using a beam generated at J-PARC (on the east coast of Japan) and using the Super-Kamiokande detector described above.

### Reactor parameter: $\theta_{13}$

The most recent parameter to be measured and found to be non-zero is  $\theta_{13}$ , with current best fit results yielding a value of  $\theta_{13} \sim 8.5^\circ$  with  $\sim 0.25^\circ$  of uncertainty (note that this is now the most tightly constrained of all the PMNS mixing angles).

Primarily,  $\theta_{13}$  measurements come from reactor experiments measuring electron antineutrino disappearance,  $P(\bar{\nu}_e \rightarrow \bar{\nu}_e)$ . The Daya Bay [56, 57], RENO [58, 59], and

Double Chooz [60] experiments located in China, South Korea, and France respectively all published the strongest results for this measurement at a similar time.

Long-baseline accelerator experiments are also sensitive to  $\theta_{13}$  through the electron neutrino appearance channel  $P(\nu_\mu \rightarrow \nu_e)$ . Measurements have been made by MINOS [52], T2k [61], and NOvA [62] but with much greater uncertainties than reactor experiments.

### 2.5.2 Open questions

There are still many open questions (mainly ambiguities) regarding the parameters of the PMNS matrix. CHIPS and other long-baseline accelerator experiments can help resolve those discussed below by studying the appearance of electron neutrinos in a muon neutrino beam. The approximate oscillation probability for this transition, including the MSW effect, takes the form [12]:

$$\begin{aligned} P(\nu_\mu \rightarrow \nu_e, \bar{\nu}_\mu \rightarrow \bar{\nu}_e) \sim & 4 \sin^2 \theta_{13} \sin^2 \theta_{23} \frac{\sin^2 \Delta}{(1 - A)^2} \\ & + \alpha^2 \sin^2 2\theta_{12} \cos^2 \theta_{23} \frac{\sin^2 A \Delta}{A^2} \\ & + 8\alpha J \cos(\Delta \pm \delta_{CP}) \frac{\sin \Delta A}{A} \frac{\sin \Delta(1 - A)}{(1 - A)}, \end{aligned} \quad (2.23)$$

with

$$J = \cos \theta_{12} \sin \theta_{12} \cos \theta_{23} \sin \theta_{23} \cos^2 \theta_{13} \sin \theta_{13}, \quad (2.24)$$

$$\Delta = \frac{\Delta m_{31}^2 L}{4E_\nu}, \quad (2.25)$$

$$A = \pm \frac{2E_\nu V}{\Delta m_{31}^2}, \quad (2.26)$$

$$\alpha = \frac{\Delta m_{21}^2}{\Delta m_{31}^2}, \quad (2.27)$$

where  $V$  is the effective matter potential of the Earth's crust, and  $\pm$  is positive for neutrinos and negative for antineutrinos.

### Octant of $\theta_{23}$

The mixing angle  $\theta_{23}$  is known to be non-zero and large. Initially thought to be maximal such that  $\theta_{23} = \pi/4 = 45^\circ$ , it is now known that this is not the case. What is still unclear is if  $\theta_{23} < 45^\circ$  or  $\theta_{23} > 45^\circ$ , commonly referred to as the octant. Although  $\theta_{23}$  is easily measured by studying  $\nu_\mu$  disappearance, a degeneracy in the oscillation probability removes the ability to determine the octant. However,  $\nu_e$  appearance via the first term in equation (2.23) allows for the octant to be resolved. Current results suggest the  $\theta_{23} > 45^\circ$  octant is preferred; however, a significant measurement is yet to be made.

### Mass hierarchy

The value of  $\Delta m_{21}^2$  is known to be small and positive, meaning that  $m_2 > m_1$  where  $m_1$  is defined to be the dominant mass state of the electron neutrino. However, the sign of  $\Delta m_{32}^2$  is still currently unknown. This allows for two possible scenarios, either  $m_1 < m_2 < m_3$ , known as the *normal hierarchy*, or  $m_3 < m_1 < m_2$ , known as the *inverted hierarchy*, as illustrated in Figure 2.9. Resolving this ambiguity will significantly improve the ability of experiments to both determine the value of  $\delta_{CP}$  (discussed next) and discover if neutrinos are Dirac or Majorana in nature.

Oscillations in vacuum are not sensitive to the sign of the  $\Delta m_{kj}^2$  parameters. However, matter effects allow for the sign to be determined. Long-baseline  $\nu_e$  appearance is sensitive to the sign of  $\Delta m_{32}^2$  via the  $\Delta$ ,  $A$ , and  $\alpha$  parameters in equation (2.23). Alternatively, determining the hierarchy is also possible using future reactor experiments such as JUNO [63].

### CP violation

The current level of CP violation observed in the quark sector does not fully explain the matter-antimatter asymmetry of the universe. However, if CP violation is shown to exist in the leptonic sector, leptogenesis models of the early universe allow this to go some way to resolving the issue. Neutrino CP violation, when  $P(\nu_\alpha \rightarrow \nu_\beta) \neq P(\bar{\nu}_\alpha \rightarrow \bar{\nu}_\beta)$ , is possible in the PMNS matrix when  $\delta_{CP}$  is not 0 or  $\pi$ .  $\nu_e$  appearance, sensitive to  $\delta_{CP}$  via the third term in equation (2.23) is the most promising channel for measurement. The oscillation probabilities are seen to change significantly with  $\delta_{CP}$ , as shown in Figure 2.10.

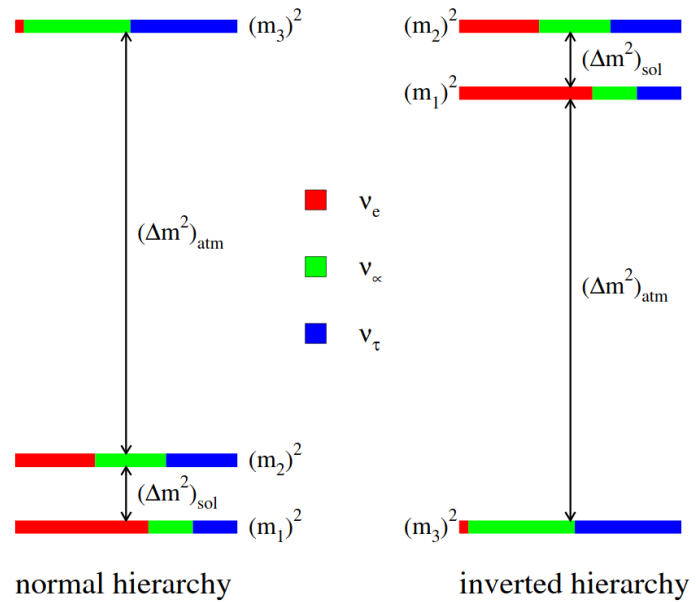


**Figure 2.9:** Diagram of the two possible neutrino mass hierarchies. The atmospheric (atm) and solar (sol) naming convention is used for the mass differences.  $\Delta m_{21}^2$  (sol) is small and positive, while  $\Delta m_{32}^2$  (atm) is large and its sign is unknown. Figure taken from reference [64].

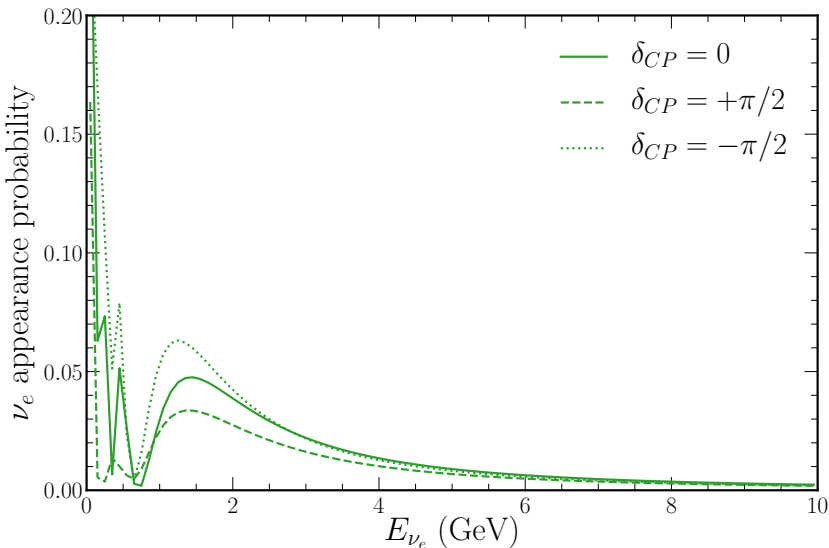


**Figure 2.10:** Appearance probability for  $\nu_e$  oscillating from  $\nu_\mu$  at a baseline of 712 km. The oscillations are shown for three different values of  $\delta_{CP}$ .

Current results from both NOvA [53] and T2k [65] hint at a possible non-zero value; however, a significant measurement is yet to be made.

### 2.5.3 The future

The current generation of long-baseline accelerator experiments (NO<sub>ν</sub>A and T2K) are not expected to unambiguously determine the octant of  $\theta_{23}$ , the mass hierarchy, or the value of  $\delta_{CP}$ . To finally answer these questions, primarily two next-generation experiments are planned. The USA based Deep Underground Neutrino Experiment (DUNE) and Hyper-Kamiokande in Japan. Both will have rich neutrino physics programs alongside their primary goals, studying atmospheric and supernova neutrinos, as well as nucleon decay.

DUNE [66, 67], will consist of four 10 kt liquid argon time projection chambers (LArTPCs) located 1.5 km underground at the Sanford Underground Research Facility, South Dakota. This location is the same as the Homestake mine chlorine experiment previously mentioned in Section 2.1.2. LArTPCs have been chosen as they provide excellent track reconstruction and particle identification performance.

The DUNE experiment will also use a new high intensity beam constructed at Fermilab (1285 km away) named the Long-Baseline Neutrino Facility (LBNF). Replacing the current 700 kW NuMI (Neutrinos at the Main Injector) beam, LBNF is initially planned to run at 1.2 MW, but will eventually reach 2.4 MW.

The initial cost estimate for DUNE combined with LBNF was forecast at between \$1.26 billion and \$1.86 billion [68]. However, due to rising underground excavation costs, this has recently risen to approximately \$2.6 billion [69], an extremely high cost for a neutrino experiment.

Hyper-Kamiokande [70, 71], will be the next-generation replacement for the currently running Super-Kamiokande detector. When completed, it will consist of two cylindrical water Cherenkov detectors each 60 m in height and 74 m in diameter. Both will be built under 650 m of rock at the Tochibora mine in Japan, close to the current Super-Kamiokande location. New high-efficiency photomultiplier tubes will be used, covering 40% of the detector walls to record the Cherenkov radiation emitted from neutrino events.

Moreover, there will be upgrades to the existing J-PARC neutrino beam, currently used by T2k. This will increase the beam power from 400 kW to 1.3 MW. In total, the Hyper-Kamiokande project is expected to cost nearly \$700 million [72].

# Chapter 3

## The CHIPS R&D project

In pursuit of answers to the open questions presented in the previous chapter, neutrino experiments are becoming increasingly, and possibly prohibitively, expensive and impractical. This trend is particularly true of the next generation of long-baseline experiments, DUNE and Hyper-Kamiokande, with cost estimates reaching billions of dollars and construction times of greater than half a decade. It is also telling that the vast majority of global research effort goes into just these two future projects, such is their complexity, cost, and lead time.

It is evident that for detectors to remain practical and affordable into the future, a novel design strategy is highly desirable. This approach is especially the case if megaton scale detectors are ever to become a reality. While instrumentation will continue to improve with time steadily, the statistics of low event counts will always limit neutrino experiments until vastly larger detectors can be built. Therefore, R&D efforts must focus on such detectors now, whilst also attempting to complement the current and upcoming generation of experiments.

The CHIPS R&D project aims to develop novel strategies and technologies for very large yet practical ‘cheap as chips’ water Cherenkov detectors [73]. Primarily aimed for deployment in long-baseline accelerator beam scenarios, CHIPS aims to lower the cost per kt of sensitive mass to between \$200k-\$300k. For comparison, the Super-Kamiokande detector cost approximately \$4 million per kt to build. As physics sensitivity depends on more than just sensitive mass, this comparison is not entirely rigorous; however, it highlights the scale of possible cost savings.

This chapter aims to describe the fundamental aspects of the CHIPS R&D project in detail and explain how it achieves its goals. Firstly, the CHIPS concept will be outlined

along with both neutrino beam and Cherenkov detector physics for context. The design, construction, deployment, and status of the CHIPS-5 prototype detector will then follow. Finally, a description of the Monte Carlo methods used to simulate CHIPS detectors is given, alongside how the input neutrino events are generated.

### 3.1 The CHIPS concept

The CHIPS concept is to deploy cylindrical water Cherenkov detector modules into deep bodies of water on the Earth’s surface such as lakes, reservoirs, and flooded mine pits. Initially constructed on land, CHIPS detectors can be floated into position before being sunk. The water above the sunken detector provides a modest overburden from cosmic rays, whilst the surrounding water provides support for a lightweight structure. By removing the need for underground excavation and expensive structural support, the cost of construction can be dramatically reduced.

Additionally, the common practice of building majority bespoke components is replaced by using modern commercially available components wherever possible. The number of expensive elements, such as photomultiplier tubes are also reduced by only considering multi-GeV accelerator beam neutrino events, such that full high-density detector instrumentation is not required.

Furthermore, CHIPS detectors are not only designed to be cheap, but practical. Easy to build, quick to deploy, and upgradable once operational, multiple detector modules can be flexibly combined depending on available resources and funding. When compared to DUNE and Hyper-Kamiokande both which require a large upfront budget and many years to construct, cheap CHIPS detector modules can be deployed as needed in under a year by a relatively small team.

To date, CHIPS R&D efforts have been based in the USA to exploit the NuMI beam before the end of its lifetime. Plans are focused on the scaling of CHIPS detectors for the deployment of multiple modules within the LBNF beam once operational. Collaborators from primarily University College London, The University of Wisconsin Madison, and Nikhef are focused on multiple R&D efforts, each aiming to prove the viability of a crucial component of the CHIPS concept:

- **Detector construction:** Aiming to prove that the construction and deployment of CHIPS concept detector modules are possible. Two prototype detectors have so far

been deployed. Firstly, the small CHIPS-M module shown in Figure 3.1, deployed into a flooded mine pit in northern Minnesota during the summer of 2014 [74–76]. Secondly, the much larger 5 kt CHIPS-5 module, deployed into the same pit during the summer of 2019 and detailed in Section 3.2.

- **Water filtration:** Aiming to prove that adequate water purity can be achieved using cheap, commercially available filtration. Extensive studies have proven that by filtering water directly from bodies of water on the Earth’s surface (including flooded mine pits), adequate photon attenuation lengths of greater than 100 m are achievable [77, 78].
- **Physics sensitivity:** Aiming to prove that CHIPS concept detector modules (even the prototypes) can provide significant physics contributions alone or alongside the current and next generation of experiments. Single modules in the current NuMI beam (discussed in Section 3.1.1) and multiple modules in the future LBNF beam have been studied [76, 79, 80].
- **Data acquisition:** Aiming to prove that a cheap data acquisition (DAQ) system using commercially available components and software is viable [81]. Outlined in Chapter 4, CHIPS implements a novel use of cheap single-board computers to collect photomultiplier tube data.
- **Event reconstruction and classification:** Aiming to prove that deep learning techniques can be successfully applied to the reconstruction and classification of neutrino events from large water Cherenkov concepts such as CHIPS. The primary contribution of this thesis (detailed in Chapter 5 and Chapter 6), this work feeds directly into both the physics sensitivity studies mentioned above and detector design optimisation.

Although the author’s primary focus was on work for the final two efforts above, a contribution to non DAQ related CHIPS-5 construction efforts were also made. This work included helping with both the instrumentation testing and calibration as well as installation within CHIPS-5. Furthermore, the author played a significant role in the development of the event generation and detector simulation framework presented in Section 3.3.



**Figure 3.1:** Picture of the 3.3 m high CHIPS-M detector just before deployment. Temporary floatation bags are attached to the top rim of the detector, while the umbilical cord carrying data, power, and filtered water is attached to the base.

### 3.1.1 The neutrino beam

CHIPS detectors will primarily study the appearance of  $\nu_e$  oscillating from  $\nu_\mu$  over a long-baseline. To generate a sufficient number of GeV scale  $\nu_\mu$ , a high-intensity accelerator beam is required. Currently, only two such beams exist, the J-PARC based beam in Japan used by the T2K experiment and the NuMI beam in the USA used by NOvA. Here we describe the NuMI beam [82] as it is directly relevant to current CHIPS efforts. However, it is essential to note that CHIPS detectors are designed to be deployed into any high-intensity neutrino beam, including the future NuMI replacement, LBNF.

The NuMI beam is an accelerator muon neutrino beam produced at Fermilab near Chicago in the USA. Beginning operation in 2005 for the MINOS experiment, NuMI was upgraded in 2013 to provide a higher intensity and energy, principally to achieve a peak in neutrino energy near the  $\sim 1.5$  GeV  $\nu_\mu \rightarrow \nu_e$  oscillation maximum for NOvA. Currently, the NuMI beam achieves an intensity of 700 kW (740 kW at peak) making it the most powerful such beam in the world. A schematic of the NuMI beamline configuration is shown in Figure 3.2.

Every 1.33 seconds a 10  $\mu$ s long spill of protons accelerated to 120 GeV by the Main Injector ring are directed towards a stationary graphite target. The resulting interactions create a shower of hadrons containing predominantly pions and kaons. The hadrons are passed through a focusing system of two magnetic horns tuned principally to focus positively charged pions along the beamline while rejecting other particles. After focusing,

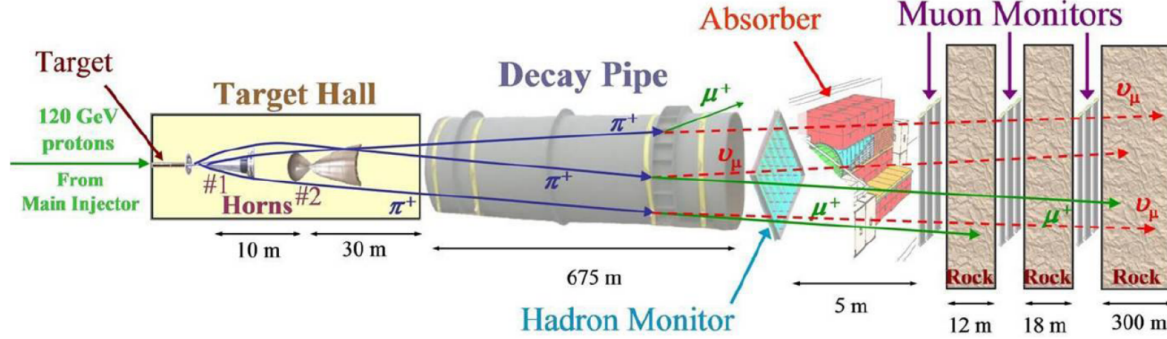


**Figure 3.2:** Schematic of the main components of the NuMI beamline. The MINOS and NOvA near detectors and the MINERvA experiment are located just to the right of what is shown. Figure taken from reference [82].

any surviving hadrons are allowed to decay in flight to a beam of muon neutrinos in a 675 m long decay pipe via the processes:

$$\pi^+ \rightarrow \mu^+ + \nu_\mu, \quad (3.1)$$

$$K^+ \rightarrow \mu^+ + \nu_\mu. \quad (3.2)$$

The resulting muons also decay such that  $\mu^+ \rightarrow e^+ + \nu_e + \bar{\nu}_\mu$ , producing an intrinsic  $\nu_e$  component as well as wrong sign  $\nu_\mu$  contamination.

Alternatively, the polarity of the horns can be used to switch the dominant sign of the hadrons focused, allowing NuMI to operate as either a neutrino or antineutrino beam. These two modes of operation are called *forward horn current* and *reverse horn current*, for primarily a neutrino or antineutrino beam composition respectively. Any remaining hadrons, alongside electrons, muons, and surviving primary protons are absorbed by rock downstream of the decay pipe, leaving just the neutrino components of the beam.

Long-baseline neutrino experiments typically consist of a *near* detector to measure the neutrino composition at source and a much larger *far* detector to measure the oscillated composition after many hundreds of kilometres. The NuMI beamline contains three detectors after 300 m of rock: The MINERvA spectrometer [83], the near detector for MINOS (now used by MINERvA), and the near detector for NOvA. CHIPS prototypes within the NuMI beam (such as CHIPS-5) will not have a dedicated near detector; therefore, data from the above detectors will be crucial for physics analysis in order to constrain the beam composition and flux.

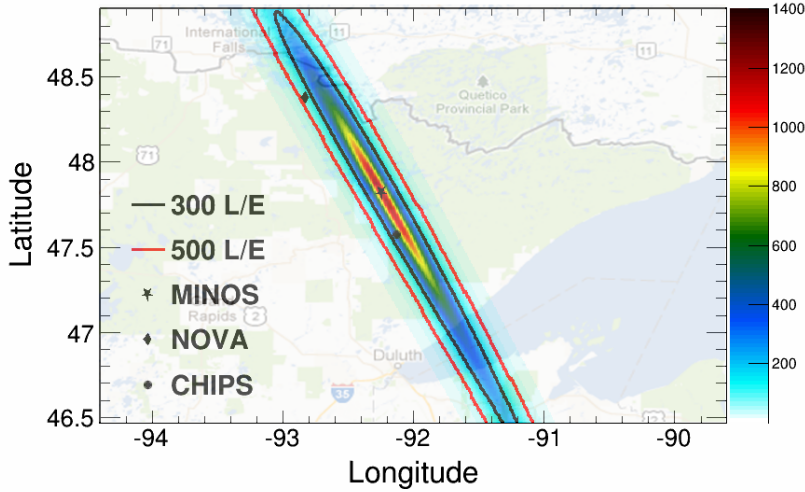


**Figure 3.3:** Map of the MINOS, NOvA and CHIPS locations in the NuMI beam as it surfaces in northern Minnesota. Shown is the expected neutrino event rate assuming no oscillations, with lines of constant L/E indicated with contours. The western extent of Lake Superior can be seen in the lower right of the map for reference. Image taken from reference [73].

The NuMI neutrino beam passes through the Earth’s crust until it finally emerges in northern Minnesota. This is where the MINOS, NOvA, and prototype CHIPS far detectors are located (used to be located in the MINOS case), as shown in Figure 3.3. The Minnesota state nickname ‘land of 10,000 lakes’ is not an overstatement, with a vast number of potential lakes for CHIPS detector deployment. Additionally, intense iron ore mining on the ‘Iron Range’ provides many suitable, disused (and now flooded) mine pits. The exact CHIPS-5 prototype detector location is discussed in greater detail within Section 3.2.1.

Due to the kinematics of pion decay, whether the far detector is placed directly on the beam axis or not can have a significant impact on the observed energy spectrum of beam neutrinos, as shown in Figure 3.4. For neutrinos directly on the beam axis, there is a strong dependence on the energy of the parent pion within equation (3.1). However, as the off-axis angle increases, the neutrino energy becomes less and less dependent on the parent pion energy and is restricted to a narrowing range of decreasing energies.

Known as the *off-axis effect* this phenomenon is used by both NOvA and T2K to create a narrow energy peak focused on the important  $\nu_\mu \rightarrow \nu_e$  oscillation maximum. By reducing the tail of high energy neutrinos, the number of background NC events can also be greatly reduced, as is the case for the 7 mrad off-axis CHIPS-5 detector module.

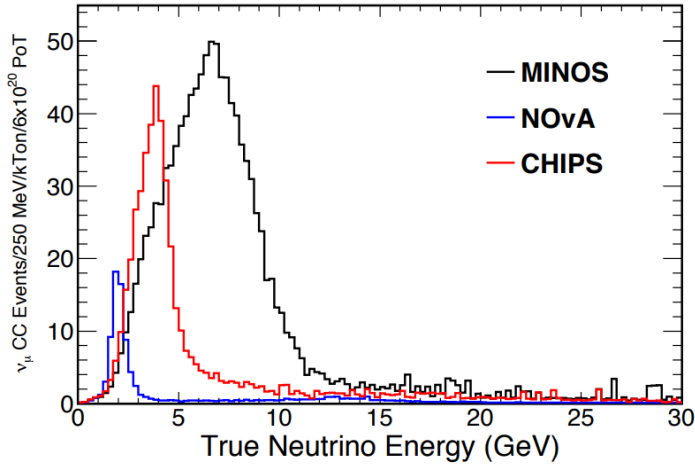


**Figure 3.4:** Muon neutrino flux for different NuMI detectors at different off-axis angles. Shown are the neutrino energy spectra for MINOS (on-axis), CHIPS-5 (7 mrad off-axis), and NOvA (14 mrad off-axis). Figure taken from reference [73].

### 3.1.2 Water Cherenkov detectors

The CHIPS detector concept is based upon the water Cherenkov technique for neutrino detection. A large body of target water is instrumented with photomultiplier tubes (PMTs) to record the Cherenkov radiation produced by sufficiently relativistic charged particles produced in neutrino interactions. By using readily available water as the target material and only instrumenting the surface of the volume, water Cherenkov detectors provide the best detection methodology for maximising volume and reducing cost.

Cherenkov radiation is emitted by all electrically charged particles travelling faster than the local phase velocity of light in a dielectric medium. Similar to the sonic boom created by a supersonic aircraft, Cherenkov radiation forms a shock wave of coherent light, as shown in Figure 3.5. Typically, the emitted light has wavelengths in the optical to ultraviolet range ( $\sim 400$  nm). When projected onto the detector wall, the resulting cone of radiation generates a distinctive ring shape. The cone opening angle (the angle at which light is emitted)  $\theta_c$ , is given by

$$\cos \theta_c = \frac{1}{\beta n(\lambda)}, \quad (3.3)$$

where  $\beta = v/c$  and  $n$  is the refractive index of the medium [12]. Note that  $n$  is a function of the wavelength of emission  $\lambda$ , and so is the opening angle. As the refractive index of water is  $\sim 1.33$  for typical wavelengths of emission, and using the ultrarelativistic limit  $\beta \sim 1$ , the opening angle is found to be  $\sim 41^\circ$ .

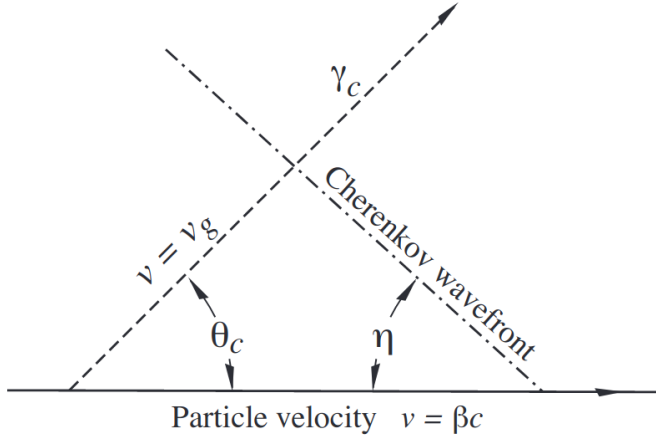


**Figure 3.5:** Diagram of Cherenkov radiation emission and wavefront angles. The angles  $\theta_c$  and  $\eta$  are not equal in a dispersive medium. Figure taken from reference [12]

In equation (3.3) there is no Cherenkov emission when  $\cos \theta_c > 1$ , which is the case when  $\beta n(\lambda) < 1$ . Therefore, a Cherenkov energy threshold  $E_t$ , exists for charged particles. When expressed in terms of the particle mass  $m$ , the threshold is given by

$$E_t = \gamma m = \frac{m}{\sqrt{1 - (1/n)^2}}. \quad (3.4)$$

Again using  $n \sim 1.33$ , a Cherenkov emission threshold energy of  $\sim 1.5 m$  is typical.

The number of Cherenkov photons emitted by a particle of charge  $ze$ , per unit wavelength per unit path length is given by

$$\frac{d^2N}{d\lambda dx} = \frac{2\pi\alpha z^2}{\lambda^2} \left( 1 - \frac{1}{1 - \beta^2 n^2(\lambda)} \right), \quad (3.5)$$

where  $\alpha$  is the fine structure constant ( $\sim 1/137$ ) [12]. Integrating over the range of wavelengths for which PMTs are typically sensitive, 350 nm to 650 nm, and using  $\beta \sim 1$  and  $n \sim 1.33$  gives approximately 240 photons emitted per cm travelled by the charged particle [84].

By analysing the Cherenkov rings of light recorded by the PMTs on the walls of the detector, information about the charged particles within an event can be determined. The underlying neutrino interaction can then be understood indirectly. Primarily, the challenge for accelerator beam water Cherenkov detectors is the identification and reconstruction of an electron or muon ring likely to have been produced from a beam

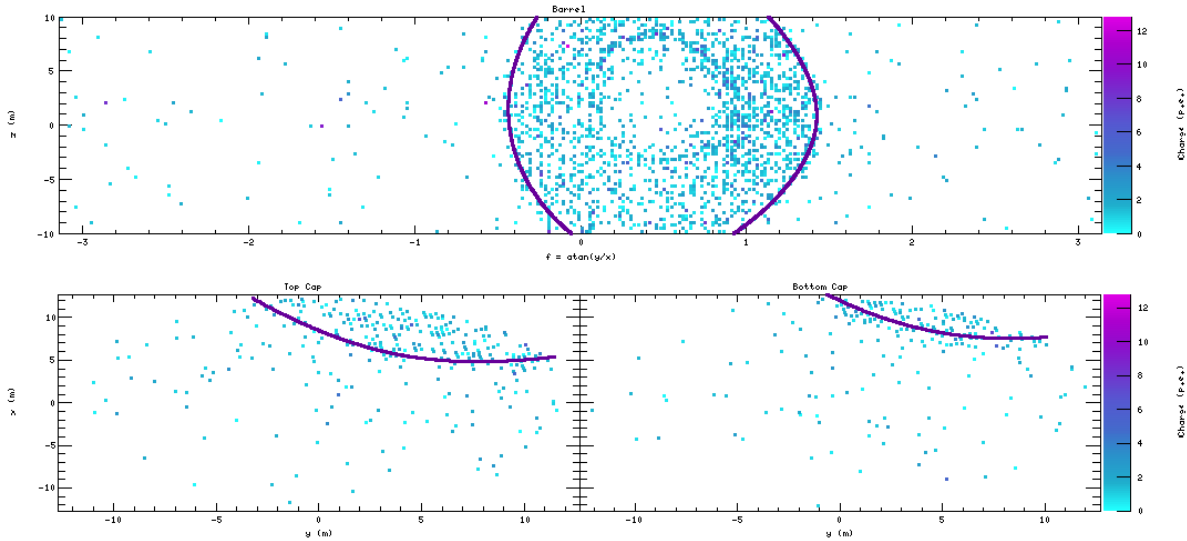


**Figure 3.6:** Event display of a simulated beam CC  $\nu_\mu$  quasi-elastic event with a single muon in the final state of energy 2.36 GeV. Both the unrolled barrel and endcaps are shown with every entry representing a hit PMT with the colour indicating the collected charge. The purple ring indicates the true muon Cherenkov cone boundary projected onto the detector walls.

neutrino and not a cosmic ray. This event topology indicates a beam CC  $\nu_e$  or CC  $\nu_\mu$  event respectively, rejecting NC and cosmic events.

The basic shape of a Cherenkov ring can be used to tell which charged particle created it. Muons are long-lived and typically travel many metres within the detector, producing a clean ring with sharp edges as shown in Figure 3.6. Conversely, electrons almost immediately initiate an electromagnetic shower; therefore, the observed ring is the sum of multiple rings produced from the individual electrons and positrons within the shower. As a consequence, when compared to a muon ring, electron rings are characteristically fuzzy, as shown in Figure 3.7. Additionally, a factor of this difference can be seen in Figure 3.8, which shows how the total amount of Cherenkov radiation is emitted for both electrons and muons as a function of distance from the interaction vertex.

The situation quickly becomes complicated when multiple charged particles above the Cherenkov threshold are involved, common at multi-GeV energies. In this case, multiple overlapping rings are observed, making reconstruction difficult. The worst-case scenario is when two rings overlap entirely, removing any ability to tell them apart. This topology is often the case for NC interactions producing a  $\pi^0$  in the final state, forming the primary background for the signal CC  $\nu_e$  appearance channel.

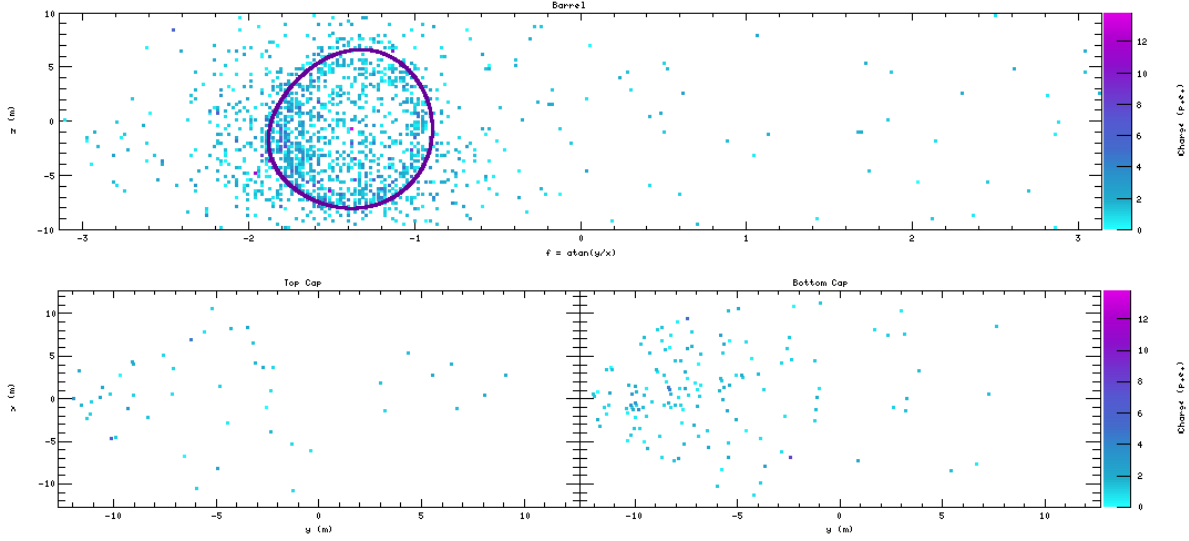


**Figure 3.7:** Event display of a simulated beam CC  $\nu_e$  quasi-elastic event with a single electron in the final state of energy 1.05 GeV. Both the unrolled barrel and endcaps are shown with every entry representing a hit PMT with the colour indicating the collected charge. The purple ring indicates the true electron Cherenkov cone boundary projected onto the detector walls.

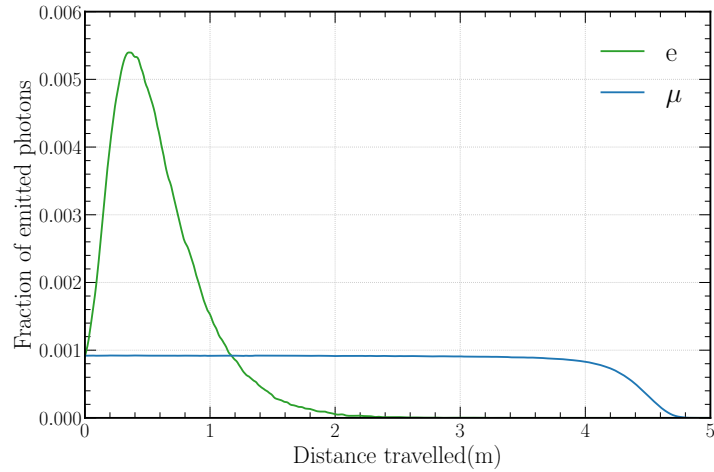


**Figure 3.8:** Fraction of the total number of Cherenkov photons emitted as a function of the distance from the interaction vertex for both electrons and muons with an initial energy of 2.5 GeV. Multiple particles within the electron-induced electromagnetic shower emit their Cherenkov radiation over a short distance and in slightly different directions (fuzzy). Conversely, a muon travels relatively much further emitting an approximately constant level of Cherenkov radiation as it does so (clean).

$\pi^0$  particles decay to a pair of photons with a 98.82% branching ratio, both which almost immediately initiate an electromagnetic shower, just like an electron [12]. This process leads to the formation of two electron like rings separated by an angle  $\theta_{ij}$ , given by

$$(1 - \cos \theta_{ij}) = \frac{m_\pi^2}{2E_i E_k}, \quad (3.6)$$

where  $m_\pi$  is the invariant mass of the  $\pi^0$  and  $E_i$  and  $E_j$  are the energies of the two photons respectively. Therefore, for a  $\pi^0$  decaying to two 1 GeV photons, there is just  $8^\circ$  of separation between the rings, making them difficult to tell apart. This distinction is especially hard when electron like rings are also fuzzy. Alternatively, if the two photons have an unequal energy distribution, such that one is much more energetic than the other, the higher energy photon ring can dominate, and the other can not be identified, leading to what looks like a single electron ring, producing a misidentification.

## 3.2 CHIPS-5

CHIPS-5 is the first large scale prototype detector module for the CHIPS project. At 25 m wide and 12 m high, CHIPS-5 has an inner surface area of  $1924\text{ m}^2$  and a total target mass of 5.9 kt. Via the process of design, construction, deployment, and data taking, CHIPS-5 primarily aims to refine the CHIPS concept for future full-scale ( $\sim 15\text{ kt}$ ) modules. Consequently, CHIPS-5 is designed such that the details outlined in this section are entirely characteristic of what a full-sized CHIPS module is envisioned to be.

First, the location, structure, instrumentation, and water filtration are detailed for the complete detector. A discussion of the construction and deployment procedure follows before the current status is presented. The CHIPS-5 DAQ implementation is detailed separately in Chapter 4.

### 3.2.1 Location

CHIPS-5 is located at the Wentworth 2W pit in northern Minnesota, USA, near the small town of Hoyt Lakes. A disused and flooded surface Taconite ore (a type of iron ore) mine pit, Wentworth 2W is located 7 mrad off the NuMI axis at a distance of 712 km from the beam target. Roughly 0.8 km by 1.2 km in size with a maximum depth of 60 m ( $\pm 3\text{ m}$



**Figure 3.9:** Satellite view of the Wentworth 2W flooded mine pit in northern Minnesota, showing key CHIPS-5 locations. The PolyMet building, shore huts, construction site, and deployment location are shown. For both the construction site and deployment location, the red circle shows the true CHIPS-5 detector size to scale.

throughout the year), the pit allows for a water overburden of approximately 50 m above CHIPS-5 when resting on the bottom. With an average daily low temperate of  $-24^{\circ}\text{C}$  in January, the pit freezes over during winter, therefore, work is only possible during the summer months of May to October.

A sizeable earthen ramp on the south side of Wentworth 2W is used for detector construction. The construction site is easily accessible by road and well connected to power due to the heavy infrastructure in place for mining. Additionally, the nearby PolyMet mining administration building is used as a laboratory environment for the construction and testing of individual components before their installation within the detector. A labelled satellite view of Wentworth 2W is given in Figure 3.9 for context, with an aerial picture of the construction site shown in Figure 3.10.



**Figure 3.10:** Aerial picture of the CHIPS-5 construction site facing south. The Wentworth 2W pit is in the lower half of the image, with the part built CHIPS-5 detector visible at the bottom of the earthen construction ramp. The two white shore huts can be seen halfway up the ramp.



**Figure 3.11:** Picture of the CHIPS-5 structural frame with humans for scale. The endcaps can be seen separated by steel struts. Rows of stainless steel *stringers* are attached to the inside of each endcap for instrumentation mounting.

### 3.2.2 Structure

The structure of CHIPS-5 consists primarily of two 26 m diameter and 1.3 m high lightweight stainless steel circular *endcaps* that form the top and bottom of its cylindrical shape. During construction the conveniently named *top-cap* is held above the *bottom-cap* by 1.5 m long steel struts as shown in Figure 3.11. This configuration allows for the endcap instrumentation, detailed in Section 3.2.3, to be easily installed.



**Figure 3.12:** Graphical rendering of the fully deployed and expanded CHIPS-5 detector module with a section of the liner cutaway. The bottom endcap and wall instrumentation is visible, as well as the top endcap structure and floatation. The green lines indicate the Dyneema cables holding the endcaps together.

The two endcaps are connected by 28 Dyneema cables attached around their perimeter, each 12 m in length. Additionally, a total of 48 air-filled Polyvinyl Chloride (PVC) pipes, each 16 inches in diameter, are attached to the frame of the top-cap to make it buoyant. Once deployed into the pit, the bottom-cap sinks while the top-cap floats, pulling the Dyneema cable taut and forming the final expanded detector shape shown in Figure 3.12.

A lightproof and watertight liner is also installed to surround the fully expanded structure. Designed to isolate the clean internal water from the external pit water and to prevent non-Cherenkov light from reaching the PMTs, the liner is made from *geomembrane*, a flexible reinforced polymer membrane. Commercially available in large rolls, the liner is welded together during construction to form the top, bottom, and sides. Note that when fully deployed, the liner does not take any of the structural strain.

### 3.2.3 Instrumentation

CHIPS-5 is instrumented with PMTs arranged within distinct plane like structures called Planar Optical Modules (POMs), which take inspiration from the Digital Optical Modules

(DOMs) used by IceCube and KM3NeT [85, 86]. Each POM is a roughly 2 m by 3 m array of watertight PVC tubing equipped with between 15 to 30 PMTs, as well as the lowest level of DAQ electronics. Commercially available PVC piping and connectors are used to form the structure of each plane, glued together with standard PVC primer and cement.

There are two types of POM used within CHIPS-5, differentiated by the PMTs and DAQ electronics they use and named after the institution at which they were primarily developed. Firstly, *Nikhef* POMs use 88 mm wide HZC PMTs [87], with electronics developed for the KM3NeT experiment [88, 89]. Secondly, *Madison* POMs use 3 inch wide Hamamatsu PMTs [90], with electronics developed by CHIPS in collaboration with the Wisconsin IceCube Particle Astrophysics Centre (WIPAC) in Madison, Wisconsin.

The HZC PMTs have a high ratio of output electrons to incident photons (quantum efficiency) of 24.4% at a wavelength of 400 nm, compared to the low 12.0% ratio achieved by the Hamamatsu PMTs. Furthermore, the photon hit time resolution is  $\sim$ 2 ns and  $\sim$ 5 ns for the HZC and Hamamatsu PMTs respectively.

In total 6114 HZC, and 450 Hamamatsu PMTs are arranged into 226 Nikhef and 30 Madison POMs. Every PMT is housed within an assembly as shown in Figure 3.13 for the Nikhef case and Figure 3.14 for the Madison case. Importantly, to increase the level of light collection, each Nikhef PMT is equipped with a *light-cone* consisting of a circular reflective surface at  $45^\circ$  to the PMT normal. The Madison PMT assembly is similar but has no light-cone. For POMs attached to either endcap, their PMTs are angled at  $45^\circ$  facing the direction of the beam to optimise light collection.

All PMTs within a POM are connected to the lowest level of DAQ electronics contained within a dedicated onboard electronics box, either made from aluminium or PVC in the Nikhef or Madison case, respectively. A flexible PVC *pigtail* is attached to each POM electronics box containing connections to the higher level DAQ and power supply. A *water-block* within each pigtail ensures that if either the external link or POM becomes flooded, the other is still capable of withstanding the 6 atm of water pressure at the bottom of the pit. A fully assembled and installed Nikhef POM is shown in Figure 3.15 for reference.

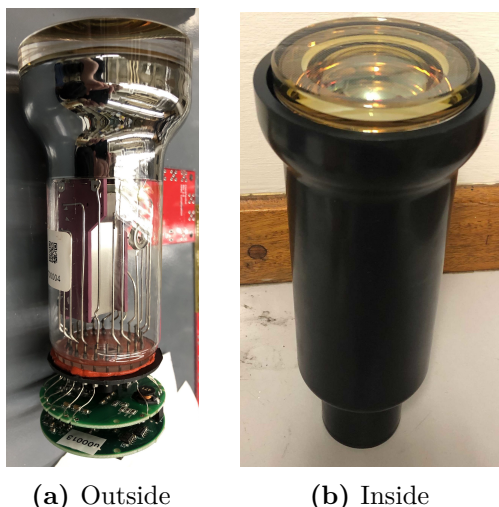
The POMs are tiled next to each other on the detector walls, attached to either the stainless steel stringers on the top-cap and bottom-cap, or clipped to the Dyneema cables on the vertical walls of the *barrel*. As mentioned previously, full high-density detector instrumentation is not required for CHIPS detector modules, for two main reasons.



(a) Disassembled

(b) Assembled

**Figure 3.13:** Disassembled (a) and assembled (b) Nikhef PMT assembly components. The assembly comprises of a black PVC insert, a HZC PMT, a transparent acrylic cover, and a reflective light-cone. The PMT is glued to the inside surface of the cover using a silicone-based optical gel, and a watertight seal is made between the insert and cover using an O-ring. The reflective light-cone is clipped to the front of the cover, and the whole assembly is glued into the POM PVC structure.



(a) Outside

(b) Inside

**Figure 3.14:** A Hamamatsu PMT outside (a) and inside its insert (b). The PMT is potted inside its black PVC insert to create a watertight seal that can withstand the 6 atm of water pressure at the bottom of the pit. A  $\mu$ DAQ detailed in Chapter 4, is seen attached to the base of the PMT in (a).



**Figure 3.15:** Picture of a single Nikhef full-density POM installed on the top-cap of the CHIPS-5 detector. Both the inward-facing and veto PMTs are visible as well as the aluminium electronics container and pigtail, whose end is covered in green tape.

Firstly, only highly directional accelerator beam events are to be studied. Therefore, the vast majority of neutrino interaction Cherenkov radiation is deposited on a relatively small downstream region of the detector walls. Secondly, beam neutrinos predominantly have multi-GeV energies, yielding a relatively large amount of Cherenkov radiation. Therefore, a smaller number of PMTs are required to capture adequate Cherenkov radiation from each interaction.

Consequently, the distribution of the percentage of the detector walls covered by sensitive PMT surface area (*photocathode coverage*) is optimised within CHIPS-5 to reduce the total number of PMTs used. The detector is split into three distinct regions of PMT photocathode coverage, whose boundaries are defined by their azimuth angle  $\phi$  from the centre of the downstream wall (where  $\phi = 0^\circ$ ) using the centre of the detector as the origin. Each boundary is chosen by inspecting the fraction of beam Cherenkov photons that hit the detector walls as a function of  $\phi$ . This distribution, generated by the detector simulation (outlined in Section 3.3.1), is shown in Figure 3.16 alongside the chosen boundaries.

Firstly, there is a *full-density* Nikhef POM region in the most downstream  $\phi = \pm 75^\circ$  region of the detector with a  $\sim 3\%$  photocathode coverage. Secondly, a *half-density* Nikhef POM region covering the  $\phi = \pm 75^\circ$  to  $\phi = \pm 180^\circ$  region of the endcaps and

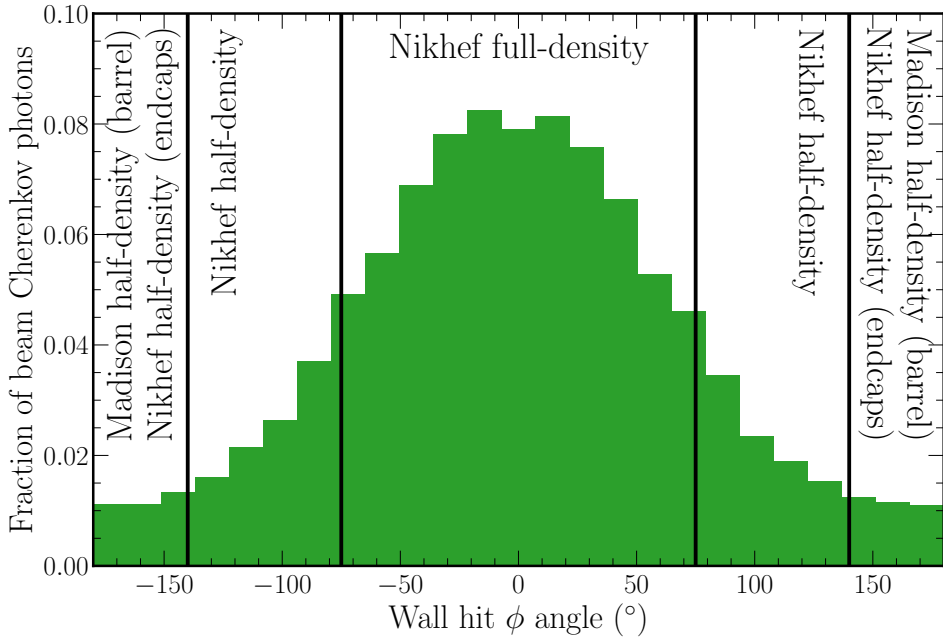


**Figure 3.16:** Fraction of beam event Cherenkov photons that hit the detector walls as a function of the hit angle  $\phi$ . The different photocathode coverage regions are indicated.

the  $\phi = \pm 75^{\circ}$  to  $\phi = \pm 140^{\circ}$  region of the barrel with a  $\sim 1.5\%$  photocathode coverage. Finally, a *half-density* Madison POM region covering the  $\phi = \pm 140^{\circ}$  to  $\phi = \pm 180^{\circ}$  upstream region of the barrel with a  $\sim 0.8\%$  photocathode coverage. Simulation studies have shown that this configuration results in a negligible change in performance, whilst vastly reducing the number of required PMTs [91].

The CHIPS-5 detector module is equipped with a veto region within the top-cap frame structure to aid cosmic muon rejection. Separated from the main detector volume by a geomembrane liner, the 1.3 m high region allows for the rejection of predominantly downward going cosmic muons by detecting the Cherenkov radiation they produce. A total of 324 upward-facing HZC veto PMTs within the top-cap Nikhef POMs give a veto photocathode coverage of  $\sim 0.6\%$ . A graphical rendering of the full top-cap instrumentation, showing the different density regions and veto PMTs, is shown in Figure 3.17.

All CHIPS-5 instrumentation receives power and is connected to the highest level DAQ systems through a 500 m long flexible PVC umbilical resting on the pit floor. The umbilical contains a single optical fibre for data and two shielded gauge 10 cables for power. One end of the umbilical is attached to the bottom-cap of the detector while

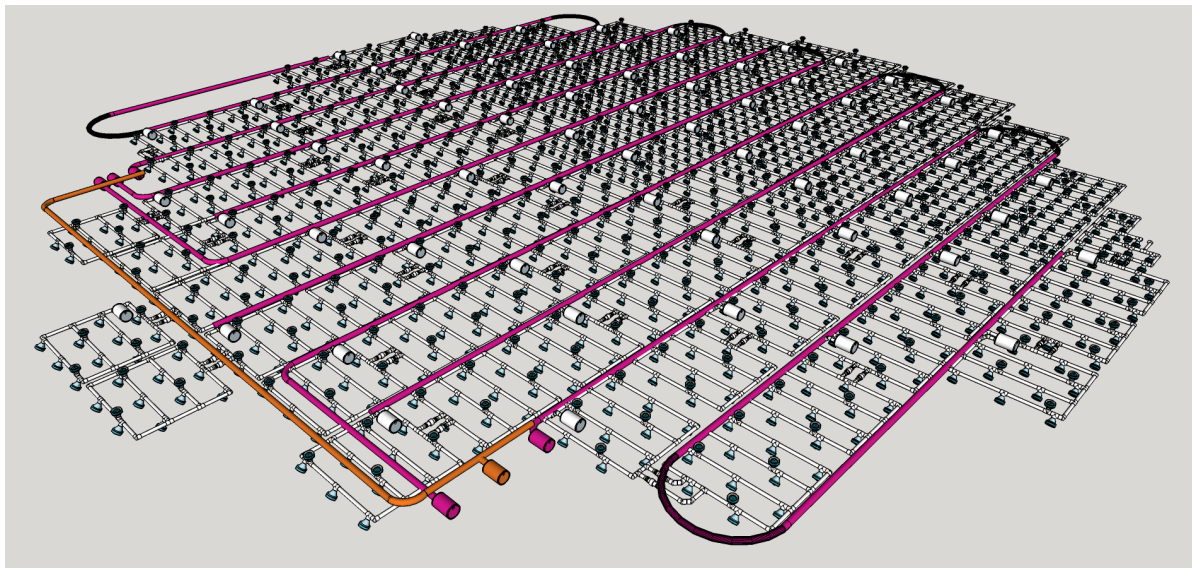


**Figure 3.17:** Graphical rendering of the top-cap POMs. Both the different photocathode coverage regions and the veto PMTs (contained within the top-cap POMs) are visible. The *manifolds* connecting the POMs with the higher level DAQ components are also shown in pink and orange.

the other enters a hut onshore containing the master power supply and onshore DAQ equipment.

### 3.2.4 Filtration

Though surprisingly clear, the Wentworth 2W pit water requires filtration to reach the necessary 30 m photon attenuation length for adequate light collection. Therefore, a high volume pump is used to continually pull the internal detector water through a 500 m long pipe to a filtration hut on the shore. After filtration, the water is returned to the detector through a second such pipe.

Within the hut, ten parallel sets of filters are installed in order to achieve a reasonable flow rate, allowing for the full detector volume to be filtered every ten days. Each filter set consists of a 20 inch 10  $\mu\text{m}$  carbon block filter followed by a 20 inch 0.5  $\mu\text{m}$  polypropylene filter, as shown in Figure 3.18. This configuration is found to achieve a photon attenuation length of 133(2) m after approximately two months of constant filtering [78].



**Figure 3.18:** Picture of the CHIPS-5 filtration system within one of the shore huts. The pipes to and from the detector can be seen entering and exiting the hut respectively via a gap in the back wall.

### 3.2.5 Construction and deployment

The construction and deployment of any CHIPS detector module is a bespoke process that is relatively complex when compared to other experiments. This complexity is primarily due to a body of water being used for activities rather than solid ground. Below a simplified version of the CHIPS-5 construction and deployment procedure is outlined.

1. An earthen barrier is built separating the main body of Wentworth 2W from the construction area. As the pit water level rises during the summer, this acts as a dam preventing the construction area from flooding (at least in theory).
2. The bottom-cap liner is welded together before the endcap structural frames are constructed above, resulting in that shown in Figure 3.11.
3. The barrel liner is partly constructed starting from the detector base. Using a vertical liner roll for each of the 28 sides, the barrel liner is welded up to the height of the top-cap, as is shown in Figure 3.19. The top-cap liner is also installed but not welded to the barrel liner.
4. A strongly buoyant *floating-dock*, made from steel and large plastic floats, is constructed surrounding the detector. The bottom-cap is attached with metal chains to winches on the floating-dock and with the Dyneema cables to winches on the top-cap.



**Figure 3.19:** Picture of the CHIPS-5 detector module with liner welded up to the height of the top-cap. A section of the floating-dock can also be seen in the foreground.

5. The pre-assembled and tested endcap POMs are installed along with their associated power and data connections as well as other high-level DAQ components.
6. The earthen barrier is removed and the construction area flooded, causing the detector and floating-dock structure to float. The detector is towed by a boat to its deployment location.
7. The detector is slowly filled with water at the same time as being lowered using the winches on the floating-dock. This process continues until the top-cap reaches the surface of the water and begins the float. At this point, the steel struts separating the endcaps are removed.
8. The barrel POMs are installed in layers, brought to the detector location by boat. The gap between the barrel and top-cap liner allows this to happen. After a complete layer has been installed the bottom-cap is lowered using the winches on the floating-dock and top-cap and the barrel liner is correspondingly welded to a greater height before the procedure repeats.
9. After all the POMs layers have been installed, the barrel and top-cap liner are welded together, the detector umbilical attached, and the whole detector lowered until it finally rests at the bottom of the pit.



**Figure 3.20:** Some CHIPS-5 construction work.

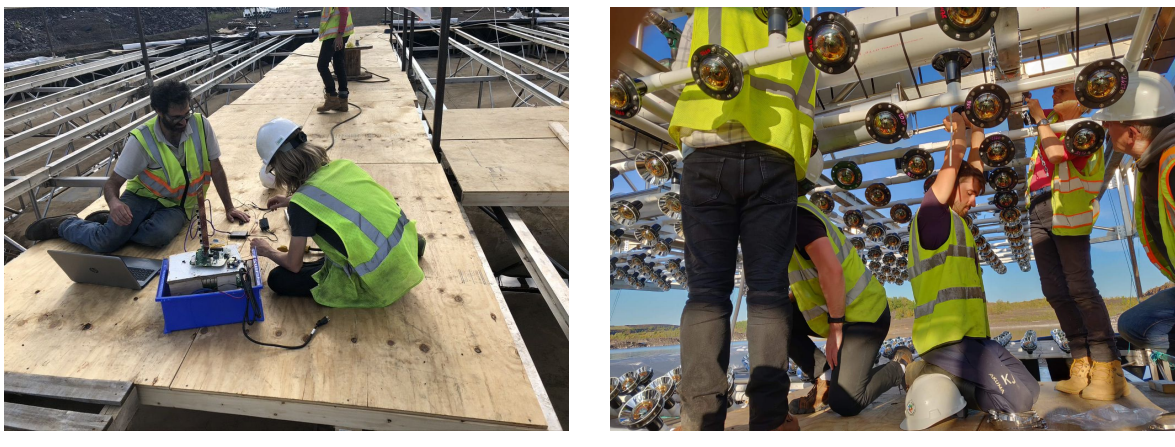


**Figure 3.21:** More CHIPS-5 construction work.

### 3.2.6 Current status

During the summer of 2018 and 2019 extensive CHIPS-5 construction work was carried out by a team of 10 to 15 collaborators at any one time. Given the novel nature of the project, most tasks, some of which are pictured in Figure 3.20 and Figure 3.21, proved both challenging and time consuming.

By late summer 2019, it became apparent that deployment of a fully instrumented CHIPS-5 would be impossible before the pit started to freeze over in October. Therefore, the decision was taken to only partially instrument the endcaps, leave the barrel walls bare, not include the veto separation liner, and reduce the module height to 8 m. In

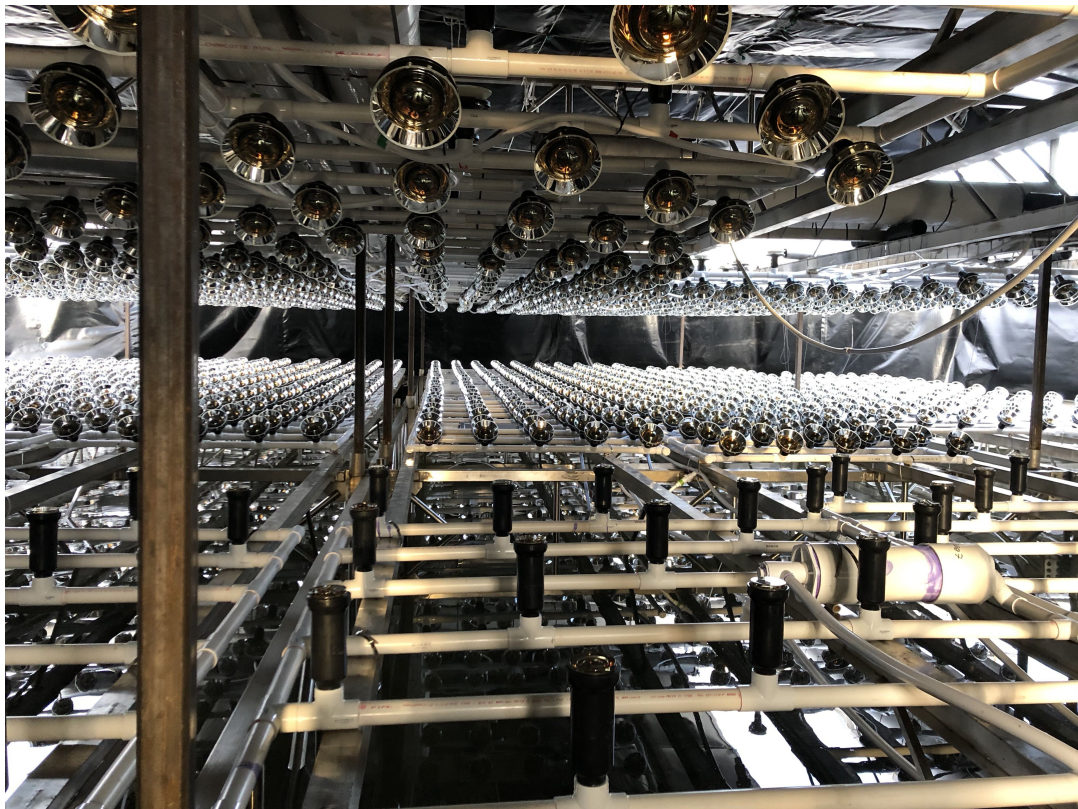


**Figure 3.22:** Inside picture of CHIPS-5 just before deployment, with a section of the total instrumentation shown. In total 56 Nikhef and 6 Madison POMs were installed. Instead of being mounted on the upstream detector walls the Madison POMs were mounted on the bottom-cap and can be seen in the foreground of the image. The flexible PVC tube pigtails and manifolds can also be seen connecting each POM to the higher level DAQ electronics and power supply.

October 2019 this version of CHIPS-5, shown in Figure 3.22, was deployed into the Wentworth 2W pit.

Analysis of preliminary data was successful in isolating individual cosmic muon events, one of which is shown in Figure 3.23. However, extensive data taking was paused due to a deployment induced tear in the liner preventing filtration of the internal water. Given the outbreak of the worldwide SARS-CoV-2 epidemic, all plans for work over the summer of 2020 were suspended, including essential repairs and instrumentation of the barrel walls. Plans for summer 2021 are currently under review.

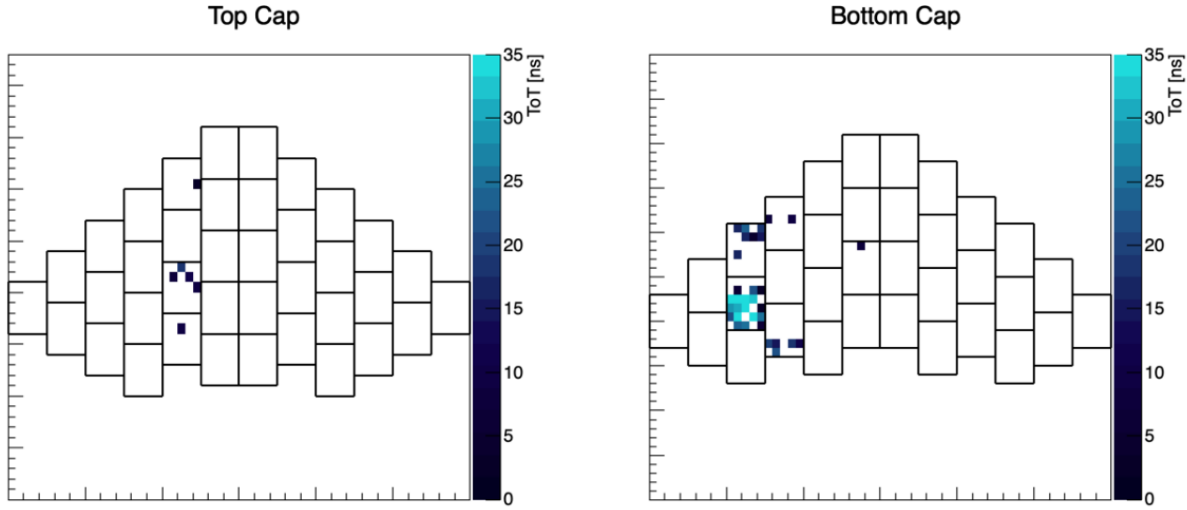


**Figure 3.23:** A cosmic muon event recorded within CHIPS-5, found by clustering hits in time. PMT hits from both the top-cap (left) and bottom-cap (right) are shown with the colour indicating the measured ToT value. Due to the small attenuation length of unfiltered water, only a single bottom-cap POM has significant activity.

### 3.3 Detector simulation and event generation

To describe CHIPS-5 and other CHIPS concept detectors in a simulated environment, a Monte Carlo simulation framework is used. Monte Carlo detector simulation and event generation methods are an indispensable tool within high energy particle physics. This is particularly true during the design and prototyping phase of an experimental project when no real-world data is available, as is predominantly the case with CHIPS. By matching the observables of a real-world detector as close as possible, these methods allow for the optimisation of detector design, the testing of reconstruction techniques, and the study of physics sensitivities.

Here, a description of the detector simulation and the beam and cosmic event generation procedures used by CHIPS are described. All are employed extensively for the principal work of this thesis presented in Chapter 5 and Chapter 6.

#### 3.3.1 Detector simulation

The detector simulation uses the WCSim water Cherenkov simulation package [92] built on top of the Geant4 simulation framework [93–95]. Developed initially to simulate possible water Cherenkov detectors in the LBNF beam, WCSim is now used more widely

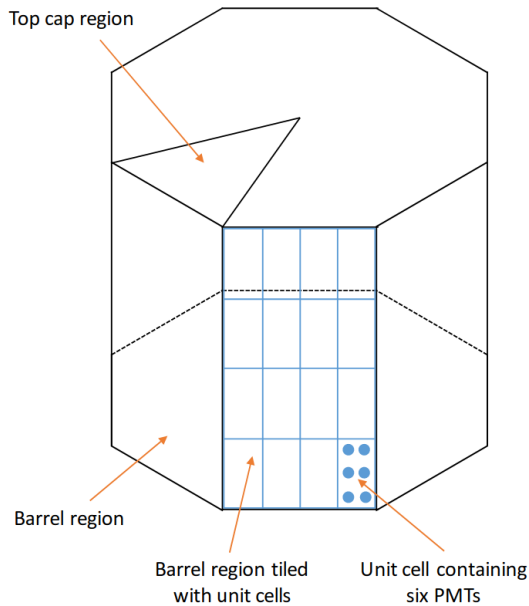


**Figure 3.24:** Illustrative diagram of a WCSim detector geometry. The endcap and barrel regions, tiled unit cells, and PMTs within a unit cell are all shown. Figure taken from reference [91].

in the field. Heavily modified for the CHIPS project, WCSim allows for generic water Cherenkov detector geometries to be easily loaded at runtime via a series of simple XML configuration files. These changes allow for a broad range of detector geometries to be quickly considered without recompilation of the code.

The simulation builds an n-sided, regular polygonal prism consisting of two endcaps and a barrel, filled with water and lined with a low reflectivity *blacksheet*. The geometry is separated into *regions* within both the barrel and endcaps, defined either by a list of barrel sides or an opening angle, respectively. Each region is filled with a unique base unit of geometry known as the *unit cell*, as shown in Figure 3.24.

The unit cell defines a pattern of any number of PMTs, including their relative positions and in which direction they face. The final geometry is built by tiling the defined regions with their respective unit cell scaled to match the required regional photocathode coverage. Note that although exact PMT positions are not used in this procedure, a given configuration will always generate the same geometry (it is deterministic). In this work, the CHIPS-5 geometry is generated with 28 sides and regions matching the boundary angles and photocathode coverage detailed in Section 3.2.3.

The geometry shape, regions, and unit cells are defined in a configuration file. Additionally, a file for PMT definitions containing their shape, time resolution, and quantum efficiency is also used. Light-cones are described by a list of radial profile points in a further file. Although the underlying Geant4 material properties are mostly hardcoded, values within yet another configuration file are used to scale them. This scaling controls the water absorption, scattering (Rayleigh and Mie) lengths, and both the blacksheet and PMT glass reflectivity. In this work a photon attenuation length of 50 m at 405 nm is used with negligible scattering, the blacksheet reflectivity is set to 4% and the PMT glass reflectivity 24%.

A veto volume can also be defined. The veto is built as either a concentric shell around the whole inner volume with a given thickness or solely above the top-cap with a given height. Any PMTs defined as facing outwards within a unit cell look into the veto volume instead of the inner volume. In this work, the CHIPS-5 geometry is given a top-cap veto of height 1.3 m with a photocathode coverage matching that described in Section 3.2.3.

Once the full generation of the Geant4 geometry is complete, the final state tracks for each successive event to be simulated are loaded from either the beam or cosmic event generator files described in Section 3.3.2 and Section 3.3.3. Beam event vertices are randomly placed within the inner detector volume, while cosmic vertices are set at 1 m above the detector volume. WCSim then simulates the passage of all particles through the detector materials, with interactions, decays, and Cherenkov emission all considered.

Whenever a photon is calculated to have hit the photocathode of a PMT, an angular dependent acceptance efficiency is applied to see if it is recorded. If accepted, all hits within 200 ns windows are grouped to form a single recorded hit, with a smeared first hit time used as the recorded time. The standard WCSim methodology is used to determine the total output charge of the hit, given the number of incident photons. This procedure involves a single photoelectron charge distribution being repeatedly probed for each photon, before the combined sum is returned [96].

By sampling this procedure multiple times, the output charge probability distribution given the number of incident photons can be generated, as shown in Figure 3.25. The reverse likelihood function of an actual number of incident photons given a measured digitised charge is also shown (with a lower value being more likely). The reverse likelihood function is used for the standard reconstruction methods outlined in Section 5.2.1.

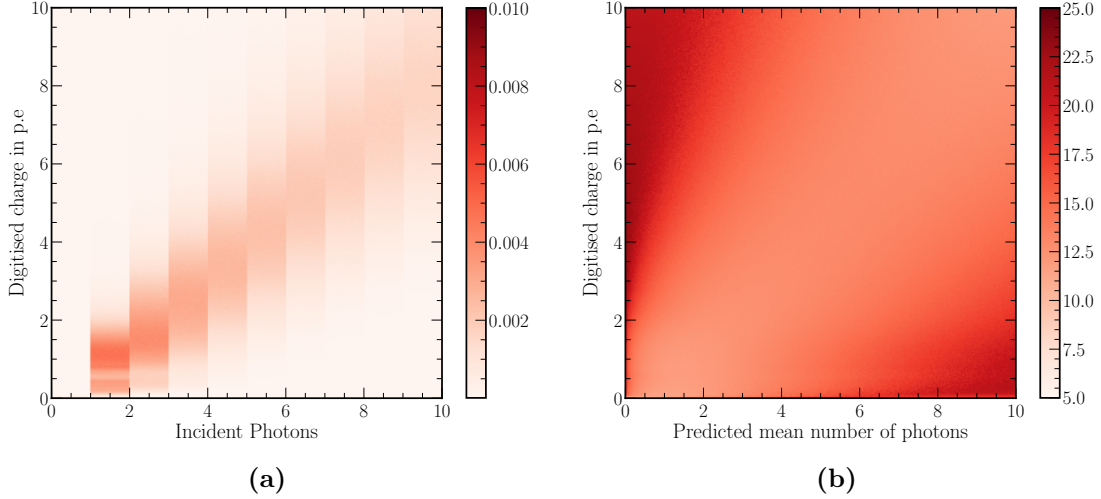


**Figure 3.25:** The probability of a digitised output charge given an incident number of photons used within the detector simulation is shown in (a). The reverse function, showing the likelihood of a measured digitised charge being caused by a number of incident photons is shown in (b).

The simulated PMT hits for each event are stored in an output file along with truth information and track descriptions. A full event takes approximately three seconds to simulate on a standard batch farm computing node.

### 3.3.2 Beam event generation

The expected flux of beam neutrinos at the CHIPS-5 detector location, shown in Figure 3.26, is generated using the existing beam simulation written for the NuMI experiments. Using the generated fluxes as input, the GENIE neutrino event generator (version 3.0.6) [31, 32] is used to generate beam neutrino events. Default neutrino cross-sections on water provided by GENIE are used during generation. All initial, intermediate, and final state particle tracks for each event are stored as output in a NUANCE formatted file for use in the detector simulation. Note that unoscillated input fluxes are used such that analyses samples must be later weighted to match the desired oscillated neutrino composition.

### 3.3.3 Cosmic event generation

The Cosmic-Ray Shower Library (CRY) [97, 98] is used for cosmic ray event generation. Both the solar cycle and Earth's geomagnetic field are taken into account, with the

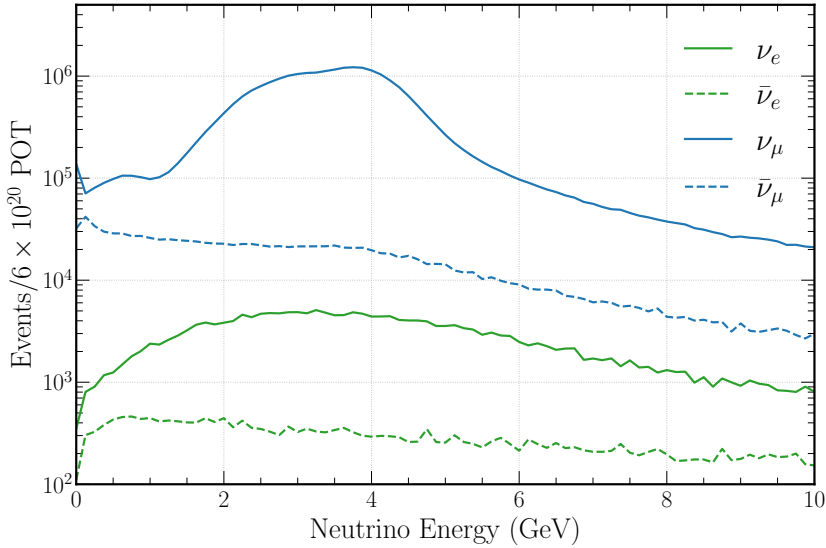


**Figure 3.26:** The neutrino mode (forward horn current) NuMI beam neutrino energy spectrum at the CHIPS-5 detector module location. Shown are the individual contributions from the different neutrino types and signs. No cross-sections or oscillations have been applied.

CHIPS-5 latitude ( $47.56^\circ$  N) and deployment date (30th October 2019) used as input. Single muons are generated at sea level by CRY within a 1 km by 1 km area, with the detector at its centre. Note that only single muon events (the dominant cosmic component) are considered for simplicity.

Assuming a CHIPS-5 overburden of 50 m and a  $2.2 \text{ MeV/cm}^2$  muon energy loss in water as suggested by reference [99], the muon parameters are updated to estimate their values at 1 m above the detector. All muons whose path does not cross the detector volume or do not have sufficient energy to reach the detector are discarded [100]. All accepted muon tracks are stored as output in a NUANCE formatted file for use in the detector simulation.

To use generated cosmic events in analysis, studies have looked at the likely cosmic rate for CHIPS detector modules at different water overburden depths [101]. In this work, the fits shown in Figure 3.27 for a cylindrical detector of both height and diameter equal to 24 m are used to estimate a CHIPS-5 cosmic muon rate of 11.8 KHz at 50 m of overburden.

Given the 10  $\mu\text{s}$  long NuMI beam spill occurring every 1.33 seconds, an in spill cosmic rate of  $\sim 2.1$  million events per year is calculated with an in spill occupancy of 9%. Considering a typical event takes  $\sim 100$  ns to unfold, there is approximately a 0.3% chance

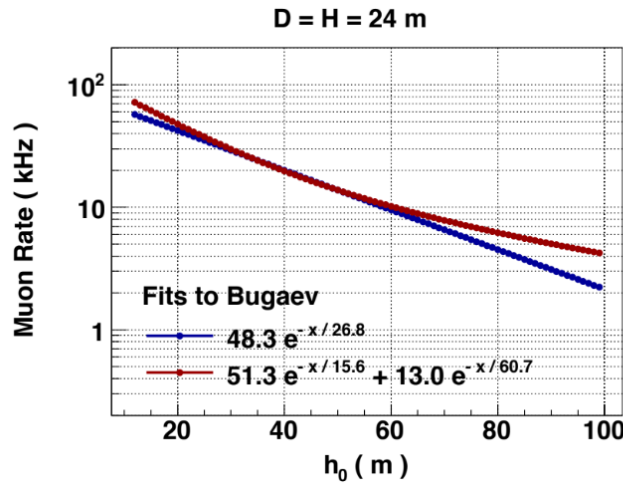


**Figure 3.27:** Expected cosmic muon rate as a function of water overburden depth for a 24 m high and 24 m wide CHIPS detector module. Shown are fits made to the work originally conducted in reference [102]. Figure taken from reference [101].

that any beam event overlaps with a cosmic muon. This low coincidence shows just how powerful a short beam spill can be at reducing the significant cosmic background.



# Chapter 4

## Data acquisition for CHIPS

The primary task of any data acquisition system is the processing of low-level signals measuring real-world physics and their transfer to permanent storage for further analysis. Commonly, this procedure also includes decision making as to whether the signal is deemed interesting enough to record, known as a *trigger*. Both of these tasks can make DAQ systems incredibly complex, especially when they must operate efficiently and resiliently for vast amounts of data in real-time, whilst also providing detector control and monitoring.

In the context of the CHIPS project, the DAQ system records all PMT hits, timestamps them using a common clock, and transfers them out of the detector for processing. A trigger is applied to select those hits that fall within the interesting NuMI beam spill time window before the selected hits are moved to permanent storage for further analysis. Alongside these processes, the DAQ system also configures the detector and provides hardware and data quality monitoring.

Although relatively simple when compared to the incredibly complex and time-pressured DAQ systems of the LHC experiments, the DAQ system developed for the CHIPS project contains some unique approaches to solve the goals of the CHIPS concept. Namely, deployment within a body of water and a limited resource budget. In this chapter, the DAQ system for CHIPS as applied to the CHIPS-5 prototype detector module is described. The description is presented in two broad categories, hardware and software, with a short description of the timing system to begin.

The author played a major role in both the development and construction of the DAQ system for CHIPS-5. Specifically, a significant contribution to the development of the networking solution and high-level hardware implementation was made, alongside

building the control and monitoring software. Furthermore, the author played a role in the development of the novel low-level Madison  $\mu$ DAQ and Beaglebone DAQ system.

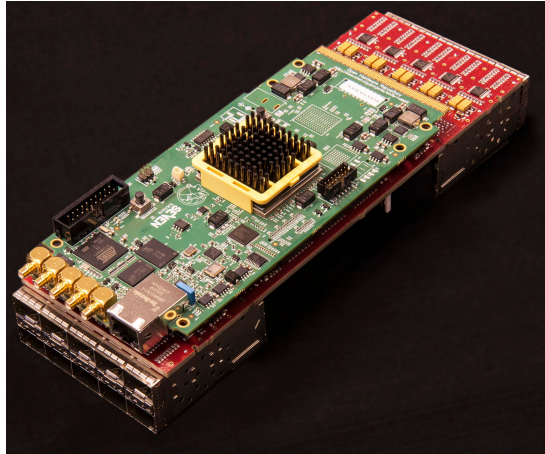
## 4.1 White Rabbit timing

To ensure PMT hit times are synchronised throughout CHIPS detectors, a common clock must be shared across all timestamping electronics. For this purpose, CHIPS uses a *White Rabbit* (WR) network [103]. Initially developed at CERN, the open-source WR project provides an ethernet-based time distribution network with sub-nanosecond synchronisation accuracy between nodes. By using two-way exchanges of WR messages, precise adjustment of individual node clock phases and offsets are possible, across thousands of devices separated by tens of kilometres. All of this is achieved alongside a standard data transfer network capable of 1 Gb speeds.

All nodes are synchronised to the clock of a *GrandMaster* node, typically a WR *switch*, the most common WR hardware component. As input, the GrandMaster switch receives an IRIG-B (Inter-Range Instrumentation Group timecode B) and a 10 MHz signal from a GPS disciplined oscillator. These inputs allow for synchronisation of the GrandMaster clock to International Atomic Time. As CHIPS detector modules require synchronisation to accelerator clocks many hundreds of kilometres away to determine the arrival time of beam spills, this GPS disciplined timing is essential.

WR hardware is commercially available from many vendors. Within CHIPS-5, two WR devices are used for time synchronisation and data transfer, both shown in Figure 4.1. Firstly, a compact version of the standard WR switch [104], specially developed for the CHIPS project at Nikhef [105]. Secondly, a WR-LEN (Lite Embedded Node) from Seven Solutions [106].

All WR components within CHIPS-5 are connected using 1 Gb bi-directional optical fibre connections, using the 1310 nm and 1550 nm wavelengths via Small Form-Factor Pluggable Transceivers (SFPs). Figure 4.2 shows the WR synchronised pulse per second rising edges for two CHIPS-5 WR switches separated by 500 m of optical fibre. With the vertical ticks representing single nanoseconds, sub-nanosecond time synchronisation accuracy between the switches is observed.



(a) White Rabbit Switch



(b) White Rabbit LEN

**Figure 4.1:** Pictures of the White Rabbit timing hardware used within CHIPS-5. The compact WR switch specially designed for CHIPS is shown in (a), while the White Rabbit Lite Embedded Node (WR-LEN) from Seven Solutions is shown in (b).

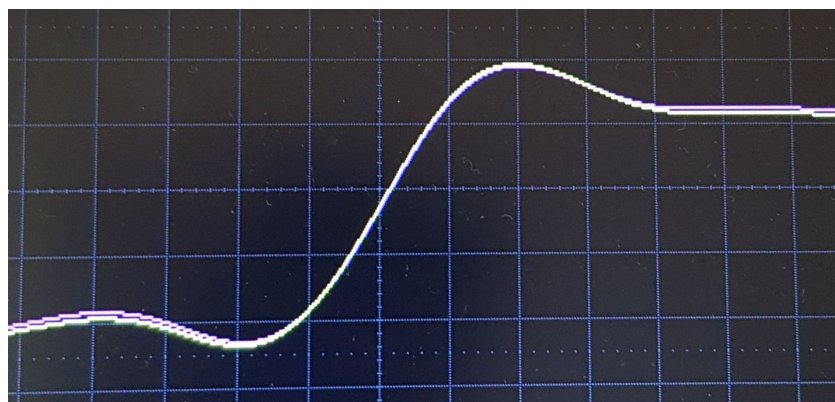


**Figure 4.2:** Oscilloscope display measuring the pulse per second output signal from two WR switches shown in pink and yellow at either end of a 500 m long optical fibre. The vertical ticks are in nanoseconds showing the sub-nanosecond synchronisation possible with the WR timing network.

## 4.2 Hardware

The hardware of the CHIPS-5 DAQ system is split into two distinct implementations at its lower levels (closest to the PMTs), corresponding to the Nikhef and Madison POM types. CHIPS R&D efforts have principally developed the novel Madison implementation with the view of using this hardware exclusively. However, as a safe stepping stone, while development and testing are still ongoing, CHIPS-5 mainly contains proven Nikhef hardware developed for the KM3NeT experiment [89].

The complete DAQ and power distribution system for CHIPS-5 is diagrammatically shown in Figure 4.3. The following subsections describe each component, starting from the lowest level and working upwards. The Nikhef and Madison descriptions are separated for clarity in addition to the high-level combined hardware systems, part of which is not physically located within the detector but in an electronics hut onshore.

As a general overview, the DAQ system within the detector follows a tree-like structure. Starting from the lowest level (the leaves), individual PMTs are arranged into POMs. Groups of POMs, spatial close within the detector, are then connected to a small number of group-specific interface containers (either a *Nikhef-container* or *Madison-container*), holding networking and power supply devices for each group. All interface containers are attached to a central aggregation box (*junction-box*) which feeds connections into a single umbilical (the tree trunk) to shore.

Common to both low-level hardware implementations is the use of the Time over Threshold (ToT) method for PMT signal digitisation. Each analogue PMT pulse is fed to a ToT discriminator coupled with a Time to Digital Converter (TDC) to generate each digitised recorded hit, as shown in Figure 4.4. Compared to the more common Analogue to Digital Converter (ADC) readout, ToT values are less accurate and do not scale linearly with deposited charge. However, as the maximum expected deposited charge within CHIPS detectors is relatively low (only a few p.e), the impact of the non-linearity is small, and the ToT implementation is used. Furthermore, ToT electronics are simpler and notably cheaper.

### 4.2.1 Nikhef hardware

All Nikhef HZC PMTs are attached directly to a simple readout board containing a high-voltage generating Cockcroft-Walton circuit [107]. Up to 30 such PMTs are connected

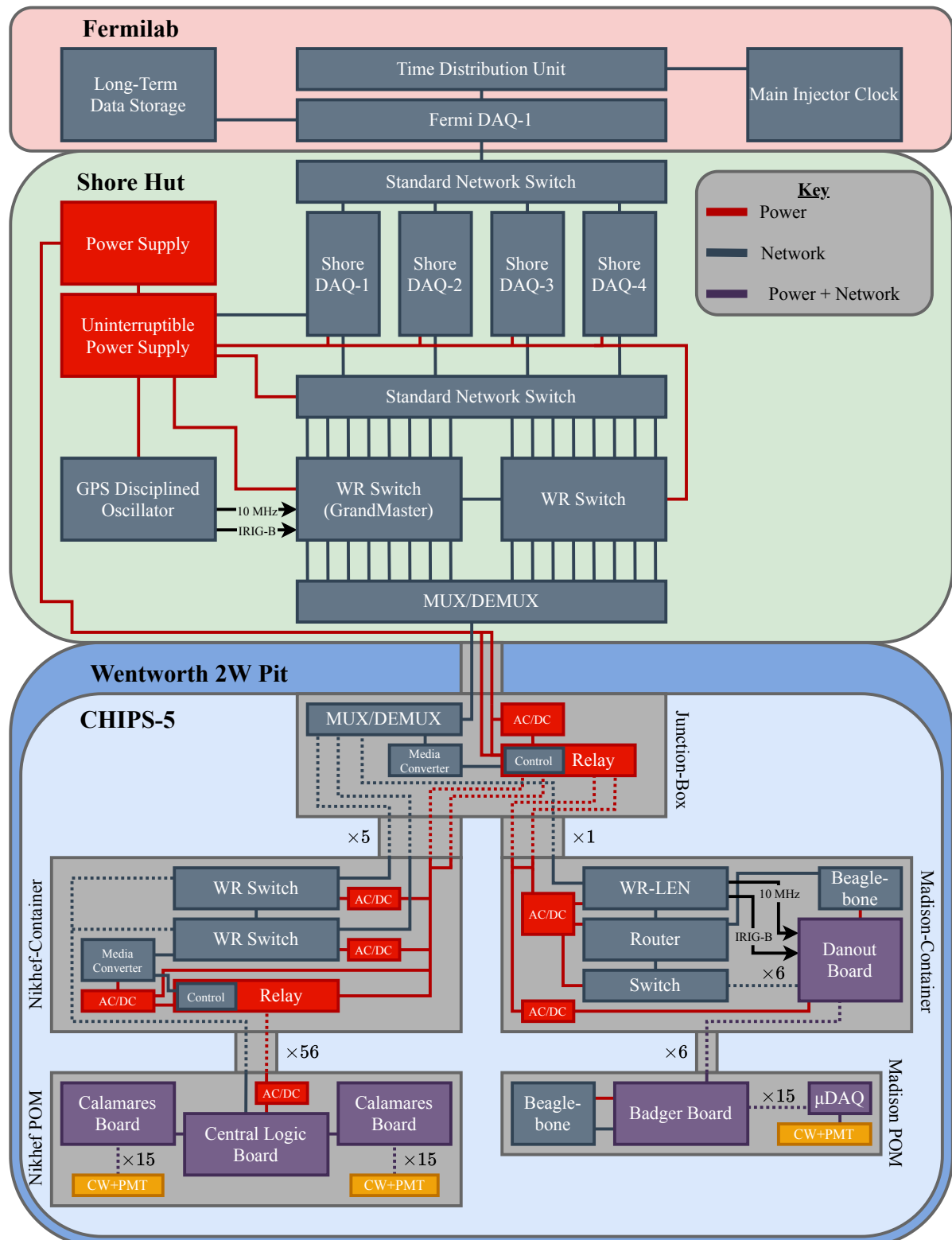
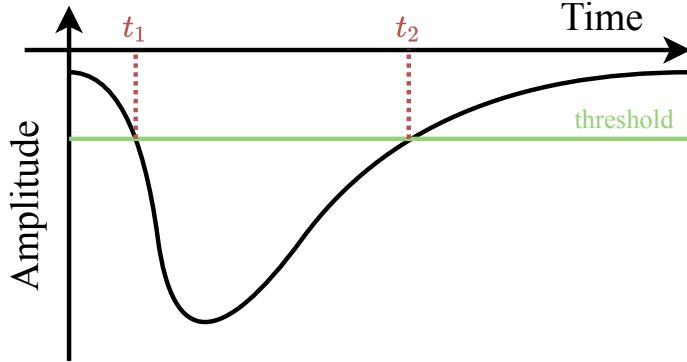


Figure 4.3: Diagram of the complete CHIPS-5 DAQ and power distribution system.



**Figure 4.4:** Illustrative diagram showing how a ToT value is measured. As soon as the rising edge of a PMT charge pulse rises above a given threshold (goes below in the negative charge case) a time is recorded  $t_1$ , when the falling edge later falls below the threshold a second time  $t_2$  is recorded. The difference in time between  $t_1$  and  $t_2$  is output by the electronics as a digitised ToT value.

to two fanout *Calamares* boards within the electronics box of each Nikhef POM via standard cables with RJ45 connectors, as shown in Figure 4.5. Both Calamares boards are directly attached to a *Central Logic Board* (CLB) [86, 108]. The CLB contains the ToT discriminators and TDCs used to digitise the recorded signals, as well as an FPGA (Field-Programmable Gate Array) programmed to provide additional logic and WR clock synchronisation for timestamping. Each Nikhef POM electronics box also contains an AC to DC power converter (AC/DC) whose output is fed into the CLB for distribution.

Every Nikhef POM is connected via a single optical fibre and a single power connection to an interface Nikhef-container, the contents of which are labelled in the bottom half of Figure 4.6. An aluminium structure holds two WR switches within each container specially designed to remove heat from the switch components and transfer it to the colder outer shell. Both switches are powered by independent AC to DC converters and connected via a single optical fibre each to the higher level DAQ systems. An additional connection is made between each switch to ensure that if one higher-level connection fails, the other can still be used for networking.

Each Nikhef-container also holds a relay board to control the power supply to individual POMs. The relay board control electronics are powered via an AC to DC converter and connected to one of the switches via a media converter for networking. The media converter is required to convert the optical fibre WR switch connection to a standard RJ45 copper cable connection. A total of five Nikhef-containers are present within CHIPS-5.

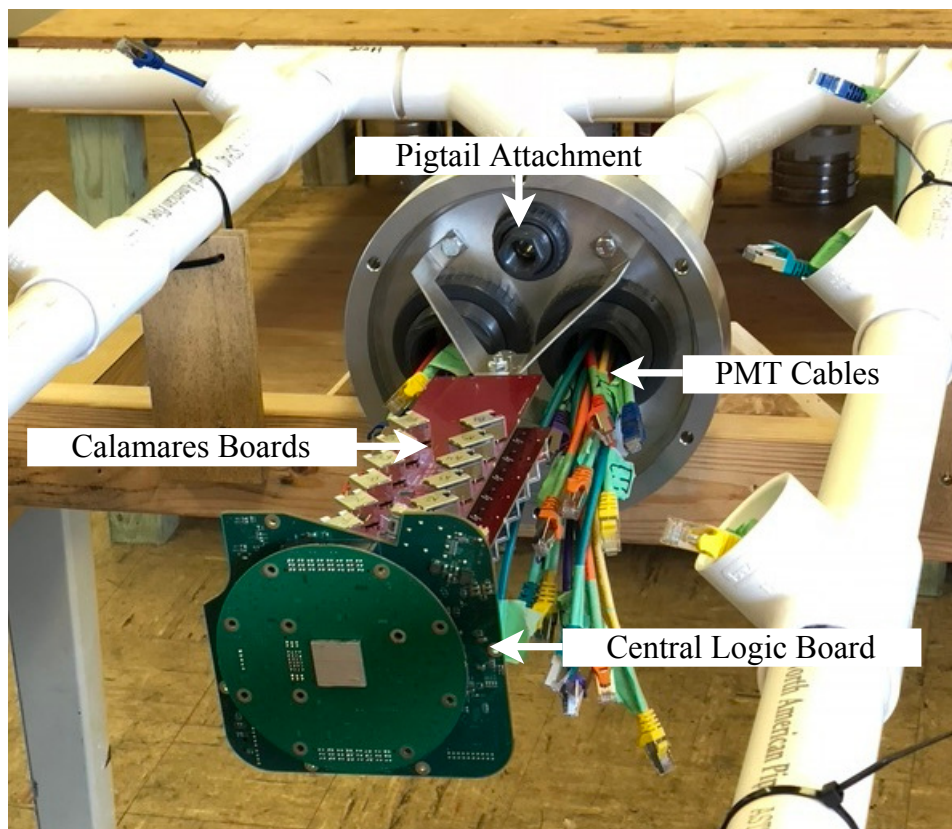


**Figure 4.5:** Labelled picture of the Nikhef POM electronics box without its aluminium casing. Both ends of the PMT cables can be seen, either at the PMT mounting points or entering the electronics box and not yet plugged into Calamares boards.

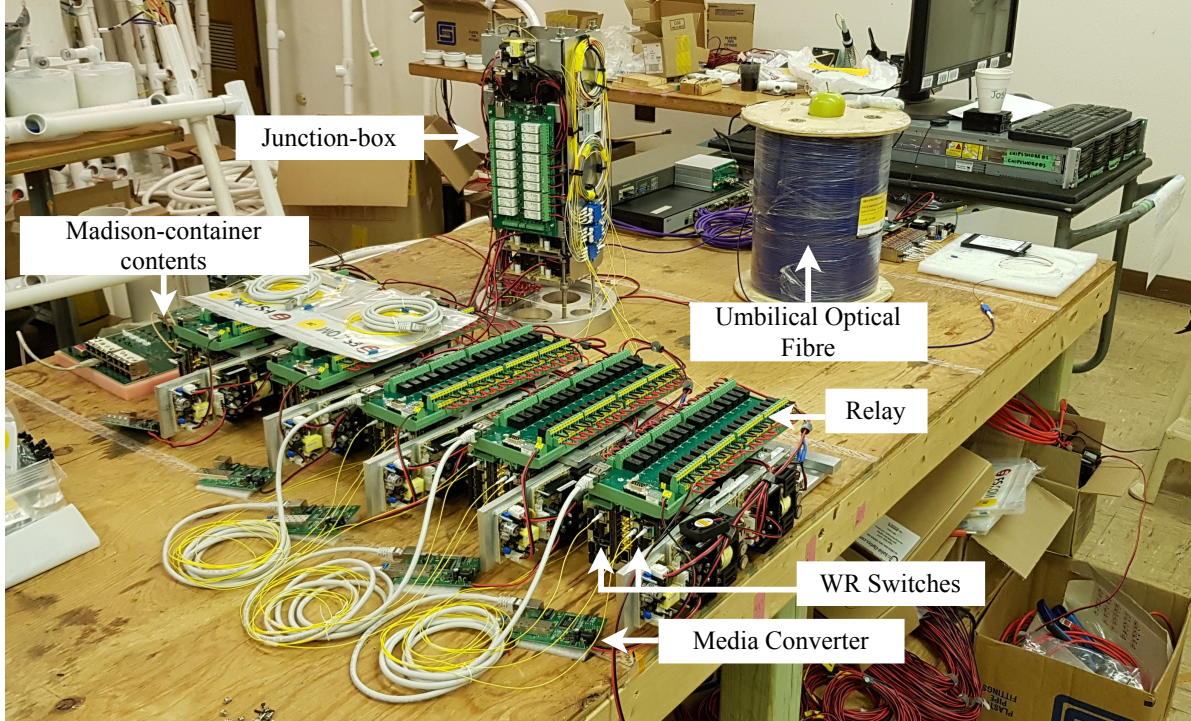


**Figure 4.6:** Labelled picture of the high-level non POM components of the CHIPS-5 DAQ system arranged on a table at the PolyMet mining administration building.

#### 4.2.2 Madison hardware

Every Madison Hamamatsu PMT is directly attached to a high-voltage generating Cockcroft-Walton board followed by a signal processing  $\mu$ DAQ, as shown in Figure 3.14. The  $\mu$ DAQ is a small microcontroller developed for both IceCube and CHIPS at WIPAC in Madison. Capable of timestamping and digitising signals directly at the PMT level, the  $\mu$ DAQ also sets the PMT operating voltage by controlling the driving frequency of the Cockcroft-Walton board [81].

Up to 16  $\mu$ DAQs receive power, networking, and WR synchronised IRIG-B and 10 MHz timing signals from a *badger-board*, as shown in Figure 4.7. Standard cables with RJ45 connectors are used for these connections. The badger-board is located within the electronics box of each Madison POM and acts as a simple fanout and power control board. For logic, each badger-board has an attached mezzanine Beaglebone [109]. This single-board Linux machine (very similar to a Raspberry Pi) controls the power supply to, and receives hits from, the attached  $\mu$ DAQs.

Similarly, up to 16 Madison POM badger-boards receive power, networking, and WR synchronised IRIG-B and 10 MHz timing signals from a *danout-board* located within a

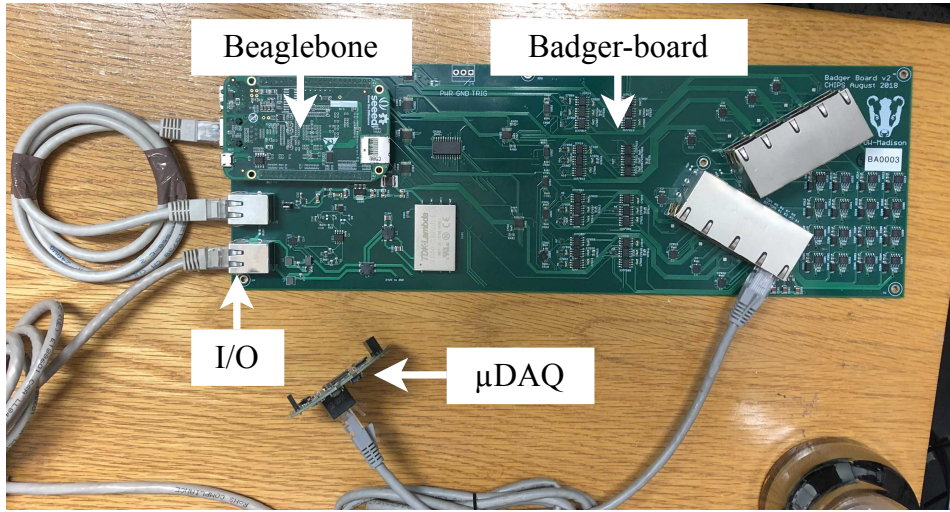


**Figure 4.7:** Labelled picture of the components of the Madison POM electronics box.

single interface Madison-container. Again, standard cables with RJ45 connectors are used for these connections. The full contents of the Madison-container are shown in Figure 4.8. Similar to the badger-board, the danout-board acts as a simple fanout and power control board with an attached mezzanine Beaglebone. However, in this case, the attached Beaglebone acts only to control the power provided by the danout-board.

PMT hits and other data are instead routed through the danout-board into a networking stack. Consisting of a WR-LEN, a router (required due to the limited WR-LEN routing table size), and a switch (non-WR), the stack provides networking to the higher-level DAQ via a single optical fibre. The WR clock synchronised IRIG-B and 10 MHz timing signals are output by the WR-LEN to the danout-board for forwarding to the lower-level components. Additionally, two AC to DC converters provide power for both the devices within the container and all lower-level components via the danout-board.

Compared to the Nikhef hardware the CHIPS developed Madison implementation has a few key advantages, primarily driven by the core CHIPS concept of reducing cost:

- Commercially available and cheap ( $\sim \text{£}50$  each) Beaglebones are leveraged for POM level processing and logic instead of expensive, FPGA based CLBs. Not only are they cheap but Beaglebones provide a fully configurable general-purpose Linux machine that can easily be enhanced with new features once deployed. This is in comparison to CLBs which can be only be reconfigured via remote reprogramming of the FPGA.

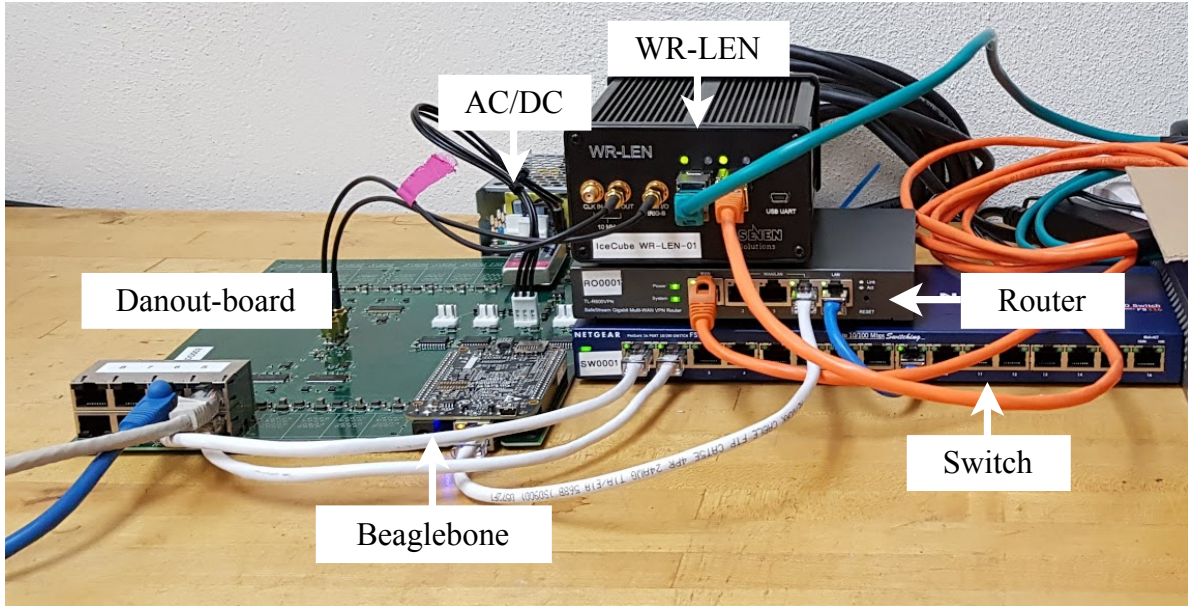


**Figure 4.8:** Labelled picture of the Madison-container components. The blue and grey cables exiting the left hand side of the image go to individual Madison POMs connecting to the I/O port shown in Figure 4.7. An optical fibre connection into the left SFP port of the WR-LEN is used in reality rather than the copper connection shown here.

- PMT hit processing and logic is pushed right to the lowest-level PMTs themselves via the use of  $\mu$ DAQs. Although not currently fully realised this can have significant implications for the DAQ system as a whole. For example, future updates will allow for beam spill hit triggering to be performed on the  $\mu$ DAQ, drastically reducing the capacity requirements of the rest of the DAQ system, further reducing costs.
- The number of expensive WR switches is reduced, with much cheaper WR-LENS taking their place. Although this change removes WR clock time synchronisation from the POM level, tests have shown that achievable cable length time corrections still allow for sub-nanosecond synchronisation accuracy to be reached.

### 4.2.3 Combined systems

Each interface container is connected to a single junction-box, labelled in Figure 4.6. This central container acts as the interface between the detector electronics and the umbilical, carrying data and power between the shore and the detector.



**Figure 4.9:** Picture of a Nikhef POM to Nikhef-container manifold (in white) attached to the top-cap of the CHIPS-5 detector. In the left of the image, two unattached Nikhef POM pigtails are seen, both covered in green tape and a plastic bag. The manifolds can also be seen in the graphical rendering of the top-cap shown in Figure 3.17.

Due to the unique CHIPS constraint of complete submersion within water, all connections to the junction-box (as well as those between POMs and the interface containers) are made within watertight, flexible PVC tubing called *manifolds*. These tubes span all corners of the CHIPS-5 detector, as shown in Figure 4.9, usually attached to the endcap frames. Additionally, as is done for the individual POMs, water-blocks are placed between all interface containers and the junction-box to compartmentalise the higher-level DAQ components and prevent a single leak from taking down the whole system.

For networking the junction-box contains a Coarse Wavelength Division Multiplexing (CWDM) multiplexer/demultiplexer (MUX/DEMUX). This device supports 32 wavelengths for a total of 16 bi-directional 1 Gb connections over the single 500 m long umbilical optical fibre. Each WR-LEN or WR switch within the detector uses one of these channels exclusively with the corresponding wavelength SFP.

The two umbilical power connections are distributed via two thick copper plates to all the relay channels within the junction-box. Two relay boards are used to provide a sufficient number of output channels, with their control electronics powered by separate AC to DC converters and each connected to one of the MUX/DEMUX networking channels via a media converter (optical fibre to RJ45). Each relay channel also has a built-in *trip gate* to immediately power-off the channel if a current surge is detected. This protection is particularly crucial for CHIPS-5 as water leaks are possible.

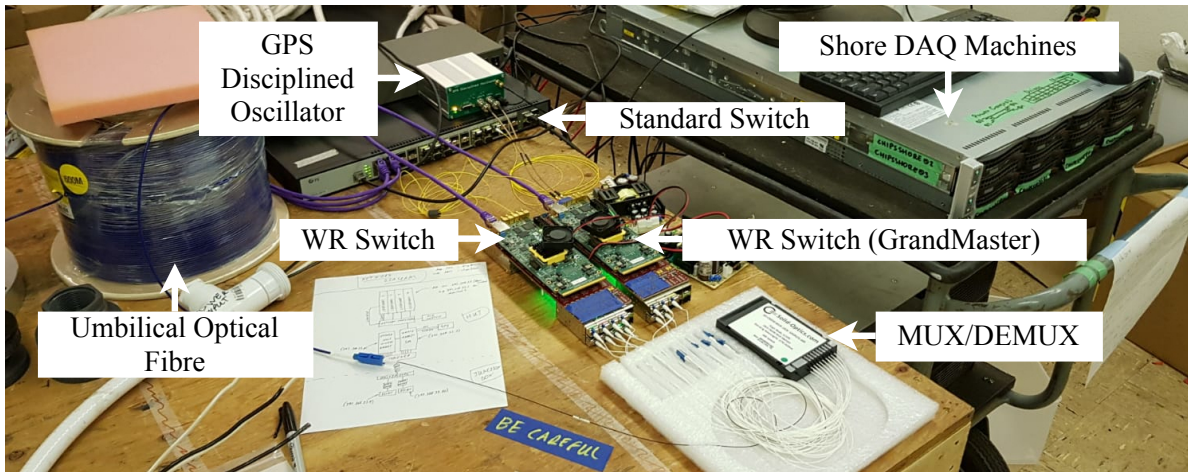


**Figure 4.10:** Labelled picture of the high-level onshore components of the CHIPS-5 DAQ system arranged on a table at the PolyMet mining administration building.

The contents of the DAQ electronics *Shore Hut* are shown in Figure 4.10. The single umbilical optical fibre connection passes through a MUX/DEMUX before each of the wavelength-specific channels are passed into one of two WR switches. Multiple Virtual Local Area Networks (VLANS) are configured on each switch such that for each wavelength channel only a single paired port on the other physical side of the switch carries that channels data to and from the standard networking switch (these connections are not present within Figure 4.10). Of the two WR switches, one is configured to be the GrandMaster with connections to a GPS disciplined oscillator. A single connection is also made between the WR switches for clock synchronisation.

The standard network switch provides 10 Gb connections to each of the Shore DAQ computing machines whose specific roles are detailed in Section 4.3. Each machine is also connected to a second switch providing connections to the external internet and DAQ components located at Fermilab. At Fermilab, a DAQ machine (Fermi DAQ-1) performs two main roles. Firstly, it forwards NuMI beam spill timing information from a Time Distribution Unit attached to the Main Injector clock to CHIPS-5. Secondly, it receives recorded detector data and places it into long-term storage.

An uninterruptible power supply provides power to all devices within the Shore Hut, supplying power for up to 15 minutes after a power cut, sadly quite a common occurrence. This protection gives all Shore Hut devices plenty of time to appropriately close any open data files and power down safely. The two detector umbilical power connections do not use the uninterruptible supply and instead draw power directly from the master supply.

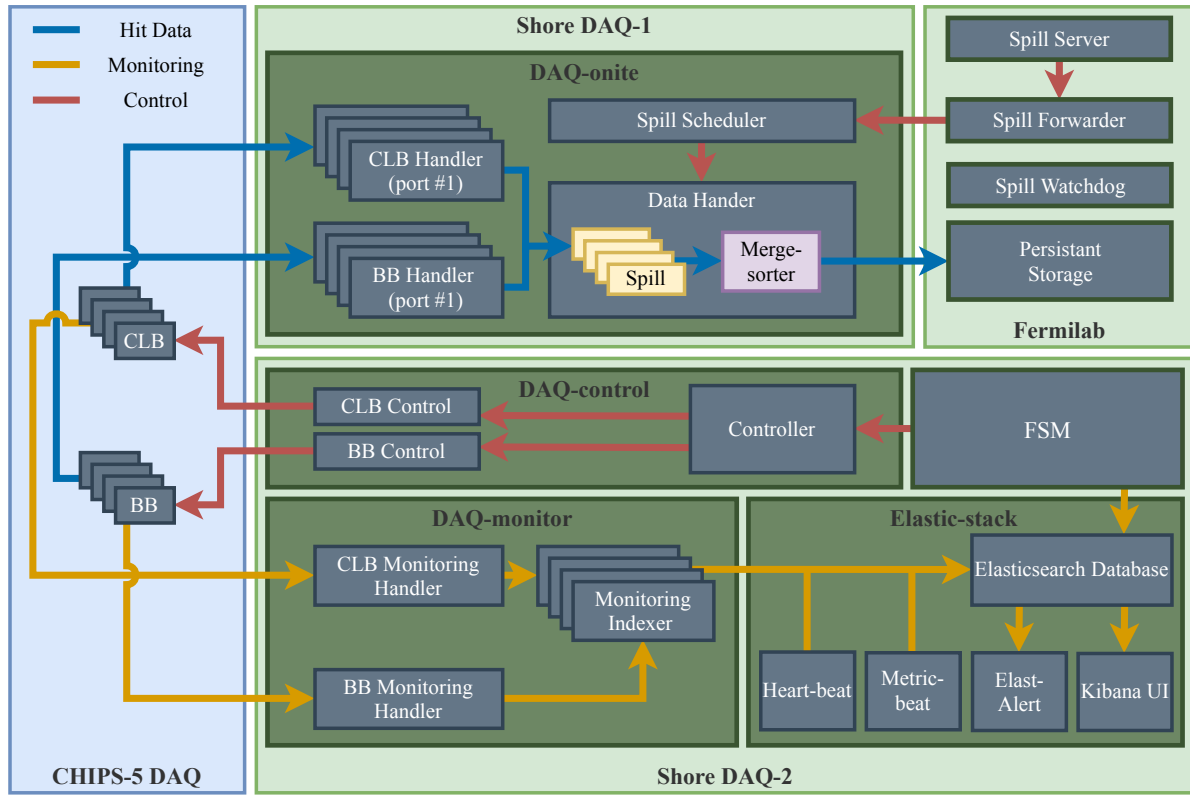


**Figure 4.11:** Diagram of the CHIPS-5 software system in terms of the flow of data between components. Beaglebone is abbreviated to BB.

### 4.3 Software and the flow of data

The software of the CHIPS-5 DAQ system provides three main functionalities: control of the detector instrumentation, the handling of recorded PMT hits, and the monitoring of hardware and data quality. Each of these functions are discussed within a specific subsection below alongside the corresponding software processes (applications) that perform them. Only the high-level software components (physically processed onshore) are detailed, with the low-level CLB, Beaglebone, and  $\mu$ DAQ software implementations omitted for brevity. An in-depth discussion of the CLB software can be found in reference [110], while the Beaglebone and  $\mu$ DAQ software implementation can be found at reference [111].

The DAQ software itself is mainly written in C++ and can be found at reference [112]. The system is comprised of multiple processes containing multiple components each (usually processed on separate threads), as is shown within Figure 4.11, expressed in terms of the flow of data between components. All DAQ processes make extensive use

of multithreading and asynchronous communication, principally implemented using the low-level Boost Asio (asynchronous input/output) library [113].

All high-level processing takes place on one of three machines: Shore DAQ-1 for hit handling, Shore DAQ-2 for control and monitoring, and Fermi DAQ-1 for NuMI spill forwarding and storage. As the processing of PMT hits is the principal software task, hit handling takes place exclusively on Shore DAQ-1 to ensure maximum available processing power. Both Shore DAQ machines have a corresponding backup machine (Shore DAQ-3 and Shore DAQ-4) to take over their functions immediately in case of a fault.

### 4.3.1 Control

All DAQ processes and low-level DAQ devices (CLBs and Beaglebones) conform to a global Finite State Machine (FSM) schema. The schema defines a finite set of states, shown in Figure 4.12, for which a DAQ process can only be in one at any given time. Specifically allowed transitions, triggered by a command signal, allow each process to move between states. During transition, the process performs the specific actions required to achieve the desired state. Every DAQ process makes its current internal state publicly known via constant publishing over a standard inter-process communication socket (Unix domain socket).

A singleton *FSM* process both issues the transition signals to and monitors the state of all DAQ processes. The *FSM* process defines the global state of the DAQ system, only transitioning to a new state once all children DAQ processes have reached the desired state. Currently, no control scheduling system is implemented to automatically configure the detector and conduct a given set of runs. Therefore, a simple command-line interface is used to issue state transition commands to the *FSM* process manually. Viewing the DAQ system as a whole, the actions performed at each state transition are as follows:

- **Initialising** occurs automatically when the DAQ system is started. During this transition all processes conduct the basic actions required for them to be able to function, such as opening inter-process communication channels, validating CLB and Beaglebone connections, and starting worker threads.
- **Configuring** occurs when the *configure* command is issued. During this transition the desired detector configuration is read from a human-readable file and all DAQ devices configured accordingly. This procedure primarily consists of setting the

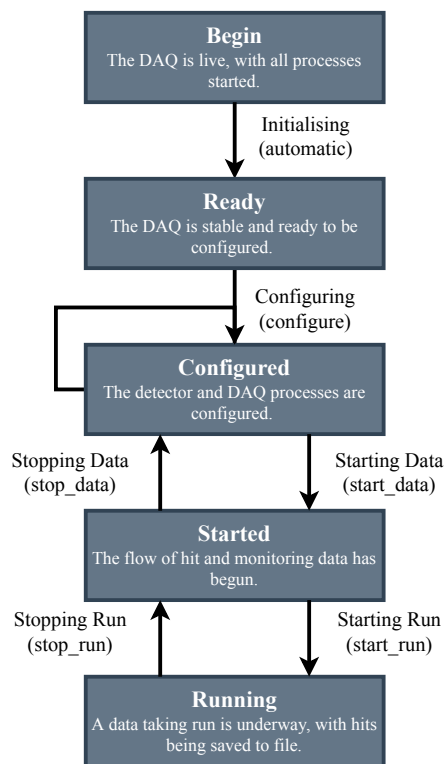


**Figure 4.12:** Diagram of the allowed states and transitions of the CHIPS-5 FSM. The command signal names for each transition are shown in brackets.

desired high-voltage level and ToT thresholds for each PMT via communication with all CLBs and Beaglebones.

- **Starting Data** occurs when the *start\_data* command is issued. During this transition commands are sent to all CLBs and Beaglebones to start the flow of PMT hit and monitoring data.
- **Stopping Data** occurs when the *stop\_data* command is issued. During this transition commands are sent to all CLBs and Beaglebones to stop the flow of PMT hit and monitoring data.
- **Starting Run** occurs when the *start\_run* command is issued. During this transition the handling of PMT hit data is started, with the resulting data saved to file. This procedure includes the selection of hits according to the NuMI beam spill trigger, as detailed in Section 4.3.2.
- **Stopping Run** occurs when the *stop\_run* command is issued. During this transition the handling of PMT hit data is stopped, and the run data file closed.

For control of the detector devices, a *DAQ-control* process issues commands to and monitors the state of all CLBs and Beaglebones. For communication, all messages are exchanged using standard TCP (Transmission Control Protocol) packets over ethernet. A DHCP server on Shore DAQ-2 assigns predefined static IP addresses to all devices to allow this to happen easily.

A single DAQ-control controller thread receives commands from the FSM process and instructs separate CLB and Beaglebone controller threads to issue the appropriate implementation-specific ‘slow-control’ commands for the given transition. A simple retry mechanism ensures that multiple attempts are made to achieve the desired state on each device. However, a CLB or Beaglebone is dropped after a maximum number of attempts have been made in order not to block the global DAQ transition due to a single faulty device.

### 4.3.2 Hit handling

As is done within the KM3NeT experiment, an ‘all-data-to-shore’ approach to PMT hit acquisition is taken, where all recorded hit data is sent via the WR network to the machines onshore. No triggering takes place within the detector. This is conducted by collecting all PMT hits within 10 ms long time windows. At the end of each window,

collected hits are packaged along with a header into UDP (User Datagram Protocol) packets and sent to shore. This process occurs on both the CLBs and Beaglebones when in either the *Started* or *Running* FSM state.

Jumbo UDP packets of maximum size 9000 bytes are used instead of typical 1500 byte packets. This is done to both reduce the proportion of bandwidth taken up by headers, and reduce the total network traffic (number of packets), leading to a decrease in the overall proportion of dropped packets. Although UDP does not contain the error-checking and correction features built into TCP, the proportion of lost packets is negligible and the increased bandwidth desirable.

PMT hit packets are handled by the *DAQ-onite* process, named after the Taconite ore that used to be extracted from the Wentworth 2W pit. The primary function of DAQ-onite is to store incoming PMT hits whose timestamp matches a NuMI beam spill trigger window and discard those that do not. This is complicated by the fact that the exact NuMI spill time is not known in advance.

Whenever the Main Injector at Fermilab releases a spill of protons for the NuMI beam, the accurate timestamp of this event is only published as it happens. Therefore, by the time the Fermilab based *Spill Server* and *Spill Forwarder* processes have received and forwarded the signal to the Shore DAQ-1 machine running DAQ-onite, approximately 0.5 seconds have passed since the neutrino spill passed CHIPS-5.

To counter this problem DAQ-onite implements a *Spill Scheduler* prediction mechanism which uses the periodicity of the spill trigger signal to continually predict the time of multiple spill windows (each 100 ms long) in advance. As PMT hits are processed, they are either attached to a matching predicted *Spill* or immediately discarded. This process is conducted by a series of CLB and Beaglebone specific handling threads which decode the raw PMT hit packets across a range of input ports to increase throughput.

Once the accurate timestamp for a beam spill has been received and a configurable period has passed to catch any late-arriving hits, the spill window is closed. Once closed, the attached PMT hits are combined and sorted using a *Merge-sorter* algorithm before being saved to file. In addition to the PMT hit data, each data file includes context metadata and flags indicating data faults. All new data files are periodically forwarded to long-term storage at Fermilab for further analysis.

During the initial CHIPS-5 DAQ commissioning in late 2019, a very high average PMT hit rate of 100 KHz was observed across all PMTs. This was expected due to both the

extended period the PMTs had been exposed to direct sunlight during construction, and the presence of a light leak through a tear in the detector liner. Somewhat beneficially, this allowed for load testing of the DAQ hit handling system with a peak WR network throughput of 5.66 Gb per second of hit data. DAQ-onite was found to behave as expected, with only negligible data loss.

### 4.3.3 Monitoring

CHIPS-5 DAQ monitoring is comprised of two principal functions: the monitoring of hardware components and the monitoring of PMT hit data quality. The first of these aims to check that all hardware is alive and performing efficiently without error, whilst the second ensures that the recorded hit data is consistent with what is expected. Both of these functions are conducted within CHIPS-5 using an implementation built around a central Elasticsearch database [114].

Elasticsearch is an open-source JSON-based search engine and NoSQL database. One of its primary applications is for logging, infrastructure observation, and application performance monitoring, making it a perfect fit for use here. Elasticsearch sits within the broader range of open source tools called the Elastic Stack [115], including those to both ingest data and produce visualisations. All Elasticsearch data is stored within collections of related JSON documents known as *indices*, which share a common set of key to value pairs.

Monitoring data is continually ingested into Elasticsearch from a wide range of sources across the CHIPS-5 DAQ system:

- *DAQ-monitor* receives and handles the monitoring data produced by the CLBs and Beaglebones. At the end of every 10 ms long PMT hit data taking window both CLBs and Beaglebones produce UDP monitoring data packets. Included within the packets are general POM wide status indicators such as temperate and humidity, as well as PMT specific hit rate values. DAQ-monitor decodes this data and continuously pushes it to Elasticsearch using a set of asynchronous *indexing* threads.
- The current FSM state of all the DAQ software processes in addition to the global state is frequently pushed to Elasticsearch by the FSM process.

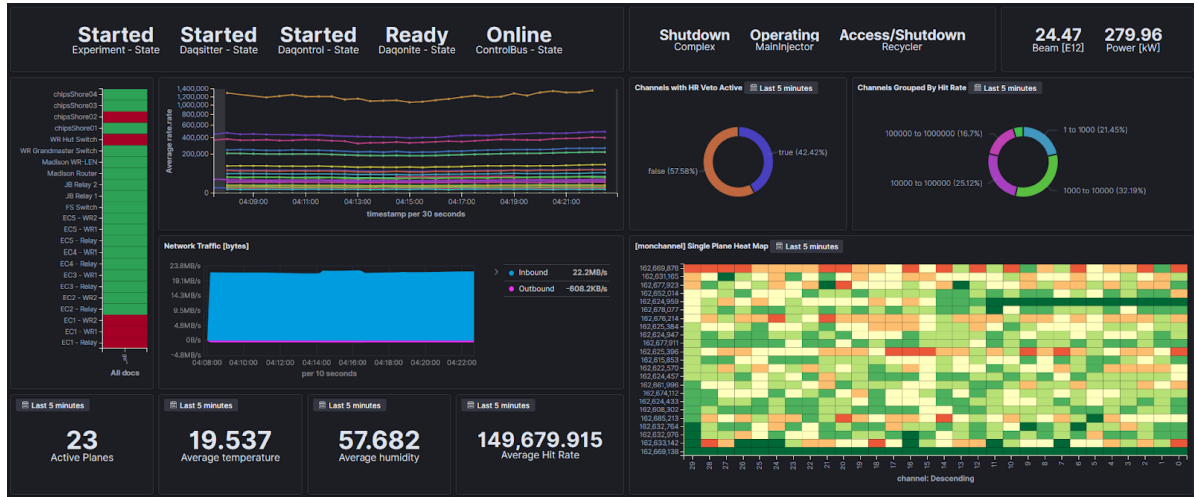


**Figure 4.13:** Screenshot of a Kibana monitoring dashboard for CHIPS-5. The dashboard pulls live monitoring data from the Elasticsearch database for its visualisations. The status of the various DAQ software components are shown in the top left above an average hit rate plot for each POM and the colour coded status indicators for various DAQ devices. A plot of the network data rates is also shown alongside global average indicators. The right hand side of the dashboard contains visualisations to monitor the overall status and specific hit rates of PMTs.

- The status of the Fermilab based Spill Server and Spill Forwarder alongside general NuMI beam metrics are forwarded to Elasticsearch using the *Spill Watchdog* process operating on the Fermi DAQ-1 machine.
- All DAQ network devices are constantly ‘pinged’ to check they are alive by the *Heartbeat* process which forwards this data to Elasticsearch.
- Shore DAQ machine system metrics (CPU usage for example) as well as system logs and data input and output rates are frequently forwarded to Elasticsearch from instances of the *Metricbeat* process running on each DAQ machine.
- Any logs produced by the DAQ software are asynchronously logged to Elasticsearch.

The Kibana browser-based user interface application is used to visualise the monitoring data stored within Elasticsearch [116]. A series of preconfigured dashboards, one of which is shown in Figure 4.13, summarise the current and historical monitoring data in an easy to digest fashion. The primary advantage of using Kibana over the more typical bespoke implementations used by HEP experiments is that it is both easily configurable by non-experts and only requires a browser and an internet connection to use from anywhere (in addition to authentication).

Furthermore, an alerting system using the ElastAlert framework [117] provides automatic notification of events for human attention. The ElastAlert process continuously checks the Elasticsearch monitoring data for any breaches of predefined rules ( $x$  events in  $y$  time, for example). Upon the occurrence of a rule trigger, multiple forms of notification (email and Slack messages) are sent to appropriate recipients for further analysis and response.

Not only is the CHIPS-5 monitoring system extensible and easy to use it also has the advantage of leveraging the efforts of an active open source community. With no additional effort by the members of the CHIPS collaboration, the monitoring implementation will continue to improve with time as updates are made to the underlying Elastic Stack software. This is likely to include both performance improvements alongside new ways of quickly ingesting data and creating visualisations. The monitoring approach firmly achieves one of the driving principles of the CHIPS project, using commercially available, cheap (free in this case) components, wherever possible.

# Chapter 5

## Convolutional neural networks for CHIPS

For the majority of HEP experiments, event analysis entails the separation of signal from background, the identification of particle types, the discovery of spatial properties, and the estimation of energies. The same is true for CHIPS detectors, with the primary aims being the selection of appeared CC  $\nu_e$  signal events from a sizeable background, and the estimation of associated neutrino energies.

For this purpose, the CHIPS project has so far relied on a human implemented reconstruction algorithm and a simple classification neural network driven by hand-engineered features. Both are prone to human error and restricted in scope to what has been implemented in software.

The work outlined in this chapter presents a replacement event analysis methodology for CHIPS. Three *Convolutional Neural Networks* (CNNs) [118], a type of *deep learning* [119] neural network have been implemented to achieve the primary aims outlined above, amongst others. One for cosmic muon rejection, one for beam event classification, and one for neutrino energy estimation. For evaluation purposes, only the implementation as applied to the CHIPS-5 detector module is considered in this work.

After mentioning previous implementations of deep learning for neutrino experiments, a description of the current (standard) techniques are given, before the theoretical background of CNNs is outlined. The baseline implementation for CHIPS is then described, followed by the specific implementations for each of the three networks. This work is solely that of the author's. A comprehensive evaluation of the trained networks is presented separately in the following chapter (Chapter 6).

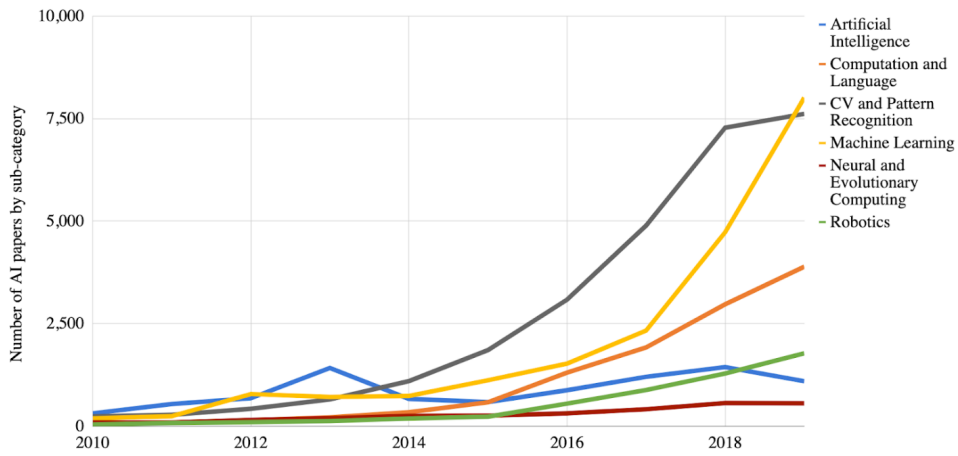


**Figure 5.1:** The number of artificial intelligence papers submitted to arXiv, broken down by sub-category. Note the particularly large increase in Computer Vision (CV) and pattern recognition papers. Figure taken from reference [121].

## 5.1 Previous applications of deep learning for neutrino experiments

Over the last few years, neutrino experiments have started to adopt deep learning techniques for a range of event analysis tasks [120]. This trend has closely followed the general explosion of interest in the field amongst the global research community, especially within the sub-field of computer vision, as can be seen in Figure 5.1.

In 2016 the NOvA experiment applied a CNN to the task of classifying the interaction type of events within their sampling calorimeter detector [122]. Two views of raw detector data were used as input to train a network based on the popular GoogLeNet architecture [123] (discussed in Section 5.3.3). Further NOvA iterations have since been applied to both the classification of individual energy deposit clusters [124] and  $\nu_e$  and  $e^-$  energy reconstruction [125].

CNNs have also been applied to liquid argon time-projection chambers. The MicroBooNE experiment [126] has shown that in addition to classification tasks, the spatial localisation of single particles within events is possible [127]. Furthermore, the DUNE collaboration has designed a network to output both the interaction class and counts of different particle types within an event [67, 128]. This approach is called *multi-task* learning and is discussed in detail within Section 5.4.3.

Applications to water Cherenkov detectors have also been made by both the Daya Bay experiment [129] and the KM3NeT/ORCA collaboration [130]. Furthermore, a type of CNN known as a *variational autoencoder* has been shown to approximate the distribution of simulated water Cherenkov data well [131]. If further such studies prove successful, this could allow for training on ‘real’ data to mitigate experimental uncertainties and vastly increase the speed of simulated data generation.

## 5.2 Standard event reconstruction and classification

It is essential to outline the standard event reconstruction and classification methods used by the CHIPS project until now. This is for two reasons. Firstly, to highlight their main weaknesses as motivation for the new CNN approach. Secondly, to provide context for the performance comparisons made in Chapter 6.

A likelihood method based on that implemented by MiniBooNE [132] is used for event reconstruction, while a simple neural network built using the TMVA package [133] is used for event classification. Both methods are representative of the mainstream approach used by the majority of water Cherenkov neutrino experiments for event analysis. A prime example is the fITQun algorithm developed for the Super-Kamiokande detector, used for both atmospheric [134] and T2K [135] analyses.

### 5.2.1 Likelihood-based reconstruction

The event reconstruction methodology is simple in theory: for a given set of hypothesised charged particle tracks, the number of Cherenkov photoelectrons and the time at which the first of these is recorded for each PMT in the detector is predicted. By comparing this prediction with the measured hit charges and times the likelihood that the given track hypothesis produced the measured signals can be calculated. The parameters that describe the hypothesised tracks are then varied until the negative logarithm of the likelihood is minimised, identifying the best-fit parameters. A brief description of the full procedure is given below, however, for a detailed description see reference [91] and reference [84]. The full C++ software implementation can also be found in the repository at reference [136].

## Seeding

The first stage of event reconstruction is the effective *seeding* of tracks that are then used in the full likelihood fit. The seeding methods aim to provide a good starting point for the minimisation, both to increase the efficiency of finding the optimal track parameters and also to avoid a false local minimum from being returned.

Firstly, the PMT hits are sliced in both space and time. Gaps in the time ordering of hits are used to separate the event into time slices. Each of these slices then undergoes basic filtering and clustering to remove outlying hits and ensure only the dominant collections of hits are considered. Each cleaned slice is then run through simple geometric vertex finding algorithms to estimate the interaction position and time, in addition to the initial track direction.

A circular *Hough transform* algorithm, traditionally used for water Cherenkov ring finding is then applied. As output, the voting-based transformation produces a space within which rings of PMT hits exist as peaks. The track direction values are further refined using this space before a search for secondary peaks is carried out to indicate if multiple particles are likely to be involved. This process results in a list of seeds, each with a score related directly to the height of the associated peak in Hough transform space.

## Likelihood fit

Each particle track in a fit hypothesis comprises a vector of parameters  $\vec{x}$ , containing the following:

- the track interaction vertex position ( $x_0, y_0, z_0$ ) and time ( $t_0$ );
- the initial track direction ( $d_\theta, d_\phi$ );
- the initial kinetic energy of the particle ( $E_k$ ); and
- the particle type (muon, electron or photon).

For a photon hypothesis the distance between the interaction vertex and the beginning of the electromagnetic shower is also included as a parameter.

The hypothesised tracks are then initialised using the list of seeds found in the seeding procedure in descending order of Hough peak height score. As the seeding algorithms

do not estimate the particle energy, a default value equal to the average particle energy observed in the Monte Carlo simulation is assigned. Additionally, constraints can be placed on a multi-track hypothesis to reduce the number of free parameters.

As an example, consider the NC  $\pi^0$  case, where a multi-track two-photon hypothesis is used. Firstly, the initial parameters for the two photons are assigned from the two highest-scoring seeds from the seeding procedure. Secondly, the vertex position for both tracks is constrained to remain the same, and the directions and energies are set to be constrained by the invariant mass of the  $\pi^0$ .

In it's simplest form the likelihood  $\mathcal{L}(\vec{x})$ , is a simple product of two terms:

$$\mathcal{L}(\vec{x}) = \mathcal{L}_{unhit}(\vec{x})\mathcal{L}_{hit}(\vec{x}) = \prod_{unhit} P_{unhit}(\vec{x}) \prod_{hit} P_{charge}(\vec{x})P_{time}(\vec{x}), \quad (5.1)$$

where the first (*unhit*) term gives the likelihood that the hypothesis  $\vec{x}$  will not predict a hit on the PMTs that do not have a measured hit, and the second (*hit*) term gives the likelihood that  $\vec{x}$  produces the observed photoelectrons and hit times on the measured hit PMTs.

By considering the negative logarithm of the likelihood the computation can be simplified into a sum of logarithms over the PMTs, such that

$$-\log \mathcal{L}(\vec{x}) = -\sum_{unhit} \log(P_{unhit}(\vec{x})) - \sum_{hit} \log(P_{charge}(\vec{x})) - \sum_{hit} \log(P_{time}(\vec{x})). \quad (5.2)$$

This form has the effect of separating the charge (number of photoelectrons) and time prediction components, which can then be dealt with separately computationally. In the actual likelihood calculation the  $P_{unhit}(\vec{x})$  and  $P_{charge}(\vec{x})$  components are combined, where the probability of an unhit PMT is treated as a PMT with an observed charge equal to zero.

The Minuit2 algorithm contained within the ROOT software package [137] is used for the minimisation process. At each iteration, the charge and hit time predictions are made, and the negative logarithm of the likelihood is calculated. The track parameters are then varied to minimise the likelihood before the next iteration begins. Through a series of stages, each fixing and freeing specific parameters, the minimisation process converges to the best-fit parameters for the given hypothesis. This procedure typically takes two minutes on a standard batch farm computing node.

## Downsides

The charge and hit time predictions and their associated likelihood contributions depend on many low-level inputs. Generally, these inputs describe how Cherenkov light is emitted from specific particles and how it propagates through the detector to be detected by the PMTs. Examples of these inputs include:

- the number of Cherenkov photons emitted by a particle of a specific type and energy;
- the fraction of Cherenkov light emitted at each step along a specific particle's track length;
- the angular distribution of Cherenkov photon emission for each type of particle;
- the survival probability of photons within the detector medium as a function of distance and energy;
- a detailed description of the PMT positions and directions;
- the angular efficiency of each PMT relative to the incident photon angle; and
- the probability of a measured charge given the predicted number of photoelectrons (see Figure 3.25b).

The above list demonstrates a fundamental problem with the likelihood-based approach. Namely, it is heavily reliant on the accuracy of multiple low-level inputs and their associated use in human implemented software. If a physical process is not modelled appropriately or more crucially overlooked, then the prediction accuracy of PMT charges and hit times is affected, impacting the performance of the best-fit parameters.

Moreover, the likelihood-based approach requires a predefined track hypothesis per fit. This restriction is at odds with the broad array of neutrino events expected within CHIPS detector modules. Many possible combinations of final state particles are possible, making the implementation of an approach where all possible events are considered, challenging. For example, the very similar Super-Kamiokande *fitQun* algorithm attempts multiple fits for each event, sequentially adding charged particles to the hypothesis until the best-fit is found. This technique not only vastly increases the time required to analyse a single event, but can never be fully rigorous as it still ignores some scenarios.

### 5.2.2 Event classification

As the standard event reconstruction is based on the calculation of a likelihood (analogous to a goodness-of-fit), the likelihood ratio between different hypotheses can be used for event classification tasks. Additional hand-engineered features derived from the reconstruction outputs are also found to have power in classifying the event type.

Two simple neural networks are used, the first for CC  $\nu_e$  - CC  $\nu_\mu$  separation and the second for CC  $\nu_e$  - NC separation. Both contain a single hidden layer (as described in the following Section 5.3) with the number of neurons equal to the number of input parameters plus five. Output variables from both a single electron track and single muon track hypothesis fit are used for both networks, including:

- the  $\Delta \log \mathcal{L}$  between  $e$  and  $\mu$  hypothesis for both time and charge components;
- the total number of hit PMTs ( $N_{hits}$ ) and total collected charge;
- $\frac{\Delta \log \mathcal{L}_{charge}}{N_{hits}}$ ;
- the fraction of hits inside, within, and outside the ring for both the  $e$  and  $\mu$  hypotheses;
- the fraction of predicted charge outside the ring for both the  $e$  and  $\mu$  hypotheses;
- the ratio of the total predicted charged to the total measured charge for both the  $e$  and  $\mu$  hypothesis;
- the ratio of the reconstructed energy to the total measured charge for both the  $e$  and  $\mu$  hypotheses;
- the reconstructed track direction under the  $e$  hypothesis;
- the fraction of hits in the downstream half of the detector;
- the number of seeds generated by the Hough transform seeding algorithm; and
- the peak height score of the first and last seeds found by the Hough transform seeding algorithm.

A sample of CC  $\nu_e$  and CC  $\nu_\mu$  beam events characteristic of those expected to be seen within CHIPS-5 are used to train the first classifier, and a corresponding sample of CC  $\nu_e$  and NC events for the second. The output values from both networks can then be

used to select CC  $\nu_e$  events from the background. Note that only the selection of CC  $\nu_e$  events has been implemented, no CC  $\nu_\mu$  selection has been developed.

The principal limitation of this approach is that the input features are restricted to those that have been imagined (requiring extensive domain knowledge) and then implemented in software. The current list is undoubtedly non-exhaustive of all the possible variables and combinations of variables that can, in theory, be used for discrimination between events. Additionally, any mistakes in the likelihood-based reconstruction and, therefore, input variables to the neural networks, can lead to incorrect classification of events.

## 5.3 The theory of neural networks

There are many machine learning techniques: linear regression, logistic regression, k-nearest neighbours, decision trees, random forests, support vector machines, amongst others, all of which learn to make predictions about data. However, none has been as successful, especially in recent years, as the deep neural network. As both the size of datasets and the amount of available computing power has increased, deep neural networks have proved incredibly powerful for many tasks, as they are well suited to this paradigm.

Here we discuss the application of neural networks for *supervised learning*, one of two broad machine learning categories concerned with using labelled example data to train algorithms. The other broad category of *unsupervised learning*, where the properties of the dataset are inferred without labelled data is not discussed, however, will be used for network *explainability* in Section 6.2.

### 5.3.1 Neural network basics

A neural network is a type of algorithm inspired by the repeating cell structure of neurons within our brains. The basic building block of a neural network is a *neuron*, which takes a vector of  $k$  inputs  $\vec{x} = (x_1, x_2, \dots, x_k)$  and outputs a scalar  $a(\vec{x})$ . Individual neurons are arranged into layers, with the input of one layer being the output from the previous layer. The first layer is commonly referred to as the *input layer*, the middle layers as *hidden layers*, and the final layer as the *output layer*, as illustrated in Figure 5.2. In

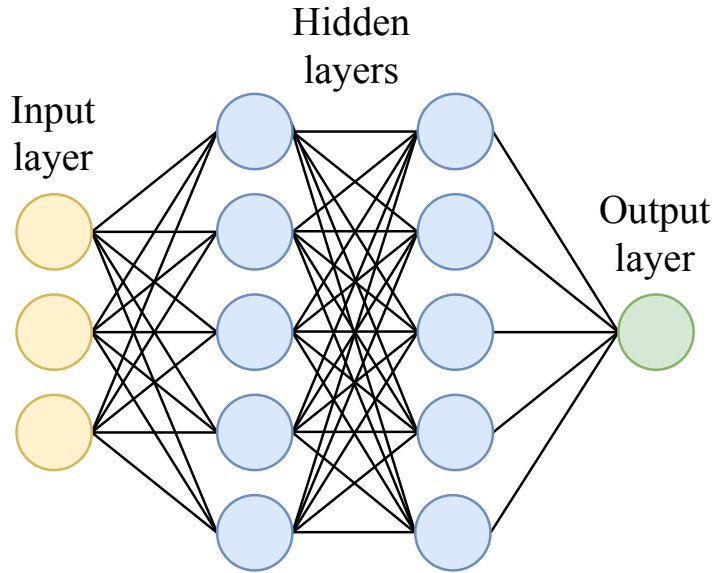


**Figure 5.2:** Illustration of a simple neural network. There is a single input layer (yellow), two hidden layers (blue), and an output layer (green). Each node corresponds to a neuron except for the input layer.

general, this simple neural network structure is referred to as *fully-connected*, as all the neurons in each layer have connections to all the neurons in the previous and following layers.

Input variables (traditionally hand-engineered features extracted from the raw data) are passed into the network via the input layer. Any number of hidden layers containing any number of neurons can then follow. The neurons contained within these layers are trained so that collectively their  $a(\vec{x})$  functions solve the task at hand. For a regression task, the output layer returns a continuous decimal value. Conversely, for a classification task, a probability value between zero and one is output for each class. The forward passing of information from one layer to the next is why neural networks can also be referred to as *feed-forward graphs*.

For a neuron  $i$ ,  $a_i(\vec{x})$  can be decomposed into a neuron specific linear operation, followed by a non-linear operation which is the same across all neurons. The linear operation consists of the dot product of the input vector  $\vec{x}$  with a vector of weights  $\vec{w}^{(i)} = (w_1^{(i)}, w_2^{(i)}, \dots, w_k^{(i)})$ , plus a bias term  $b^{(i)}$ :

$$z^{(i)} = \vec{w}^{(i)} \cdot \vec{x} + b^{(i)}. \quad (5.3)$$

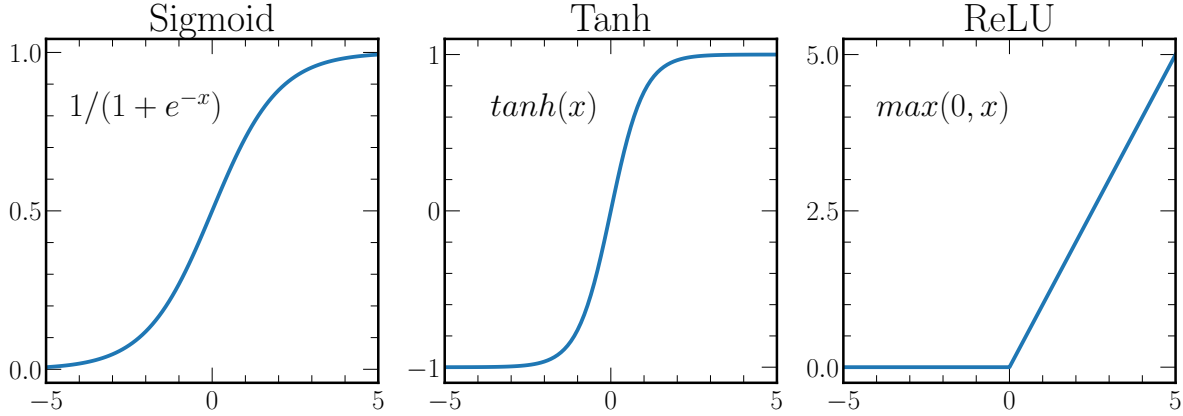


**Figure 5.3:** Common non-linear activation functions used for the neurons within neural networks.

After applying the non-linear operation  $\sigma_i$ , commonly referred to as the *activation function*, the final neuron output can be written as

$$a_i(\vec{x}) = \sigma_i(z^{(i)}). \quad (5.4)$$

Traditionally, a step-function (for networks called *perceptrons*) was used for the activation function. However, as is shown in Section 5.3.2, a non-zero gradient (only valid at  $x = 0$  for a step-function) is required for the practical training of neural networks. In fact, the choice of activation function can greatly affect how the network trains and performs.

Therefore, common activation function choices have been the *hyperbolic tangent* and the *sigmoid* functions, primarily because they are bounded and differentiable at all points. Recently, the *ReLU* and other similar functions have become popular, mainly due to their avoidance of *vanishing* gradients which occur when the tanh and sigmoid functions become saturated at large values of  $x$ . All of these functions are shown in Figure 5.3 for reference.

### 5.3.2 Training neural networks

Supervised neural network training uses labelled example data to iteratively find the optimal weights and biases (the network parameters) to maximise output performance. A *loss function*  $E(\vec{w})$ , is defined to quantify the difference between the network output and truth label for each example, where  $\vec{w}$  is the vector of network parameters. For a

given input example  $(\vec{x}_i, y_i)$ , with  $\vec{x}_i$  being the input parameters and  $y_i$  the known truth label, the network generates an output  $\hat{y}_i(\vec{w})$ . Using this notation, we can construct loss functions suitable for different tasks.

In the case of simple binary classification the most commonly used function is the *binary cross-entropy*, where

$$E(\vec{w}) = - \sum_{i=1}^n y_i \log \hat{y}_i(\vec{w}) + (1 - y_i) \log[1 - \hat{y}_i(\vec{w})], \quad (5.5)$$

with the number of examples given by  $n$ . For a classification task where the number of classes is greater than two  $y$  can instead take on  $M$  values. In this case we redefine each example so that  $y$  is instead a vector  $y_{im}$ , such that

$$y_{im} = \begin{cases} 1 & \text{if } y_i = m, \\ 0 & \text{otherwise.} \end{cases} \quad (5.6)$$

This is commonly named a *one-hot* vector. The cross-entropy then becomes the *categorical cross-entropy*, given by

$$E(\vec{w}) = - \sum_{i=1}^n \sum_{m=0}^{M-1} y_{im} \log \hat{y}_{im}(\vec{w}) + (1 - y_{im}) \log[1 - \hat{y}_{im}(\vec{w})]. \quad (5.7)$$

For a regression task predicting a continuous output variable, the *mean-squared error* is most often used as the loss function, with

$$E(\vec{w}) = \frac{1}{n} \sum_{i=1}^n (y_i - \hat{y}_i(\vec{w}))^2. \quad (5.8)$$

To find the optimal network parameters for the given task the loss function output (the *loss*) is iteratively minimised until it converges to the minimum (or in reality a local minimum that performs well). This is done by updating the network parameters at each iteration  $t$ , to move in the direction of the loss gradient, using the update rule

$$\vec{w}_{t+1} = \vec{w}_t - \eta_t \nabla_{\vec{w}} E(\vec{w}), \quad (5.9)$$

where  $\eta_t$  is the *learning rate* which determines the size of the step taken at each iteration. This methodology is known as *gradient descent* and is illustrated in Figure 5.4.

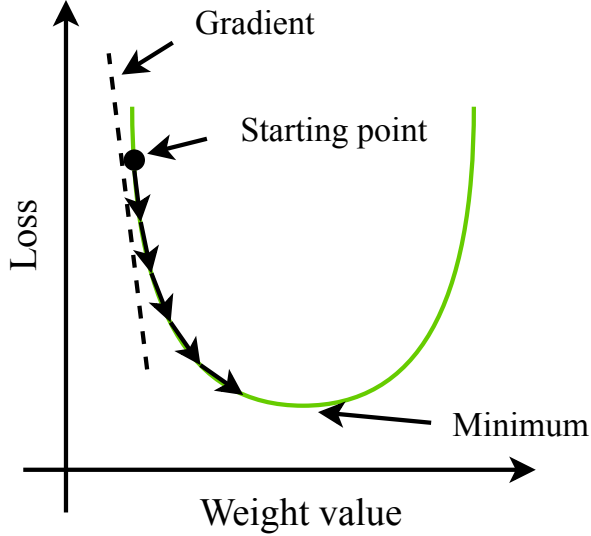


**Figure 5.4:** Illustrative diagram of the gradient descent procedure. Shown is the case for a loss function dependent on a single weight.

Therefore, to use gradient descent, we require that the gradient of the loss function with respect to the parameters of the network can be calculated. Doing this for each parameter at every iteration would render neural networks impossible to train due to the vast computational requirements. Instead, an innovative application of the chain rule, in an algorithm called *backpropagation* is used [138]. Here we follow the derivation of the four main backpropagation equations given in reference [139].

For a network containing  $L$  layers, we can index the individual layers using  $l = 1, \dots, L$ . The weight associated with the connection between the  $k$ -th neuron in layer  $l - 1$  and the  $j$ -th neuron in layer  $l$  can be denoted as  $w_{jk}^l$ , with the bias of the layer  $l$  neuron correspondingly written as  $b_j^l$ . The activation of the  $j$ -th neuron in layer  $l$  is then related to the outputs from the previous layer by

$$a_j^l = \sigma(z_j^l) = \sigma \left( \sum_k w_{jk}^l a_k^{l-1} + b_j^l \right), \quad (5.10)$$

where  $\sigma$  is the non-linear activation function.

The change in the loss function with respect to the linear weighted sum  $z_j^L$  of the  $j$ -th neuron in the last layer  $L$ , defines the error  $\Delta_j^L$ , such that

$$\Delta_j^L = \frac{\partial E}{\partial z_j^L}. \quad (5.11)$$

Using the chain rule and the fact that  $a_j^L = \sigma(z_j^L)$ , the error is found to be equivalent to

$$\Delta_j^L = \frac{\partial E}{\partial a_j^L} \sigma'(z_j^L), \quad (5.12)$$

where  $\sigma'(z_j^L)$  denotes the derivative of the non-linear activation function at  $z_j^L$ . This (equation (5.12)) is the first of the backpropagation equations.

The error  $\Delta_j^l$ , of the  $j$ -th neuron in layer  $l$  can be expressed in terms of the error in the following layer  $l + 1$ , by using

$$\begin{aligned} \Delta_j^l &= \frac{\partial E}{\partial z_j^l}, \\ &= \sum_k \frac{\partial E}{\partial z_k^{l+1}} \frac{\partial z_k^{l+1}}{\partial z_j^l}, \\ &= \sum_k \Delta_k^{l+1} \frac{\partial z_k^{l+1}}{\partial z_j^l}, \\ &= \left( \sum_k \Delta_k^{l+1} w_{kj}^{l+1} \right) \sigma'(z_j^l). \end{aligned} \quad (5.13)$$

The chain rule has again been used in addition to the fact that

$$z_k^{l+1} = \sum_j w_{kj}^{l+1} \sigma(z_j^l) + b_k^{l+1}, \quad (5.14)$$

to give the second of the backpropagation equations (equation (5.13)).

As  $\partial b_j^l / \partial z_j^l = 1$ , the error can also be viewed as the partial derivative of the loss function with respect to the bias, such that

$$\Delta_j^l = \frac{\partial E}{\partial z_j^l} = \frac{\partial E}{\partial b_j^l} \frac{\partial b_j^l}{\partial z_j^l} = \frac{\partial E}{\partial b_j^l}, \quad (5.15)$$

giving the third of the backpropagation equations (equation (5.15)).

The final backpropagation equation is given by the differential of the cost function with respect to the weight  $w_{jk}^l$ , which can be written as

$$\frac{\partial E}{\partial w_{jk}^l} = \frac{\partial E}{\partial z_j^l} \frac{\partial z_j^l}{\partial w_{jk}^l} = \Delta_j^l a_k^{l-1}. \quad (5.16)$$

The full backpropagation algorithm then proceeds as follows:

1. After calculating the activations  $a_j^1$  for all neurons in the input layer, use the feed-forward architecture of the network to calculate all the activations at every layer using equation (5.10).
2. Use equation (5.12) to calculate the errors of the last layer neurons, requiring both the derivatives of the loss and activation functions.
3. Use equation (5.13) to ‘backpropagate’ the error through the network from the last layer to the input layer, calculating all  $\Delta_j^l$  values.
4. Calculate the gradient of the loss function for all the weights and biases using equation (5.15) and equation (5.16).

A single activation finding *forward pass* followed by a single error propagating *backward pass* is all that’s required to calculate the gradients for all weights and biases within the network. This incredibly efficient procedure allows for the use of gradient descent when training neural networks.

### 5.3.3 Convolutional neural networks

The broad category of deep learning covers multiple neural network techniques spanning a range of application fields such as computer vision, speech recognition, and natural language processing. By stacking many layers on top of each other to form a ‘deep’ network, these methods offer increased problem solving capacity by allowing higher-order non-linear functions to form throughout the network. As a direct consequence, instead of requiring hand-engineered features as input, deep networks can learn to extract the most powerful features for a given task from raw data. Here we outline just the specific deep learning technique used in this work; the CNN.

#### CNN operations

The broad category of deep learning covers multiple neural network techniques spanning a range of application fields such as computer vision, speech recognition, and natural language processing. By stacking many layers on top of each other to form a ‘deep’ network, these methods offer increased problem-solving capacity by allowing higher-order non-linear functions to form throughout the network. As a direct consequence, instead

of requiring hand-engineered features as input, deep networks can learn to extract the most powerful features for a given task from raw data. Here we outline just the specific deep learning technique used in this work; the CNN.

## CNN operations

At their core, CNNs make use of a mathematical operation called *convolution*, which either entirely or in part replaces the simple vector multiplication seen in the fully-connected networks of Section 5.3.1. This difference makes CNNs incredibly powerful for applications with grid-like input data such as computer vision tasks.

Using standard CNN terminology, the discrete convolution between the *input*  $x$ , and the *kernel*  $w$ , is given by

$$f_i = (x * w)_i = \sum_{j=-\infty}^{\infty} x_j w_{i-j}, \quad (5.17)$$

where  $f$  is commonly referred to as the *feature map*. In typical applications, the input is a two-dimensional array  $X$ . Therefore, both the kernel  $W$ , and the resulting feature map  $F$ , also become two-dimensional. In this case the convolution operation becomes

$$F_i = (X * W)_{i,j} = \sum_m \sum_n X_{i+m, j+n} W_{m,n}, \quad (5.18)$$

where the infinite sum in equation (5.17) has been replaced with a discrete sum over two-dimensional elements. Analogous to the simple neural network weights  $\vec{w}$ , first described in equation (5.3), the elements of  $W_{m,n}$  are trained to minimise the loss, with the output feature maps passed through a non-linear activation function at each layer.

To illustrate the convolution operation, Figure 5.5 displays examples of a  $4 \times 4$  input grid and a  $3 \times 3$  kernel. The output feature map is generated by sliding the kernel across both dimensions of the input grid, summing the products of all associated elements at each step according to equation (5.18), as shown in Figure 5.6.

Two additional parameters impacting the feature map output size are introduced in Figure 5.6. The *stride* and *padding*. The stride  $S$ , governs how far the kernel moves at each step while the padding  $P$ , decides how the input grid is padded with zeros around its border. If  $L$  is the size of the input (both height and width) and  $K$  is the kernel size,

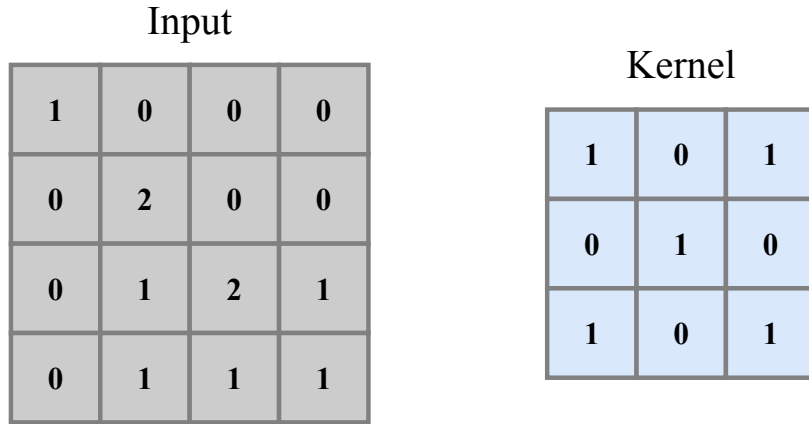
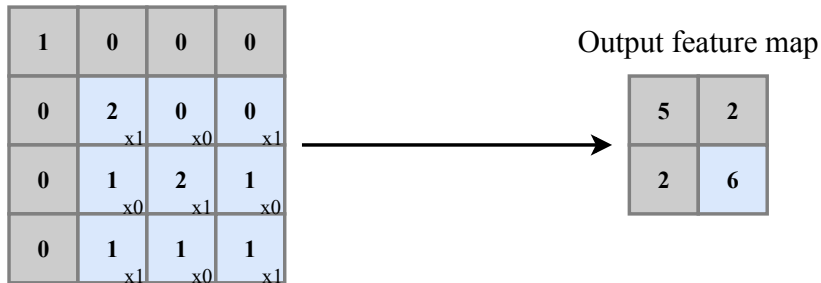


**Figure 5.5:** Example of an input grid (left) and kernel (right). The specific kernel shown is sensitive to x-shaped features

Convolve input and kernel



Convolve input and kernel

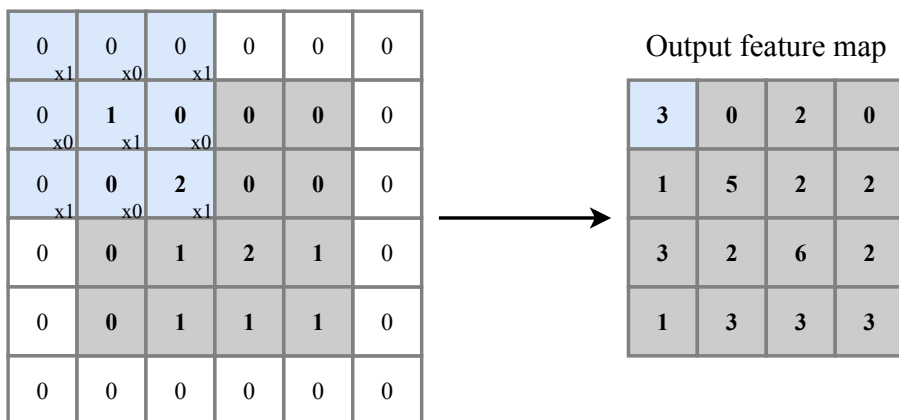


**Figure 5.6:** Example of a stride = 1 convolution operation involving the input grid and kernel from Figure 5.5. Both the operation for the case of *valid* (top) and *same* (bottom) padding are shown. The blue square in the top-left of the output feature maps indicates the output generated from the specific operation shown on the left, also in blue.

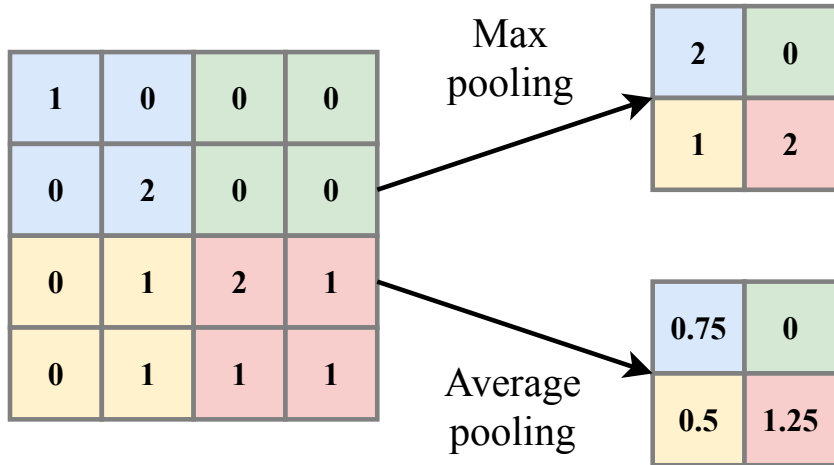


**Figure 5.7:** Example of both a max and average  $2 \times 2$  pooling operation with stride = 2.

the output feature map size  $O$ , is given by

$$O = \frac{(L - K + 2P)}{S} + 1. \quad (5.19)$$

The other essential operation used within CNNs is pooling. Pooling layers coarse-grain the spatial information of the input to reduce the number of network parameters. *Max pooling* or *average pooling* are the two common ways this is achieved. In both cases, the input is first divided into rectangular regions, and then either the maximum or average value of the region is returned as output, for max or average pooling, respectively. Both pooling procedures are illustrated in Figure 5.7.

Taking inspiration from how neurons behave in the visual cortex of animals [140], small kernels are typically used to only scan over a small patch of the input at a time. Combined with the loss of absolute position information from pooling, a key feature of CNNs is highlighted. They exhibit translational invariance and respect the local structure contained within the input. In simpler terms, they do not care wherein the input image a particular feature exists, just that it exists.

## CNN architectures

In 2012 the AlexNet CNN lowered the error rate of the ubiquitous ImageNet classification task [141] from 28% to 16% [142]. Since this breakthrough, the standard CNN has adopted a similar architecture to AlexNet. Multiple convolutional layers are stacked on top of each other, periodically interspersed with pooling layers. Once the output feature

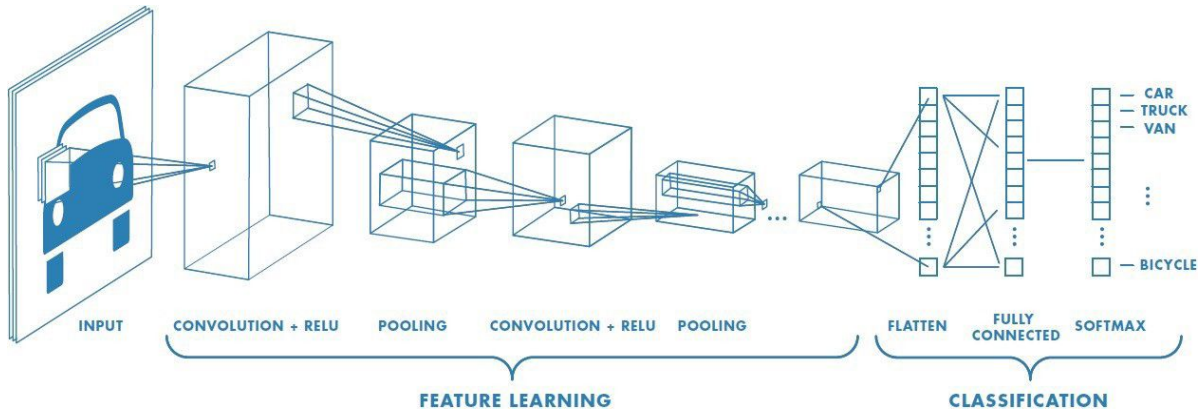


**Figure 5.8:** Illustration of a typical CNN architecture containing convolutional, pooling, and fully-connected layers before the final output layer. Figure taken from reference [143].

map size no longer allows for additional pooling, one or more fully-connected layers are appended before the output layer, as is illustrated in Figure 5.8.

Led primarily by large research teams at the technology giants, improvements upon this standard architecture have since been made. Initially, this process involved the addition of extra convolutional layers to form deeper and deeper networks, as was done by the VGG architecture in 2014 [144]. Another approach was the introduction of the *inception module* within the GoogLeNet [123] architecture, allowing for different feature scales to be considered.

ResNet introduced residual connections in 2016 [145, 146]. By adding connections skipping specific layers, a larger gradient could reach the lower layers of the network, increasing learning. Recently, the inception module and ResNet concepts have been combined [147], and there has been a significant push for efficient rather than just deeper networks [148, 149]. The common repeating layer patterns that form the above networks are shown in Figure 5.9 for reference.

### 5.3.4 Regularisation

A key challenge when training supervised machine learning models is ensuring that they can generalise to new, previously unseen data, not within the training dataset. With networks typically containing millions of trainable parameters, it can become effortless for them to learn specific features and noise of the training dataset, rather than generalisable features. This unwanted learning, called *overfitting*, is ubiquitous when training CNNs.

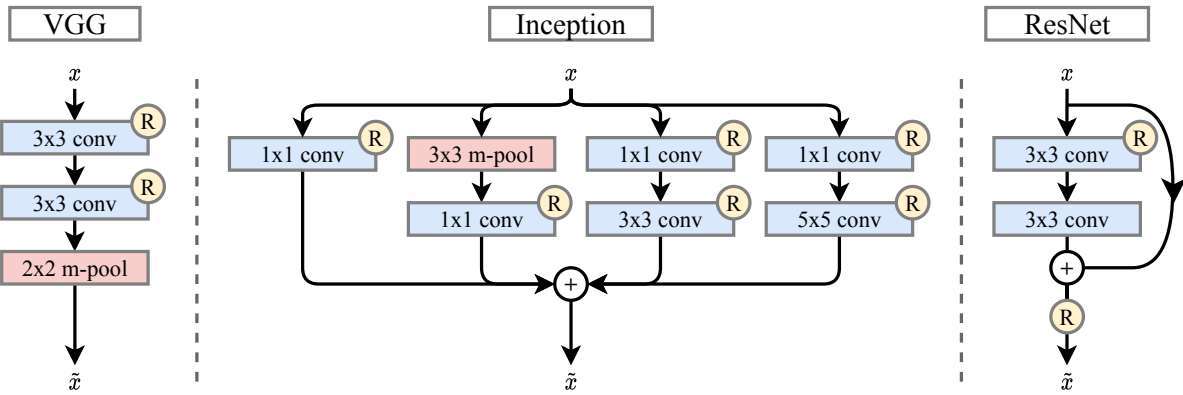


**Figure 5.9:** Common repeating layer *blocks* used within CNN architectures, taking  $x$  as input and producing  $\tilde{x}$  as output through operations whose forward pass is shown with the arrows. The blue and red boxes represent convolutional (conv) and max-pooling (m-pool) layers respectively, with the size of the operation shown. The circular yellow  $R$  indicates the use of the ReLU activation function.

Methods used within this work to prevent overfitting are outlined below, all of which are commonly referred to as *regularisation* techniques.

### Stochastic gradient descent

The gradient descent update equation outlined in equation (5.9) updates the network weights at each training iteration using the gradient calculated over the full training dataset. This procedure is called *batch training*. It is instead much more common to calculate an approximation to the complete gradient at each iteration using a *minibatch* of the full dataset. This is done by considering just a subset of the training data with a size commonly referred to as the *batch size* and typically equal to a power of two for computational reasons.

This modification to standard batch training gradient descent is called *stochastic gradient descent* as it introduces stochasticity to the training process, providing two main advantages. Firstly, the computational speed of each iteration is significantly reduced, and crucially the memory requirements lowered. Secondly, the addition of minibatch specific noise decreases the chance that the minimisation will get stuck in a local minimum suited to overfitting the training dataset.

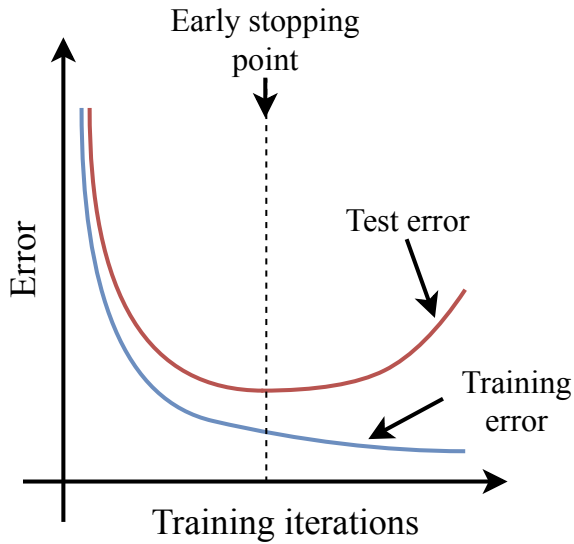


**Figure 5.10:** Illustration of the early stopping procedure. Initially both the training and test error decrease, but, at some point the test error will start to increase due to overfitting, at this point the training is stopped.

### Early stopping

*Early stopping* is another simple regularisation procedure. During training, the training dataset is commonly iterated over multiple times, with each full iteration called an *epoch*. By evaluating the error on an independent *validation* dataset at the end of each epoch, the point at which overfitting starts to occur can be determined, as illustrated in Figure 5.10. At the determined epoch, the training is stopped to return the best possible generalised model. In practice, it is common only to stop training after  $n$  epochs have passed with no validation error improvement.

### Batch normalisation

The training of a neural network is found to work best when the inputs of each neuron are centred on zero with respect to the bias of the neuron. This is because large input values can cause saturation of the activation function and subsequent vanishing of the associated gradient, reducing the ability of the network to learn. To counter this, *batch normalisation* introduces layers that standardise their inputs by using both the mean and variance of each minibatch [150]. This modification not only speeds up training by preventing the vanishing of gradients but also reduces overfitting by again using the stochasticity of the minibatch.

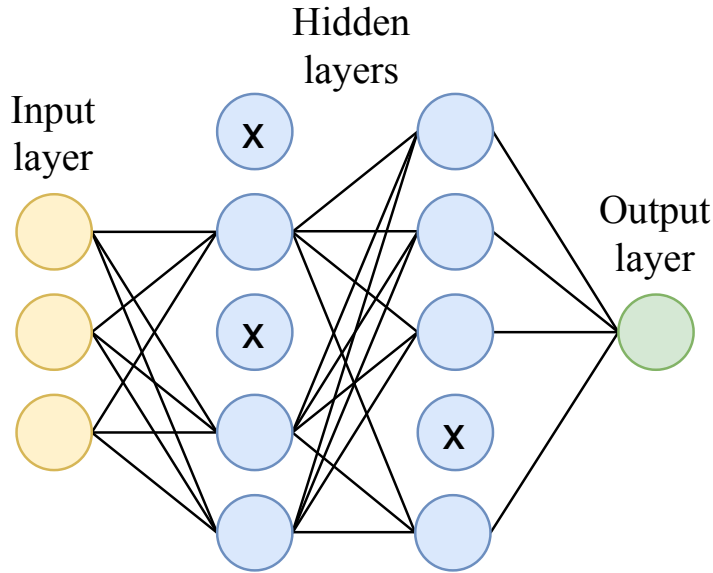


**Figure 5.11:** Example of dropout applied to the network shown in Figure 5.2. Neurons are randomly *dropped out* and not considered for a training step. This reduces the strong connections between neurons that can lead to overfitting.

## Dropout

*Dropout* is another simple technique to reduce overfitting [151]. At each training iteration, each neuron has a probability  $p_d$ , to be *dropped out* and ignored for that iterations calculation. This is illustrated in Figure 5.11. By ignoring a subset of neurons at each iteration, it is difficult for the network to form the particularly strong connections that are usually responsible for overfitting, leading to greater generalisation.

## 5.4 A baseline implementation for CHIPS

The raw output from a water Cherenkov detector, such as those envisioned by the CHIPS concept, is a simple image of each event where two channels of information are known for each PMT: the number of collected photoelectrons, and the associated hit times. Therefore, it is a natural fit to use CNNs primarily developed for image-based computer vision tasks for CHIPS event analysis.

For this purpose, a Python-based software package named *chipsnet* [152] has been built. By using the high-level *Application Programming Interfaces* (APIs) provided by the Tensorflow framework (version 2.3.0) [153], a full pipeline including data preparation,

network training, and performance evaluation has been implemented. In this section, the baseline CNN implementation built into chipsnet is outlined. The specific network implementations described in Section 5.5 share this common baseline with a few specific differences.

### 5.4.1 Baseline inputs

The primary difficulty in the application of CNNs to CHIPS is determining how to map an event captured on a cylindrical surface to a two-dimensional grid. Furthermore, this must be done in such a way as not to distort the underlying Cherenkov emission topology, which could inhibit network learning. As a solution, this work takes inspiration and then builds upon the ideas outlined in reference [154]. Simply put, an event is mapped onto a two-dimensional grid as though it is viewed from its estimated interaction vertex position. The primary motivation behind this is to remove any detector shape effects and to focus on the underlying event topology and Cherenkov emission profiles.

To estimate the interaction vertex position for each event, the top-scoring seed from the seeding procedure introduced in Section 5.2.1 is used. This process, unlike the full likelihood fit, requires no predefined track hypothesis and typically takes under 0.1 seconds per event on a standard batch farm computing node. The seed estimated vertex position resolutions for a sample of expected beam events are shown in Figure 5.12. The  $x$  component (along the direction of the beam) is commonly estimated closer to the downstream wall of the detector than reality, however, as the  $y$  and  $z$  components perpendicular to the beam primarily drive event distortions, the impact on event topology is small.

Using  $\theta$  and  $\phi$  components calculated as viewed from the estimated interaction vertex position facing along the  $x$ -axis (downstream), hit PMTs are mapped onto a  $64 \times 64$  grid. This procedure is used to generate two event *maps*. Firstly, a *hit-charge* map where each grid bin is given by the total collected photoelectrons from all PMTs mapped to that bin. Secondly, a *hit-time* map where each grid bin is given by the first hit time (in nanoseconds) across all PMTs mapped to that bin. Each hit-time map is further corrected so that the first hit time across all bins lies at zero. Note that within this work veto PMTs are ignored for simplicity.

By design, the Hough transform within the seeding procedure uses the estimated interaction vertex position to generate the transform space. Therefore, by re-binning the

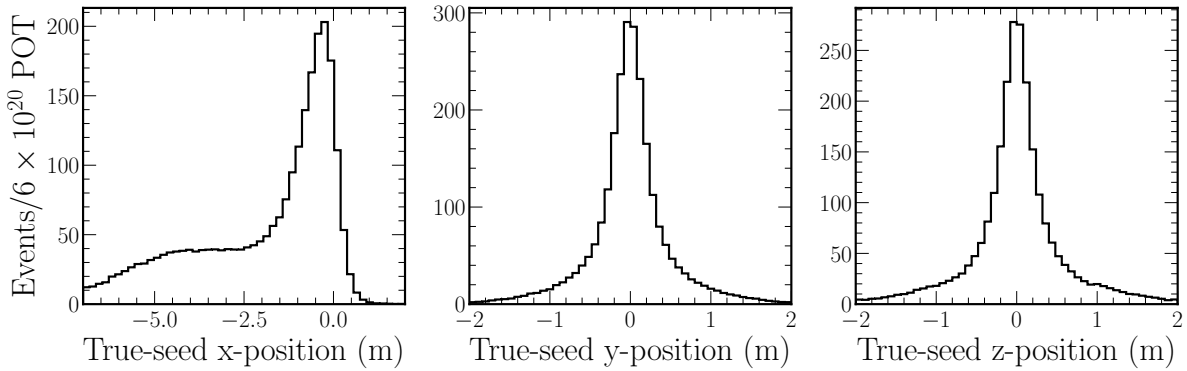


**Figure 5.12:** Seeding estimated interaction vertex position resolutions (true-seed), split by component. The large negative tail for the  $x$  component shows the tendency of the seeding procedure to estimate the  $x$  component closer to the downstream detector wall than reality.

Event map	Cap-point	Capped percentage
hit-charge	25 p.e	0.10%
hit-time	120 ns	0.15%
hough-height	3500 p.e	0.23%

**Table 5.1:** Table showing the input event map cap-points (maximum value of the encoded range) and the associated percentage of bin values that are capped at the maximum 8-bit value of 255 as a consequence. The cap-points are specifically chosen so that the capped percentage is approximately 0.1%, keeping any information loss small.

transform space to a  $64 \times 64$  grid, a third *hough-height* map is generated for each event. This event map aims to provide a complementary but different representation of the event where Cherenkov rings are instead represented as peaks, allowing for additional discriminating features to be learnt.

All three event maps: hit-charge, hit-time, and hough-height are down-sampled (from 32-bit floats) using 8-bit encoding. Encoding not only significantly reduces storage requirements but also dramatically increases the speed with which data can be loaded during training (which turns out to be the primary bottleneck). For each map type, a range over which to encode from zero up to a *cap-point* is chosen to minimise the number of bin values that are capped at the maximum encoded value of 255. Table 5.1 shows the cap-points and the associated percentage of bin values capped for each map type, while Figure 5.13 shows the distribution of bin values for each event map across the encoded range.

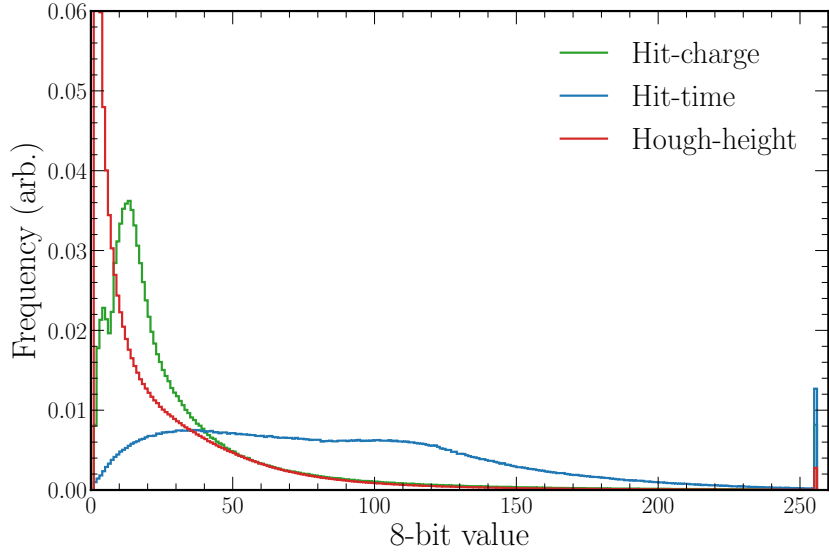


**Figure 5.13:** The distribution of encoded 8-bit values for the hit-charge, hit-time and hough-height event maps. Note the maximum (capped) bin at an 8-bit value of 255.

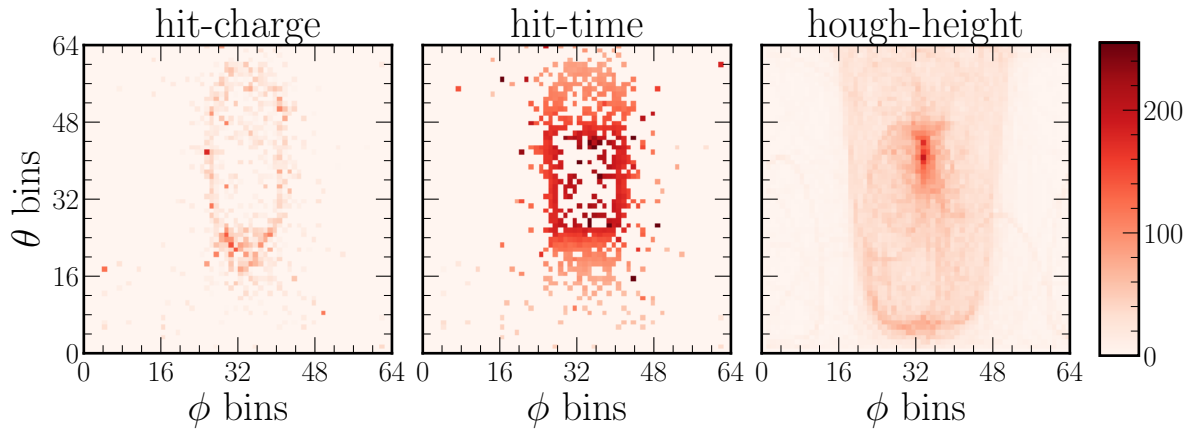


**Figure 5.14:** Three map representation of a CC resonant  $\nu_e$  event. Initiated by a  $\nu_e$  of energy 3.3 GeV the final state particles above the Cherenkov threshold include a  $e^-$  of energy 2.8 GeV and a 0.3 GeV  $\pi^0$ .

Event maps for example events generated using the above procedure are shown in Figure 5.14 for a CC resonant  $\nu_e$  event, in Figure 5.15 for a CC DIS  $\nu_\mu$  event, in Figure 5.16 for a NC DIS event, and in Figure 5.17 for a cosmic muon event.

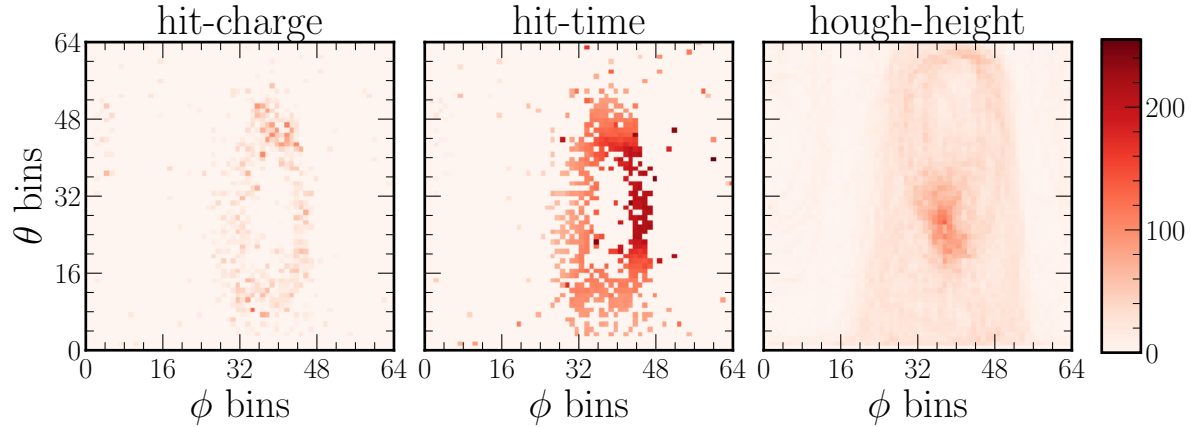


**Figure 5.15:** Three map representation of a CC DIS  $\nu_\mu$  event. Initiated by a  $\nu_\mu$  of energy 3.5 GeV the final state particles above the Cherenkov threshold include a  $\mu^-$  of energy 1.9 GeV, a proton of energy 2.0 GeV, and a 0.2 GeV  $\pi^-$ .

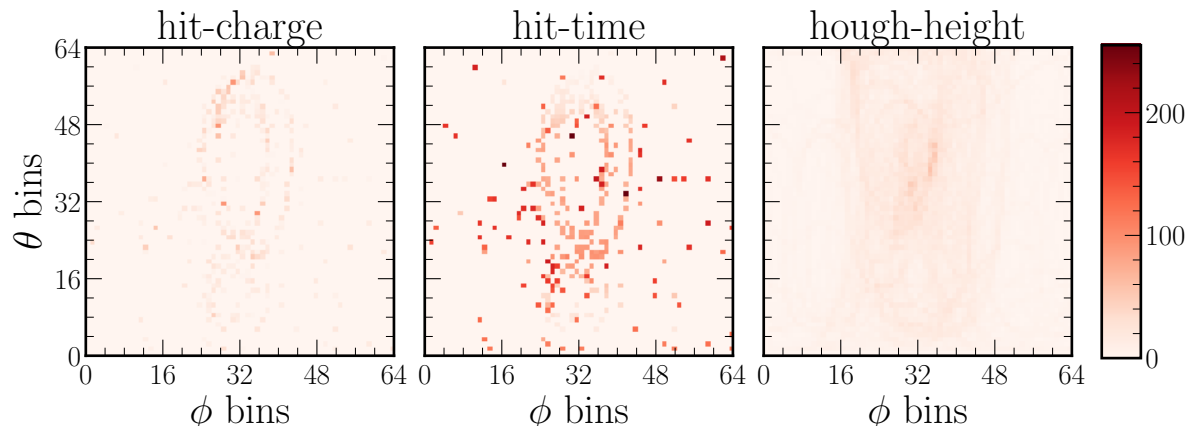


**Figure 5.16:** Three map representation of a NC DIS event. Initiated by a  $\nu_e$  of energy 9.3 GeV the final state particles above the Cherenkov threshold include a proton of energy 2.6 GeV and a 2.5 GeV  $\pi^-$ .

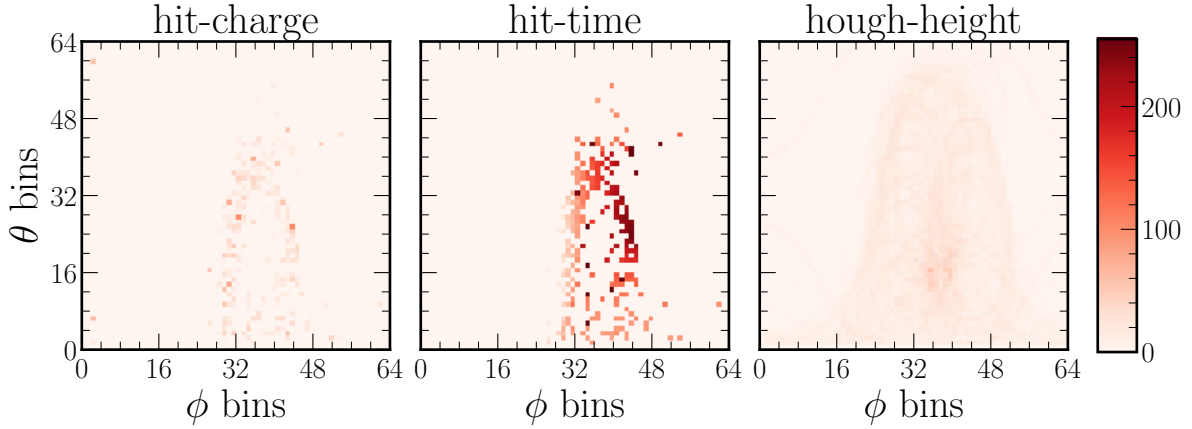


**Figure 5.17:** Three channel representation of a cosmic muon event, containing a  $\mu^-$  of energy 2.9 GeV.

### 5.4.2 Baseline architecture

An illustrative diagram of the baseline chipsnet architecture is shown in Figure 5.18. Based on the VGG network previously mentioned in Section 5.1 and detailed in reference [144] there are a few key differences from the literature defined network:

- Each of the three event maps: hit-charge, hit-time, and hough-height are initially fed into three separate branches. Each branch contains two VGG blocks with two convolutional layers each (four convolutional layers in total). The outputs from each branch are merged using a concatenation layer before being fed to the rest of the network. This configuration allows for event map specific features to be learnt independently before combined features are learnt by the rest of the network.
- Batch normalisation as described in Section 5.3.4 is included before the activation (ReLU) function for every convolutional layer.
- Squeeze-and-excitation units, as detailed in reference [155] are included after the max-pooling operation in all VGG blocks. These units introduce extra parameters to model the interdependencies between output feature maps, allowing the network to learn how to weight each feature map effectively.
- Dropout is included at the end of each VGG block as well as after the final fully-connected layer. Instead of dropping individual kernel elements, the dropout within the VGG blocks drops entire kernels at each training iteration, this is commonly called *two-dimensional spatial dropout*. The dropout after the fully-connected layers is standard, in that it drops out individual fully-connected neurons.

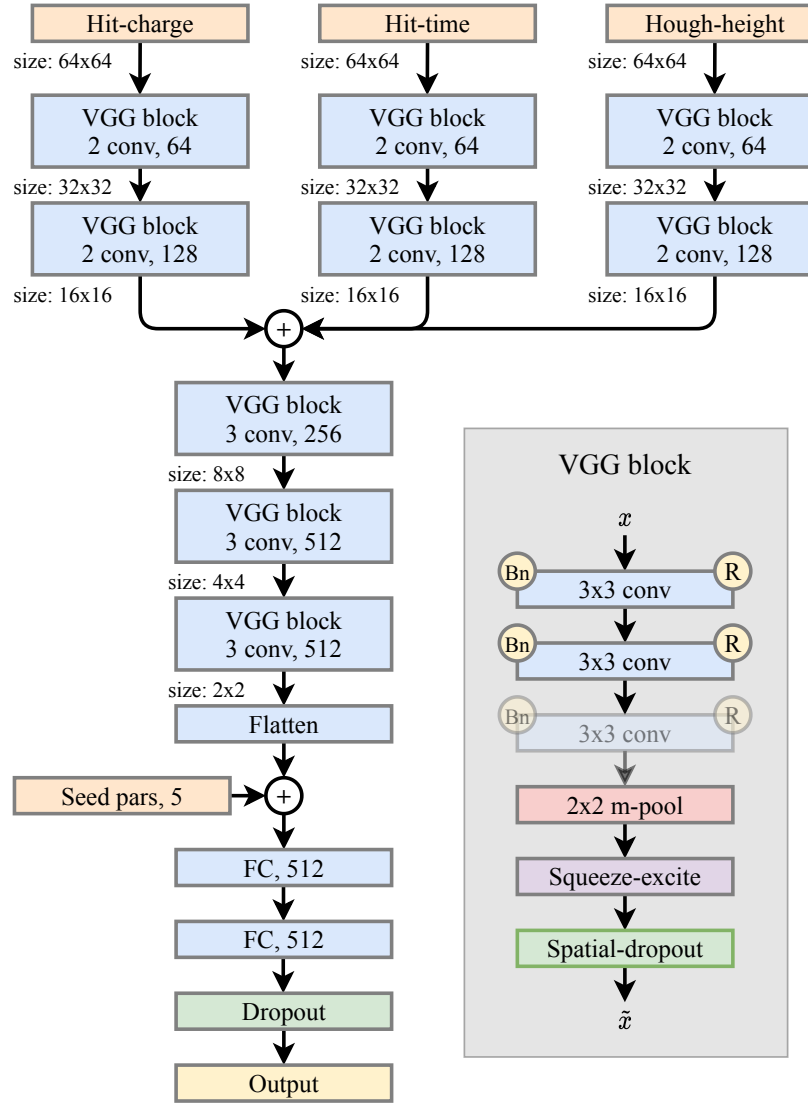


**Figure 5.18:** Illustrative diagram of the baseline chipsnet architecture. The three input event maps are separately passed through two VGG blocks each before their outputs are combined and passed through a further three VGG blocks together. The flattened VGG blocks outputs are then concatenated with five seed parameters (seed pars) and passed through two fully-connected (FC) layers of 512 neurons each before the output layer. Both the number of convolutional units and kernels is shown for each block. The detailed VGG block structure is shown within the grey box. The circular yellow *R* and *Bn* indicate the use of the ReLU activation function and batch normalisation, respectively.

- Five output parameters from the seeding process (seed pars) are concatenated with the flattened layer before the fully-connected layers. Included are the three components of the estimated interaction vertex position ( $s_x, s_y, s_z$ ), and the two components of the estimated track direction ( $s_\theta, s_\phi$ ). These parameters provide the network with spatial context as to where in the detector the input event maps have been generated and the dominant direction of PMT activity.

The chipsnet baseline architecture is implemented using the Keras API built into Tensorflow [156]. Keras allows for predefined common layers such as a two-dimensional convolution or a max-pooling layer to be easily structured into a full network definition.

### 5.4.3 Baseline outputs

Many CNN applications are found to benefit from learning multiple tasks at the same time. This is believed to be the case as training with multiple tasks tends to return a network with an improved generalised representation of the inputs, with features learnt for one task improving the performance of another. Additionally, multiple tasks work to prevent any one output from overfitting. Commonly named *multi-task* learning, this methodology is used extensively in this work.

To train a network with multiple tasks (outputs), a loss function  $E_{tot}$ , must be defined to combine the individual loss functions for each task  $E_i$ . The simplest way to do this is via a linear weighted sum, such that

$$E_{tot} = \sum_{i=1}^{i=N} w_i E_i, \quad (5.20)$$

where  $N$  is the number of tasks and  $w_i$  are the associated weights. In this work this is referred to as the *simple* multi-task loss.

However, the final network performance can strongly depend on the relative weighting between loss functions, especially when the values returned by each differ by many order of magnitude (common when combining regression and classification tasks). Therefore, finding the optimal  $w_i$  weights can be both difficult and time-consuming. Another approach outlined in reference [157] remedies this problem by learning the optimal weighting between loss functions. This is done by introducing an additional trainable

parameter  $\sigma_i$ , for each loss function, such that

$$E_{tot} = \sum_{i=1}^{i=N} \frac{1}{2\sigma_i^2} E_i + \log \sigma_i. \quad (5.21)$$

In this work we refer to this as the *learnt* multi-task loss.

The specific number and nature of outputs for the specific networks are detailed in Section 5.5. Although physically motivated to some degree, the exact set of tasks and the loss combination technique used is mainly driven by extensive trial-and-error. The chipsnet software is specifically designed to enable this process by making it easy to configure the network outputs via a simple configuration file.

#### 5.4.4 Baseline training

All networks are trained on an 18 core CPU (36 thread) machine equipped with four NVIDIA GeForce RTX 2080 graphics processing units (GPUs). The Tensorflow dataset API is used to create an efficient input data pipeline where data is loaded on-the-fly at training time. This procedure ensures all CPU threads are utilised loading, decoding, and preprocessing data for the primary GPU based network calculations before being needed, maximising computational efficiency.

During preprocessing, all 8-bit input event map values are converted to 32-bit float values bounded between zero and one. Furthermore, a random factor scaling is applied to each map bin. Generated from a normal distribution centred on one with a standard deviation of  $\sigma_r$ , by fluctuating the bin values the network is forced to focus less on the absolute bin values and more on the underlying event topology. Not only does this process provide valuable regularisation to reduce overfitting, but also makes the trained networks robust to small changes within the input (explored within Section 6.3).

A minibatch training strategy of minibatch size of  $n_b$ , using the Adam optimiser [158] ( $\beta_1 = 0.9$ ,  $\beta_2 = 0.999$ , and  $\epsilon = 1e - 7$ ) is used. The exact training sample size and composition for each specific network are given in Section 5.5, but for all networks a 95% training to 5% validation data split is employed across the full training sample. Consequently, early stopping is used. The learning rate for each epoch  $\eta_e$ , is set to

decrease throughout training according to

$$\eta_e = \frac{\eta_0}{1 + c_d(e - 1)}, \quad (5.22)$$

where  $\eta_0$  is the initial learning rate,  $e$  is the epoch number (starting at one), and  $c_d$  is the learning rate decay coefficient.

Therefore, when training each network there is a list of tunable *hyperparameters*. All are optimised specifically for each network using the SHERPA hyperparameter tuning framework [159]. To maximise performance, random configurations are tested within SHERPA across a specific range or selection of choices for each hyperparameter, with:

- the **initial learning rate**  $\eta_0$ , in a range from 0.00005 to 0.001;
- the **learning rate decay coefficient**  $c_d$ , in a range from 0.2 to 0.8;
- the **dropout probability**  $p_d$ , in a range from 0.0 to 0.5;
- the **random scaling size**  $\sigma_r$ , in a range from 0.0 to 0.1;
- the **minibatch size**  $n_b$ , choosing from either 32, 64, 128, or 256; and
- the **multi-task loss combination strategy**, choosing from either simple or learnt.

## 5.5 Specific implementations for CHIPS

The specific CNN implementations for cosmic rejection, beam classification, and energy estimation are outlined below. It is important to note that the exact configuration of networks outlined here is the result of extensive testing designed to maximise the selection of a pure and efficient sample of appeared CC  $\nu_e$  beam events whose neutrino energy can also be accurately determined.

As an example of an alternative implementation, if cosmic rejection and beam classification are combined into a single network, both objectives see a reduction in performance. The same is also true if either cosmic rejection or beam classification is combined with neutrino energy estimation. However, specific secondary outputs such as counting the number of primary particles in conjunction with beam classification are seen to improve performance. It is clear, therefore, that the multi-task approach only

works for tasks that require a similar learnt representation of the inputs. Put simply; the tasks must be similar.

### 5.5.1 Cosmic rejection

The cosmic rejection network aims to prevent the vast cosmic muon background from contaminating the final selected sample of beam events. Therefore, the primary task is a simple binary classification between beam and cosmic events. Additionally, training the network to also separate events where the primary charged lepton escapes the detector volume or not, is found to improve cosmic rejection performance. As a large proportion of cosmic muons are relatively high in energy and, therefore, escape the detector in this fashion, there is motivation as to why this additional task is helpful.

The network is trained on a sample of 3.15 million simulated events produced using the detector simulation and event generation methods outlined in Section 3.3. Roughly  $1/3^{rd}$  are  $\nu_\mu$  beam events,  $1/3^{rd}$   $\nu_e$  beam events, and  $1/3^{rd}$  cosmic muon events, the counts of which are shown in Figure 5.19. All beam events (both  $\nu_\mu$  and  $\nu_e$ ) are generated using the expected CHIPS-5  $\nu_\mu$  energy spectrum to closely mimic the dominant  $\nu_\mu$  beam component and appeared  $\nu_e$  signal. Every event in the sample is used for training with no preselection, as this is found to be the best for cosmic rejection performance.

There are two outputs to the cosmic rejection network:

1. **Cosmic score (1 classification neuron):** Returns a score between zero and one corresponding to whether the event is beam or cosmic like. The binary cross-entropy loss function in equation (5.5) is used for training with a simple multi-task weight of 1.
2. **Escapes score (1 classification neuron):** Returns a score between zero and one corresponding to whether the charged lepton in an event is contained or escapes the detector. The binary cross-entropy loss function in equation (5.5) is used for training with a simple multi-task weight of 1. NC beam events without a charged lepton are masked (do not contribute to the loss) during training for this output.

The network is allowed to train for up to 30 epochs using the SHERPA optimised hyperparameters:  $\eta_0 = 0.00005$ ,  $c_d = 0.7$ ,  $p_d = 0.1$ ,  $\sigma_r = 0.02$ , and  $n_b = 128$ , with a simple multi-task loss combination as given in equation (5.20). Typically, only 6 epochs

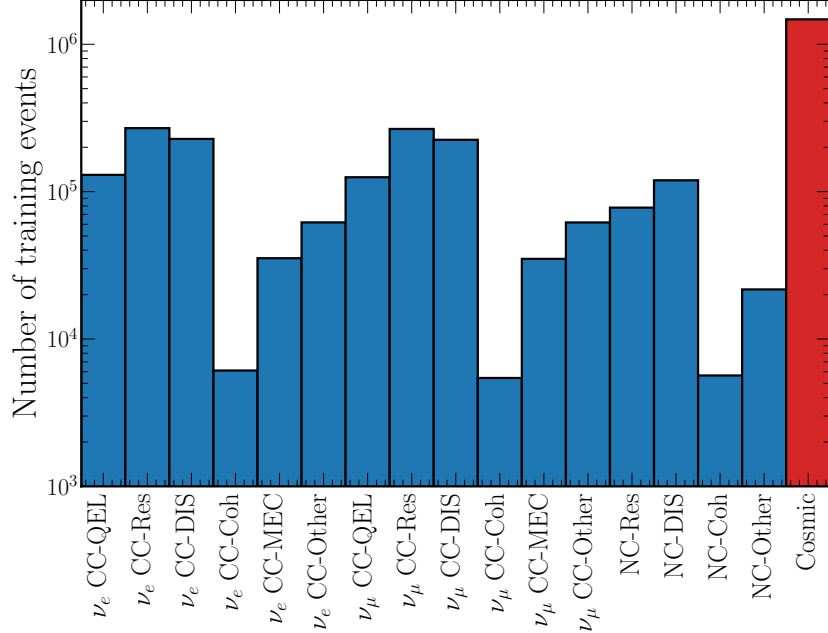


**Figure 5.19:** Number of training events per category for the cosmic rejection network. All beam event interaction types are shown, however, all are classed as beam events (blue) in training against the cosmic events (red).

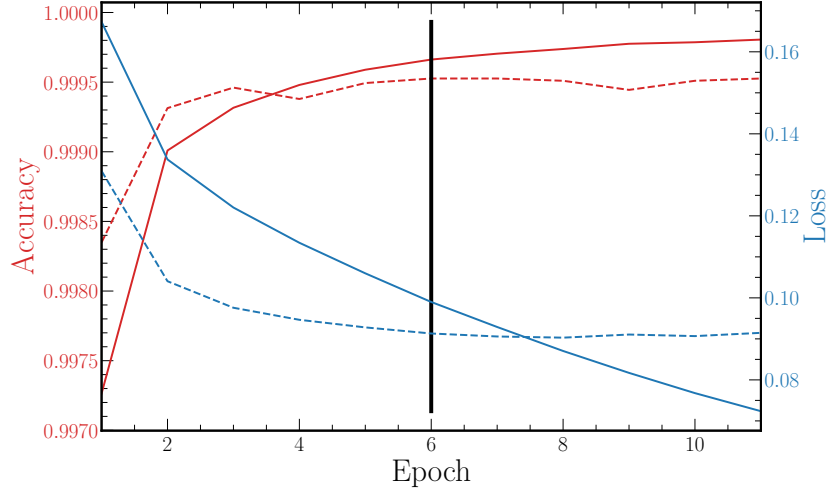


**Figure 5.20:** Total loss and *cosmic score* accuracy for both the training sample (solid) and validation sample (dashed) throughout training for the cosmic rejection network. The final network weights are taken at epoch 6 as shown by the vertical black line.

are required to reach the maximum validation sample *cosmic score* accuracy, with early stopping halting training after 11 epochs (taking 15 hours), as can be seen in Figure 5.20.

### 5.5.2 Beam classification

The beam classification network aims to separate beam events by their neutrino and interaction type to primarily select a pure and efficient sample of appeared  $\nu_e$  events, but also a sample of survived CC  $\nu_\mu$  events. Therefore, the principal task is a categorical classification between CC  $\nu_e$ , CC  $\nu_\mu$ , and NC events. No attempt is made to separate the appeared CC  $\nu_e$  and intrinsic beam CC  $\nu_e$  components as they are impossible to tell apart, except for their distribution in neutrino energy.

Similar to the implementation used by DUNE [128], alongside the core classification additional classification and particle counting tasks outlined below are included to improve performance. Note that the particle counting tasks are not used in this work for anything but increasing the primary classification performance. Future work, however, could exploit any ability to separate exclusive final states, deduced from these particle counts, to reduce both energy resolution and systematic errors. As an example of a method already in use, NOvA use their ability to accurately determine the hadronic energy of an event to split their CC  $\nu_\mu$  sample into populations of different energy resolution. Each population can then be treated separately in the analysis before being combined, increasing overall performance [160].

The network is trained on a sample of 1.67 million simulated events produced using the detector simulation and event generation methods outlined in Section 3.3. Roughly half are  $\nu_\mu$  beam events, with the other half being  $\nu_e$  beam events, as shown in Figure 5.21. All events (both  $\nu_\mu$  and  $\nu_e$ ) are generated using the expected CHIPS-5  $\nu_\mu$  energy spectrum to closely mimic the dominant  $\nu_\mu$  beam component and appeared  $\nu_e$  signal. All events are used for training with no preselection as this is found to be the best for beam classification performance, especially NC rejection.

There are nine outputs to the beam classification network:

1. **Combined category (3 classification neurons):** Returns a classification probability score between zero and one for each of CC  $\nu_e$ , CC  $\nu_\mu$ , and NC (summing to one). The categorical cross-entropy loss function in equation (5.7) is used for training with a simple multi-task weight of 1.
2. **CC category (6 classification neurons):** Returns a classification probability score between zero and one for each of CC-QEL, CC-Res, CC-DIS, CC-Coh, CC-MEC, and CC-other (summing to one). The categorical cross-entropy loss function

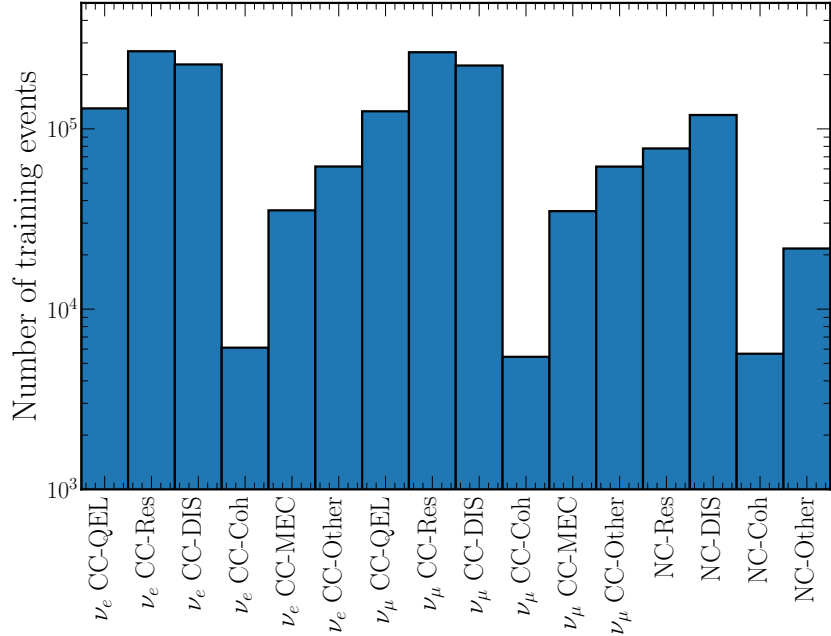


**Figure 5.21:** Number of training events per category for the beam classification network. All beam event interaction types are shown.

in equation (5.7) is used for training with a simple multi-task weight of 1. NC events are masked (do not contribute to the loss) during training for this output.

3. **NC category (4 classification neurons):** Returns a classification probability score between zero and one for each of NC-Res, NC-DIS, NC-Coh, and NC-other (summing to one). The categorical cross-entropy loss function in equation (5.7) is used for training with a simple multi-task weight of 1. CC events are masked (do not contribute to the loss) during training for this output.
4. **Electron count (4 classification neurons):** Returns a classification probability score between zero and one for each of 0, 1, 2, and 3+ electrons in the final state (summing to one). The categorical cross-entropy loss function in equation (5.7) is used for training with a simple multi-task weight of 1.
5. **Muon count (4 classification neurons):** Returns a classification probability score between zero and one for each of 0, 1, 2, and 3+ muons in the final state (summing to one). The categorical cross-entropy loss function in equation (5.7) is used for training with a simple multi-task weight of 1.
6. **Proton count (4 classification neurons):** Returns a classification probability score between zero and one for each of 0, 1, 2, and 3+ protons in the final state

(summing to one). The categorical cross-entropy loss function in equation (5.7) is used for training with a simple multi-task weight of 1.

7.  **$\pi^\pm$  count (4 classification neurons):** Returns a classification probability score between zero and one for each of 0, 1, 2, and 3+ charged pions in the final state (summing to one). The categorical cross-entropy loss function in equation (5.7) is used for training with a simple multi-task weight of 1.
8.  **$\pi^0$  count (4 classification neurons):** Returns a classification probability score between zero and one for each of 0, 1, 2, and 3+ neutral pions in the final state (summing to one). The categorical cross-entropy loss function in equation (5.7) is used for training with a simple multi-task weight of 1.
9. **Photon count (4 classification neurons):** Returns a classification probability score between zero and one for each of 0, 1, 2, and 3+ photons in the final state (summing to one). The categorical cross-entropy loss function in equation (5.7) is used for training with a simple multi-task weight of 1.

The network is allowed to train for up to 30 epochs using the SHERPA optimised hyperparameters:  $\eta_0 = 0.0002$ ,  $c_d = 0.5$ ,  $p_d = 0.1$ ,  $\sigma_r = 0.02$ , and  $n_b = 128$ , with a simple multi-task loss combination as given in equation (5.20). Typically, only 7 epochs are required to reach the maximum validation sample *combined category* accuracy, with early stopping halting training after 12 epochs (taking 15 hours), as can be seen in Figure 5.22.

### 5.5.3 Energy estimation

Accurate neutrino energy estimation is accomplished using multiple networks trained on separate samples of  $\nu_e$  and  $\nu_\mu$  events across multiple CC interaction types. It is found that separation such as this results in greater performance compared to if a single energy estimation network or even separate  $\nu_e$  and  $\nu_\mu$  networks are trained. This is expected as a single set of network weights is unlikely to be able to capture the specific topological features that contribute to the energy for all types of event.

Alongside the primary neutrino energy regression task, additionally learning the primary charged lepton energy and the interaction vertex position and time are found to improve performance. Although this improvement is relatively small for neutrino energy estimation, it dramatically improves primary charged lepton energy estimation when compared to being predicted alone. With two energy tasks, the network is encouraged

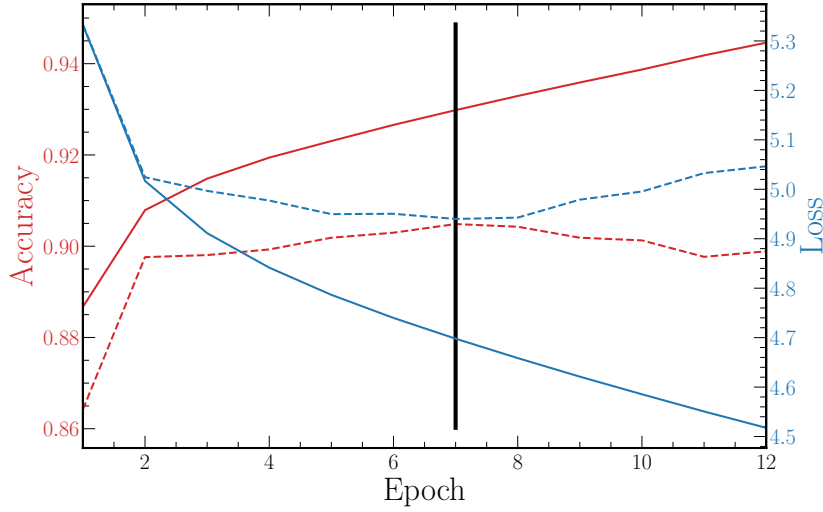


**Figure 5.22:** Total loss and *combined category* accuracy for both the training sample (solid) and validation sample (dashed) throughout training for the beam classification network. The final network weights are taken at epoch 7 as shown by the vertical black line.

to learn how the primary charged lepton and neutrino energies are related. As the interaction vertex position within the detector and hence distance from the instrumented wall can impact the number of deposited photoelectrons, there is motivation as to why this additional task is also helpful.

Separate networks are trained for each of CC-QEL (and CC-MEC), CC-Res, and CC-DIS for both  $\nu_e$  and  $\nu_\mu$  events (6 in total) using 250000 corresponding simulated events each. All events (both  $\nu_\mu$  and  $\nu_e$ ) are produced using the detector simulation and event generation methods outlined in Section 3.3. The expected CHIPS-5  $\nu_\mu$  energy spectrum is used to generate all events to closely mimic the dominant  $\nu_\mu$  beam component and appeared  $\nu_e$  signal. Only events for which the primary charged lepton is fully contained within the detector volume are used for training, with no additional preselection applied. Note that CC-QEL and CC-MEC energy estimation is combined into a single network as both have incredibly similar final state topologies (a single charged lepton).

There are six outputs to each of the energy estimation networks:

1. **Neutrino energy (1 regression neuron):** Returns the estimated neutrino energy. The mean-squared error loss function in equation (5.8) is used for training.

2. **Charged lepton energy (1 regression neuron):** Returns the estimated primary charged lepton energy. The mean-squared error loss function in equation (5.8) is used for training.
3. **Interaction vertex x-position (1 regression neuron):** Returns the estimated interaction vertex x-position. The mean-squared error loss function in equation (5.8) is used for training.
4. **Interaction vertex y-position (1 regression neuron):** Returns the estimated interaction vertex y-position. The mean-squared error loss function in equation (5.8) is used for training.
5. **Interaction vertex z-position (1 regression neuron):** Returns the estimated interaction vertex z-position. The mean-squared error loss function in equation (5.8) is used for training.
6. **Interaction time (1 regression neuron):** Returns the estimated interaction time relative to the first PMT hit for each event. The mean-squared error loss function in equation (5.8) is used for training.

Each network is allowed to train for up to 30 epochs using the SHERPA optimised hyperparameters:  $\eta_0 = 0.0002$ ,  $c_d = 0.5$ ,  $p_d = 0.1$ ,  $\sigma_r = 0.0$ , and  $n_b = 128$ , with a learnt multi-task loss combination as given in equation (5.21). Early stopping typically halts training after approximately 20 epochs (taking 2 hours). An example of how an energy estimation networks training typically proceeds is given in Figure 5.23.

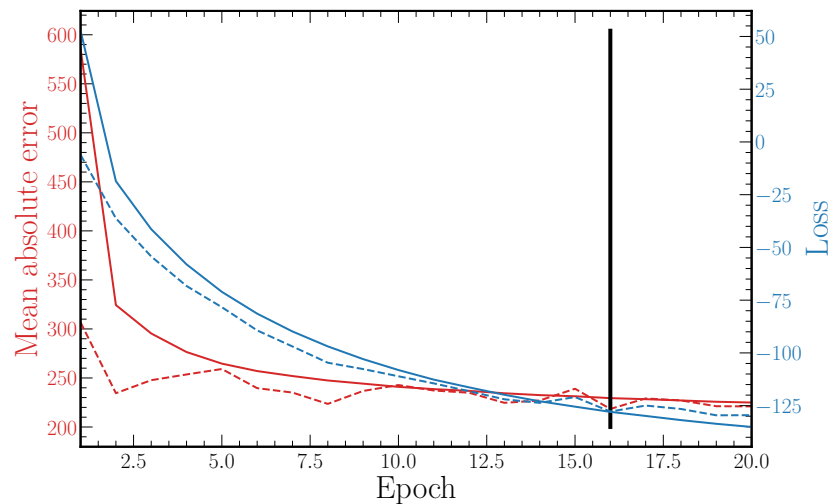


**Figure 5.23:** Total loss and *neutrino energy* mean absolute error for both the training dataset (solid) and validation dataset (dashed) throughout training for the energy estimation network trained on CC-QEL and CC-MEC  $\nu_e$  events. The final network weights are taken at epoch 16 as shown by the vertical black line.

# Chapter 6

## Network evaluation

This chapter provides a comprehensive evaluation of how the new CNN approach behaves. Four categories of understanding are explored (each a section of this chapter):

1. determining the beam selection and energy estimation performance;
2. explaining the inner workings of the trained networks;
3. studying how robust the network outputs are to changes in the input; and
4. exploring alternative implementations to see which factors drive performance.

Beforehand, a hugely impactful advantage of the CNN approach must be highlighted. Although the time taken to train the CNNs in this work is approximately two days, once trained the time required to calculate all network outputs (inference time) for a single event is on the order of 2 ms. When combined with event seeding and event map generation, the total time taken to fully reconstruct and classify a raw event is less than 0.1 seconds. Compared to the  $\sim$ 15 minutes required for each event using the standard reconstruction and classification methods (with multiple hypotheses), the difference is stark.

Armed with this incredible speed, the time taken to fully process a large dataset containing millions of events becomes a matter of hours, compared to the many weeks typically required. This change has far-reaching implications for how physics analysis is conducted. By removing the processing bottleneck, larger datasets can be used without worry, new techniques can be tested quickly, and overall analysis turnover increased.

## 6.1 Performance

Here the performance of the CNN approach is presented and compared to that achieved by the standard CHIPS methods as well as comparable experiments. Primarily this focuses on the principal aim of selecting an efficient and pure appeared CC  $\nu_e$  signal sample with accurate neutrino energy estimation. However, the survived CC  $\nu_\mu$  selection is also presented for completeness.

### 6.1.1 Evaluation sample and preselection

An independent sample of events is used to evaluate the combined performance of the trained CNNs. The evaluation sample consists of 400000 beam and 350000 cosmic muon events produced in the same way as the training and validation events, using the detector simulation and event generation methods outlined in Section 3.3. The beam events include the expected  $\nu_\mu$ ,  $\bar{\nu}_\mu$ ,  $\nu_e$  and  $\bar{\nu}_e$  components as well as events generated to mimic the appeared (sometimes referred to as *App*)  $\nu_e$  component. Only the neutrino mode (forward horn current) of NuMI beam operation is considered here. During the evaluation, the intrinsic neutrino and antineutrino components of the beam are considered the same for simplicity.

All evaluation events are weighted to match the expected spectrum at the CHIPS-5 detector using the unoscillated flux, cross-sections, and oscillation probabilities (including the MSW effect). Additional weighting also scales the sample to match data taking in the NuMI beam for a single year, corresponding to  $6 \times 10^{20}$  protons on target (POT). Cosmic muon events are weighted according to the 11.8 kHz expected CHIPS-5 rate outlined in Section 3.3.3. The final weighted spectrum of events is shown in Figure 6.1 with the combination of underlying beam neutrino interaction types shown in Figure 6.2.

Separate from the CNN driven work, a simple preselection is applied to all evaluation sample events. Designed to reject cosmic and NC events while keeping the efficiency of CC beam events high, the preselection consists of four simple cuts, shown in Figure 6.3. Firstly, the total number of collected photoelectrons (charge) across all PMTs in the event must be greater than 250. Secondly, the maximum Hough transform space height must be greater than 250 photoelectrons. Thirdly, the seeding procedure  $\cos(\theta)$  direction must be between  $\pm 0.7$ . Finally, the seeding procedure  $\phi$  direction must be between  $\pm 1.1$

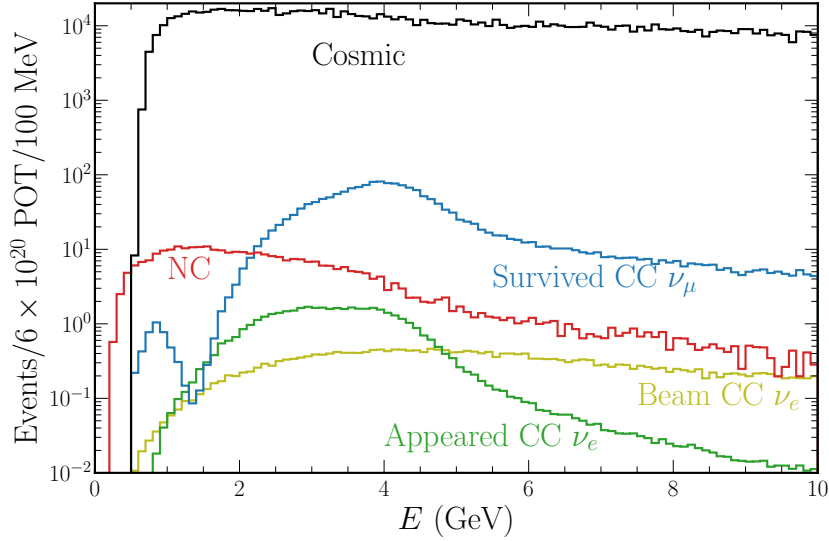


**Figure 6.1:** Weighted spectrum of events contained within the evaluation sample. The weighting is designed to mimic the expected event spectrum of the CHIPS-5 detector. Beam events are weighted by combining the expected unoscillated flux with cross-sections and standard oscillation probabilities, while cosmic events are weighted using the expected cosmic rate. Shown in blue, green, and olive are the surviving CC  $\nu_\mu$ , appearing CC  $\nu_e$ , and intrinsic beam CC  $\nu_e$  spectra respectively, binned in terms of their neutrino energy. Shown in red is the NC event spectra, binned in terms of the energy of the hadronic component (excluding the outgoing neutrino energy) to represent more accurately the energy visible to the detector. Finally, shown in black is the cosmic muon event spectra binned in terms of the muon energy.

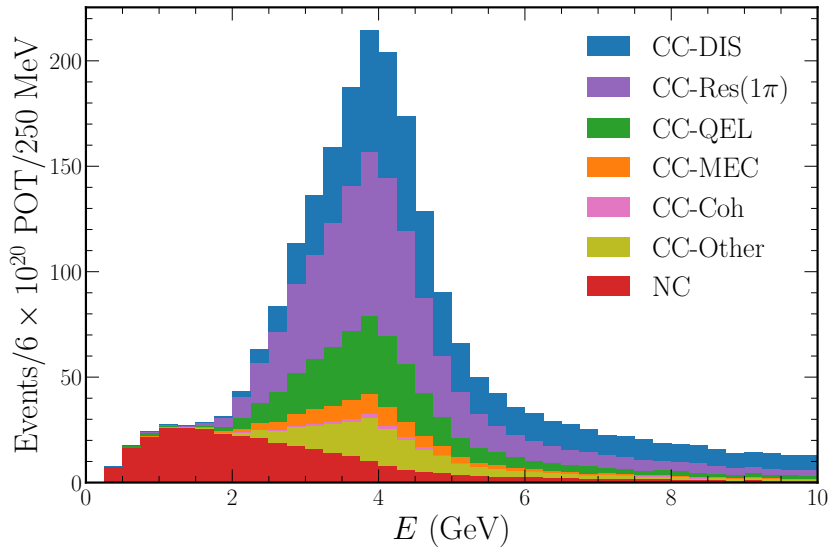


**Figure 6.2:** Weighted spectrum of  $\nu_\mu$  and  $\nu_e$  beam events contained within the evaluation sample separated by interaction type. CC events are binned in terms of neutrino energy while NC events are binned in terms of the hadronic component energy.

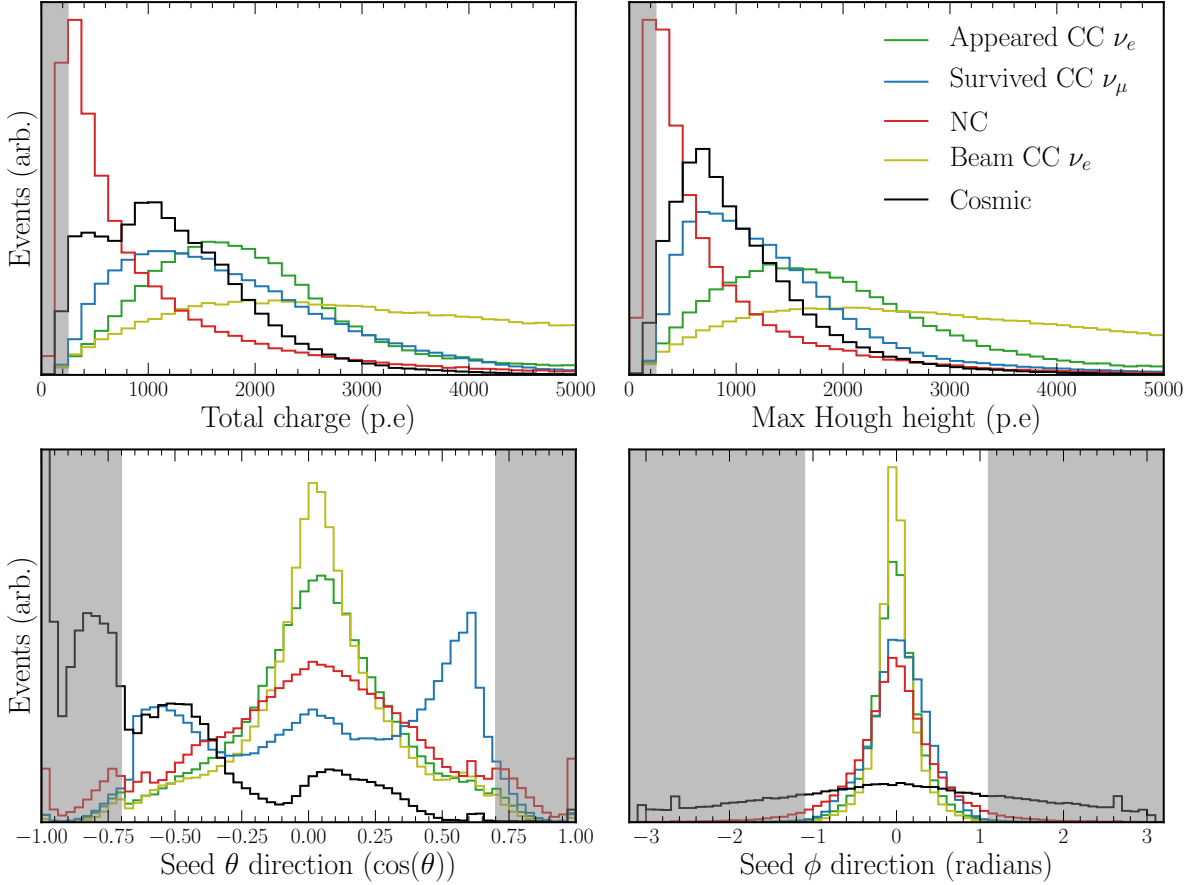


**Figure 6.3:** Plots showing the four preselection cuts and how they affect the different event categories. The grey regions indicate rejected events.

radians. The first two cuts reject low energy events which are usually NC in nature, while the last two reject events whose activity is not along the beamline, typically cosmic.

### 6.1.2 Cosmic rejection and containment

#### Cosmic score

The *cosmic score* output from the trained cosmic rejection network shows an excellent separation between beam (output close to zero) and cosmic (output close to one) events, as can be seen in Figure 6.4. Notably, the vast majority of beam events are associated with a score incredibly close to zero as is more clearly shown in Figure 6.5. Given this fact, a tight *cosmic score* cut of below 0.0001 is chosen by inspection to select beam like events. Out of the total 350000 cosmic events in the evaluation sample, all are rejected by this cut alongside preselection.

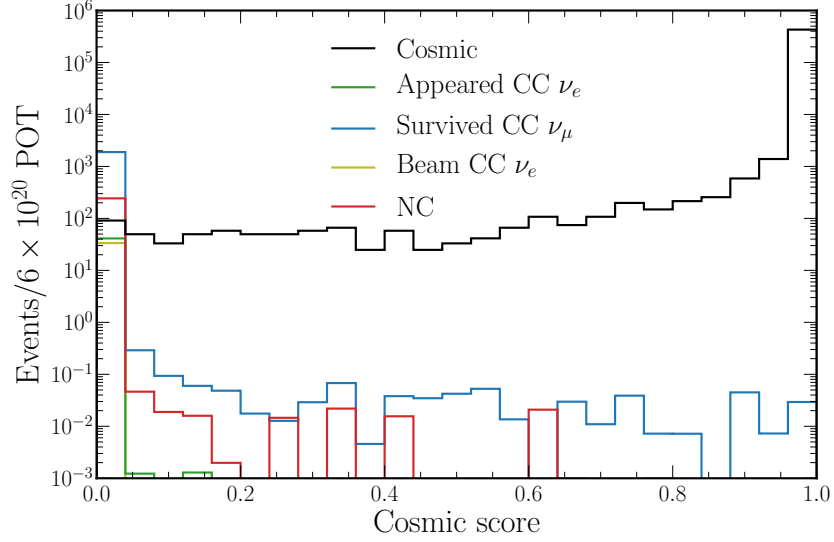


**Figure 6.4:** Distribution of *cosmic score* output values from the trained cosmic rejection network for the different event categories. A score close to one signifies a cosmic like event, while a score close to zero corresponds to a beam like event. Only preselected events are shown to better highlight the events this output aims to classify.

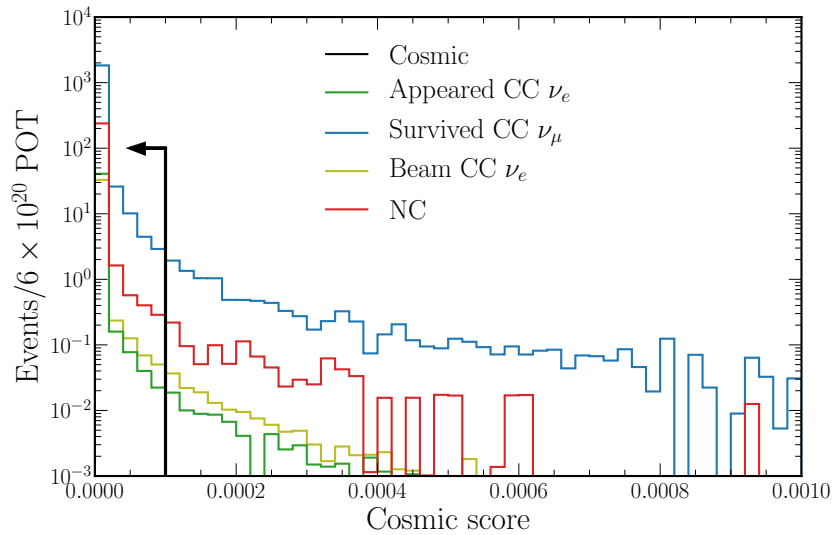


**Figure 6.5:** Distribution of *cosmic score* output values from the trained cosmic rejection network close to zero for the different event categories. The cosmic rejection cut value at 0.0001 is shown with the arrow indicating selected events. No cosmic events are within the shown range due to the statistical limitations of the evaluation sample.

## Escapes score

It is crucial for accurate neutrino energy estimation that the activity of an event is fully contained within the volume of the detector. If charged event particles instead leave the detector and emit Cherenkov radiation not captured by PMTs, it can be incredibly difficult to estimate the resulting missing energy and hence neutrino energy. Within the CHIPS-5 detector, this is particularly important for long track CC  $\nu_\mu$  events for which only 44% of the primary charged muons are fully contained within the detector volume.

Therefore, the second output from the cosmic rejection network, *escapes score* is also used to select events. Although this output only considers the primary charged lepton, instead of all event particles, it still acts as a reasonable proxy for event containment. The distribution of *escapes score* output values for each event category is shown in Figure 6.6.

An *escapes score* value below 0.5 is chosen to select events for which the primary charged lepton is fully contained within the detector. With this selection, 97% and 96% of CC  $\nu_\mu$  events for which the primary charged lepton is contained within or escapes the detector respectively are classified correctly. For the selected CC  $\nu_\mu$  events this corresponds to a 95% purity. As expected, the vast majority of CC  $\nu_e$  and NC events are selected.

For comparison with other experiments, the escapes cut effectively works as a quasi fiducial volume cut, for an energy-dependent region near the downstream wall of the detector. Fiducial volume cuts are common in HEP experiments to remove events whose activity is close to the detector walls and, therefore, can not be reconstructed well. Future work should explore how a fully implemented fiducial cut using the reconstructed interaction vertex position, impacts performance.

## Combined rejection

The total number of expected events per year that pass each successive cut (including preselection) for each event category is shown in Table 6.1. Both CC  $\nu_e$  categories are selected with an efficiency greater than 90%, while CC  $\nu_\mu$  events are reduced to a 40% efficiency, mainly by the *escapes score* cut, to ensure they are fully contained. Furthermore, NC events are found to be primarily rejected by the preselection, while cosmic events are heavily rejected by both the preselection and *cosmic score* cuts.

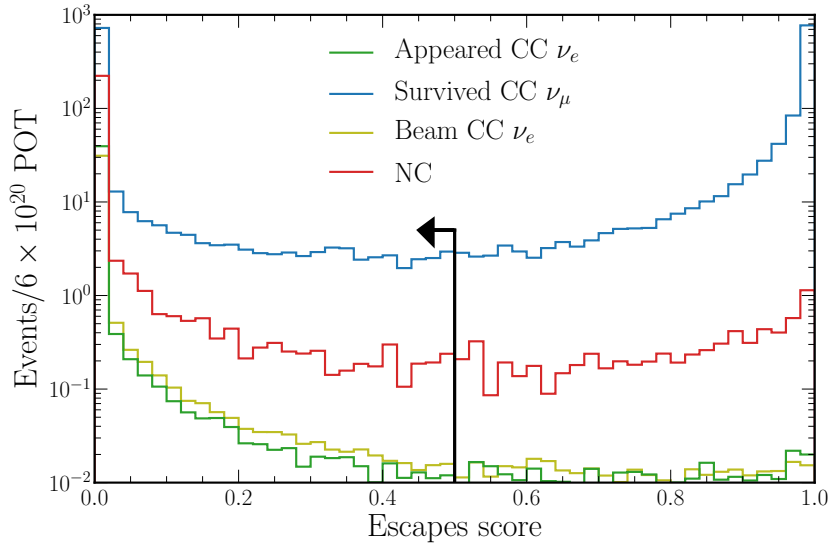


**Figure 6.6:** Distribution of *escapes score* output values from the trained cosmic rejection network for the different event categories. A score close to one signifies an escaped primary charged lepton like event, while a score close to zero corresponds to a contained primary charged lepton like event. The containment cut value at 0.5 is shown with the arrow indicating the events that are selected.

	App CC $\nu_e$	CC $\nu_\mu$	Beam CC $\nu_e$	NC	Cosmic
Total events	44.2	2045.9	35.1	348.7	1211000
+ preselection	41.2	1889.5	33.5	239.6	249260
+ cosmic cut	41.1	1874.4	33.4	238.0	0.13
+ escapes cut	40.8	818.0	33.0	231.0	0.02
Efficiency	$92.4 \pm 0.4\%$	$40.0 \pm 0.2\%$	$94.2 \pm 0.4\%$	$66.3 \pm 0.7\%$	$\sim 1.5 \times 10^{-8}$

**Table 6.1:** The total number of expected (weighted) events and the number that pass successive selection cuts for the different event categories. The preselection, *cosmic score* cut, and *escapes score* cut numbers are shown. The selection efficiency after all cuts have been applied is also shown for each event category.

When compared to the approximately 2.1 million expected cosmic events per year, the zero selected out of 350000 evaluation events is not statistically significant. However, the generation of a sufficiently sized cosmic evaluation sample is deemed infeasible due to the vast computational resources required.

Therefore, to more accurately gauge the number of cosmic events likely to be classified as beam events, we consider the more statistically significant number that passes a loose *cosmic score* cut below a value of 0.9. In this case, when combined with the preselection and *escapes score* cut, 38 out of 350000 evaluation sample cosmic events are selected, which when weighted gives 317 events per year. Assuming a flat distribution of events between a *cosmic score* of 0.0 and 0.9, and using the actual 0.0001 cut value, 0.035 events are expected to be selected. This number corresponds to an excellent cosmic muon rejection factor of  $\sim 1.5 \times 10^{-8}$ .

Additionally, of the 317 events under a *cosmic score* value of 0.9, 167 would be selected as CC  $\nu_\mu$  and zero as CC  $\nu_e$  by the beam classification detailed in Section 6.1.3. Therefore, even if a tiny number of cosmic events are selected, they would likely be classified as CC  $\nu_\mu$  events, not contaminating the principal CC  $\nu_e$  selection. In summary, the expected cosmic muon contamination of both beam selections is expected to be negligible and ignored for the rest of this performance evaluation.

### 6.1.3 Beam classification

The output values from each of the *combined category* neurons of the trained beam classification network give the probability score that an event belongs to the corresponding category. As the neuron output scores collectively sum to one, the highest-scoring neuron can be used to classify events as either CC  $\nu_e$ , CC  $\nu_\mu$ , or NC in nature. Figure 6.7 shows the resulting classification matrix using this approach.

To access the beam classification performance more rigorously, a selection score for each of the output categories, found by maximising a figure-of-merit (FOM), is instead calculated. All events with a score above this optimised value are then deemed signal. To minimise the expected measurement statistical error, the value of efficiency  $\times$  purity (proportional to  $s/\sqrt{s+b}$ ) is optimised as the FOM [161]. Below, the results for both appeared CC  $\nu_e$  and survived CC  $\nu_\mu$  selections using this methodology are presented.

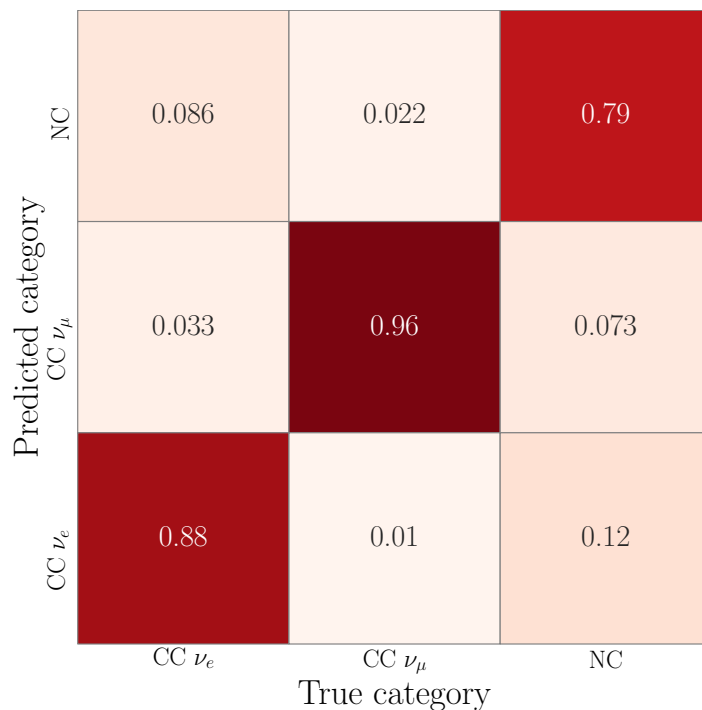


**Figure 6.7:** Classification matrix for the *combined category* output of the trained beam classification network. Events are simply classified using the categorical score for which they have the highest value. The numbers shown are the fraction of true category events classified into each of the three possible categories.

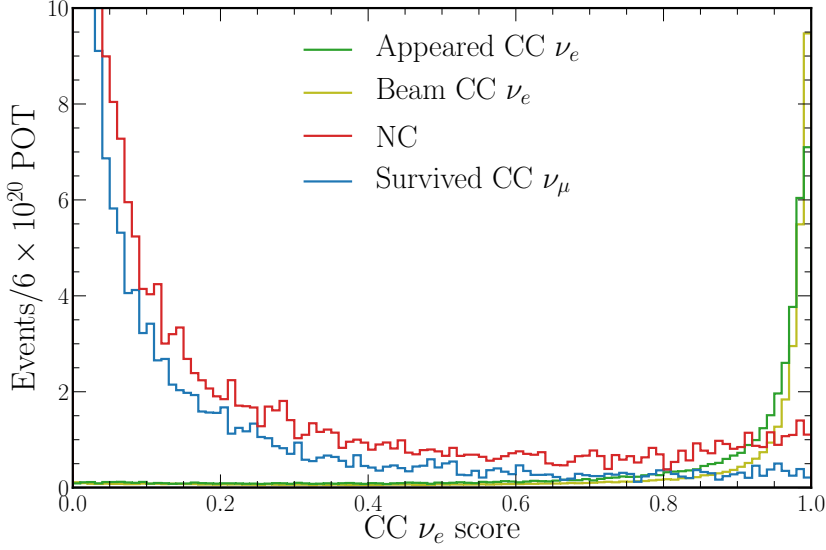


**Figure 6.8:** Distribution of *combined category* CC  $\nu_e$  scores from the trained beam classification network for the different event categories. A score close to one signifies a CC  $\nu_e$  like event. The y-axis has been truncated so that the CC  $\nu_\mu$  and NC components are not fully visible to better show the distribution of signal CC  $\nu_e$  events.

### CC $\nu_e$ selection

The distribution of CC  $\nu_e$  scores for the different event categories are shown in Figure 6.8. A strong separation between appeared CC  $\nu_e$  signal and both CC  $\nu_\mu$  and NC background events is achieved. As no attempt is made to separate the appeared CC  $\nu_e$  signal component from the intrinsic beam CC  $\nu_e$  background, both are clustered with scores close to one as expected.

The efficiency, purity, and their product (the FOM) for CC  $\nu_e$  events (both appeared and beam) as a function of selecting events above a certain CC  $\nu_e$  score are shown in Figure 6.9. Efficiency  $\times$  purity is optimised by selecting events with a CC  $\nu_e$  score above 0.8, achieving a value of 0.519. Note that efficiency  $\times$  purity is optimised considering both appeared and beam CC  $\nu_e$  components as signal due to their indistinguishable nature.

The corresponding number and efficiency of selected events for each event category, as well as the appeared signal CC  $\nu_e$  purity, are shown in Table 6.2. The final FOM selected signal purity of  $38.3 \pm 0.5\%$  may appear low, but this is mainly due to the indistinguishable intrinsic beam CC  $\nu_e$  contamination. When both CC  $\nu_e$  components are considered signal, the selection purity becomes  $71.0 \pm 0.6\%$ .

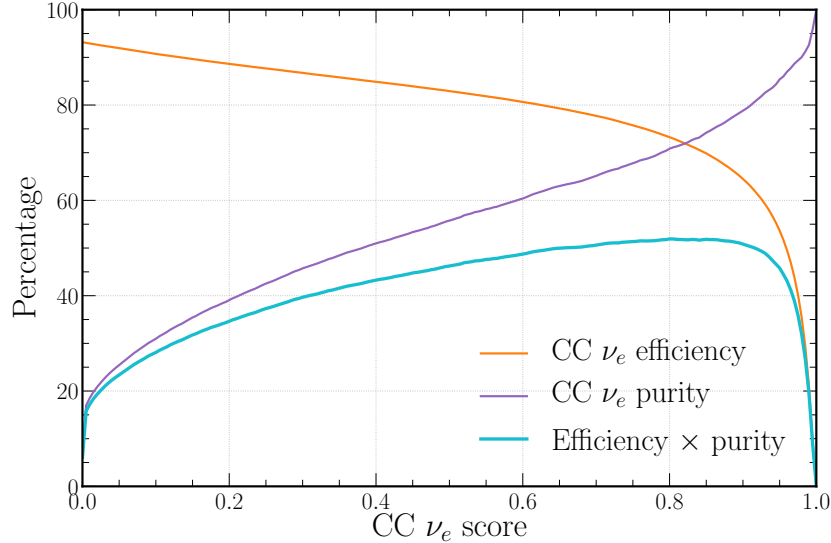


**Figure 6.9:** CC  $\nu_e$  efficiency, purity, and efficiency  $\times$  purity curves for different values of CC  $\nu_e$  score selection.

	CC $\nu_e$ sig	Beam CC $\nu_\mu$ bkg	CC $\nu_e$ bkg	NC bkg	Sig Purity
Cuts Num	40.8	818.0	33.0	231.0	$3.6 \pm 0.1\%$
FOM Num	31.3	6.1	26.7	17.6	$38.3 \pm 0.5\%$
FOM Eff	$70.9 \pm 0.4\%$	$0.3 \pm 0.02\%$	$76.3 \pm 0.3\%$	$5.1 \pm 0.2\%$	-

**Table 6.2:** Table showing CC  $\nu_e$  selected event numbers and corresponding efficiencies for the various event categories as well as the associated signal purity. Shown are the numbers for both the post preselection, *cosmic score* cut, and *escapes score* cut numbers (Cuts) in addition to the numbers after the efficiency  $\times$  purity (FOM) optimised selection for which the efficiency is shown.

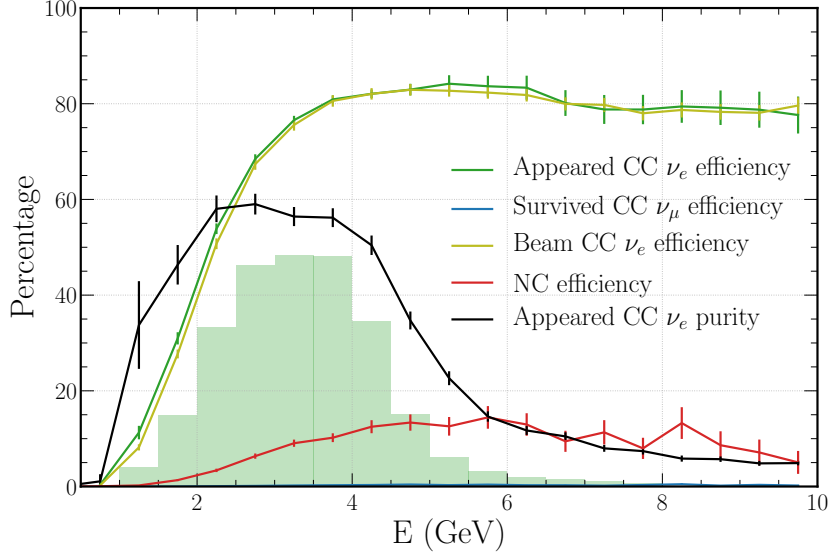


**Figure 6.10:** Efficiency of the CC  $\nu_e$  selection for the different event categories as well as appeared CC  $\nu_e$  purity as a function of energy. All CC categories are shown in terms of neutrino energy, while NC events are shown in terms of the hadronic component energy. The survived CC  $\nu_\mu$  efficiency is so low it is barely visible near zero. For reference, the true appeared CC  $\nu_e$  neutrino energy distribution is shown in the green.

The efficiency  $\times$  purity optimised CC  $\nu_e$  selection efficiency as a function of energy for the different event categories is shown in Figure 6.10. From low neutrino energies, both CC  $\nu_e$  category selection efficiencies rise steeply to a plateau of approximately 80% beginning at 4 GeV. This is expected as low energy CC  $\nu_e$  events have less well-defined electron Cherenkov rings, leading to their rejection. Due to the abundance of selected intrinsic beam CC  $\nu_e$  events at higher energies, the appeared CC  $\nu_e$  purity is observed to peak at approximately 2.5 GeV (reasonably close to the oscillation maximum) before declining. The NC efficiency is seen to slowly increase, approaching 15% for hadronic component energies above 5 GeV; this is likely due to misidentification of high energy pions or protons as electrons. Importantly, however, within the key signal region from 2 to 4 GeV, NC selection efficiency remains low.

The best way to understand the relative performance of the CNN CC  $\nu_e$  classification is by comparison with the standard event selection presented in Section 5.2.2. The distribution of output scores from both simple neural networks used in the standard selection are shown in Figure 6.11. By optimising the selection values for both networks, 0.91 and 0.78 respectively, to maximise efficiency  $\times$  purity, the standard CC  $\nu_e$  selected

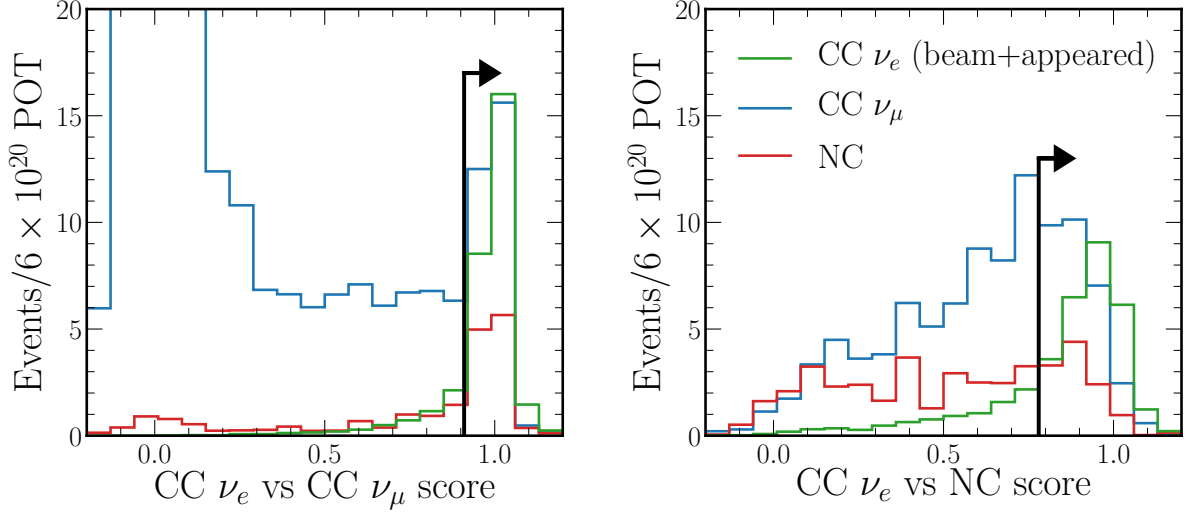


**Figure 6.11:** Distributions of CC  $\nu_e$  vs CC  $\nu_\mu$  (left) and CC  $\nu_e$  vs NC (right) output scores from the two standard event selection neural networks for the different event categories. A score close to one signifies a CC  $\nu_e$  like event in both cases. Each plot shows events which have passed both the preselection and the optimised cut from the other network. This is done to better show the events which the network in question rejects. Selected CC  $\nu_e$  events are shown by the arrows. The y-axis for the CC  $\nu_e$  vs CC  $\nu_\mu$  distributions has been truncated so that the CC  $\nu_\mu$  component is not fully visible to better show the distribution of signal CC  $\nu_e$  events. Due to the long reconstruction time required, a smaller evaluation sample is used here.

sample is found. All events that pass the preselection, not just those shown in Figure 6.11 are used in this optimisation.

A maximum efficiency  $\times$  purity of 0.132 is achieved; only 25% the value reached by the CNN approach. Both the combined appeared and beam CC  $\nu_e$  efficiency of 34% compared to 71% and purity of 39% compared to 71% are considerably lower than that provided by the new CNN classification.

Furthermore, the new signal efficiency of 71% compares well to the 62% and 64% achieved by the NOvA and T2K CC  $\nu_e$  selections, respectively. However, purity is significantly lower at 38% compared to the 78% and 80% reached by NOvA and T2K [53, 162]. A large proportion of this difference can be explained by the lower neutrino energies at which these experiments operate. Not only does this increase the proportion of easy to identify CC-QEL events, but also lowers the indistinguishable intrinsic beam CC  $\nu_e$  contamination.

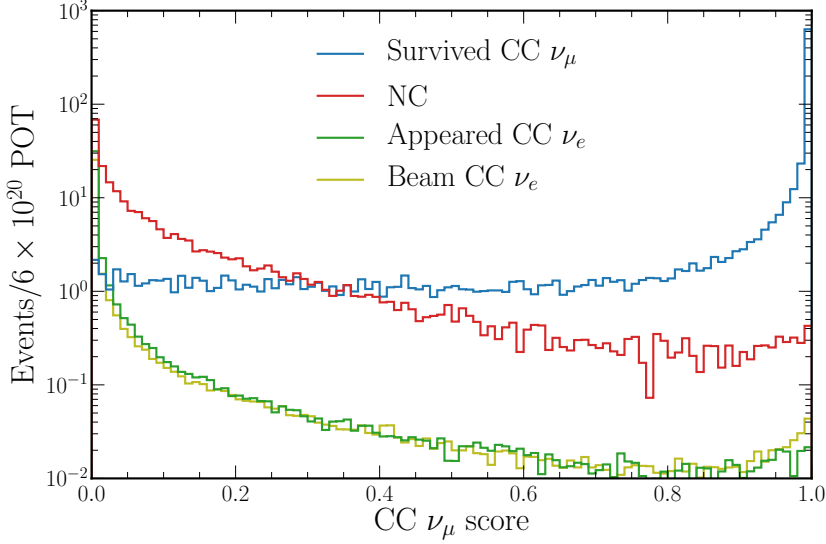


**Figure 6.12:** Distribution of *combined category* CC  $\nu_\mu$  scores from the trained beam classification network for the different event categories. A score close to one signifies a CC  $\nu_\mu$  like event.

### CC $\nu_\mu$ selection

The distribution of CC  $\nu_\mu$  scores for the different event categories are shown in Figure 6.12. Excellent separation between appeared CC  $\nu_\mu$  signal and both CC  $\nu_e$  components and NC background is achieved. For high CC  $\nu_\mu$  scores (close to one) the difference between signal and background event counts is approximately three orders of magnitude.

The efficiency, purity, and their product (the FOM) for CC  $\nu_\mu$  events as a function of selecting events above a particular CC  $\nu_\mu$  score are shown in Figure 6.13. Efficiency  $\times$  purity is optimised by selecting events with a CC  $\nu_\mu$  score above 0.315, achieving a value of 0.365. The corresponding number and efficiency of selected events for each event category, as well as the signal purity, are shown in Table 6.3.

The signal efficiency of 38% compares well to the 31% and 36% achieved by the NOvA and T2K CC  $\nu_\mu$  selections, respectively [53, 162]. This is also the case for the signal purity of 96% compared to the 98.6% and 94% purities of the NOvA and T2K selections. Although the final signal efficiency is low, this is desirable to ensure events are fully contained for energy estimation. When considering just those CC  $\nu_\mu$  events for which the primary charged muon is truthfully contained, an 87% selection efficiency is achieved.

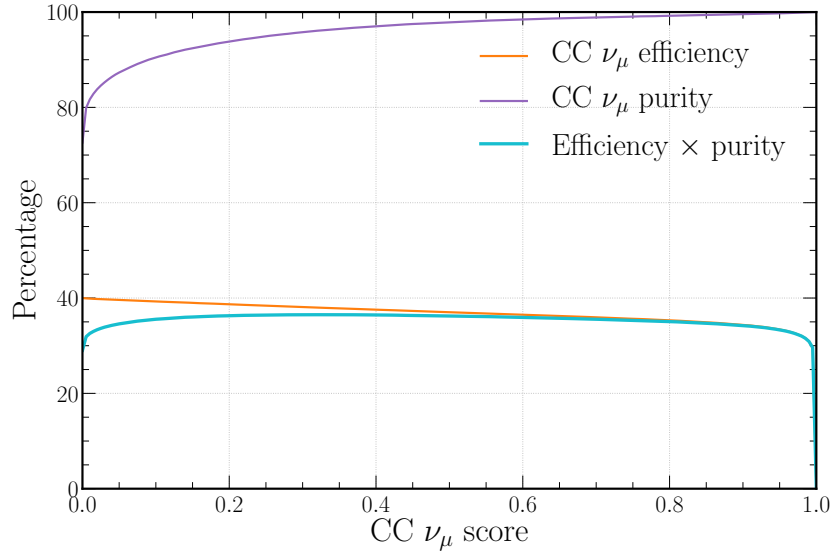


**Figure 6.13:** CC  $\nu_\mu$  efficiency, purity, and efficiency  $\times$  purity curves for different values of CC  $\nu_\mu$  score selection.

	CC $\nu_\mu$ sig	App CC $\nu_e$ bkg	Beam CC $\nu_e$ bkg	NC bkg	Sig Purity
Cuts Num	818.0	40.8	33.0	231.0	$72.9 \pm 0.5\%$
FOM Num	777.9	1.32	1.37	29.3	$96.1 \pm 0.6\%$
FOM Eff	$38.0 \pm 0.2\%$	$3.0 \pm 0.1\%$	$4.0 \pm 0.1\%$	$8.4 \pm 0.2\%$	-

**Table 6.3:** Table showing CC  $\nu_\mu$  selected event numbers and corresponding efficiencies for the various event categories as well as the associated signal purity. Shown are the numbers for both the post preselection, *cosmic score* cut, and *escapes score* cut numbers (Cuts) in addition to the numbers after the efficiency  $\times$  purity (FOM) optimised selection for which the efficiency is shown.

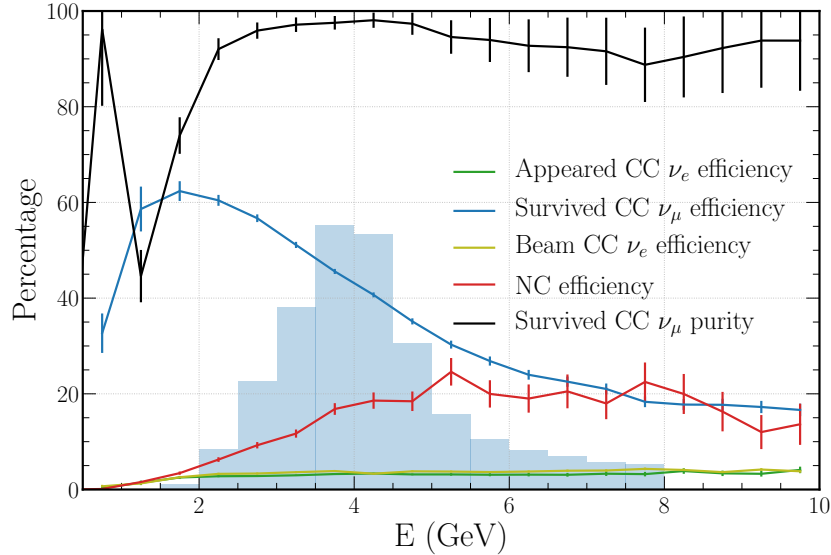


**Figure 6.14:** Efficiency of the CC  $\nu_\mu$  selection for the different event categories as well as survived CC  $\nu_\mu$  purity as a function of neutrino energy. All CC categories are shown in terms of neutrino energy, while NC events are shown in terms of the hadronic component energy. For reference, the true survived CC  $\nu_\mu$  neutrino energy distribution is shown in the blue.

The efficiency  $\times$  purity optimised CC  $\nu_\mu$  selection efficiency as a function of energy for the different event categories is shown in Figure 6.14. Survived CC  $\nu_\mu$  selection efficiency peaks at just below 2 GeV before slowly declining, this is explained by higher energy events being less likely to have their primary charged muon fully contained within the detector. Of interest is the expected dip in the otherwise very high ( $> 90\%$ ) CC  $\nu_\mu$  purity at approximately 1.5 GeV, corresponding to the oscillation maximum (shown in Figure 2.10). As in the CC  $\nu_e$  selection case, the NC efficiency is seen to rise with energy, again likely due to misidentification of energetic protons and pions.

### Interaction type classification

Using the *CC category* output of the trained beam classification network, the CC interaction type (used for energy estimation in Section 6.1.4) for both CC  $\nu_e$  and CC  $\nu_\mu$  selected events can be determined. As in the *combined category* output case, the highest-scoring neuron can be used for classification, resulting in the matrix shown in Figure 6.15. Note that only events which are selected by either the CC  $\nu_e$  or CC  $\nu_\mu$  selection are shown.

		CC-Other	0.019	0.012	0.012	0.034	0.0036	0.16	0.016
		CC-MEC	0	0	0	0	0	0	0
Predicted category	CC-Coh	5e-06	0.00032	0.0004	0.054	0	3.9e-06	0.00042	
	CC-DIS	0.017	0.17	0.8	0.29	0.00016	0.31	0.64	
	CC-Res	0.27	0.63	0.17	0.51	0.19	0.36	0.24	
	CC-QEL	0.69	0.19	0.014	0.11	0.81	0.18	0.096	
	CC-QEL	0.69	0.19	0.014	0.11	0.81	0.18	0.096	True category
	CC-Res	0.27	0.63	0.17	0.51	0.19	0.36	0.24	
	CC-DIS	0.017	0.17	0.8	0.29	0.00016	0.31	0.64	
	CC-Coh	5e-06	0.00032	0.0004	0.054	0	3.9e-06	0.00042	
	CC-MEC	0	0	0	0	0	0	0	
	CC-Other	0.019	0.012	0.012	0.034	0.0036	0.16	0.016	
	NC								

**Figure 6.15:** Classification matrix for the *CC category* output of the trained beam classification network. Shown are events that have either been selected by the CC  $\nu_e$  or CC  $\nu_\mu$  selection. Events are simply classified using the categorical score for which they have the highest value. The numbers shown are the fraction of true category events classified into each of the six possible categories.

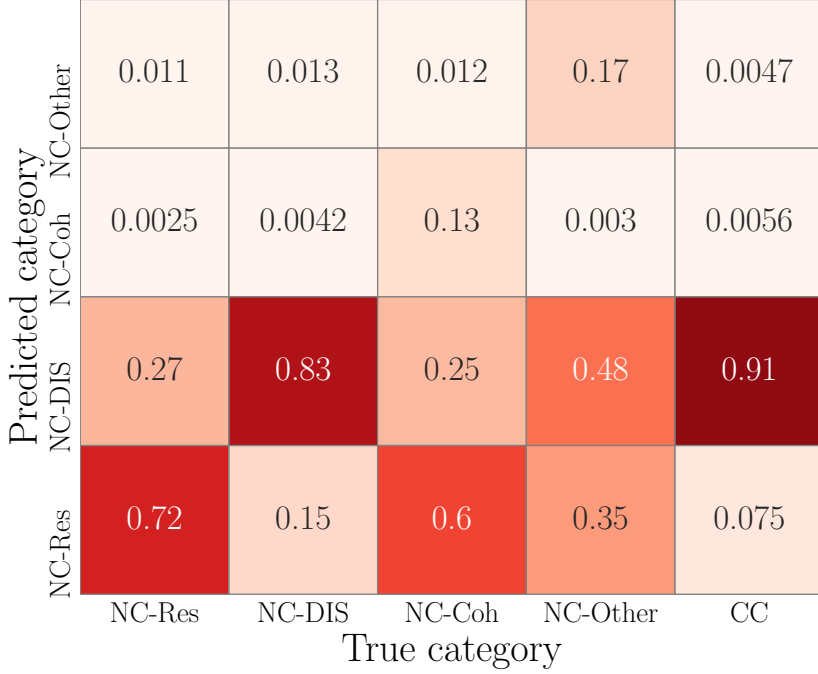


**Figure 6.16:** Classification matrix for the *NC category* output of the trained beam classification network. Events are simply classified using the categorical score for which they have the highest value. The numbers shown are the fraction of true category events classified into each of the four possible categories.

Reasonable classification accuracy greater than 60% is achieved across the three dominant interaction types, CC-QEL, CC-Res, and CC-DIS. The less common CC-Coh and CC-MEC types are found to be commonly misidentified as CC-Res and CC-QEL respectively, likely due to the imbalanced training dataset and their corresponding topological similarities. Background NC events which pass either CC  $\nu_e$  or CC  $\nu_\mu$  selection (commonly high in energy) are found to be typically classified as CC-DIS; this is expected as they commonly contain multiple energetic particles in the final state.

For completeness, the *NC category* classification matrix is shown in Figure 6.16 for events that are neither classified as CC  $\nu_e$  or CC  $\nu_\mu$ . As in the CC case, the dominant interaction types NC-Res and NC-DIS are classified well, with NC-Coh events typically being classified as NC-Res. Of the CC events that are not selected, the vast majority are classified as NC-DIS events. Similarly to before, this is likely due to multiple energetic particles in the final state, for which the beam classification network determined no clear charged lepton.

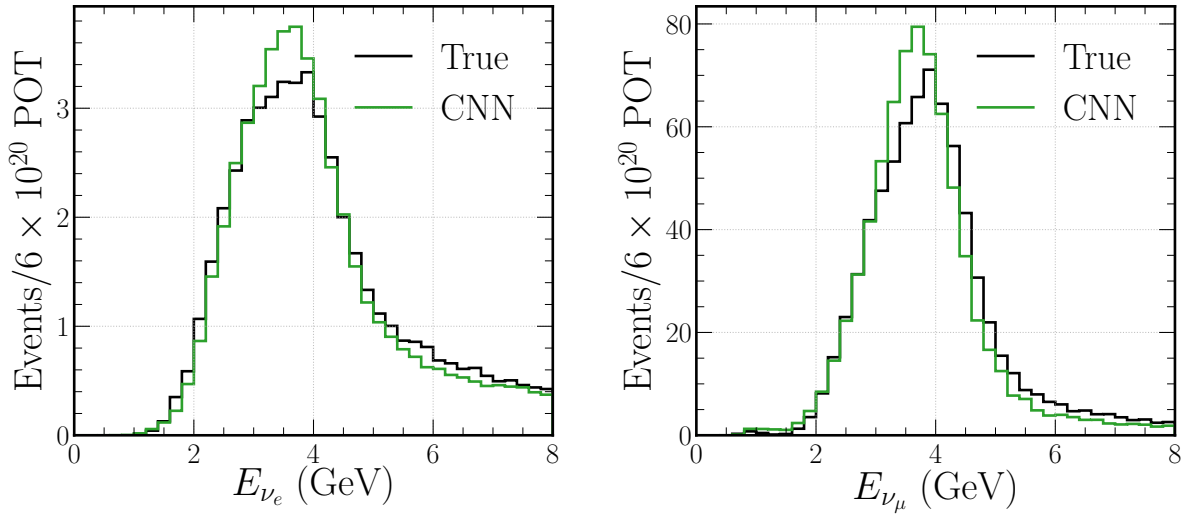


**Figure 6.17:** Distributions of true and CNN estimated neutrino energy for CC  $\nu_e$  (left) and CC  $\nu_\mu$  (right) beam events. Only true CC  $\nu_e$  and CC  $\nu_\mu$  events that are also selected by the CC  $\nu_e$  and CC  $\nu_\mu$  selections respectively are shown.

#### 6.1.4 Energy and vertex estimation

By using the CC interaction type classification just presented, the differences between CC interaction types can be exploited to improve neutrino energy, charged lepton energy, and interaction vertex position and time estimation. For events classified as either CC  $\nu_e$  or CC  $\nu_\mu$  with an associated *CC category* interaction type, the corresponding bespoke trained network outlined in Section 5.5.3 is used for estimation.

Only three networks for each neutrino type are trained, one for each of the dominant interaction types CC-QEL (and CC-MEC), CC-Res, and CC-DIS. For events not classified by the *CC category* output as one of these categories, such as CC-Coh or CC-Other, the CC-Res network is used as it is the most topologically similar interaction type.

#### Energy estimation

The distributions of CNN estimated (*neutrino energy* output) and true  $\nu_e$  and  $\nu_\mu$  neutrino energies for true CC  $\nu_e$  and CC  $\nu_\mu$  events respectively that are also selected by their corresponding CC selection are shown in Figure 6.17. The CNN estimated distributions match the truth well across the full range of neutrino energies expected within CHIPS-5, except in the peak regions where the truth distribution shape is not fully captured.

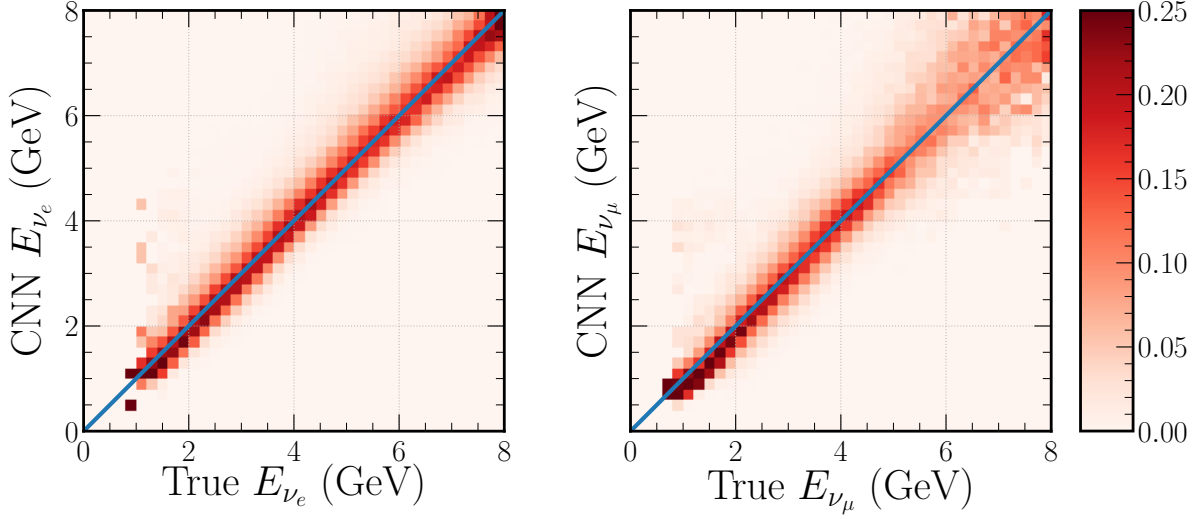


**Figure 6.18:** Probability of CNN estimated neutrino energy given a true neutrino energy for CC  $\nu_e$  (left) and CC  $\nu_\mu$  (right) beam events, with their equality shown in blue. Only true CC  $\nu_e$  and CC  $\nu_\mu$  events that are also selected by the CC  $\nu_e$  and CC  $\nu_\mu$  selections respectively are shown.

As the training samples contain a spectrum of events typical of the beam, it is important to check that the CNN neutrino energy estimation is not simply predicting an energy close to the expected peak beam energy. The probability of a CNN estimated neutrino energy given a true neutrino energy is shown in Figure 6.18 for both CC  $\nu_e$  and CC  $\nu_\mu$  events. CNN estimated energy is found to be roughly equivalent to true energy across the full range of expected CHIPS-5 beam energies, proving the desired response.

To fully understand CNN energy estimation performance, histograms of ratios of differences between CNN estimated (reco) and true neutrino energy to true neutrino energy for both CC  $\nu_e$  and CC  $\nu_\mu$  beam events are shown in Figure 6.19. Distributions are shown for both *all* selected events and just the true *signal* component within the corresponding beam selection. Similar distributions splitting the *signal* component by interaction type are shown in Figure 6.20. Furthermore, a summary of the neutrino energy resolutions achieved for both CC  $\nu_e$  and CC  $\nu_\mu$  events is shown in Table 6.4.

The tail of negative values for the *all* selected CC  $\nu_e$  distribution in Figure 6.19 indicates that wrongly classified CC  $\nu_e$  events, mainly NC in nature, are typically estimated with a neutrino energy lower than the actual value. This is expected given the missing energy of the final state neutrino. Additionally, the interaction type resolutions follow the expected pattern, with the simple to reconstruct single charged lepton QEL

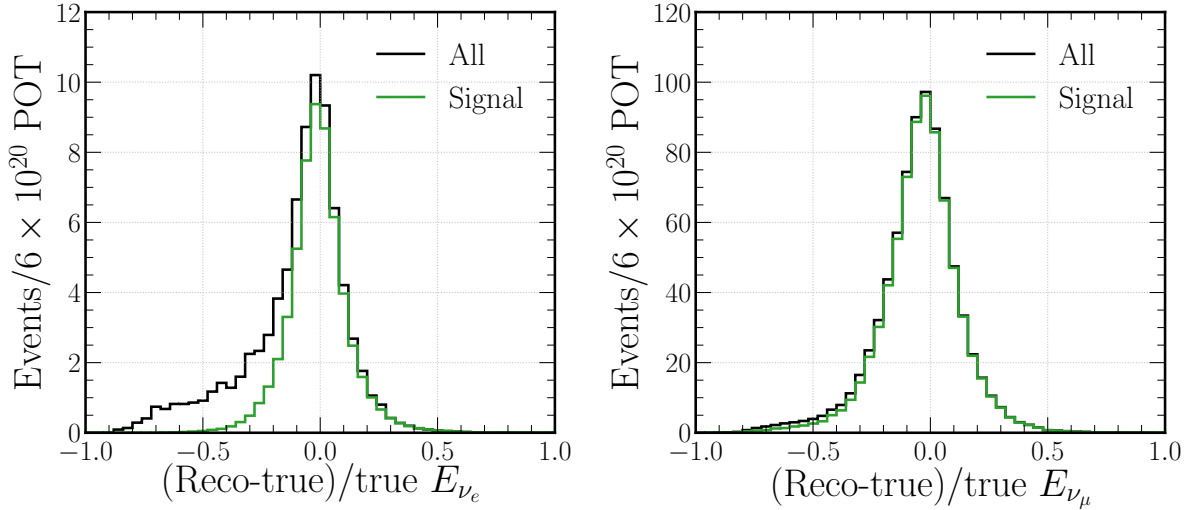


**Figure 6.19:** Distributions of (reco-true)/true neutrino energies for both CC  $\nu_e$  (left) and CC  $\nu_\mu$  (right) beam events. Distributions for both *all* respectively selected events and just the *signal* component of each selection are shown.

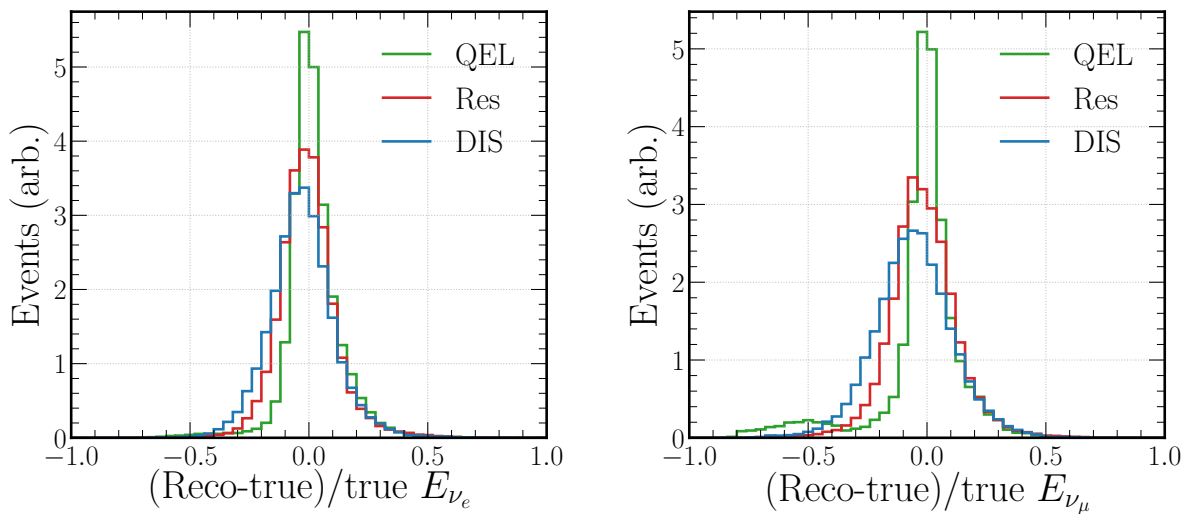


**Figure 6.20:** Distributions of (reco-true)/true neutrino energies for both CC  $\nu_e$  (left) and CC  $\nu_\mu$  (right) signal beam events by interaction types. The relative number of events between interaction types has been scaled for clearer comparison.

Event type	All	Signal	Signal-QEL	Signal-Res	Signal-DIS
CC $\nu_e$	12.9%	10.3%	7.1%	10.3%	13.6%
CC $\nu_\mu$	12.9%	12.6%	6.2%	11.7%	14.9%

**Table 6.4:** Summary of CC  $\nu_e$  and CC  $\nu_\mu$  neutrino energy resolutions. Shown for each sample are the resolutions for *all* selected events, the true *signal* selected events and the three dominant *signal* interaction type components, QEL, Res, and DIS. The resolutions are calculated from the standard deviations of gaussian fits made to the distributions shown in Figure 6.19 and Figure 6.20.

interactions achieving a stronger resolution than multi-particle DIS events. Furthermore, these results are similar to the selected signal energy resolutions obtained by NOvA of 10.7% for CC  $\nu_e$  events and 9.1% for CC  $\nu_\mu$  events [53].

By making gaussian fits to the (reco-true)/true signal neutrino energy distributions shown in Figure 6.19 in 1 GeV wide true neutrino energy bins, the energy dependence of the energy resolution can be explored. The means and standard deviations of these fits are shown in Figure 6.21 and Figure 6.22 for CC  $\nu_e$  and CC  $\nu_\mu$  events respectively, split by interaction type.

Reasonably significant bias in the means is observed with respect to the true neutrino energy for both CC  $\nu_e$  and CC  $\nu_\mu$  events. This is particularly true of DIS events, but still significant for Res and QEL events. As the energy spectrum of events used for training peaks, this is expected. Any future energy estimation work should consider using a flat energy spectrum for training, as done in reference [125].

The standard deviation is seen to decrease with true neutrino energy for all interaction types, except for energies above the flux peak. Again, this is most likely due to the spectrum of events used in the training sample. A contributing factor, however, will be due to the inability of PMTs to distinguish between numbers of incident photons at higher counts, more likely at higher energies.

As in the CC  $\nu_e$  selection case, the best way to understand the relative performance of the energy estimation is by comparison with the standard CHIPS reconstruction presented in Section 5.2.1. Although the standard reconstruction does not attempt to estimate the neutrino energy, the energy of the primary charged lepton in each CC event is predicted. The value can be compared to the *charged lepton energy* output of the energy estimation CNNs. Histograms of ratios of differences between CNN estimated (reco) and true

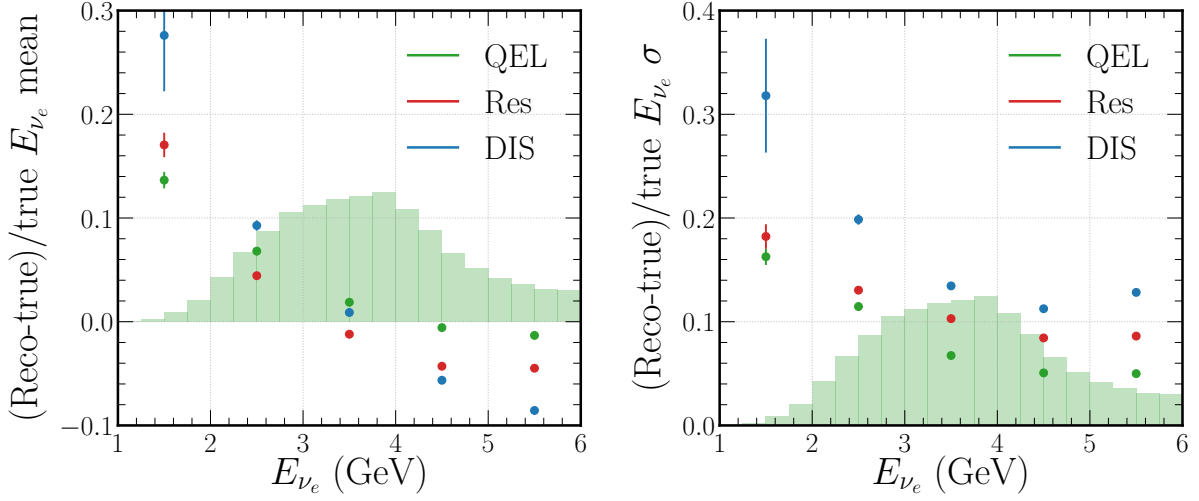


**Figure 6.21:** Means (left) and standard deviations (right) of gaussian fits made to distributions of (reco-true)/true neutrino energy for CC  $\nu_e$  events across a range of 1 GeV wide true neutrino energy bins and split by interaction type. The true distribution of CC  $\nu_e$  events is shown in green.

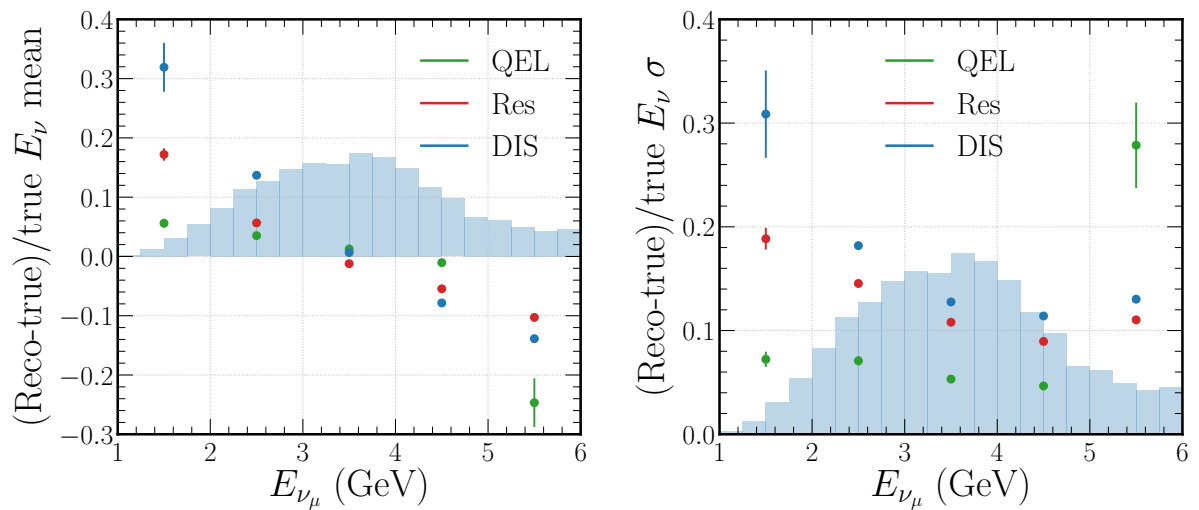


**Figure 6.22:** Means (left) and standard deviations (right) of gaussian fits made to distributions of (reco-true)/true neutrino energy for CC  $\nu_\mu$  events across a range of 1 GeV wide true neutrino energy bins and split by interaction type. The true distribution of CC  $\nu_\mu$  events is shown in blue.

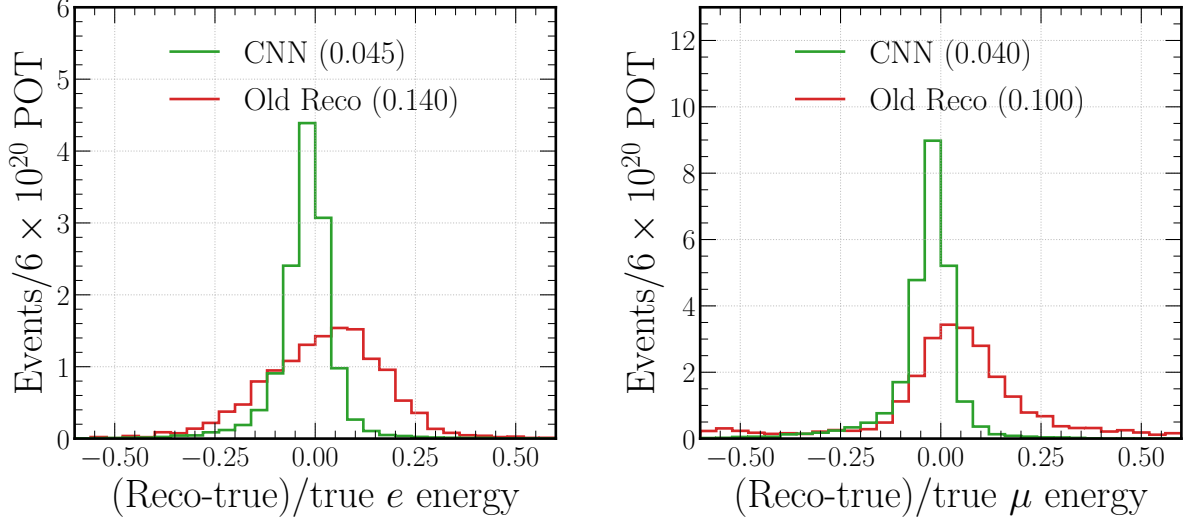


**Figure 6.23:** Distributions of (reco-true)/true primary charged lepton energies for both CC  $\nu_e$  (left) and CC  $\nu_\mu$  (right) beam events for both the new CNN approach and standard (old) methods. Only QEL events are shown for clearer comparison with the standard reconstruction methods. The standard deviation of a gaussian fit made to each distribution is shown in the corresponding brackets.

charged lepton energy to true charged lepton energy for both CC  $\nu_e$  and CC  $\nu_\mu$  beam QEL events are shown in Figure 6.23.

A significant improvement is made using the new CNN approach. An energy resolution 32% and 40% the size of the standard reconstruction resolution for CC  $\nu_e$  and  $\nu_\mu$  QEL events respectively is achieved, at 4.5% and 4.0%. When compared to the approximately 2.5% CC QEL charged lepton energy resolution reached by the Super-Kamiokande fITQun algorithm [134], the performance presented here is impressive, particularly given the significant differences in detector design.

### Interaction vertex estimation

The *interaction vertex x-position*, *interaction vertex y-position*, *interaction vertex z-position*, and *interaction time* outputs from the energy estimation networks can also be used. Although not employed in this work, future analyses may require accurate fiducial volume cuts or separation of events in time, therefore, strong performance is desirable. The CNN estimated (reco) minus truth distributions are shown for selected signal CC  $\nu_e$  and CC  $\nu_\mu$  QEL events in Figure 6.24 and Figure 6.25, respectively, with the standard reconstruction method distributions shown for comparison.

Comparable resolutions are achieved for CC  $\nu_e$  events, while CC  $\nu_\mu$  events display considerable improvements in interaction vertex z-position and time prediction. The Super-Kamiokande fitQun algorithm reaches an interaction vertex position resolution of 20 cm for CC  $\nu_e$  and 15 cm for CC  $\nu_\mu$  events [134], compared to the approximately 50 cm and 70 cm resolutions in this work. Again, a relatively small difference when comparing detectors.

The charged lepton energy, interaction vertex position, and interaction vertex time resolutions also display a clear advantage of the CNN approach. Long tails and biased means are common in the distributions associated with the standard reconstruction methods when compared to the generally symmetric distributions of the CNN approach. This difference, which is particularly stark for non-QEL event types, highlights how both the tunable (human-influenced) inputs of the standard reconstruction and the need for a predefined hypothesis can easily bias the outputs and not generalise well to all event types.

### 6.1.5 Combined performance

By combining CC  $\nu_e$  and CC  $\nu_\mu$  selections with neutrino energy estimation, the final selected spectrum of events within CHIPS-5 running for a year can be estimated. These are shown in Figure 6.26 and Figure 6.27 for CC  $\nu_e$  and CC  $\nu_\mu$  selections respectively. Although a detailed CHIPS-5 sensitivity analysis is not included in this work, the expected curves for different values of  $\delta_{CP}$  are shown in the CC  $\nu_e$  case for interest.

## 6.2 Explainability

A common and justified concern with CNNs is their tendency to be used as a black box (inputs in, outputs out) with no understanding of their inner working. For detailed physics analyses, this can have significant confidence implications for the final results. Although difficult quantitatively, qualitative assessments of the trained networks can go a long way to proving they behave as desired. Here, a sample of efforts to explain the inner workings of the trained CNNs presented in this work are described.

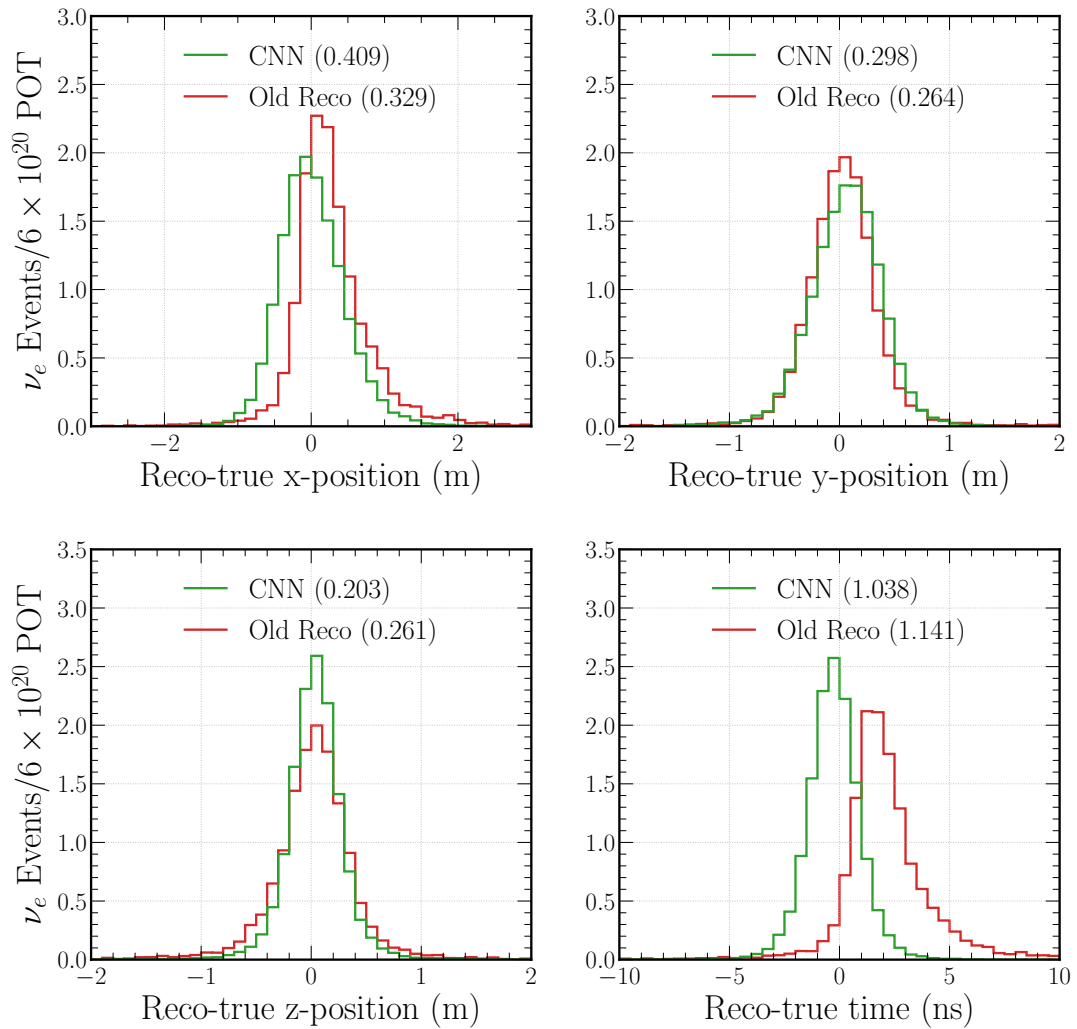


**Figure 6.24:** Reco-true distributions for the interaction vertex position components and time for CC  $\nu_e$  QEL events. Both the distributions for the new CNN approach and standard (old) reconstruction methods are shown. The standard deviation of a gaussian fit made to each distribution is shown in the corresponding brackets.

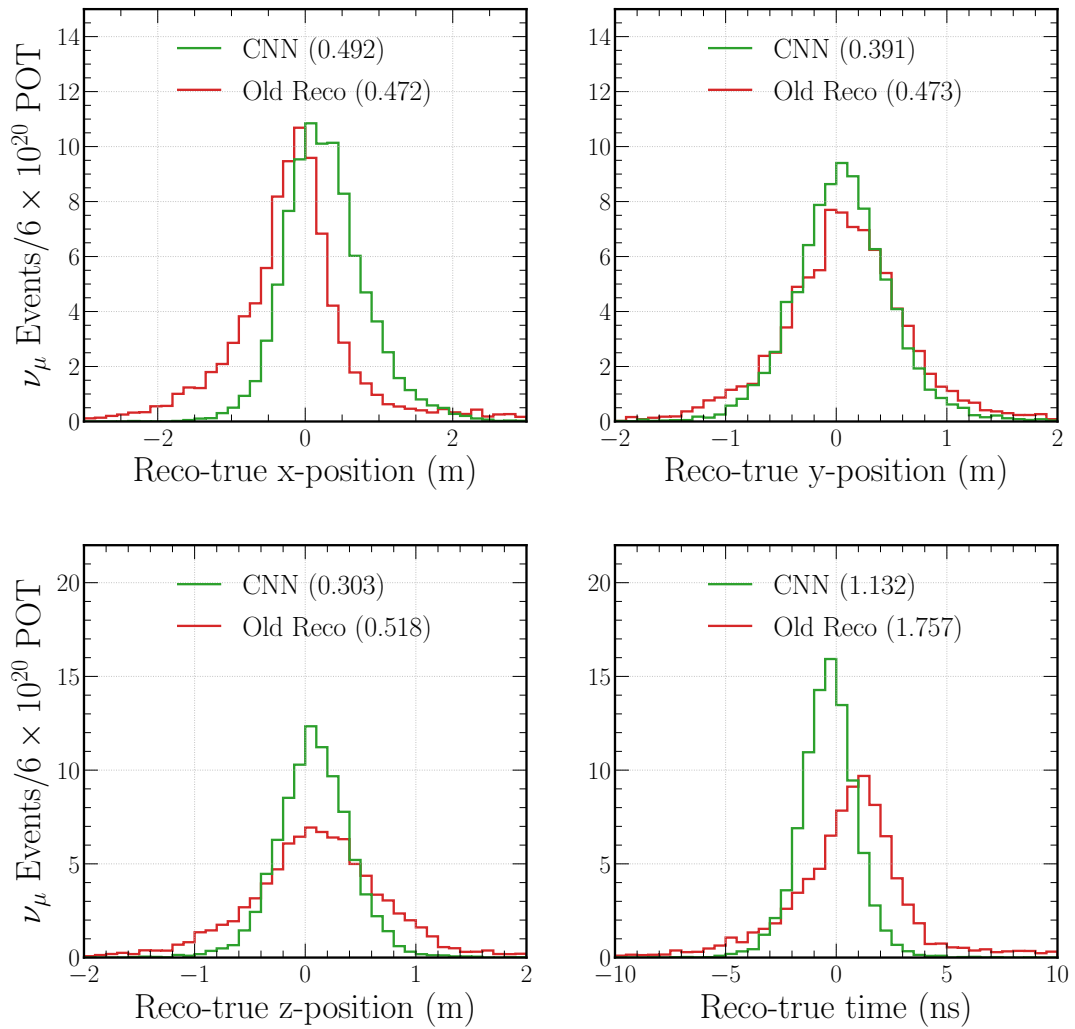


**Figure 6.25:** Reco-true distributions for the interaction vertex position components and time for CC  $\nu_\mu$  QEL events. Both the distributions for the new CNN approach and standard (old) reconstruction methods are shown. The standard deviation of a gaussian fit made to each distribution is shown in the corresponding brackets.

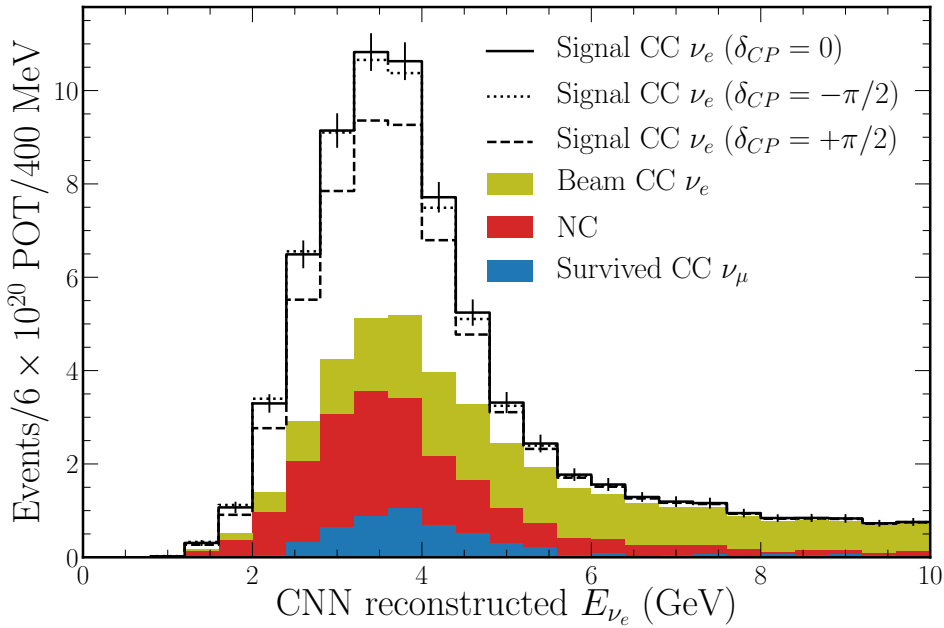


**Figure 6.26:** Distribution of CNN reconstructed  $\nu_e$  energies for CC  $\nu_e$  selected events. The appeared CC  $\nu_e$  signal component as well as the intrinsic beam CC  $\nu_e$ , NC and survived CC  $\nu_\mu$  background components are shown stacked to generate the full distribution. Expected totals are show in each bin for  $\delta_{CP} = -\pi/2$ , 0, and  $+\pi/2$ .

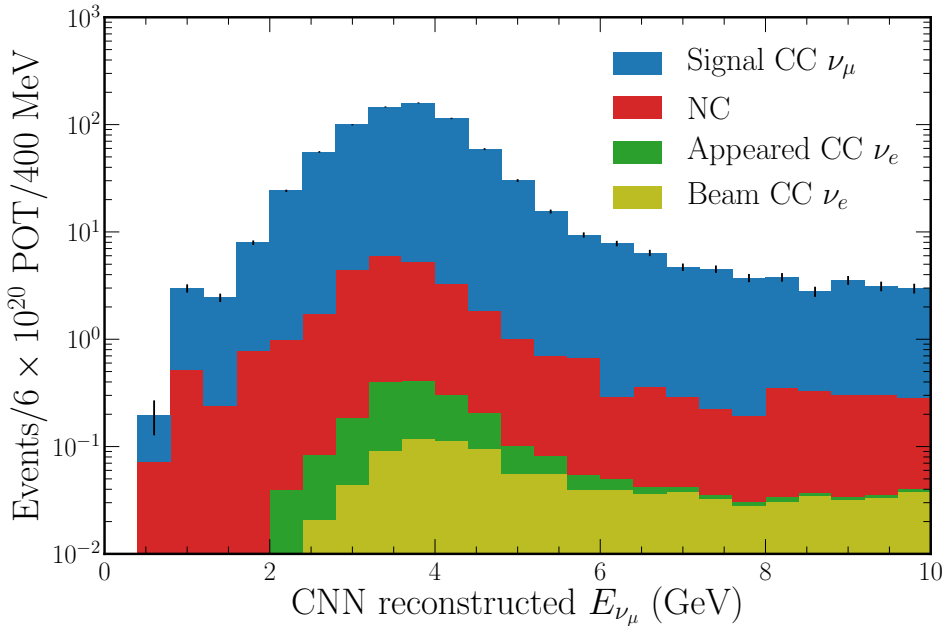


**Figure 6.27:** Distribution of CNN reconstructed  $\nu_\mu$  energies for CC  $\nu_\mu$  selected events. The survived CC  $\nu_\mu$  signal component as well as the appeared CC  $\nu_e$ , intrinsic beam CC  $\nu_e$ , and NC background components are shown stacked to generate the full distribution.

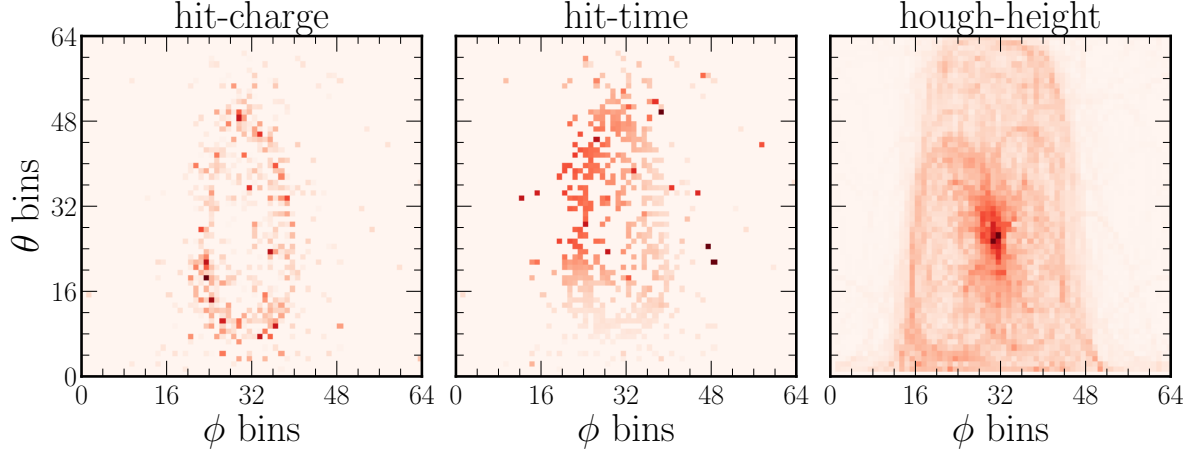


**Figure 6.28:** Three map representation of a CC quasi-elastic  $\nu_e$  event. Initiated by a  $\nu_e$  of energy 2.4 GeV with a final state  $e^-$  of energy 1.6 GeV.

### 6.2.1 Feature map visualisation

Visualisations of the output feature maps from the first, second, and third VGG blocks for each of the trained networks (cosmic rejection, beam classification, and energy estimation) are shown in Figure 6.29, using the event shown in Figure 6.28 as input. Learnt Cherenkov ring features are observed: ring edges, ring holes, outlying hits, Hough peaks, and a myriad of combinations are seen. Furthermore, there are clear differences between the specific networks, proving each network learns those features found to be important for its tasks.

### 6.2.2 t-SNE visualisation

Another technique to analyse trained CNNs is t-Distributed Stochastic Neighbour Embedding (t-SNE) [163]. The t-SNE procedure is an unsupervised learning algorithm to visualise the learnt high-dimensional feature-space of a trained network in a lower number of dimensions. It accomplishes this by clustering events with similar features nearby in two-dimensional space and separating events with dissimilar features. Here, the outputs from the last fully connected layer before the output layer (with 512 dimensions) are used as input, as they provide the final representation of the learnt network features.

Visualisations of the t-SNE algorithm outputs, when applied to both the trained cosmic rejection and beam classification networks, are shown in Figure 6.30 and Figure 6.31, respectively. The very strong cosmic like to beam like separation presented in Section 6.1.2

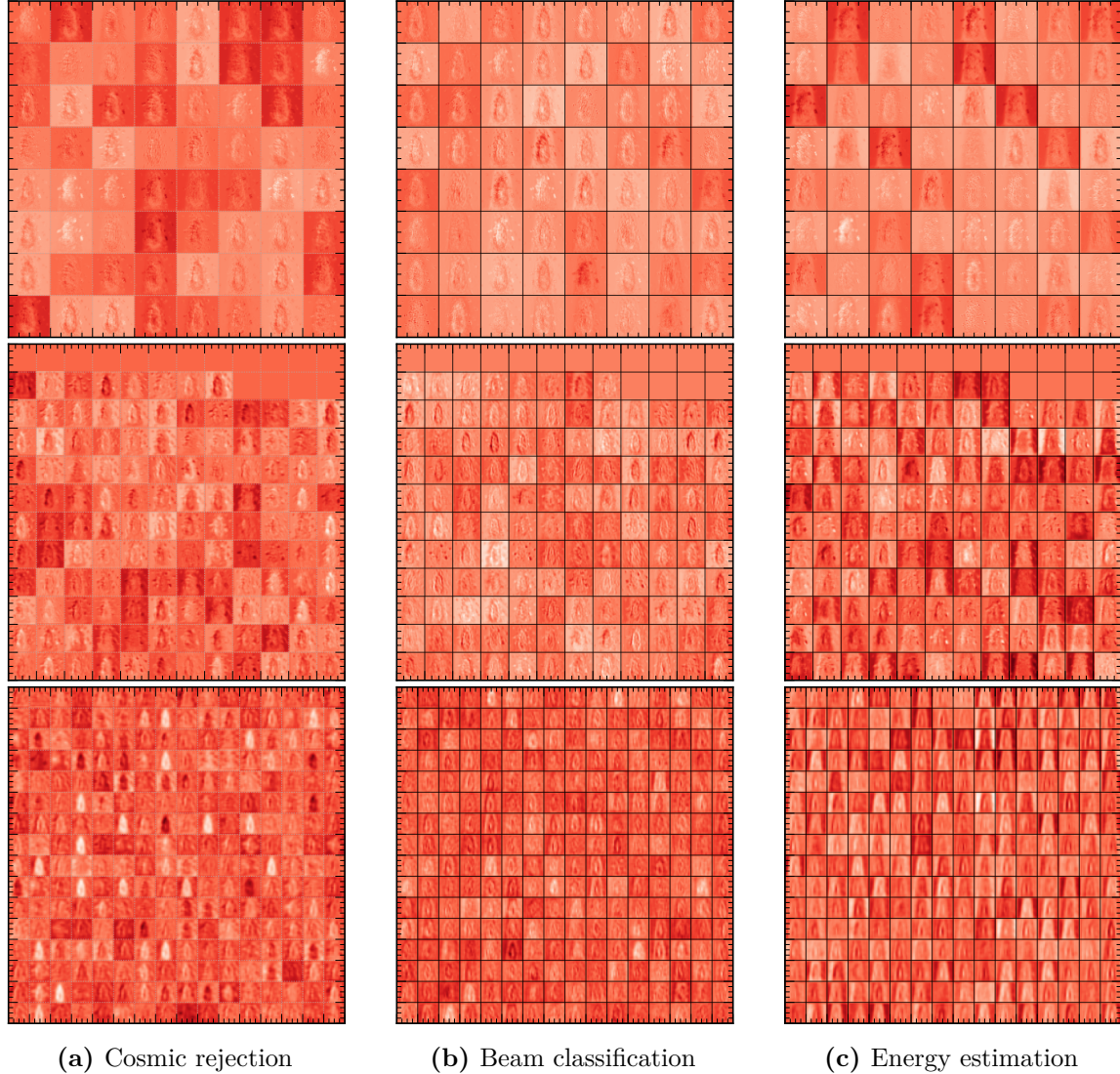


**Figure 6.29:** Visualisations of the feature map outputs, using as input the event shown in Figure 6.28. Shown are the activated feature map outputs from the first (top), the second (middle), and the third (bottom) VGG blocks for each of the trained network types. A chipsnet architecture with only a single branch and all three input event maps stacked into a single three-channel input image is used for simplicity.

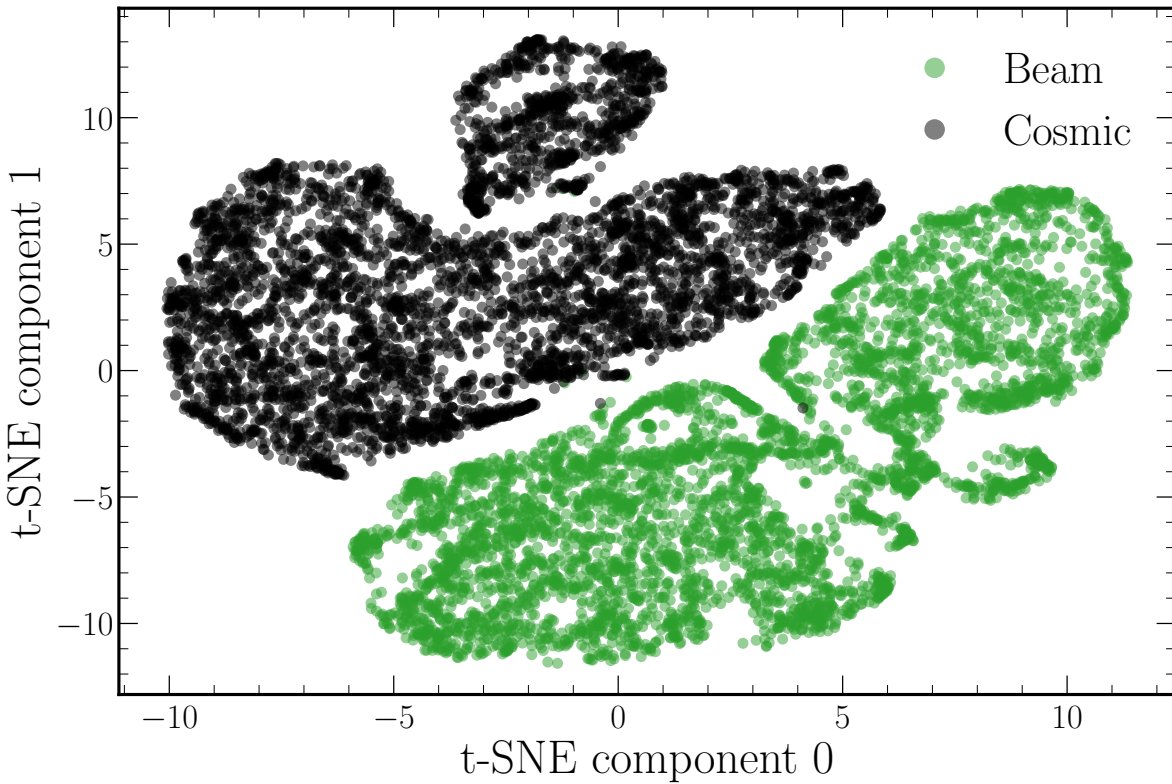


**Figure 6.30:** Two dimensional probability space of beam and cosmic events generated using the t-SNE procedure on the final fully-connected layer of the trained cosmic rejection network.

is clear from the cosmic rejection visualisation. Conversely, for the beam classification network, the separation is weaker, with major overlap between categories, especially for CC  $\nu_e$  and NC events.

For the beam classification network, three events, labelled in the t-SNE space of Figure 6.31, are shown in Figure 6.32. Each event is highly representative of its class, achieving a high respective *combined category* score. Both the CC  $\nu_e$  and NC events are typical of that expected. However, the CC  $\nu_\mu$  event contains a primary charged lepton that escapes the detector volume, identified by the central peak. This topology suggests that strongly classified CC  $\nu_\mu$  events can be identified by this ‘escaping’ feature rather than the shape of the muon ring. Future work, therefore, should explore using only fully contained events during beam classification training.

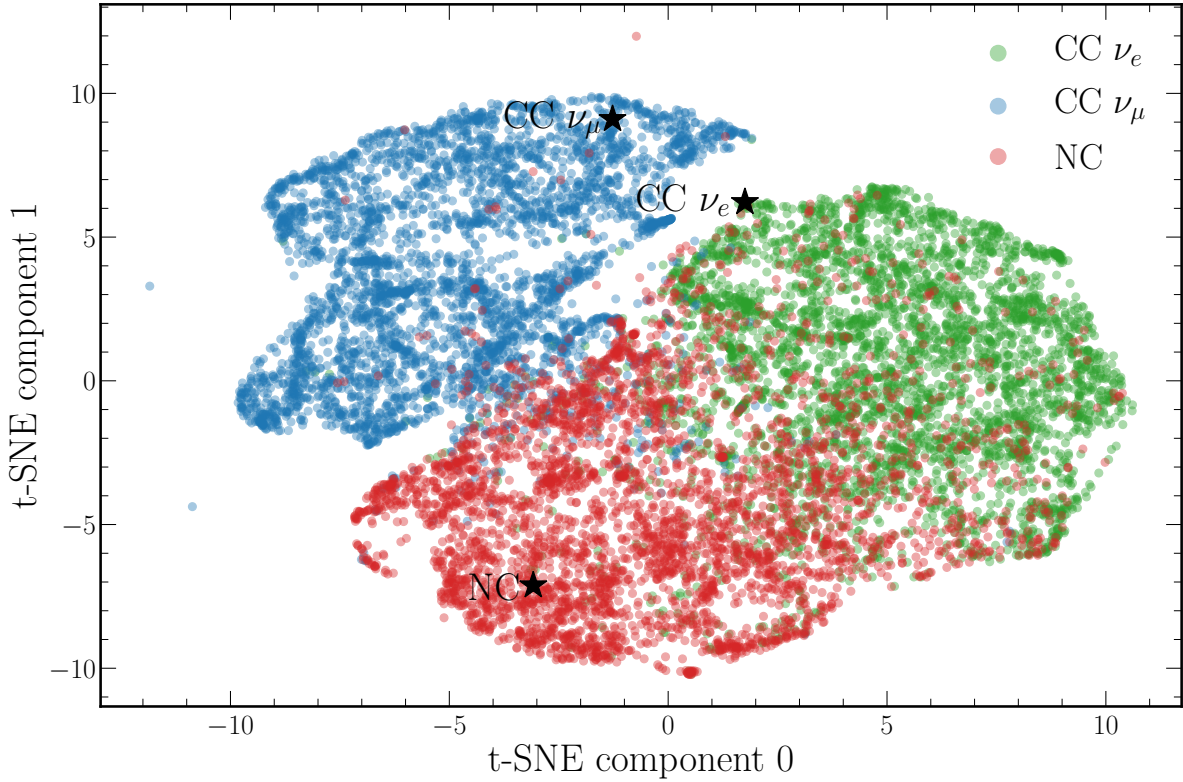


**Figure 6.31:** Two dimensional probability space of different beam events generated using the t-SNE procedure on the final fully-connected layer of the trained beam classification network. Three events, one highly CC  $\nu_e$  like, one highly CC  $\nu_\mu$  like, and one highly NC like are highlighted and shown in Figure 6.32.

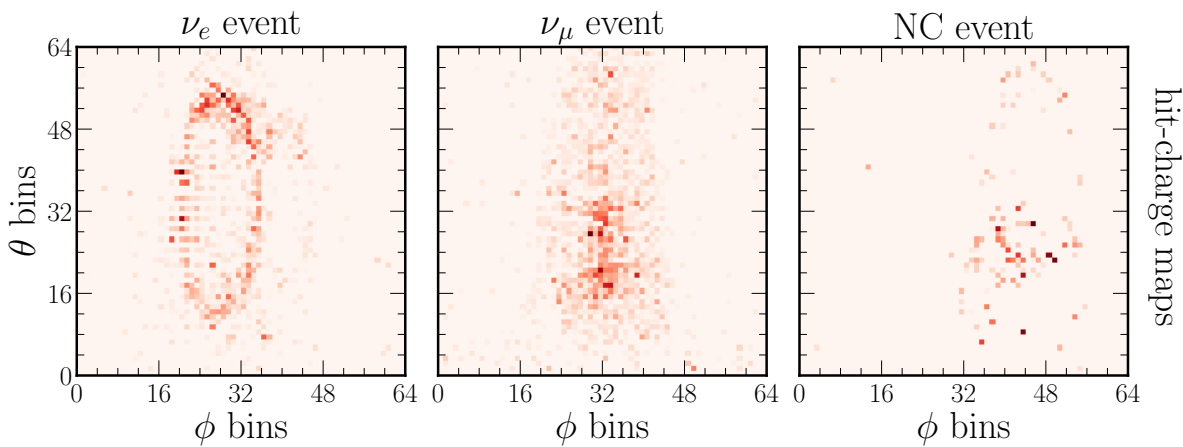


**Figure 6.32:** Hit-charge maps of the highly CC  $\nu_e$  like, CC  $\nu_\mu$  like, and NC like events from Figure 6.31.

## 6.3 Robustness

Recent CNN research has focused on another concern; they tend to not generalise well under distributional changes within the input data [164]. As the CNNs presented in this work are trained and evaluated on simulated Monte Carlo events, this effect is of particular relevance. If the neutrino events used differ from those measured by the real CHIPS-5 detector, the network outputs may not be reliable. An effective calibration procedure and simulation improvements can ensure any discrepancy is minimised; however, a small distributional difference is inevitable.

Studies are presented here to prove the robustness of the trained CNNs to such changes within the input. Broadly, the CNN inputs can be characterised as being dependent on three sets of PMT information: the hit times, the hit charges, and the hit positions. An accurate PMT position is deemed unimportant to the trained networks as the  $64 \times 64$  input grid roughly corresponds to bins of size 2.5 m in  $\theta$  by 2.0 m in  $\phi$  within the CHIPS-5 detector. As this binning is much larger than the actual distance between PMTs, resolving individual PMTs becomes impossible. Consequently, changes in only the PMT hit times and hit charges are considered in three studies: the smearing of hit times, the smearing and shifting of hit charges, and the addition of random noise.

Five classification performance metrics are used for comparison during this section and the next (Section 6.4):

1. **Max FOM:** The optimised figure-of-merit (efficiency  $\times$  purity) value. As the FOM is proportional to  $s/\sqrt{s+b}$  which increases linearly with detector exposure, an improvement in the FOM value linearly decreases the exposure time required to reach the same physics sensitivity.
2. **High Score Eff (Pur):** The CC  $\nu_e$  selection efficiency (purity) using the simple highest-scoring output neuron classification methodology. The simple classification strategy is used here instead of the FOM selection as it is less susceptible to trading off between efficiency and purity, making for easier comparison.
3. **ROC Integral:** The area under the Receiver Operating Characteristic (ROC) curve; a standard tool for classification performance comparison. The curve corresponds to the signal CC  $\nu_e$  efficiency plotted against the background efficiency as the CC  $\nu_e$  score cut value is varied. A curve which reaches closer to the top-left (high signal

efficiency, low background efficiency) signifies a stronger classification performance. An example ROC curve is shown for the smearing of hit times in Figure 6.34.

4. **PR Integral:** The area under the Precision-Recall (PR) curve; another standard tool for classification performance comparison. The curve corresponds to the signal CC  $\nu_e$  purity plotted against the signal efficiency as the CC  $\nu_e$  score cut value is varied. A curve closer to the top-right (high signal purity, high signal efficiency) signifies a stronger classification performance. For imbalanced class frequencies such as those expected within the CHIPS-5 detector, the PR curve is seen as a more reliable indicator of performance than the ROC curve [165]. An example PR curve is shown for the smearing of hit times in Figure 6.34.

### 6.3.1 Time smearing

The smearing of input hit times is found to produce a minimal reduction in output performance. For every event, each hit-time bin for which there is an entry not equal to zero is smeared using an absolute time randomly generated using a normal distribution with a mean of zero and a standard deviation of  $\sigma$  nanoseconds. The cases when  $\sigma = 0$  ns (no smearing),  $\sigma = 2$  ns, and  $\sigma = 5$  ns are considered. The actual smearing values used are scaled to the zero to one input range, and any post smearing out-of-range values are clipped to the range boundaries.

For each case of  $\sigma$ , the resulting efficiency, purity, and their product (the FOM) for CC  $\nu_e$  events as a function of selecting events above a particular CC  $\nu_e$  score is shown in Figure 6.33. The classification performance metrics are presented in Table 6.5 with the ROC and PR curves shown in Figure 6.34. Cosmic rejection and energy estimation performance are not presented, as the resulting output changes are negligible.

With an effective calibration, a realistic discrepancy in hit times of less than 1 ns should be expected. Given this, it is promising to observe that even for the smearing of  $\sigma = 2$  ns the beam classification performance change is minimal. At  $\sigma = 5$  ns more significant degradation starts to occur; however, there is no dramatic fall-off in performance. Interestingly, the *High Score Pur* is seen to increase with greater hit-time smearing, indicating that CC  $\nu_e$  signal events are proportionally more robust to hit-time input smearing than background events.

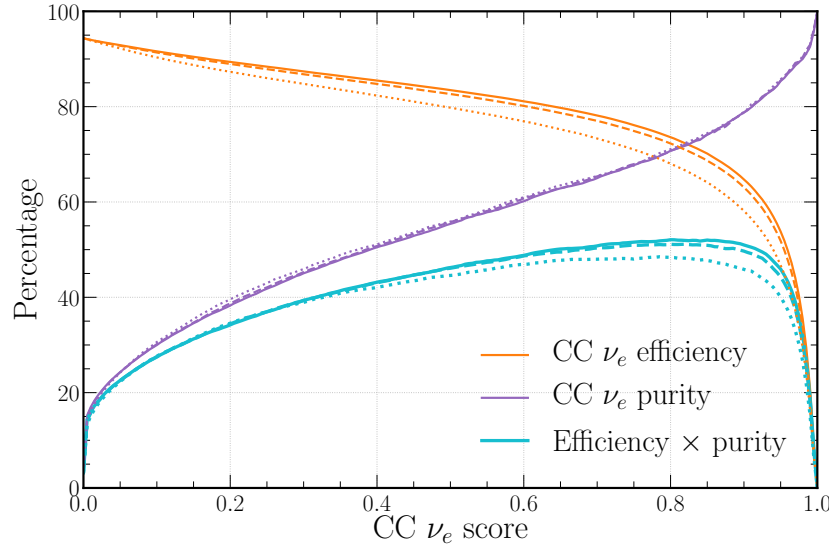


**Figure 6.33:** CC  $\nu_e$  efficiency, purity, and efficiency  $\times$  purity at different values of CC  $\nu_e$  score selection for different levels of hit-time smearing. The  $\sigma = 0$  ns curves are shown by the solid lines,  $\sigma = 2$  ns curves by the dashed lines, and  $\sigma = 5$  ns curves by the dotted lines.

Metric	$\sigma = 0$ ns	$\sigma = 2$ ns	$\sigma = 5$ ns
Max FOM	<b>0.519</b>	0.513	0.484
High Score Eff	<b>0.835</b>	0.826	0.798
High Score Pur	0.554	0.556	<b>0.561</b>
ROC Integral	<b>0.828</b>	0.828	0.826
PR Integral	<b>0.756</b>	0.751	0.730

**Table 6.5:** Classification performance metrics for different levels of hit-time smearing. The ROC and PR integrals are taken from under the curves shown in Figure 6.34.

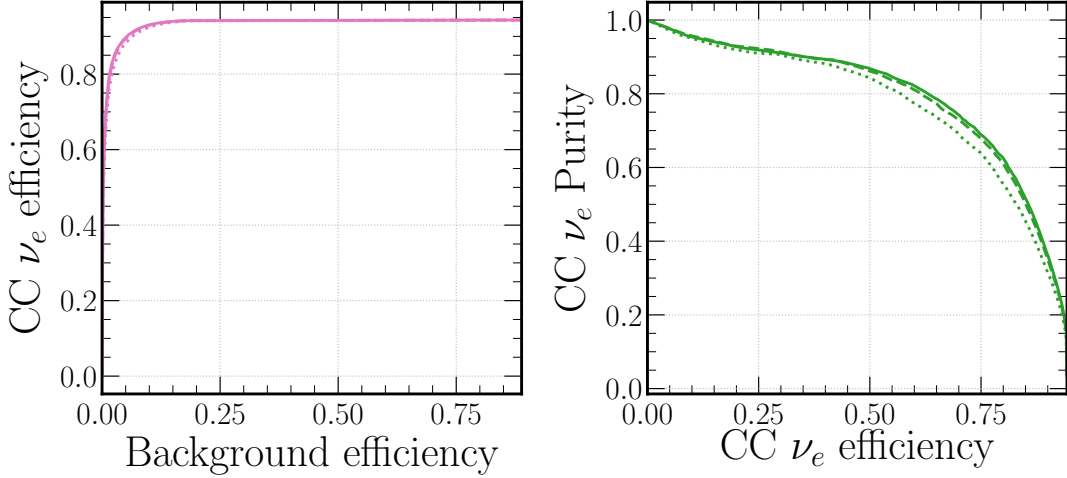


**Figure 6.34:** ROC (left) and PR (right) curves for different levels of hit-time smearing. The  $\sigma = 0$  ns curves are shown by the solid lines,  $\sigma = 2$  ns curves by the dashed lines, and  $\sigma = 5$  ns curves by the dotted lines.

### 6.3.2 Charge smearing and shifting

The smearing and shifting of input hit charges behave as expected and produce no significant reduction in output performance. For every event, each hit-charge and hough-height bin is scaled by a factor randomly drawn from a normal distribution with a mean of  $\mu$  and a standard deviation of  $\sigma$ . This methodology differs from the absolute hit-time smearing above by modifying bins proportional to their charge, instead of using an absolute value. Any post modification bin values outside the zero to one input range are clipped to the range boundaries.

Alongside the default case when  $\mu = 1.0$  and  $\sigma = 0.0$ , two smearing and two shifting cases are considered:  $\mu = 1.0, \sigma = 0.2$  and  $\mu = 1.0, \sigma = 0.4$  for smearing; and  $\mu = 1.2, \sigma = 0.2$  and  $\mu = 1.4, \sigma = 0.2$  for shifting. Note that for the shifting cases a standard deviation of  $\sigma = 0.2$  is used to introduce some randomness.

For each smearing case, the resulting efficiency, purity, and their product (the FOM) for CC  $\nu_e$  events as a function of selecting events above a particular CC  $\nu_e$  score is shown in Figure 6.35. The equivalent plot for each shifting case is shown in Figure 6.36. The classification performance metrics are presented in Table 6.6, with distributions of (reco-true)/true CC QEL  $\nu_e$  energies for each case also shown in Figure 6.37. Cosmic rejection performance is not presented as the resulting output changes are negligible.

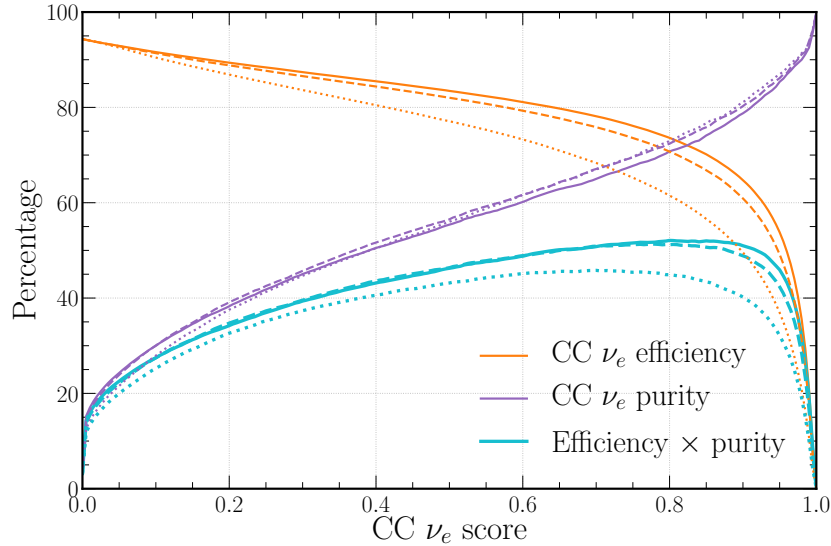


**Figure 6.35:** CC  $\nu_e$  efficiency, purity, and efficiency  $\times$  purity curves at different values of CC  $\nu_e$  score selection for different levels of hit-charge smearing where  $\mu = 1.0$ . The  $\sigma = 0.0$  curves are shown by the solid lines,  $\sigma = 0.2$  curves by the dashed lines, and  $\sigma = 0.4$  curves by the dotted lines.

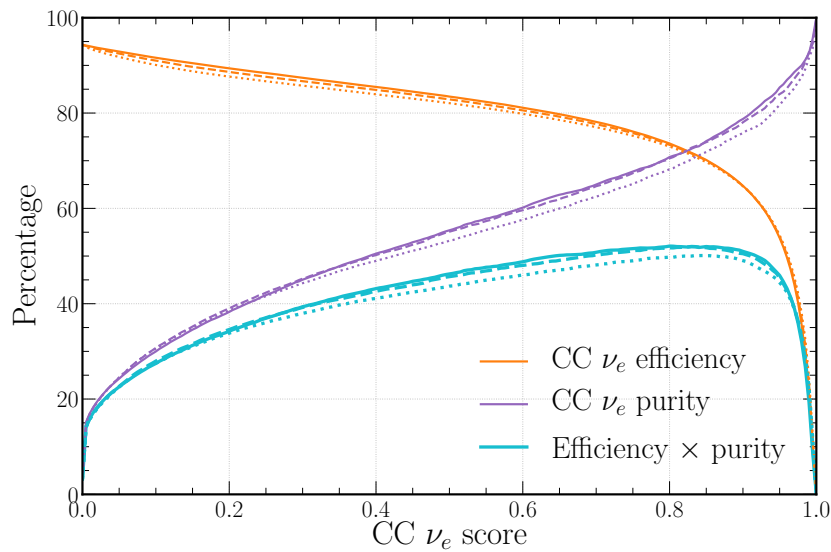


**Figure 6.36:** CC  $\nu_e$  efficiency, purity, and efficiency  $\times$  purity curves at different values of CC  $\nu_e$  score selection for different levels of hit-charge shifting. The  $\mu = 1.0$  curves are shown by the solid lines,  $\mu = 1.2$  curves by the dashed lines, and  $\mu = 1.4$  curves by the dotted lines.

Scaling ( $\mu, \sigma$ )	(1.0, 0.0)	(1.0, 0.2)	(1.0, 0.4)	(1.2, 0.2)	(1.4, 0.2)
Max FOM	<b>0.519</b>	0.513	0.458	0.519	0.501
High Score Eff	<b>0.835</b>	0.820	0.771	0.829	0.821
High Score Pur	0.554	<b>0.565</b>	0.560	0.551	0.532
ROC Integral	<b>0.828</b>	0.828	0.825	0.827	0.825
PR Integral	<b>0.756</b>	0.751	0.707	0.750	0.733

**Table 6.6:** Classification performance metrics for different levels of hit-charge smearing and shifting.

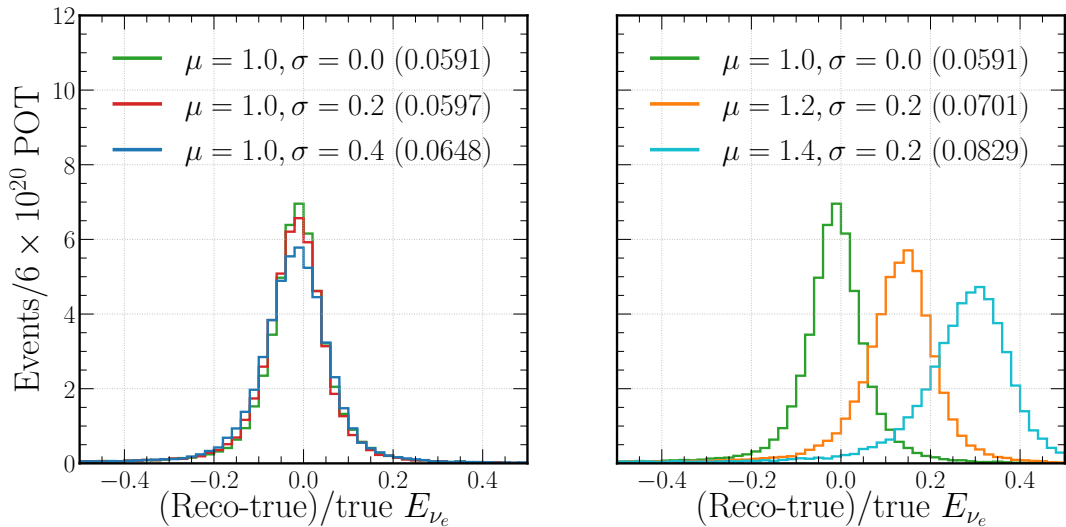


**Figure 6.37:** Distributions of (reco-true)/true CC QEL  $\nu_e$  energies for different levels of hit-charge smearing and shifting. Shown are the different smearing levels (left) and the different shifting levels (right). Standard deviations found from fits made to each distribution are shown in brackets.

With an effective calibration in the smearing case and reasonable modelling in the shifting case, it is realistic to assume differences on the order of a few per cent for the hit-charge and hough-height inputs. Given this, the extensive modifications made here (40% shifts, for example) still produce only relatively small reductions in beam classification performance; therefore, a negligible effect can be assumed. Interestingly, smearing of  $\sigma = 0.4$  is seen to impact performance to a greater degree than shifting with  $\mu = 1.4$ . This behaviour can be explained by the overall relative event topology remaining consistent under a shift compared to when smeared.

For neutrino energy estimation, the impact of smearing is small, but shifting is seen to produce significant changes. This is understandable when assuming that the energy estimation (even for a CNN) relies principally on the counting of the deposited charge for each event, as is the case for most experimental particle physics predictions. Therefore, any systematic shift in the measured input data is always expected to bias the output prediction heavily. However, for realistic input differences on the order of a few per cent, only small output changes should be expected here.

### 6.3.3 Random noise

Random PMT noise added to the input is found to have a negligible impact on output performance. For every event hit-charge bin, a normal distribution with a mean of zero and a standard deviation of  $\mu$  photoelectrons is randomly sampled. If a value greater than that corresponding to a single photoelectron is returned, the bin charge is incremented by the returned value. Furthermore, for each modification made, the corresponding hit-time bin is updated by randomly sampling a uniform time distribution and choosing the earliest of the return value and the already set bin time. Alongside the default case with no noise (0.0%), values of  $\mu$  are chosen so that either 2.3% or 6.7% of bins are modified by random noise in each event.

For each case, the resulting efficiency, purity, and their product (the FOM) for CC  $\nu_e$  events as a function of selecting events above a particular CC  $\nu_e$  score is shown in Figure 6.38. The classification performance metrics are presented in Table 6.7. Cosmic rejection and energy estimation performance are not presented as the resulting output changes are negligible.

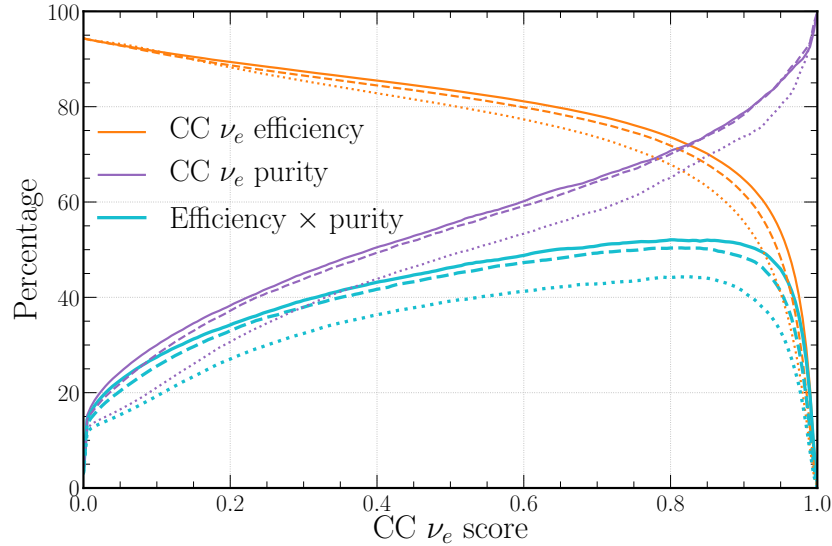


**Figure 6.38:** CC  $\nu_e$  efficiency, purity, and efficiency  $\times$  purity curves at different values of CC  $\nu_e$  score selection for different levels of random noise. The 0.0% curves are shown by the solid lines, 2.3% curves by the dashed lines, and 6.7% curves by the dotted lines.

Metric	0.0%	2.3%	6.7%
Max FOM	<b>0.519</b>	0.503	0.316
High Score Eff	<b>0.835</b>	0.824	0.717
High Score Pur	<b>0.554</b>	0.545	0.414
ROC Integral	<b>0.828</b>	0.827	0.810
PR Integral	<b>0.756</b>	0.740	0.559

**Table 6.7:** Classification performance metrics for different levels of random noise.

The cases presented here represent a PMT noise rate more than two orders of magnitude greater than that expected within CHIPS-5. Testing has shown that at room temperate the Nikhef POM HZC PMTs produce a dark noise rate of  $\sim 1$  KHz. Therefore, only  $\sim 0.02\%$  of event map bins are expected to be affected by PMT noise throughout a typical 100 ns event. Given this, excellent beam classification robustness is observed, with the small reduction in performance seen for the 2.3% chance of noise case indicating any realistic output changes would be negligible.

## 6.4 Alternative implementations

Here a sample of alternative (but ultimately unsuccessful) CHIPS CNN implementations are presented and compared to the final implementation used. Those chosen highlight interesting factors that are found to drive (or not drive) performance. Only the beam classification performance, specifically the primary CC  $\nu_e$  selection is considered here for comparison; however, these findings also translate to cosmic rejection and energy estimation performance.

### 6.4.1 Alternative inputs

How the raw PMT hits of an event are represented is found to impact performance significantly. Three different representations are considered. Firstly, the (successful) *vertex view*, were event maps are generated in  $\theta$  and  $\phi$  as viewed from the seed estimated interaction vertex position. Secondly, the *origin raw view*, were event maps are generated in  $\theta$  and  $\phi$  as viewed from the centre of the detector (the origin). Finally, the *origin iso view*, were event maps are generated using a PMT position parametrisation in  $X_+$  and  $X_-$  as viewed from the centre of the detector.

The origin iso view follows the parametrisation from reference [166], used for exploratory Super-Kamiokande (and Hyper-Kamiokande) CNN studies. This mapping attempts to equally distribute PMT density across the whole two-dimensional input representation. The PMT positions in cylindrical coordinates  $(\rho, \phi, z)$  are mapped to two

dimensions,  $X_+$  and  $X_-$  using

$$X_{\pm} = \begin{cases} 1 - \chi_{\mp} & (z \geq 0) \\ \chi_{\pm} & (z < 0), \end{cases} \quad (6.1)$$

where

$$\chi_{\pm} = W(\rho, z) \frac{\pi \pm \phi}{2\pi}, \quad (6.2)$$

and

$$W(\rho, z) = \sqrt{\frac{\rho^2 - 2R|z| + RH}{R^2 + RH}}, \quad (6.3)$$

with  $R$  and  $H$  being the radius and height of the cylindrical detector respectively.

The same example CC resonant  $\nu_e$  event for each representation is shown in Figure 6.39 for reference. The example event highlights the advantages of representing the event as viewed from its estimated interaction vertex position. The emitted Cherenkov radiation and resulting ring are viewed without detector or representation parametrisation distortions, showing their true physical topology. This clarity allows the CNN to solely learn the underlying topological differences between event types instead of also having to untangle distortions.

A beam classification network is trained for each representation. Only the hit-charge and hit-time event maps are used as input as the hough-height map can only be generated from the seed estimated interaction vertex position. For each representation the resulting efficiency, purity, and their product (the FOM) for CC  $\nu_e$  events as a function of selecting events above a particular CC  $\nu_e$  score is shown in Figure 6.40. Performance comparison metrics are also presented in Table 6.8.

A significant reduction in performance is observed when using either origin view representation, quantifying the qualitative description using the example event given above. Interestingly, both origin view representations result in a very similar performance, showing that a uniform PMT distribution across the input representation does not provide an improvement. Future work should consider other methods to reduce distortions, such as the smearing of hits across nearby bins to reduce isolated peaks and an improved interaction vertex position estimation procedure.

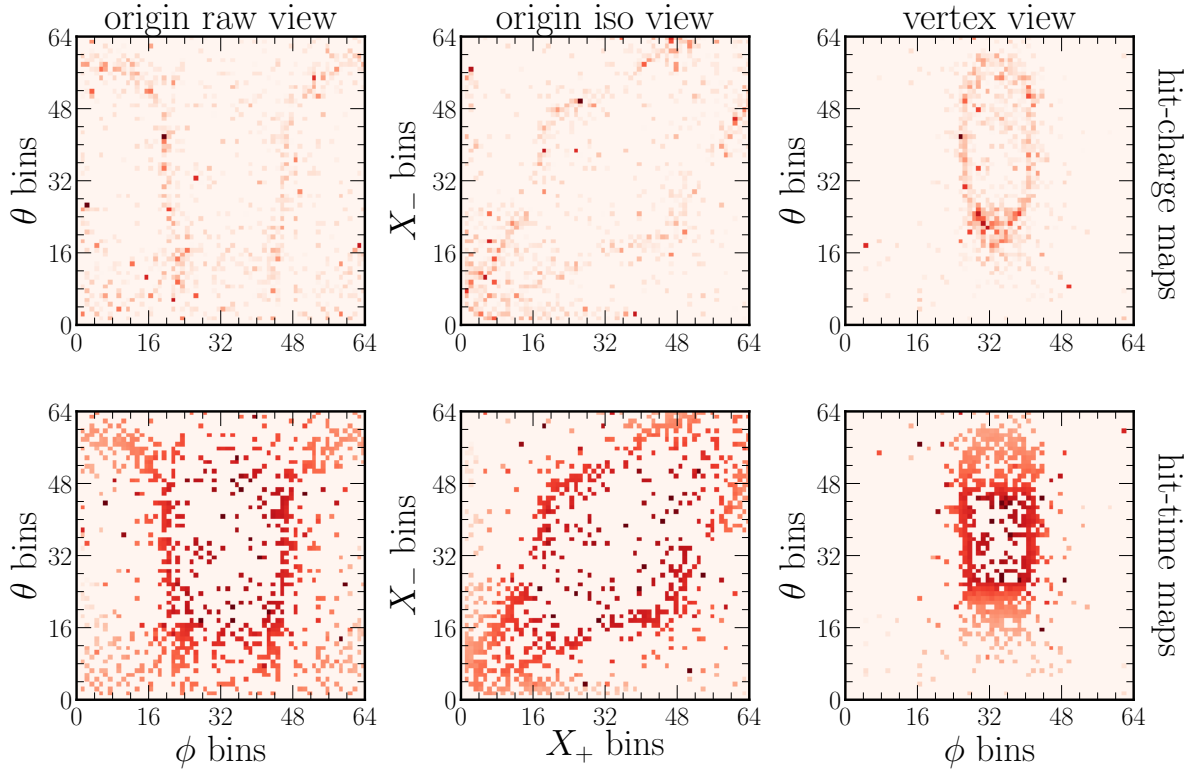


**Figure 6.39:** Example CC resonant  $\nu_e$  event shown for each of the three input representations, with the hit-charge (top) and hit-time (bottom) event maps shown for each. The event is initiated by a  $\nu_e$  of energy 3.3 GeV with the final state particles above the Cherenkov threshold including a  $e^-$  of energy 2.8 GeV and a 0.3 GeV  $\pi^0$ .

Metric	Vertex View	Origin Raw View	Origin Iso View
Max FOM	<b>0.461</b>	0.422	0.419
High Score Eff	<b>0.878</b>	0.874	0.867
High Score Pur	<b>0.354</b>	0.291	0.298
ROC Integral	<b>0.825</b>	0.822	0.821
PR Integral	<b>0.707</b>	0.675	0.670

**Table 6.8:** Classification performance metrics for the three input representations.

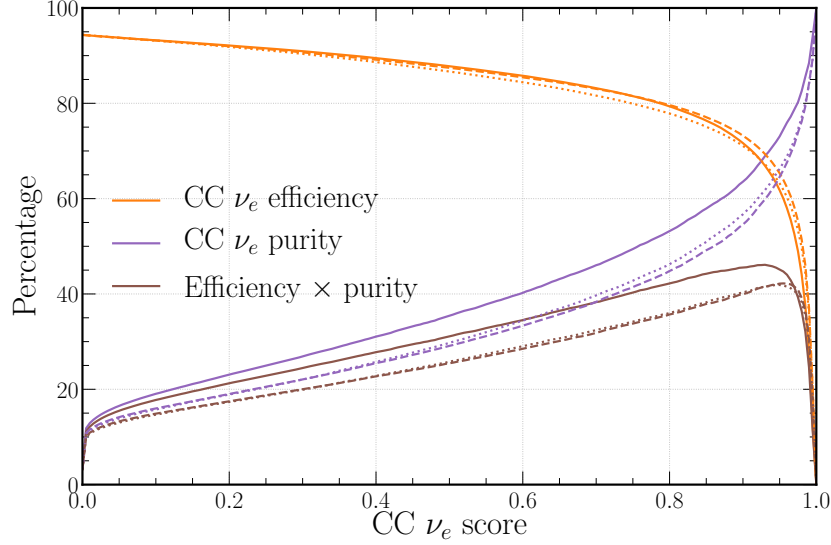


**Figure 6.40:** CC  $\nu_e$  efficiency, purity, and efficiency  $\times$  purity curves for different values of CC  $\nu_e$  score selection for the three input representations. The *vertex view* curves are shown by the solid lines, the *origin raw view* curves by the dashed lines, and the *origin iso view* curves by the dotted lines.

### 6.4.2 Alternative training samples

The relative proportions of training sample interaction types should match the expected sample as closely as possible. Three different training samples are considered. Firstly, the (successful) *flux* sample representative of the expected spectrum. Secondly, a *uniform* sample, using a similar number of events per interaction type as shown in Figure 6.41. Finally, a *both* sample using an equivalent combination of both.

A beam classification network is trained using each of the samples with an equal number of events. For each sample the resulting efficiency, purity, and their product (the FOM) for CC  $\nu_e$  events as a function of selecting events above a particular CC  $\nu_e$  score is shown in Figure 6.42. Performance comparison metrics are also presented in Table 6.9.

Using the uniform training sample is found to reduce beam classification performance significantly. Given that the *both* sample performance lies between the uniform and flux cases, it can be assumed that as the training sample tends towards the expected distribution of events, the performance increases. This finding highlights a key feature of CNNs; they play the game of statistics and only statistics, making them less smart than they may first appear.

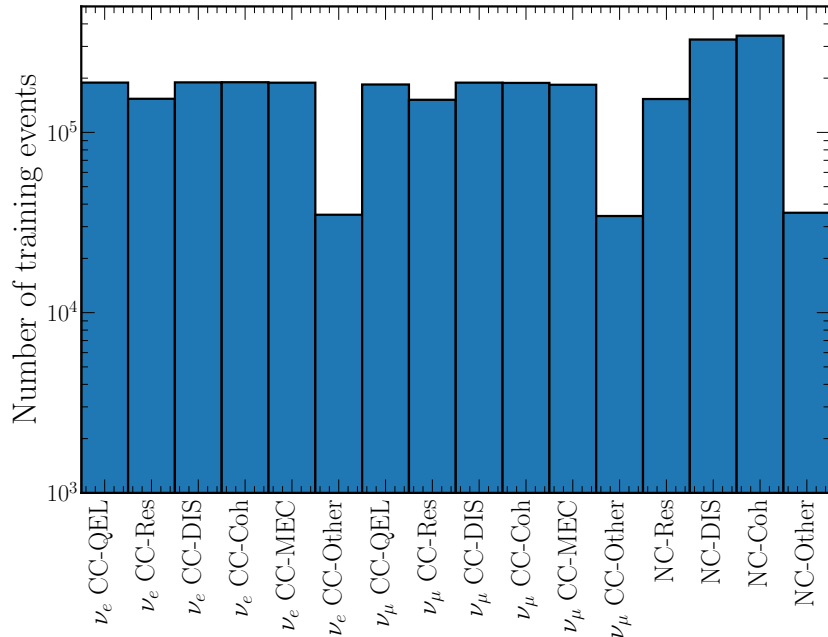


**Figure 6.41:** Number of training events per category for the uniform beam classification network training sample. All beam event interaction types are shown.

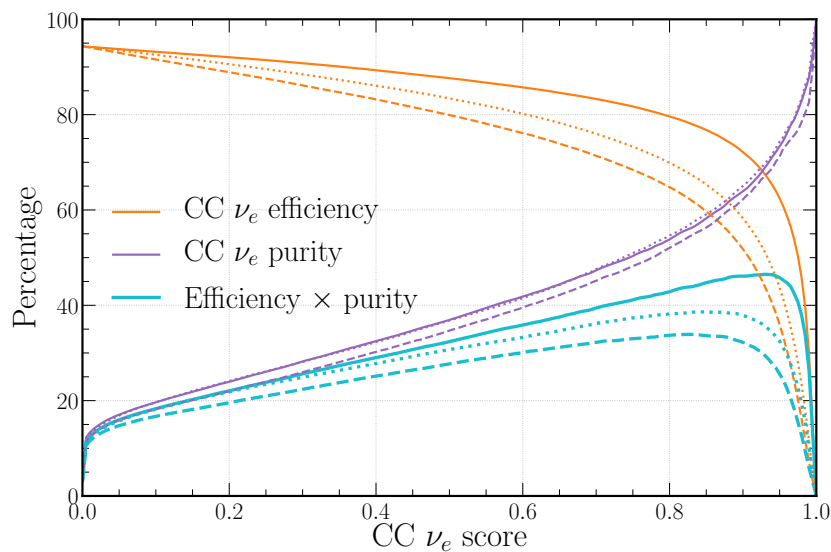


**Figure 6.42:** CC  $\nu_e$  efficiency, purity, and efficiency  $\times$  purity curves for different values of CC  $\nu_e$  score selection for the different training samples. The *flux* sample curves are shown by the solid lines, the *uniform* sample curves by the dashed lines, and the *both* curves by the dotted lines.

Metric	Flux	Uniform	Both
Maximum FOM	<b>0.465</b>	0.339	0.386
High Score Eff	<b>0.877</b>	0.799	0.834
High Score Pur	<b>0.369</b>	0.347	0.368
ROC Integral	<b>0.826</b>	0.815	0.820
PR Integral	<b>0.712</b>	0.568	0.634

**Table 6.9:** Classification performance metrics for the different training samples.

In the beam classification case, the CNN learns to minimise the categorical cross-entropy loss function, maximising the fraction of total training events that are classified correctly. An easy way to do this is to become heavily biased by the averages of the sample used during training, such that the final performance does not generalise well to a different evaluation sample.

For the flux training sample case, less common event classes are ignored by the network during training, as solely focusing on the dominant classes is found to be the easiest way to minimise the loss. The effect of this can be seen in the interaction type classification matrices in Section 6.1.3 for CC-Coh and CC-MEC events. Future work should consider the use of a different loss function to promote learning for the less common interaction types and to maximise the physics sensitivity rather than majority accuracy.

### 6.4.3 Alternative architectures

The choice of CNN architecture is found to have a minimal impact on performance. Four different network architectures are considered: the default VGG based chipsnet architecture, an Inception (GoogLeNet) based architecture [123], a ResNet based architecture [146], and an Inception-ResNet based architecture [147]. Each is modified to fit the standard chipsnet pattern with separate initial branches for each event map followed by a series of combined layers. For a fair comparison, each network is scaled so that they all have approximately the same number of trainable parameters as the default VGG based architecture.

A beam classification network is trained using each network architecture with individually optimised hyperparameters (using SHERPA). For each network architecture, the classification performance metrics are presented in Table 6.10 along with the number of

Metric	VGG	Inception	ResNet	Inception-ResNet
Number of pars	17,225,296	16,893,216	<b>16,526,288</b>	17,145,238
Iter time (ms)	<b>88</b>	192	112	209
Maximum FOM	<b>0.465</b>	0.459	0.445	0.444
High Score Eff	<b>0.877</b>	0.870	0.869	0.874
High Score Pur	0.369	0.373	<b>0.374</b>	0.349
ROC Integral	<b>0.825</b>	0.825	0.824	0.824
PR Integral	<b>0.712</b>	0.706	0.688	0.699

**Table 6.10:** Classification performance metrics for the different network architectures.

trainable parameters (Number of pars) and the time taken in milliseconds to complete a single training iteration step (Iter time).

Only small performance differences are observed across the different CNN architectures, with the simplest and least modern, the VGG architecture, proving the highest performing. Furthermore, the VGG architecture provides the fastest training step iteration time by a significant margin, leading to drastically lower overall training times.

The other architectures are primarily the result of advances aimed at improving the classification of real-world objects, such as cars, trees, and dogs, with image sizes typically  $256 \times 256$  pixels or greater. Therefore, it is likely that the task of learning subtle changes in Cherenkov ring topologies, with a relatively limited number of classes, on small  $64 \times 64$  images, does not require the advanced feature representation they provide. Using the increased complexity models instead introduces additional bias, acting to decrease performance instead of providing additional discriminating power.



# Chapter 7

## Summary and conclusion

This thesis presented a range of work for the CHIPS neutrino detector R&D project. CHIPS puts forward a novel water Cherenkov based concept to counter the vast expense, increased complexity, and long construction time expected from future long-baseline neutrino oscillation experiments. As detailed, this feat is possible via a series of steps: deploying detector modules in bodies of water on the Earth’s surface rather than deep underground; using commercially available rather than bespoke components wherever possible; and optimising photocathode coverage to study accelerator beam neutrinos exclusively. These steps reduce the total cost per kt of sensitive mass to between \$200k-\$300k and should allow for megaton scale detectors to become a reality.

Moreover, CHIPS detector modules are expected to be relatively easy to build, quick to deploy, and can be upgraded once operational, making them a much more attractive proposition when resources are constrained. It is hoped that future CHIPS detectors will be able to help answer some of the key unsolved questions of neutrino physics, such as the mass hierarchy ambiguity and the search for CP violation in neutrino oscillations.

During the summer of 2019 a CHIPS prototype, CHIPS-5 was deployed into the Wentworth 2W disused mine pit in northern Minnesota, USA. Although CHIPS-5 is not yet fully proven and future plans are still in flux, the amount of knowledge gained during its construction, deployment, and initial commissioning can not be understated. Alongside proving that a large CHIPS detector module can be constructed and deployed, CHIPS-5 acted as a brilliant testbed for the development of the CHIPS data acquisition system.

Notably, the use of commercially available single-board Beaglebone machines and the open-source Elasticsearch monitoring solution were found to be highly successful. Within

both future CHIPS detectors, and hopefully the broader experimental particle physics field, bespoke components should continue to be phased out, with commercially available or open-source components used instead. Not only does this drastically reduce the implementation effort required by collaborators and cost, but leads to a much improved final result due to the pooling of resources.

As is the case within the world around us, future CHIPS concept detectors will also make ever-increasing use of modern deep learning techniques. This comes as a direct result of the dramatic improvement in CHIPS-5 reconstruction and classification performance brought about by the principal work presented in this thesis. Three forms of a Convolutional Neural Network have been trained to reject cosmic muon events, classify beam events, and estimate neutrino energies, all using only a slightly modified version of the raw detector event as input. This new approach replaces the standard likelihood-based reconstruction and simple neural network classification, greatly increasing generalisability and processing speed, whilst reducing human influence (bias).

With the primary goal of selecting an efficient and pure appeared CC  $\nu_e$  signal, the new approach is found to provide excellent performance. The vast cosmic muon background of CHIPS-5 is found to be rejected (without the help of a veto) by a factor of  $\sim 1.5 \times 10^{-8}$ , leading to negligible contamination of the beam selection. Beam classification performance is found to be surprisingly comparable to the more complex NOvA and T2K experiments, with a  $70.9 \pm 0.4\%$  efficiency and  $71.0 \pm 0.6\%$  purity of the selected CC  $\nu_e$  sample when both the appeared and intrinsic CC  $\nu_e$  beam components are considered signal. Similarly, neutrino energy estimation is relatively comparable to other experiments. A 10.3% and 12.6% neutrino energy resolution on signal CC  $\nu_e$  and CC  $\nu_\mu$  events respectively, is achieved, falling to 7.1% and 6.2% when just quasi-elastic events are considered.

Not only are the trained convolutional neural networks found to provide excellent performance, but their inner workings are found to be explainable and their outputs robust to distributional changes in the input. These findings rebut the common and justified concern that they are too often just used as a black box (input in, outputs out). Cherenkov ring and Hough peak features are clearly extracted from the input images, resulting in a learnt representation of the inputs that are seen to have strong discriminating power between categories when visualised using the t-SNE technique. Additionally, realistic modifications to the input hit times and charges, as well as the addition of random noise, are all found to have a negligible effect on output performance.

It is sincerely hoped that other water Cherenkov neutrino experiments will take inspiration from, and then build upon the work presented in this thesis for their own Convolutional Neural Network implementations. Although the results presented in this work are incredibly compelling, there are still clear avenues for exploration and improvement. These are all principally related to the critical performance drivers outlined within this thesis.

Firstly, generating the input event maps to focus on the underlying Cherenkov profiles is found be incredibly important; therefore, any methodology to remove distortions further or more accurately determine the interaction vertex position will be beneficial. Secondly, the distribution of events (in energy or type) used within the training sample heavily impacts performance; thus, a comprehensive study of this behaviour could optimise the sample used. Finally, multi-task learning clearly shows promise, with further trial-and-error or a more generalised approach likely to uncover additional useful tasks.

It is highly likely that the true potential of these methods is just beginning to be realised. As is always the case, only time will tell.



# Bibliography

- [1] J. Chadwick, “The intensity distribution in the magnetic spectrum of beta particles from radium (B+C)”, Verh. Phys. Gesell. **16**, 383–391 (1914).
- [2] W. Pauli, “Letter to the radioactive ladies and gentlemen”, Letter to the physical society of Tübingen (1930).
- [3] E. Fermi, “An attempt of a theory of beta radiation”, Zeitschrift für Physik **88**, 161–177 (1934).
- [4] H. Bethe and R. Peierls, “The ‘Neutrino’”, Nature **133**, 532–532 (1934).
- [5] C. Cowan, F. Reines, F. Harrison, H. Kruse, and A. McGuire, “Detection of the free neutrino: a confirmation”, Science **124**, 103–104 (1956).
- [6] G. Danby, J. Gaillard, A. Konstantin, L. Lederman, B. Nari, M. Schwartz, and J. Steinberger, “Observation of high-energy neutrino reactions and the existence of two kinds of neutrinos”, Physical Review Letters **9**, 36–44 (1962).
- [7] G. Arnison et al. (UA1 Collaboration), “Experimental observation of lepton pairs of invariant mass around  $95 \text{ GeV}/c^2$  at the CERN SPS collider”, Physics Letters B **126**, 398–410 (1983).
- [8] G. Arnison et al., “Experimental observation of isolated large transverse energy electrons with associated missing energy at  $s=540 \text{ GeV}$ ”, Physics Letters B **122**, 103–116 (1983).
- [9] The ALEPH Collaboration, the DELPHI Collaboration, the L3 Collaboration, the OPAL Collaboration, the SLD Collaboration, the LEP Electroweak Working Group, the SLD electroweak, heavy flavour groups, “Precision electroweak measurements on the Z resonance”, Physics Reports **427**, 257–454 (2006).
- [10] M. L. Perl et al., “Evidence for anomalous lepton production in  $e^+ - e^-$  annihilation”, Physical Review Letters **35**, 1489–1492 (1975).
- [11] K. Kodama et al., “Observation of tau neutrino interactions”, Physics Letters B **504**, 218–224 (2001).

- [12] P. Zyla et al. (Particle Data Group Collaboration), “Review of particle physics”, Progress of Theoretical and Experimental Physics **2020**, 083C01 (2020).
- [13] R. Davis Jr, D. Harmer, and K. Hoffman, “Search for neutrinos from the sun”, Physical Review Letters **20**, 1205 (1968).
- [14] J. Bahcall, N. Bahcall, and G. Shaviv, “Present status of the theoretical predictions for the Cl-36 solar neutrino experiment”, Physical Review Letters **20**, 1209 (1968).
- [15] K. Hirata et al. (Kamiokande-II Collaboration), “Observation of B-8 solar neutrinos in the Kamiokande-II detector”, Physical Review Letters **63**, 16 (1989).
- [16] A. Abazov et al. (SAGE Collaboration), “Search for neutrinos from the sun using the reaction Ga-71 ( $\nu_e e^-$ ) Ge-71”, Physical Review Letters **67**, 3332 (1991).
- [17] P. Anselmann et al. (GALLEX Collaboration), “GALLEX results from the first 30 solar neutrino runs”, Physics Letters B **327**, 377–385 (1994).
- [18] K. Hirata et al. (Kamiokande-II Collaboration), “Experimental study of the atmospheric neutrino flux”, Physics Letters B **205**, 416 (1988).
- [19] R. Becker-Szendy et al., “Electron-and muon-neutrino content of the atmospheric flux”, Physical Review D **46**, 3720 (1992).
- [20] T. Kajita et al. (Super-Kamiokande Collaboration), “Atmospheric neutrino results from Super-Kamiokande and Kamiokande - Evidence for  $\nu_\mu$  oscillations”, Nuclear Physics B Proceedings Supplements **77**, 123–132 (1999).
- [21] Q. R. Ahmad et al. (SNO Collaboration), “Measurement of day and night neutrino energy spectra at SNO and constraints on neutrino mixing parameters”, Physical Review Letters **89**, 011302 (2002).
- [22] Wikipedia contributors, *Standard Model — Wikipedia, The Free Encyclopedia*, [https://en.wikipedia.org/w/index.php?title=Standard\\_Model&oldid=970721485](https://en.wikipedia.org/w/index.php?title=Standard_Model&oldid=970721485).
- [23] N. Aghanim et al. (Planck Collaboration), “Planck 2018 results. VI. Cosmological parameters”, (2018), arXiv:1807.06209 [astro-ph.CO].
- [24] M. Aker et al. (KATRIN Collaboration), “Improved upper limit on the neutrino mass from a direct kinematic method by KATRIN”, Physical Review Letters **123**, 10.1103/physrevlett.123.221802 (2019).
- [25] Z. Maki, M. Nakagawa, and S. Sakata, “Remarks on the unified model of elementary particles”, Progress of Theoretical Physics **28**, 870–880 (1962).

- [26] B. Pontecorvo, “Neutrino experiments and the problem of conservation of leptonic charge”, Soviet Physics JETP **26**, 984–988 (1968).
- [27] V. Gribov and B. Pontecorvo, “Neutrino astronomy and lepton charge”, Physics Letters B **28**, 493–496 (1969).
- [28] L. Wolfenstein, “Neutrino oscillations in matter”, Physical Review D **17**, 2369–2374 (1978).
- [29] S. Mikheyev and A. Smirnov, “Resonance amplification of oscillations in matter and spectroscopy of solar neutrinos”, Soviet Journal of Nuclear Physics **42**, 913–917 (1985).
- [30] T. Katori, “Meson exchange current (MEC) models in neutrino interaction generators”, AIP Conference Proceedings **1663**, 030001 (2015), arXiv:1304 . 6014 [nucl-th].
- [31] C. Andreopoulos et al., “The GENIE neutrino Monte Carlo generator”, Nucl. Instrum. Meth. A **614**, 87–104 (2010), arXiv:0905 . 2517 [hep-ph].
- [32] C. Andreopoulos, C. Barry, S. Dytman, H. Gallagher, T. Golan, R. Hatcher, G. Perdue, and J. Yarba, “The GENIE neutrino Monte Carlo generator: physics and user manual”, (2015), arXiv:1510 . 05494 [hep-ph].
- [33] J. A. Formaggio and G. P. Zeller, “From eV to EeV: neutrino cross sections across energy scales”, Reviews of Modern Physics **84**, 1307–1341 (2012).
- [34] I. Esteban, M. Gonzalez-Garcia, A. Hernandez-Cabezudo, M. Maltoni, and T. Schwetz, “Global analysis of three-flavour neutrino oscillations: synergies and tensions in the determination of  $\theta_{23}$ ,  $\delta_{CP}$ , and the mass ordering”, Journal of High Energy Physics **2019**, 1–35 (2019).
- [35] I. Esteban, M. Gonzalez-Garcia, M. Maltoni, T. Schwetz, and A. Zhou, “The fate of hints: updated global analysis of three-flavor neutrino oscillations”, (2020), arXiv:2007 . 14792 [hep-ph].
- [36] B. T. Cleveland, T. Daily, J. Raymond Davis, J. R. Distel, K. Lande, C. K. Lee, P. S. Wildenhain, and J. Ullman, “Measurement of the solar electron neutrino flux with the Homestake chlorine detector”, The Astrophysical Journal **496**, 505–526 (1998).
- [37] F. Kaether, W. Hampel, G. Heusser, J. Kiko, and T. Kirsten, “Reanalysis of the GALLEX solar neutrino flux and source experiments”, Physics Letters B **685**, 47–54 (2010).

- [38] J. N. Abdurashitov et al. (SAGE Collaboration), “Measurement of the solar neutrino capture rate with gallium metal. III. Results for the 2002–2007 data-taking period”, *Physical Review C* **80**, 015807 (2009).
- [39] J. Maneira et al. (SNO Collaboration), “Combined analysis of all three phases of solar neutrino data from the Sudbury neutrino observatory”, in 13th ICATPP Conference on Astroparticle, Particle, Space Physics and Detectors for Physics Applications (2012), pp. 360–366.
- [40] J. Hosaka et al. (The Super-Kamiokande Collaboration), “Solar neutrino measurements in Super-Kamiokande-I”, *Physical Review D* **73**, 112001 (2006).
- [41] J. P. Cravens et al. (The Super-Kamiokande Collaboration), “Solar neutrino measurements in Super-Kamiokande-II”, *Physical Review D* **78**, 032002 (2008).
- [42] K. Abe et al. (The Super-Kamiokande Collaboration), “Solar neutrino results in Super-Kamiokande-III”, *Physical Review D* **83**, 052010 (2011).
- [43] Y. Nakano et al., “Solar neutrino results from Super-Kamiokande”, *Proceedings of Science* **ICHEP2016**, 462 (2017).
- [44] G. Bellini et al. (Borexino Collaboration), “Precision measurement of the  $^7\text{Be}$  solar neutrino interaction rate in Borexino”, *Physical Review Letters* **107**, 141302 (2011).
- [45] G. Bellini et al. (Borexino Collaboration), “Measurement of the solar  $^8\text{B}$  neutrino rate with a liquid scintillator target and 3 MeV energy threshold in the Borexino detector”, *Physical Review D* **82**, 033006 (2010).
- [46] G. Bellini, J. Benziger, D. Bick, G. Bonfini, D. Bravo, B. Caccianiga, L. Cadonati, F. Calaprice, A. Caminata, P. Cavalcante, et al., “Neutrinos from the primary proton–proton fusion process in the sun”, *Nature* **512**, 383–386 (2014).
- [47] A. Gando et al. (The KamLAND Collaboration), “Constraints on  $\theta_{13}$  from a three-flavor oscillation analysis of reactor antineutrinos at KamLAND”, *Physical Review D* **83**, 052002 (2011).
- [48] A. Karle, J. Ahrens, J. Bahcall, X. Bai, T. Becka, K.-H. Becker, D. Besson, D. Berley, E. Bernardini, D. Bertrand, et al., “IceCube – the next generation neutrino telescope at the south pole”, *Nuclear Physics B-Proceedings Supplements* **118**, 388–395 (2003).
- [49] M. G. Aartsen et al. (IceCube Collaboration), “Determining neutrino oscillation parameters from atmospheric muon neutrino disappearance with three years of IceCube DeepCore data”, *Physical Review D* **91**, 072004 (2015).

- [50] K. Abe et al. (Super-Kamiokande Collaboration), “Atmospheric neutrino oscillation analysis with external constraints in Super-Kamiokande I-IV”, Physical Review D **97**, 072001 (2018).
- [51] P. Adamson et al. (MINOS Collaboration), “Measurement of neutrino and antineutrino oscillations using beam and atmospheric data in MINOS”, Physical Review Letters **110**, 251801 (2013).
- [52] P. Adamson et al. (MINOS Collaboration), “Electron neutrino and antineutrino appearance in the full MINOS data sample”, Physical Review Letters **110**, 171801 (2013).
- [53] M. A. Acero et al. (NOvA Collaboration), “First measurement of neutrino oscillation parameters using neutrinos and antineutrinos by NOvA”, Physical Review Letters **123**, 151803 (2019).
- [54] A. Himmel, *New oscillation results from the NOvA experiment*, <https://zenodo.org/record/4142045>, Talk given at the XXIX International Conference on Neutrino Physics and Astrophysics, Chicago, USA, July 2020.
- [55] P. Dunne, *Latest neutrino oscillation results from T2K*, <https://zenodo.org/record/4154355>, Talk given at the XXIX International Conference on Neutrino Physics and Astrophysics, Chicago, USA, July 2020.
- [56] F. An et al. (Daya Bay Collaboration), “Observation of electron-antineutrino disappearance at Daya Bay”, Physical Review Letters **108**, 171803 (2012).
- [57] F. P. An et al., “Improved measurement of the reactor antineutrino flux and spectrum at Daya Bay”, Chinese Physics C **41**, 013002 (2017).
- [58] J. Ahn et al. (RENO Collaboration), “Observation of reactor electron antineutrinos disappearance in the RENO experiment”, Physical Review Letters **108**, 191802 (2012).
- [59] G. Bak et al. (RENO Collaboration), “Measurement of reactor antineutrino oscillation amplitude and frequency at RENO”, Physical Review Letters **121**, 201801 (2018).
- [60] Y. Abe et al. (Double Chooz Collaboration), “Reactor electron antineutrino disappearance in the Double Chooz experiment”, Physical Review D **86**, 052008 (2012), arXiv:1207.6632 [hep-ex].
- [61] K. Abe et al. (T2K Collaboration), “Evidence of electron neutrino appearance in a muon neutrino beam”, Physical Review D **88**, 032002 (2013).

- [62] P. Adamson and other (NOvA Collaboration), “First measurement of electron neutrino appearance in NOvA”, *Physical Review Letters* **116**, 151806 (2016).
- [63] F. An, G. An, Q. An, V. Antonelli, E. Baussan, J. Beacom, L. Bezrukov, S. Blyth, R. Brugnera, M. B. Avanzini, and et al., “Neutrino physics with JUNO”, *Journal of Physics G: Nuclear and Particle Physics* **43**, 030401 (2016).
- [64] A. de Gouvea et al., “Neutrinos”, (2013), arXiv:1310.4340 [hep-ex].
- [65] K. Abe and other (T2K Collaboration), “Search for  $CP$  violation in neutrino and antineutrino oscillations by the T2K experiment with  $2.2 \times 10^{21}$  protons on target”, *Physical Review Letters* **121**, 171802 (2018).
- [66] R. Acciarri et al., “Long-Baseline Neutrino Facility (LBNF) and Deep Underground Neutrino Experiment (DUNE) conceptual design report volume 1: the LBNF and DUNE projects”, (2016), arXiv:1601.05471 [physics.ins-det].
- [67] B. Abi et al. (DUNE Collaboration), “Deep Underground Neutrino Experiment (DUNE), far detector technical design report, Volume II DUNE physics”, (2020), arXiv:2002.03005 [hep-ex].
- [68] U.S. Department Of Energy Office Of Project Management Oversight And Assessments, *Independent cost review of the Long Baseline Neutrino Facility/Deep Underground Neutrino Experiment project at Fermi National Accelerator Laboratory*, Aug. 2015.
- [69] American Institute of Physics, *FY21 budget request: DOE office of science*, <https://www.aip.org/fyi/2020/fy21-budget-request-doe-office-science>, Mar. 2020.
- [70] Hyper-Kamiokande Proto-Collaboration, “Hyper-Kamiokande design report”, (2018), arXiv:1805.04163 [physics.ins-det].
- [71] Hyper-Kamiokande Working Group, “A long baseline neutrino oscillation experiment using J-PARC neutrino beam and Hyper-Kamiokande”, (2014), arXiv:1412.4673 [physics.ins-det].
- [72] Nature, *Japan will build the worlds largest neutrino detector*, <https://www.nature.com/articles/d41586-019-03874-w>, Dec. 2019.
- [73] P. Adamson et al. (CHIPS Collaboration), “CHerenkov detectors In mine PitS (CHIPS) letter of intent to FNAL”, (2013), arXiv:1307.5918 [physics.ins-det].
- [74] A. Perch, “Construction of the CHIPS-M prototype and simulations of a 10 kiloton module”, (2015), arXiv:1505.00042 [physics.ins-det].

- [75] M. Pfützner, “Prototype detection unit for the CHIPS experiment”, Journal of Physics: Conference Series **888**, 012059 (2017).
- [76] M. Pfützner, “Sensitivity study and first prototype tests for the CHIPS neutrino detector R&D program”, [https://discovery.ucl.ac.uk/id/eprint/10052874/1/Pfutzner\\_thesis.pdf](https://discovery.ucl.ac.uk/id/eprint/10052874/1/Pfutzner_thesis.pdf), PhD thesis (University College London, July 2018).
- [77] F. Amat et al. (CHIPS Collaboration), “Measuring the attenuation length of water in the CHIPS-M water Cherenkov detector”, Nuclear Instruments and Methods in Physics Research Section A: Accelerators, Spectrometers, Detectors and Associated Equipment **844**, 108–115 (2017).
- [78] M. Campbell, “Measuring neutrino oscillations in the NOvA and CHIPS Detectors”, [https://discovery.ucl.ac.uk/id/eprint/10097512/1/Campbell\\_10097512\\_thesis\\_sig-removed.pdf](https://discovery.ucl.ac.uk/id/eprint/10097512/1/Campbell_10097512_thesis_sig-removed.pdf), PhD thesis (University College London, Aug. 2020).
- [79] E. Adde Chase, “Sensitivity determination in the CHIPS neutrino detector”, <https://scholarworks.wm.edu/honortheses/927>, MA thesis (College of William and Mary, 2016).
- [80] K. Lang, “Prospects for CHIPS (R&D of water Cherenkov detectors in mine pits)”, (2015), arXiv:1504.08330 [physics.ins-det].
- [81] D. van Eijk, “Electronics and DAQ for the CHIPS experiment”, (2018), arXiv:1805.12206 [physics.ins-det].
- [82] P. Adamson et al., “The NuMI neutrino beam”, Nuclear Instruments and Methods in Physics Research Section A: Accelerators, Spectrometers, Detectors and Associated Equipment **806**, 279–306 (2016).
- [83] K. S. McFarland (MINERvA), “MINERvA: a dedicated neutrino scattering experiment at NuMI”, Nuclear Physics B Proceedings Supplements **159**, 107–112 (2006), arXiv:physics/0605088.
- [84] A. J. Perch, “Three-flavour neutrino oscillations with MINOS and CHIPS”, [https://discovery.ucl.ac.uk/id/eprint/1551615/1/Perch\\_ID\\_thesis.pdf](https://discovery.ucl.ac.uk/id/eprint/1551615/1/Perch_ID_thesis.pdf), PhD thesis (University College London, Jan. 2017).
- [85] K. Hanson and O. Tarasova, “Design and production of the IceCube digital optical module”, Nuclear Instruments and Methods in Physics Research Section A: Accelerators, Spectrometers, Detectors and Associated Equipment **567**, Proceedings of the 4th International Conference on New Developments in Photodetection, 214–217 (2006).

- [86] R. Bruijn and D. van Eijk, “The KM3NeT multi-PMT digital optical module”, PoS **ICRC2015**, 1157 (2016).
- [87] *HZC PMT Datasheet*, <http://www.hzcpotonics.com/products/ProductManual.pdf>.
- [88] U. Katz, K. Consortium, et al., “Status of the KM3NeT project”, Nuclear Instruments and Methods in Physics Research Section A: Accelerators, Spectrometers, Detectors and Associated Equipment **602**, 40–46 (2009).
- [89] A. Martinez et al., “Letter of intent for KM3NeT 2.0”, Journal of Physics G: Nuclear and Particle Physics **43**, 084001 (2016).
- [90] *Hamamatsu R6091 PMT Datasheet*, <https://www.hamamatsu.com/resources/pdf/etd/R6091 TPMH1114E.pdf>.
- [91] A. Blake, S. Germani, Y. B. Pan, A. J. Perch, M. M. Pfützner, J. Thomas, and L. H. Whitehead (CHIPS Collaboration), “CHIPS event reconstruction and design optimisation”, (2016), arXiv:1612.04604 [physics.ins-det].
- [92] *WCSim git repository*, <https://github.com/WCSim/WCSim>.
- [93] S. Agostinelli et al., “Geant4 – a simulation toolkit”, Nuclear Instruments and Methods in Physics Research Section A: Accelerators, Spectrometers, Detectors and Associated Equipment **506**, 250–303 (2003).
- [94] J. Allison et al., “Geant4 developments and applications”, IEEE Transactions on Nuclear Science **53**, 270–278 (2006).
- [95] J. Allison et al., “Recent developments in Geant4”, Nuclear Instruments and Methods in Physics Research Section A: Accelerators, Spectrometers, Detectors and Associated Equipment **835**, 186–225 (2016).
- [96] *WCSim: How to add your own photodetector tutorial*, <https://github.com/WCSim/WCSim/wiki/Tutorial:-How-to-add-your-own-photodetector>.
- [97] C. Hagmann, D. Lange, J. Verbeke, and D. Wright, “Cosmic-ray shower library (CRY)”, (2012).
- [98] C. Hagmann, D. Lange, and D. Wright, “Monte Carlo simulation of proton-induced cosmic-ray cascades in the atmosphere”, (2012).
- [99] S. Klimushin, E. Bugaev, and I. A. Sokalski, “Precise parametrizations of muon energy losses in water”, in 27th international cosmic ray conference, Vol. 3 (June 2001), p. 1009, arXiv:hep-ph/0106010.

- [100] *chipsgen git repository*, <https://gitlab.com/chipsneutrino/chips-gen>.
- [101] S. V. Cao, H. Junting, L. Karol, and N. Federico, “Cosmic ray muon rates in water Cherenkov detectors at shallow depths”, (2013).
- [102] E. V. Bugaev, A. Misaki, V. A. Naumov, T. Sinegovskaya, S. Sinegovsky, and N. Takahashi, “Atmospheric muon flux at sea level, underground, and underwater”, Physical Review D **58**, 054001 (1998), arXiv:hep-ph/9803488.
- [103] M. Lipiski, T. Wostowski, J. Serrano, and P. Alvarez, “White Rabbit: a PTP application for robust sub-nanosecond synchronization”, in 2011 ieee international symposium on precision clock synchronization for measurement, control and communication (2011), pp. 25–30.
- [104] *WR switch open hardware repository*, <https://ohwr.org/projects/white-rabbit/wiki/switch>.
- [105] *WR chromium switch webpage*, <https://redmine.nikhef.nl/et/projects/chromium/wiki/Backplane-20SFP>.
- [106] *WR-LEN webpage*, <https://sevensols.es/index.php/index/timing-products/wr-len>.
- [107] J. D. Cockcroft and E. T. Walton, “Experiments with high velocity positive ions.(i) further developments in the method of obtaining high velocity positive ions”, Proceedings of the royal society of London. Series A, containing papers of a mathematical and physical character **136**, 619–630 (1932).
- [108] S. Biagi, T. Chiarusi, P. Piattelli, and D. Real (KM3NeT), “The data acquisition system of the KM3NeT detector”, PoS **ICRC2015**, 1172 (2016).
- [109] *Beaglebone webpage*, <https://beagleboard.org/bone>.
- [110] S. Aiello et al. (KM3NeT), “KM3NeT front-end and readout electronics system: hardware, firmware and software”, J. Astron. Telesc. Instrum. Syst. **5**, 046001 (2019), arXiv:1907.06453 [astro-ph.IM].
- [111] *microDAQ git repository*, <https://github.com/WIPACrepo/microdaq>.
- [112] *chipsdaq git repository*, <https://gitlab.com/chipsneutrino/chips-daq>.
- [113] *BOOST.Aasio webpage*, [https://www.boost.org/doc/libs/1\\_66\\_0/doc/html/boost\\_asio.html](https://www.boost.org/doc/libs/1_66_0/doc/html/boost_asio.html).
- [114] *Elasticsearch webpage*, <https://www.elastic.co/elasticsearch>.
- [115] *Elastic stack webpage*, <https://www.elastic.co/elastic-stack>.

- [116] *Kibana webpage*, <https://www.elastic.co/kibana>.
- [117] *Kibana webpage*, <https://elastalert.readthedocs.io/en/latest/elastalert.html>.
- [118] K. Fukushima and S. Miyake, “Neocognitron: a self-organizing neural network model for a mechanism of visual pattern recognition”, in Competition and cooperation in neural nets (1982), pp. 267–285.
- [119] I. Goodfellow, Y. Bengio, and A. Courville, *Deep Learning*, <http://www.deeplearningbook.org> (MIT Press, 2016).
- [120] F. Psihas, M. Groh, C. Tunnell, and K. Warburton, “A Review on Machine Learning for Neutrino Experiments”, (2020), arXiv:2008.01242 [physics.comp-ph].
- [121] R. Perrault, Y. Shoham, E. Brynjolfsson, J. Clark, J. Etchemendy, B. Grosz, T. Lyons, J. Manyika, S. Mishra, and J. C. Niebles, “The AI index 2019 annual report”, AI Index Steering Committee, Human-Centered AI Institute, Stanford University, Stanford, CA (2019).
- [122] A. Aurisano, A. Radovic, D. Rocco, A. Himmel, M. Messier, E. Niner, G. Pawloski, F. Psihas, A. Sousa, and P. Vahle (NOvA Collaboration), “A convolutional neural network neutrino event classifier”, Journal of Instrumentation **11**, P09001–P09001 (2016).
- [123] C. Szegedy, W. Liu, Y. Jia, P. Sermanet, S. Reed, D. Anguelov, D. Erhan, V. Vanhoucke, and A. Rabinovich, “Going deeper with convolutions”, in Proceedings of the IEEE conference on computer vision and pattern recognition (2015), pp. 1–9.
- [124] F. Psihas, E. Niner, M. Groh, R. Murphy, A. Aurisano, A. Himmel, K. Lang, M. D. Messier, A. Radovic, and A. Sousa (NOvA Collaboration), “Context-enriched identification of particles with a convolutional network for neutrino events”, Physical Review D **100**, 10.1103/physrevd.100.073005 (2019).
- [125] P. Baldi, J. Bian, L. Hertel, and L. Li (NOvA Collaboration), “Improved energy reconstruction in NOvA with regression convolutional neural networks”, Physical Review D **99**, 10.1103/physrevd.99.012011 (2019).
- [126] R. Acciarri et al., “Design and construction of the MicroBooNE detector”, Journal of Instrumentation **12**, P02017 (2017).
- [127] R. Acciarri et al. (MicroBooNE Collaboration), “Convolutional neural networks applied to neutrino Events in a liquid argon time projection chamber”, Journal of Instrumentation **12**, P03011–P03011 (2017).

- [128] B. Abi et al. (DUNE Collaboration), “Neutrino interaction classification with a convolutional neural network in the DUNE far detector”, (2020), arXiv:2006.15052 [physics.ins-det].
- [129] E. Racah, S. Ko, P. Sadowski, W. Bhimji, C. Tull, S.-Y. Oh, P. Baldi, and Prabhat (Daya Bay Collaboration), “Revealing fundamental physics from the Daya Bay neutrino experiment using deep neural networks”, 2016 15th IEEE International Conference on Machine Learning and Applications (ICMLA), 10.1109/icmla.2016.0160 (2016).
- [130] S. Aiello et al. (KM3NeT Collaboration), “Event reconstruction for KM3NeT/ORCA using convolutional neural networks”, (2020), arXiv:2004.08254 [astro-ph.IM].
- [131] A. Abhishek, W. Fedorko, P. de Perio, N. Prouse, and J. Z. Ding, “Variational autoencoders for generative modelling of water Cherenkov detectors”, (2019), arXiv:1911.02369 [physics.ins-det].
- [132] R. Patterson, E. Laird, Y. Liu, P. Meyers, I. Stancu, and H. Tanaka (MiniBooNE Collaboration), “The extended-track event reconstruction for MiniBooNE”, Nuclear Instruments and Methods in Physics Research Section A: Accelerators, Spectrometers, Detectors and Associated Equipment **608**, 206–224 (2009).
- [133] A. Hocker et al., “TMVA - Toolkit for multivariate data analysis”, (2007), arXiv:physics/0703039.
- [134] M. Jiang et al. (Super-kamiokande Collaboration), “Atmospheric neutrino oscillation analysis with improved event reconstruction in Super-Kamiokande IV”, Progress of Theoretical and Experimental Physics **2019**, 053F01, 10.1093/ptep/ptz015 (2019), eprint: <https://academic.oup.com/ptep/article-pdf/2019/5/053F01/28638877/ptz015.pdf>.
- [135] A. D. Missant et al. (T2K Collaboration), “Improving the T2K oscillation analysis with fitQun: a new maximum-likelihood event reconstruction for Super-Kamiokande”, JPhCS **888**, 012066 (2017).
- [136] *chips-reco git repository*, <https://gitlab.com/chipsneutrino/chips-reco>.
- [137] R. Brun and F. Rademakers, “ROOT – an object oriented data analysis framework”, Nuclear Instruments and Methods in Physics Research Section A: Accelerators, Spectrometers, Detectors and Associated Equipment **389**, New Computing Techniques in Physics Research V, 81–86 (1997).
- [138] P. Werbos, “Beyond regression: new tools for prediction and analysis in the behavioral sciences”, PhD thesis (Harvard University, 1974).

- [139] P. Mehta, M. Bukov, C.-H. Wang, A. G. Day, C. Richardson, C. K. Fisher, and D. J. Schwab, “A high-bias, low-variance introduction to machine learning for physicists”, *Physics Reports* **810**, 1–124 (2019).
- [140] Y. LeCun, Y. Bengio, and G. Hinton, “Deep Learning”, *Nature* **521**, 436–44 (2015).
- [141] J. Deng, W. Dong, R. Socher, L.-J. Li, K. Li, and L. Fei-Fei, “Imagenet: a large-scale hierarchical image database”, in *2009 IEEE conference on computer vision and pattern recognition* (Ieee, 2009), pp. 248–255.
- [142] A. Krizhevsky, I. Sutskever, and G. E. Hinton, “Imagenet classification with deep convolutional neural networks”, in *Advances in Neural Information Processing Systems* (2012), pp. 1097–1105.
- [143] *A Comprehensive Guide to Convolutional Neural Networks*, <https://towardsdatascience.com/a-comprehensive-guide-to-convolutional-neural-networks-the-eli5-way-3bd2b1164a53>.
- [144] K. Simonyan and A. Zisserman, “Very deep convolutional networks for large-scale image recognition”, (2014), arXiv:1409.1556 [cs.CV].
- [145] K. He, X. Zhang, S. Ren, and J. Sun, “Deep residual learning for image recognition”, in *Proceedings of the IEEE conference on computer vision and pattern recognition* (2016), pp. 770–778.
- [146] K. He, X. Zhang, S. Ren, and J. Sun, “Identity mappings in deep residual networks”, in *European Conference on Computer Vision* (Springer, 2016), pp. 630–645, arXiv:1603.05027 [cs.CV].
- [147] C. Szegedy, S. Ioffe, V. Vanhoucke, and A. Alemi, “Inception-v4, Inception-ResNet and the impact of residual connections on learning”, (2016), arXiv:1602.07261 [cs.CV].
- [148] M. Sandler, A. Howard, M. Zhu, A. Zhmoginov, and L.-C. Chen, “Mobilenetv2: inverted residuals and linear bottlenecks”, in *Proceedings of the IEEE conference on computer vision and pattern recognition* (2018), pp. 4510–4520.
- [149] M. Tan and Q. V. Le, “EfficientNet: rethinking model scaling for convolutional neural networks”, (2019), arXiv:1905.11946 [cs.LG].
- [150] S. Ioffe and C. Szegedy, “Batch Normalization: accelerating deep network training by reducing internal covariate shift”, in *Proceedings of the 32nd International Conference on International Conference on Machine Learning - Volume 37, ICML’15* (2015), pp. 448–456, arXiv:1502.03167 [cs.LG].

- [151] G. E. Hinton, N. Srivastava, A. Krizhevsky, I. Sutskever, and R. Salakhutdinov, “Improving neural networks by preventing co-adaptation of feature detectors”, (2012), arXiv:1207.0580 [cs.NE].
- [152] *chipsnet git repository*, <https://gitlab.com/chipsneutrino/chips-net>.
- [153] Martn Abadi et al., *TensorFlow: large-scale machine learning on heterogeneous systems*, Software available from <https://www.tensorflow.org/>, 2015.
- [154] T. Theodore, “Particle identification in Cherenkov detectors using convolutional neural networks”, [https://particlephysics.ca/wp/wp-content/uploads/CERN\\_summer\\_student\\_report\\_2016\\_Theodore\\_Tomalty.pdf](https://particlephysics.ca/wp/wp-content/uploads/CERN_summer_student_report_2016_Theodore_Tomalty.pdf), MA thesis (University of Toronto, 2016).
- [155] J. Hu, L. Shen, and G. Sun, “Squeeze-and-excitation networks”, in Proceedings of the IEEE conference on computer vision and pattern recognition (2018), pp. 7132–7141.
- [156] F. Chollet et al., *Keras*, <https://keras.io>, 2015.
- [157] A. Kendall, Y. Gal, and R. Cipolla, “Multi-task learning using uncertainty to weigh losses for scene geometry and semantics”, in Proceedings of the IEEE conference on computer vision and pattern recognition (2018), pp. 7482–7491.
- [158] D. P. Kingma and J. Ba, “Adam: a method for stochastic optimization”, (2014), arXiv:1412.6980 [cs.LG].
- [159] L. Hertel, J. Collado, P. Sadowski, J. Ott, and P. Baldi, “Sherpa: robust hyperparameter optimization for machine learning”, (2020), arXiv:2005.04048 [cs.LG].
- [160] M. Acero et al. (NOvA), “New constraints on oscillation parameters from  $\nu_e$  appearance and  $\nu_\mu$  disappearance in the NOvA experiment”, Physical Review D **98**, 032012 (2018), arXiv:1806.00096 [hep-ex].
- [161] B. List, “Why and when to optimize efficiency times purity”, ETH Zurich internal note (2002).
- [162] K. Abe et al. (T2K Collaboration), “Measurements of neutrino oscillation in appearance and disappearance channels by the T2K experiment with  $6.6 \times 10^{20}$  protons on target”, Phys. Rev. D **91**, 072010 (2015).
- [163] L. v. d. Maaten and G. Hinton, “Visualizing data using t-SNE”, Journal of Machine Learning Research **9**, 2579–2605 (2008).

- [164] J. Djolonga, J. Yung, M. Tschannen, R. Romijnders, L. Beyer, A. Kolesnikov, J. Puigcerver, M. Minderer, A. D'Amour, D. Moldovan, S. Gelly, N. Houlsby, X. Zhai, and M. Lucic, “On robustness and transferability of convolutional neural networks”, (2020), arXiv:2007.08558 [cs.CV].
- [165] T. Saito and M. Rehmsmeier, “The precision-recall plot is more informative than the ROC plot when evaluating binary classifiers on imbalanced datasets”, PloS one **10**, e0118432 (2015).
- [166] L. Berns, “New ideas for ring formation and reconstruction in water-Cherenkov detectors”, Journal of Physics: Conference Series **1468**, 012165 (2020).

# List of figures

2.1	Hadron production cross-section measurements from LEP . . . . .	19
2.2	The particles of the Standard Model . . . . .	21
2.3	Feynman diagram of a charged-current coherent scattering interaction . .	27
2.4	Feynman diagram of a charged-current interaction . . . . .	27
2.5	Feynman diagram of a neutral-current interaction . . . . .	27
2.6	$\nu_e$ cross-sections on oxygen . . . . .	29
2.7	The total charged-current cross-section of $\nu_\mu$ and $\nu_\tau$ . . . . .	29
2.8	Three-flavour results from the NuFIT v5.0 global neutrino oscillation fit .	31
2.9	Diagram of the two possible neutrino mass hierarchies . . . . .	35
2.10	$\nu_e$ appearance probability for different $\delta_{CP}$ values . . . . .	35
3.1	Picture of the CHIPS-M detector just before deployment . . . . .	40
3.2	Schematic of the main components of the NuMI beamline . . . . .	41
3.3	Map of detector locations in the NuMI beam . . . . .	42
3.4	Muon neutrino flux for different NuMI detectors at different off-axis angles	43
3.5	Diagram of Cherenkov radiation emission . . . . .	44
3.6	Event display of a simulated beam CC $\nu_\mu$ event . . . . .	45
3.7	Event display of a simulated beam CC $\nu_e$ event . . . . .	46
3.8	Fraction of Cherenkov photons emitted as a function of distance . . . . .	46

---

3.9	Satellite view of the Wentworth 2W mine pit in northern Minnesota . . . . .	48
3.10	Aerial picture of the CHIPS-5 construction site . . . . .	49
3.11	Picture of the CHIPS-5 structural frame . . . . .	49
3.12	Graphical rendering of the CHIPS-5 detector . . . . .	50
3.13	Disassembled and assembled Nikhef PMT housing components . . . . .	52
3.14	Pictures of the Madison PMT assembly . . . . .	52
3.15	Picture of a Nikhef POM . . . . .	53
3.16	Fraction of beam event Cherenkov photons that hit the detector walls as a function of the hit angle . . . . .	54
3.17	Graphical rendering of the top-cap Planar Optical Modules . . . . .	55
3.18	Picture of the CHIPS-5 filtration system . . . . .	56
3.19	Picture of the CHIPS-5 detector module with liner . . . . .	57
3.20	Some CHIPS-5 construction work . . . . .	58
3.21	More CHIPS-5 construction work . . . . .	58
3.22	Inside picture of CHIPS-5 just before deployment . . . . .	59
3.23	A cosmic muon event recorded within CHIPS-5 . . . . .	60
3.24	Illustrative diagram of a WCSim detector geometry . . . . .	61
3.25	Detector simulation PMT digitisation function . . . . .	63
3.26	NuMI neutrino flux at the CHIPS-5 detector location . . . . .	64
3.27	Expected CHIPS-5 cosmic muon rate as a function of water overburden depth . . . . .	65
4.1	Pictures of the White Rabbit timing hardware used within CHIPS-5 . . . . .	69
4.2	Picture of White Rabbit timing synchronisation seen within CHIPS-5 . . . . .	69
4.3	Diagram of the complete CHIPS-5 data acquisition and power distribution system . . . . .	71

4.4	Illustrative diagram showing how Time over Threshold is measured . . . . .	72
4.5	Labelled picture of the Nikhef POM electronics box . . . . .	73
4.6	Labelled picture of the high-level components of the CHIPS-5 DAQ system	74
4.7	Labelled picture of the components of the Madison POM electronics box .	75
4.8	Labelled picture of the Madison-container components . . . . .	76
4.9	Picture of a manifold connection within the CHIPS-5 detector . . . . .	77
4.10	Labelled picture of the high-level onshore components of the CHIPS-5 DAQ system . . . . .	78
4.11	Diagram of the CHIPS-5 software system in terms of the flow of data between components . . . . .	79
4.12	Diagram of the allowed states and transitions of the CHIPS-5 Finite State Machine . . . . .	81
4.13	Screenshot of a Kibana monitoring dashboard for CHIPS-5 . . . . .	85
5.1	The number of artificial intelligence papers submitted to arXiv . . . . .	88
5.2	Illustration of a simple neural network . . . . .	95
5.3	Common non-linear activation functions . . . . .	96
5.4	Illustrative diagram of the gradient descent process . . . . .	98
5.5	Example of a Convolutional Neural Network input grid and kernel . . . . .	102
5.6	Example of a convolution operation . . . . .	102
5.7	Example of pooling operation . . . . .	103
5.8	Illustration of a typical Convolutional Neural Network architecture . . . . .	104
5.9	Common Convolutional Neural Network architecture blocks . . . . .	105
5.10	Illustration of the early stopping procedure . . . . .	106
5.11	Example of dropout applied to a neural network . . . . .	107
5.12	Seeding estimated interaction vertex position resolutions . . . . .	109

---

5.13 Event map encoded 8-bit distributions . . . . .	110
5.14 Example of a CC resonant $\nu_e$ event . . . . .	110
5.15 Example of a CC DIS $\nu_\mu$ event . . . . .	111
5.16 Example of a NC DIS event . . . . .	111
5.17 Example of a cosmic muon event . . . . .	112
5.18 Illustrative diagram of the baseline chipsnet architecture . . . . .	113
5.19 Number of training events per category for the cosmic rejection network .	118
5.20 Loss and accuracy throughout training for the cosmic rejection network .	118
5.21 Number of training events per category for the beam classification network	120
5.22 Loss and accuracy throughout training for the beam classification network	122
5.23 Loss and mean absolute error throughout training for the energy estimation network . . . . .	124
6.1 Weighted spectrum of evaluation sample events . . . . .	127
6.2 Weighted spectrum of interaction types within the evaluation sample .	127
6.3 Plots detailing evaluation sample preselection cuts . . . . .	128
6.4 Distribution of cosmic score output values . . . . .	129
6.5 Distribution of cosmic score output values close to zero . . . . .	129
6.6 Distribution of escapes score output values . . . . .	131
6.7 Classification matrix for the combined category output of the beam classification network . . . . .	133
6.8 Distribution of CC $\nu_e$ scores from the trained beam classification network	134
6.9 CC $\nu_e$ efficiency, purity, and efficiency $\times$ purity curves . . . . .	135
6.10 Efficiency of the CC $\nu_e$ selection as a function of energy . . . . .	136
6.11 Distributions of standard event selection neural network output scores .	137
6.12 Distribution of CC $\nu_\mu$ scores from the trained beam classification network	138

6.13 CC $\nu_\mu$ efficiency, purity, and efficiency $\times$ purity curves . . . . .	139
6.14 Efficiency of the CC $\nu_\mu$ selection as a function of energy . . . . .	140
6.15 Classification matrix for the CC category output of the beam classification network . . . . .	141
6.16 Classification matrix for the NC category output of the beam classification network . . . . .	142
6.17 Distributions of true and CNN estimated neutrino energy . . . . .	143
6.18 Probability of CNN estimated neutrino energy given a true neutrino energy	144
6.19 Distributions of (reco-true)/true neutrino energies . . . . .	145
6.20 Distributions of (reco-true)/true neutrino energies by interaction type .	145
6.21 Means and standard deviations of fits to $\nu_e$ energy distributions . . . . .	147
6.22 Means and standard deviations of fits to $\nu_\mu$ energy distributions . . . . .	147
6.23 Distributions of (reco-true)/true primary charged lepton energies for the CNN and standard methods . . . . .	148
6.24 Reco-true distributions for the interaction vertex parameters for CC $\nu_e$ QEL events . . . . .	150
6.25 Reco-true distributions for the interaction vertex parameters for CC $\nu_\mu$ QEL events . . . . .	151
6.26 Distribution of CNN reconstructed $\nu_e$ energies for CC $\nu_e$ selected events .	152
6.27 Distribution of CNN reconstructed $\nu_\mu$ energies for CC $\nu_\mu$ selected events	152
6.28 Example CC quasi-elastic $\nu_e$ event for explainability . . . . .	153
6.29 Visualisations of trained feature map outputs . . . . .	154
6.30 Cosmic rejection network output t-SNE space . . . . .	155
6.31 Beam classification network output t-SNE space . . . . .	156
6.32 Hit-charge maps of highly CC $\nu_e$ like, CC $\nu_\mu$ like, and NC like events .	156
6.33 CC $\nu_e$ efficiency and purity curves for different levels of hit-time smearing	159

---

6.34 Receiver operating characteristic and precision-recall curves for different levels of hit-time smearing . . . . .	160
6.35 CC $\nu_e$ efficiency and purity curves for different levels of hit-charge smearing	161
6.36 CC $\nu_e$ efficiency and purity curves for different levels of hit-charge shifting	161
6.37 Distributions of (reco-true)/true $\nu_e$ energies for different levels of hit-charge smearing and shifting . . . . .	162
6.38 CC $\nu_e$ efficiency and purity curves for different levels of random noise . . . . .	164
6.39 Example CC resonant $\nu_e$ event shown for different input representations . . . . .	167
6.40 CC $\nu_e$ efficiency and purity curves for different input representations . . . . .	168
6.41 Number of training events per category for the uniform beam classification network training sample . . . . .	169
6.42 CC $\nu_e$ efficiency and purity curves for different training samples . . . . .	169

# List of tables

5.1	Table of input event map 8-bit cap-points and percentages . . . . .	109
6.1	Number of events passing successive selection cuts for each event category	131
6.2	Table showing CC $\nu_e$ selected event numbers, efficiencies and signal purity	135
6.3	Table showing CC $\nu_\mu$ selected event numbers, efficiencies and signal purity	139
6.4	Summary of CC $\nu_e$ and CC $\nu_\mu$ neutrino energy resolutions . . . . .	146
6.5	Classification performance metrics for different levels of hit-time smearing	159
6.6	Classification performance metrics for different levels of hit-charge smearing and shifting . . . . .	162
6.7	Classification performance metrics for different levels of random noise . .	164
6.8	Classification performance metrics for different input representations . . .	167
6.9	Classification performance metrics for different training samples . . . . .	170
6.10	Classification performance metrics for different network architectures . .	171